FACULTY OF ENGINEERING
AND ARCHITECTURE

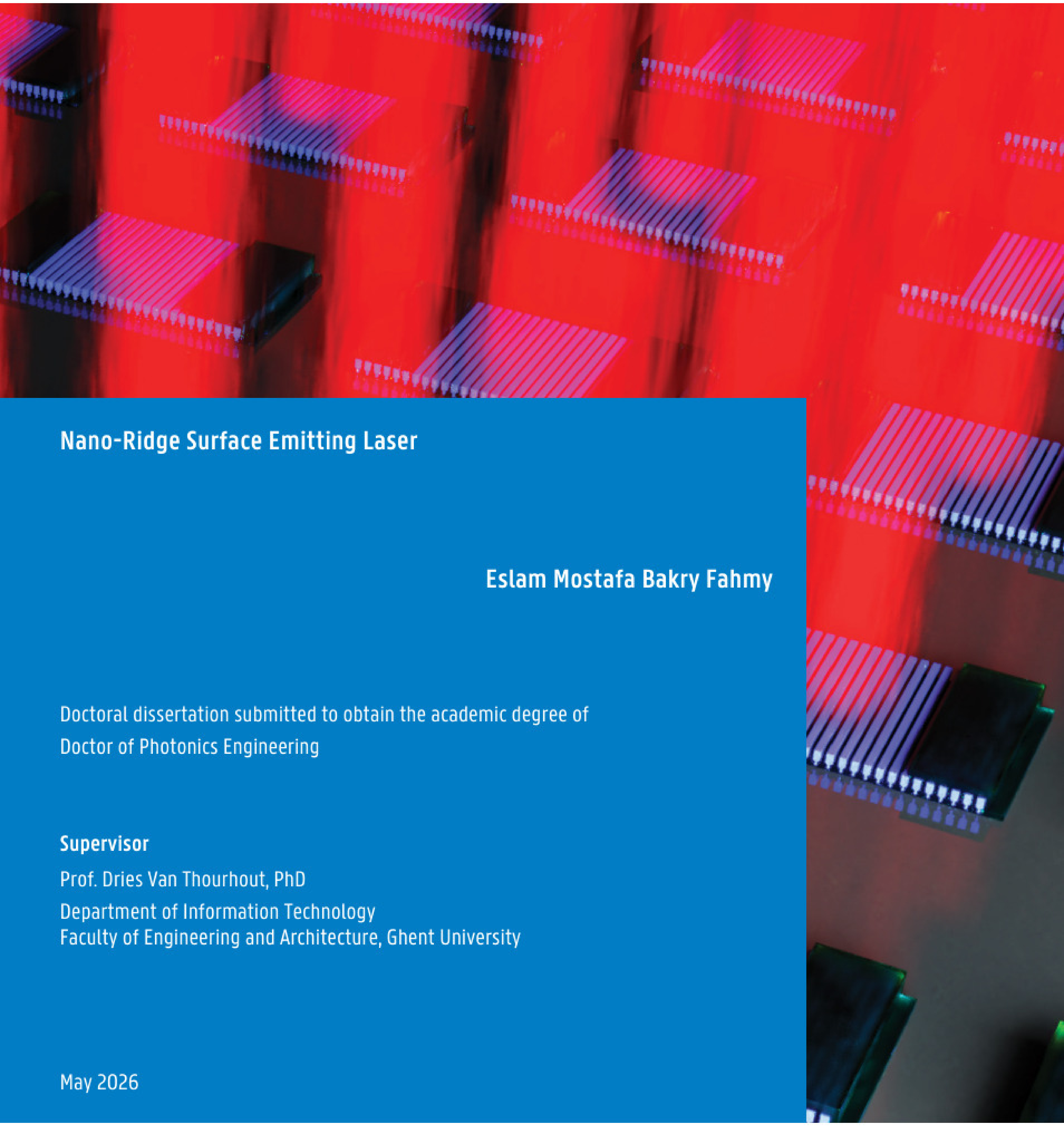

Nano-Ridge Surface Emitting Laser

Eslam Mostafa Bakry Fahmy

Doctoral dissertation submitted to obtain the academic degree of
Doctor of Photonics Engineering

Supervisor
Prof. Dries Van Thourhout, PhD
Department of Information Technology
Faculty of Engineering and Architecture, Ghent University

May 2026

GHENT
UNIVERSITY

FACULTY OF ENGINEERING
AND ARCHITECTURE

Nano-Ridge Surface Emitting Laser

Eslam Mostafa Bakry Fahmy

Doctoral dissertation submitted to obtain the academic degree of
Doctor of Photonics Engineering

Supervisor
Prof. Dries Van Thourhout, PhD
Department of Information Technology
Faculty of Engineering and Architecture, Ghent University

May 2026

GHENT
UNIVERSITY

ISBN 978-94-93513-49-5
NUR 964
Wettelijk depot: D/2026/10.500/57

Members of the Examination Board

Chair

Prof. Filip De Turck, PhD, Ghent University

Other members entitled to vote

Sébastien Cueff, PhD, École Centrale de Lyon, France
Qingzhong Deng, PhD, imec
Prof. Pieter Geiregat, PhD, Ghent University
Prof. Nicolas Le Thomas, PhD, Ghent University

Supervisor

Prof. Dries Van Thourhout, PhD, Ghent University

Acknowledgement

بسم الله الرحمن الرحيم

I'm sitting at Faja Lobi Cafe in Gent's city center, drinking my usual cappuccino, until they come up with something better. Come to think of it, I don't think I have written any piece of work without working on at least part of it here. Today, in April, the sky is clear and sunny, a rare occurrence in Belgium, making this the perfect setting for writing the final piece of the thesis.

At the beginning of this PhD, there was a sense of innocence and ambition. I think there's a kind of mercy in that. If we knew from the outset what it truly takes and how difficult things can be, we might never find the desire to begin. We had an ambition of making a new surface emitting laser using imec's nano-ridge technology, without knowing if it would ultimately work. Professor Dries saw the potential of the platform, and I was given the opportunity to be creative, to find ways to make it work, and to explore whether this technology could be competitive with conventional vertical cavity surface emitting lasers (VCSELs).

Through this PhD, I had the opportunity to develop a wide range of skills and, in Dries's words, to "know a bit about many things." I would like to thank Dries for giving me that opportunity, and for the many discussions, questions, and challenges that shaped this research and pushed it forward. I would also like to thank imec's epitaxy team, and especially Dr. Bernardette Kunert, for the discussions and the many wafers with excellent active material. I would like to thank Professor Nicolas Le Thomas for taking the time, when I was struggling with a problem, to sit down with me and patiently work through it with pen and paper. I would also like to thank my collaborators, Toon Coenen from Delmic and Hai Son Nguyen from EC Lyon, for their time, support, and valuable help with the angle-resolved measurements. As the saying goes, we stand on the shoulders of giants. This work would not have been possible without their contributions.

I would like to sincerely thank the members of the jury for taking the time to read and evaluate this thesis. I am especially grateful for your willingness to travel and be present at the defense. Your time, effort, and expertise are deeply appreciated.

I have come a long way since the start of this PhD. Getting here was not easy, and I often needed encouragement and support, especially when things were not working, which was often the case. I have been lucky to be surrounded by friends who are ambitious and accomplished, many of whom have completed a PhD themselves. The people we surround ourselves with shape who we become, and being part of that circle has inspired me and played an important role in helping me reach this point.

To my friend Mohamed Radwan, thank you. I'm lucky I had your support during the PhD, giving me pointers on how to handle different uncomfortable situations politically, conference recommendations, and also various scientific comments on my papers and experiments. To my friend Ruini Huang, you are always supportive and smiling. You not only taught me how to cook Chinese food, but you were also always a source of positivity since my first day in Belgium seven years ago. Being away from family wasn't easy, especially when combined with fasting during Ramadan. Thanks to Marwan Yusuf and Najla, who invited me over for iftar during Ramadan over the past years, I had the chance to feel at home. Thank you, Marwan, for always being dependable, grounding, and there when needed. It's always nice to have a friend who checks in and asks if you want to go on a three-hour drive to eat seafood in the Netherlands. Thank you, Ayman Morsi, for always being there and for the constant support. We started this journey together all the way back in Egypt more than a decade ago, and insha'Allah to many more happy and successful years. To my friends and colleagues Toon Snauwaert and Khannan Rajendran, thanks for the good advice, for listening to my vents, and for the lighthearted coffee meets.

I would also like to thank my many friends and colleagues inside and outside the PRG who made this experience unforgettable: Ahmed Kandeel, Zhongtao Ouyang, Chao Pang, Islam Abdelhadi, Abdul Rahim, Nader Hozayin, Ahmed Bayoumi, Bingchun Fu, Clemens Krückel, Manuel Chapa, Ruifeng Li, Korneel Molkens, Ahmed Gomaa, Mohamed Salah, Norhan Aly, Adam Barzanji, Meryem benelajla. I would also like to thank all the friends I have not mentioned by name, but who supported me in ways both big and small throughout this journey.

To my fiancée and dear friend Eryn, thank you for being a part of this journey. I cannot imagine how life would have turned out without you. You bring light into my life, and I'm deeply grateful and lucky to have your support and, simply, your presence. I was under constant pressure, and you tried your best to help me stay hopeful. Thank you for your patience, and your kindness. Going on our little trips together fills me with so much happiness. You are the best partner I could have asked for, thoughtful, brilliant, kind, and loving. I'm proud of you and of how much you push yourself. I love you. To more trips, more new food, and more beautiful memories together.

To my mother, Amal, where do I even begin? Amal means hope in Arabic, and you are an embodiment of hope. You always think so highly of me and believe in me more than I believe in myself. Thank you for the constant check-ins, duaa, and patience. You are so smart, cheerful, and warm, and your strength has always been an inspiration. You are one of the kindest people I know and truly the best mom I could have asked for. You have always fought for us, sacrificed so much, and endured a great deal to get us where we are today. I owe you everything, and I will do my best to make you proud, insha'Allah. My father, Mostafa, thank you for doing your best to give me and my brothers a comfortable life and for always being a grounding, patient constant in our lives. You taught me to be fair and just, and those are values I carry with me every day. I love you. It makes me so happy every time I get a phone call from you. I always love hearing your voice and catching up whenever we can. Thank you for your constant support and for always being in my corner, no matter the distance. My brothers, Amr and Mohamed, I have been living away for years, but I always think of you. Thank you for always being there for me and for the constant support. I couldn't have asked for better brothers, and I am always so proud of you. Amr, the person you have become and everything you have achieved fills me with immense pride, and I know in my heart that there is so much more success and happiness ahead of you. You are fair, kind, and driven, and you inspire me more than you realize. I find myself learning from you more than you might think, and I hope that one day the three of us can build something together. Mohamed, you have just started your journey and I know it has been tough, but your patience and resilience say so much about your character. You deserve so much more, and I have no doubt that you will find it. We all have to start somewhere, and insha'Allah, success and fulfillment are well on their way to you. You are incredibly smart, and you will go so much further than you can even imagine right now. To my grandparents, I am lucky to have your support, optimism, and kindness every step of the way. I have been blessed with a wonderful family, and I am deeply grateful for all the love and encouragement you have given me. I would also like to thank my aunts and cousins, especially Ahmed Mousa and my uncle Mousa Hussien, for their continued support and encouragement throughout this journey. I love you all.

I conclude with sincere gratitude to Allah, for every achievement is by His mercy and guidance: "And my success is not but through Allah. Upon Him I have relied, and to Him I return." Qur'an 11:88

Gent, April 2026
Eslam Fahmy

Contents

Acknowledgement i

Contents v

List of Figures ix

List of Tables xxv

List of Acronyms xxvii

Samenvatting xxxiii

Summary xli

1 Introduction 1

1.1 Vertical-Cavity Surface-Emitting Lasers (VCSELs) 2
1.2 Recent Advances and Applications of VCSELs 5
1.3 Photonic-Crystal Surface-Emitting Lasers (PCSELs) 8
1.4 Recent Advances and Applications of PCSELs 10
1.4.1 Challenges and Ongoing Research 13
1.4.2 Outlook and Future Directions 14
1.5 Comparison of EELs, VCSELs, and PCSELs 16
1.6 Silicon Photonics 20
1.7 Integration Techniques 20
1.7.1 Heterogeneous Integration 21

1.7.2 Monolithic Integration 23
1.7.3 Monolithic III–V on Silicon via ART and NRE 24
1.8 Research Objectives and Thesis Outline 27
1.9 Publications and Patents 29
1.9.1 Patent Application 29
1.9.2 Publications in International Journals 29
1.9.3 Publications in International Conferences 29
Bibliography 31

2 Theory and Design of Nano-Ridge Surface-Emitting Lasers 43
2.1 Photonic Crystal Foundations 44
2.2 Bound States in the Continuum 49
2.2.1 Symmetry-Protected BICs in 1D Photonic Crystal Slabs . 51
2.2.2 BICs for Lasers 51
2.3 Design of Nano-Ridge Surface-Emitting Lasers 53
2.4 Effect of Nano-Ridge Dimensions for Infinite Arrays 56
2.4.1 Effect of Geometry on Resonance Frequency 56
2.4.2 Effect of Nano-ridge's width on Q-factor 57
2.5 Design of NRSEL With Finite Dimensions 60
2.6 Summary 62
Bibliography 64

3 Metrology and Fabrication of NRSELs 67
3.1 Wafers Overview 68
3.2 Nano-Ridge Epitaxy 71
3.3 Wafer Metrology 72
3.3.1 Measuring Dimensions Using SEM 73
3.3.2 PL Characterization Using CW Excitation 78
3.3.3 PL characterization Using Pulsed Excitation 80

3.4 NRSEL Definition 80
3.4.1 Optical Lithography Mask Design 80
3.4.2 NRSEL Fabrication Process 83
3.5 Summary 87
Bibliography 89

4 Laser Characterization 91

4.1 Introduction 91
4.2 Laser Characterization 93
4.2.1 Lasing from Quasi-Infinite Arrays 93
4.2.2 Lasing from Micro NRSELs 95
4.3 Farfield Imaging 101
4.4 Summary 105
Bibliography 106

5 Probing BIC in NRSELs with Angle-Resolved CL and PL 107

5.1 Measurement Techniques 108
5.2 Angle-Resolved Measurements of Nano-Ridge Laser Photonic Bands 110
5.3 Effect of NR Dimensions on Band Structure and BIC Resonance . 112
5.4 BIC Lasing Confirmation via Angle-Resolved Photoluminescence 117
5.5 Finite Cavity and Quantization Effects 118
5.6 Summary 124
Bibliography 127

6 Advanced Design Concepts 129

6.1 Increasing Efficiency Using Bottom Reflector 130
6.2 Shaping Output Field 132
6.3 Electrical Injection 135
6.3.1 Strategy for Small NRSELs 135

6.3.2 Strategy for Large NRSELs 137
6.4 Alternative Nano-Ridge Shape for Electrical Injection 138
6.5 2D NRSELs 140
6.6 Additive/Post-Growth Wavelength Tuning 144
6.7 Summary 145
Bibliography 146

7 Conclusion and outlook 147
7.1 Conclusions 147
7.2 Outlook 149
Bibliography 150

A Appendix A 151
A.1 NRSEL Fabrication Process Flow 151
A.2 ARCL Measurements for Different Periods 153
A.3 Polarized AR Reflection Measurements 155
A.4 ARPL Scan at Different Locations on the Field 155
A.5 Four-Wave Mixing 156
A.6 Effect of Fabrication Variability on the Mode 158

List of Figures

1 Nano-ridge surface-emitting laser (NRSEL) op silicium. (a) Illustratie van de voorgestelde nano-ridge surface-emitting laser (NRSEL). (b) Scanning electron microscope (SEM) beeld van de dwarsdoorsnede van een gekliefde rij van nano-ridges. (c) Bovenaanzicht-SEM beeld van een rij van nano-ridges op een siliciumwafer. xxxiv

2 Representatieve μPL spectra, lijnbreedte-vernauwing en statistische drempeltrends als functie van caviteitsbreedte. xxxvi

3 (a, b) Real-space beelden van devices met caviteitsgroottes van 20 μm en 25 μm onder optische pumping boven de lasdrempel. In het 20 μm device is het licht voornamelijk in de caviteit geconcentreerd, hoewel er ook emissie uitbreidt in de photoresist mirror-regio rechts. In contrast is bij het 25 μm device de emissie volledig gelokaliseerd in de caviteit, met een duidelijke reflectie aan de interface tussen de caviteit en de photoresist side mirrors. (c) Real-space beeld van een quasi-oneindig array boven de lasdrempel, met emissie over een groot nano-ridge gebied. (d) Back-focal-plane beeld voor het 25 μm device boven drempel, met een hoek-divergentie van ongeveer 6.5°. (e) Back-focal-plane beeld van het quasi-oneindige array boven de lasdrempel. xxxvii

4 Hoek-resolved metingen die de experimentele fotonische banden en de linewidth collapse naar Γ tonen, consistent met een BIC. . . xxxviii

5 Nano-ridge surface emitting laser (NRSEL) on silicon. (a) Illustration of the proposed nano-ridge surface emitting laser (NRSEL). (b) Scanning electron microscope (SEM) image of the cross section of a cleaved array of nano-ridges. (c) Top-view SEM image of arrays of nano-ridges on a silicon wafer. xlii

6 Representative μPL spectra, linewidth narrowing, and statistical threshold trends versus cavity width. xliv

7 (a, b) Real-space images of devices with cavity sizes of 20 μm and 25 μm under optical pumping above the lasing threshold. In the 20 μm device, light is mostly confined to the cavity, although some emission extends into the photoresist mirror region on the right. In contrast, for the 25 μm device the emission is entirely localized within the cavity, with a clear reflection observed at the interface between the cavity and the photoresist side mirrors. (c) Real-space image of a quasi-infinite array under optical pumping above the lasing threshold, showing the emission from a large area of nanoridges. (d) Back focal plane image for the 25 μm device above the lasing threshold, showing an angular divergence of approximately 6.5°. (e) Back focal plane image of the quasi-infinite array above the lasing threshold. xlv

8 Angle-resolved measurements showing the experimental photonic bands and the linewidth collapse toward Γ, consistent with a BIC. xlvi

1.1 Sketch of the first VCSEL conceived in 1977 by Kenichi Iga [1]. . 2

1.2 Schematic of a multimode edge-emitting laser due to the wide facet. (reproduced from [5]) 3

1.3 Schematic structure of a fabricated GaAlAs/GaAs vertical cavity surface-emitting laser (first room temperature VCSEL) reproduced from [8]). 4

1.4 3D Schematic structure of a modern vertical cavity surface-emitting laser (reproduced from [9]). 4

1.5 (a) Some applications of VCSELs. OCT figure reproduced from [10] (b) Timeline of VCSEL development (reproduced from [11]). 5

1.6 3D Schematic structure of a photonic-crystal surface-emitting laser (reproduced from [5]). 8

1.7 Comparison between edge-emitting lasers (EELs), vertical-cavity surface-emitting lasers (VCSELs), and photonic-crystal surface-emitting lasers (PCSELs) (reproduced from [38]). 9

1.8 (a) A 3-millimeter-wide PCSELs on a wafer. (b) 50-watt PCSEL cutting steel (reproduced from [5]). 11

1.9 PCSEL at 1550 nm (reproduced from [43]). (a) Far-field pattern (b) Near-field pattern. 12

1.10 (a) Lattice constant vs bandgap energy for different semiconductor materials. (b) Diagram showing the lattice mismatch because of the different lattice constant of two materials. 21

1.11 Nanoridges grown on silicon via ART and NRE. (a) TEM of single nanoridge [85]. (b) SEM of array of nanoridges [86]. (c) Top SEM view of nanoridge array [87]. 24

1.12 Cross-sectional and lateral TEM images of GaAs nano-ridges grown in 300 nm deep and a)40 nm, b)100 nm, c)300 nm, wide trenches. Higher aspect ratio trapping improves the defect trapping. Reproduced from [90]. 25

1.13 SEM images of GaAs ridges with different MOVPE growth conditions were applied. Reproduced from [92]. 27

2.1 (a) Dispersion relation (band diagram), frequency ω versus Bloch wavenumber k_x, of a uniform bulk material, where the dashed lines indicate the apparent "folding" produced by applying Bloch's theorem with an artificial periodicity Λ. A physical periodic modulation of the dielectric function (inset) lifts the degeneracies at the Brillouin-zone boundaries and opens a band gap at $k_x = \pm\pi/\Lambda$, as well as a higher-order gap at $k_x = 0$. (b) Electic field of the corresponding band-edge modes. The degenerate $k_x = \pm\pi/\Lambda$ plane waves of the uniform medium are split into standing waves $\cos(\pi x/\Lambda)$ and $\sin(\pi x/\Lambda)$ by the dielectric periodicity, forming the lower and upper edges of the band gap, respectively. The $\cos(\pi x/\Lambda)$ mode has electric-field peaks in the high-index regions (n_{high}) and therefore lies at a lower frequency than the $\sin(\pi x/\Lambda)$ mode, which peaks in the low-index regions. c) the band diagram caluclated for three different cases with a fill-factor of 50%. Left: Bulk GaAs, Center: periodic structure of two materials with dielectric constants 13 and 12. Right: periodic structure of GaAs and air.[reproduced from [1]] 46

2.2 Schematic of first- and second-order Bragg gratings. (a) First-order (m=1) Bragg provides strong in-plane feedback (gap near $k \approx G/2$) but does not by itself give near-normal out-coupling. (b) Second-order uses the same period to realize both in-plane feedback and vertical out-coupling: feedback via m=2 ($2k \approx 2G \Rightarrow k \approx G$) and near-normal emission via the m=1 harmonic ($k \approx G$). The green arrows indicates the light propagating wave vector. Black arrows are the corresponding reciprocal lattice vector G(reproduced from [2]) 47

2.3 Bound states in the continuum. (a) Schematic Illustration explaining BIC modes: Open systems have two main kinds of states: extended “continuum” waves (blue) and localized bound states trapped by a confining potential (green). Normally, any state that sits in the continuum couples to extended waves and leaks energy (orange), becoming a radiating resonance. Bound states in the continuum (BICs) (red) are the exception: they exist within the continuum’s frequency range yet stay localized and non-radiating, producing no outgoing flux [reproduced from [3]]. (b) Schematic illustration of a symmetry protected bound state in the continuum (BIC) in a photonic crystal slab. In periodic structure the modes at the band edge couple and form a band gap. the mode at the lower band edge is odd with respect to the mirror symmetry plane of the slab, while the radiating channel is even. Due to this symmetry mismatch, the mode cannot couple to the radiating channel and becomes a BIC. (c) A schematic illustration showing the band structure of a photonic crystal slab with a symmetry-protected BIC at the Γ point. The BIC lies above the light line (dashed), within the radiation continuum, yet remains perfectly confined due to symmetry protection. a second BIC could also exist away from the Γ point, arising from destructive interference (parameter tuning or accidental) between leaky modes [reproduced from [3]]. (d) the corresponding quality factor (Q) plot showing the diverging Q at the BIC points. 50

2.4 Nano-ridge surface emitting laser (NRSEL) on silicon. (a) Illustration of the proposed nano-ridge surface emitting laser (NRSEL). (b) Scanning electron microscope (SEM) image of the cross section of a cleaved array of nano-ridges. (c) Top-view SEM image of arrays of nano-ridges on a silicon wafer. 53

2.5 Nano-ridge 1D photonic crystal (a) Schematic representation showing an array of nano-ridges with the most relevant dimensional parameters. (b) Dispersion diagram for an array of nano-ridges calculated using 2D-FDTD. The radiation continuum lies above the light line (red). (c) Calculated electric field for the first two band edge modes at the Γ point $k_x/k_0 = 0$. 54

2.6 Quality factor for BIC mode vs leaky mode. (a) Quality factor for an array of nano-ridges without a silicon substrate using bloch boundary conditions calculated for different k values. For the asymmetric BIC modes TE_{21L}, TE_{22L}, and TE_{23L} the quality factor drops significantly off-gamma $k_x = 0$. The leaky symmetric mode TE_{21H} has a low quality factor and a weak dependence of the quality factor on the k value. (b) Quality factor for an array of nano-ridges with a silicon substrate using bloch boundary conditions calculated for different k values. For the asymmetric BIC modes TE_{21L}, TE_{22L}, and TE_{23L} the quality factor drops significantly off-gamma $k_x = 0$. The substrate limits the maximum achievable quality factor as it allows leakage. (c) Mode profiles for the TE_{21L}, TE_{22L}, and TE_{23L} modes at the Γ point, showing the antisymmetric field distribution that leads to the BIC behavior. The TE_{21H} mode shows a symmetric field distribution, which allows coupling to radiating channels and results in a low quality factor. . 56

2.7 Geometry dependent resonance frequency shift. (a) Sweep of the resonance frequency of the TE_{21L} mode, as function of nano-ridge array period ($Lambda$) and fill factor, for varying nano-ridge heights (H). b) Resonance wavelength (λ) for the chosen design period $Lambda$ = 0.38 μm, as function of height (H), for different widths (W). 57

2.8 Q-factor dependence on nano-ridge width with bloch boundary conditions to simulate an infinite structure. (a) Calculated Q-factor and resonance frequency for the TE_{21L} mode at the Γ point as function of the nano-ridge width without a substrate. (b) Calculated Q-factor and resonance frequency for the TE_{21L} mode at the Γ point as function of the nano-ridge width with a silicon substrate below the nano-ridge array. 59

2.9 Q-factor dependence on nano-ridge width for a finite array. (a) schematic showing a 2d FDTD simulation for a 15 μm wide array. (b) Calculated Q-factor and resonance frequencyfor the TE_{21L} mode at the Γ point as function of the nano-ridge width for a finite array of 42 nano-ridges ($H = 480nm, \Lambda = 380nm$) with a silicon substrate below the nano-ridge array. 59

2.10 Bloch mode confinement with side mirrors. (a) Side mirrors defined by locally shifting the slow Bloch mode to a longer wavelength. This forms a barrier around the middle cavity, enhancing the electric field in the cavity, and reducing the lateral losses. (b, d) A 2D FDTD simulation of a finite nano-ridge crystal without and with mirrors, showing a cross-section of the TE_{21L} mode. The side mirror is formed by adding photoresist of index 1.6 between and on top of the nano-ridges. (c) Calculated Q-factor for the TE_{21L} mode without and with side mirrors, as function of the number of periods. 61

3.1 (a) Photograph of a 300 mm silicon wafer after the epitaxial growth of InGaAs/GaAs nano-ridges using NRE. (b) Optical microscope image of a die from the wafer, showing the patterned trenches filled with nano-ridges. c) Zoomed-in view of the nano-ridge array in field C13 using SEM, which has a trench period of 380 nm. d) Cross-sectional SEM image of the nano-ridge array in field C13, showing the box-like shape of the nano-ridges. 69

3.2 a) Schematic illustration of the Tower35 mask design used for the epitaxial growth of InGaAs/GaAs nano-ridges. The mask contains 20 fields of nano-ridge arrays with varying trench periods and widths. b) Picture from the GDS layout of the Tower35 mask, showing the different fields and their respective trench dimensions. 70

3.3 Simulated photonic band structures (resonance frequency of TE_{21L} mode) for InGaAs/GaAs nano-ridge arrays with trench periods of (a) 380 nm (C13), (b) 400 nm (C18), and (c) 480 nm (C8). The change in nano-ridge width has the biggest influence on the resonance frequency for TE_{21L} mode for the 480 nm period, while the 380 nm period shows the least sensitivity to width variations. This means that fabrication tolerances will have less impact on the lasing wavelength for the 380 nm period. 71

3.4 Cross-sectional SEM images of InGaAs/GaAs nano-ridge arrays in fields C8 ($\Lambda = 480$ nm), C13 ($\Lambda = 380$ nm) and C18 ($\Lambda = 400$ nm) for wafer D03. The images show the nano-ridge dimensions for both center and edge dies of each field. 73

3.5 Cross-sectional SEM images of InGaAs/GaAs nano-ridge arrays in field C13 ($\Lambda = 380$ nm) for wafer D04, showing the nano-ridge dimensions from center to edge dies. The images demonstrate the uniformity of the nano-ridge dimensions across the 300 mm wafer. 74

3.6 (a) Schematic of the double trench-patterned oxide template (left) after opening the wide trench in the second oxide, (center) after silicon recess etch to create a 111-faceted V-groove at the bottom of the narrow trench and (right) after epitaxial deposition of a HBT layer stack. (b)Cross-section (stitched) TEM images of a HBT layer stack viewed under (left) two-beam BF (220) and (right) HAADF-STEM conditions with all device layers indicated. (reproduced from [9]) 77

3.7 Cross-sectional SEM images of InGaAs/GaAs nano-ridge arrays in field C13 ($\Lambda = 380$ nm) for wafers D04, D05, D06 and D07. . . . 78

3.8 Room-temperature PL spectra for the center dies of wafers D02 to D04 in fields: C8 ($\Lambda = 480$ nm), C13 ($\Lambda = 380$ nm) and C18 ($\Lambda = 400$ nm). The spectra show the peak emission wavelength and intensity for each wafer, with wafer D03 exhibiting the highest peak intensity. 79

3.9 Optical lithography mask design for NRSEL fabrication. (a) GDS layout of the whole lithography mask. it consists of 5 different designs each spanning 4 fields to cover C13 and C18 (diagonal fields). for each design there's a corresponding mirror mask that aligns via the markers defined in ICP at the same time as the cavities. The lower half of the mask is the same design inverted for negative photoresist. (b) A zoom in on design 1: it includes arrays of NRSEL devices with varying cavity widths (W_{NRSEL}) and heights (H_{NRSEL}), as well as side mirrors formed by filling the space between the nano-ridges with a low refractive index material (c). 82

3.10 Fabrication steps. (a) Schematic illustration of the NRSEL. (b) Schematic illustration of the NRSEL fabrication process, including photoresist patterning to define the NRSEL devices, ICP RIE etching to remove the nano-ridge material outside the NRSELs, and photoresist spin coating and patterning to define the side mirrors. 83

3.11 (a,b) SEM image showing the definition of the NRSEL array after ICP etching of the nano-ridge material using SiCl4/N2 chemistry. The photoresist mask remains intact after etching, indicating successful process optimization. (c) SEM of a single NRSEL cavity after ICP etching, showing the successful removal of the nano-ridge material outside the NRSEL cavity while preserving the integrity of the photoresist mask. 84

3.12 (a,b) Microscope image of NRSEL fabrication, showing incomplete removal of the photoresist after ICP etching and development in acetone. (c,d) Microscope image of the same sample, Using AZ100 at 80°C for 10 mins the resist was almost removed completely, revealing the well-defined NRSEL cavities. 85

3.13 (a) SEM image showing definition of the NRSEL array after successful etching of the nano-ridge material using ICP. (b) FIB cross-section image of a single NRSEL cavity after ICP etching, showing the successful removal of the nano-ridge material outside the NRSEL cavity. (c) False coloured cross-section SEM image after defining the side mirrors using photoresist, showing successful infilling and coverage with a height of 900 nm on top of the nano-ridges. (d) Optical image after NRSEL definition and development of the side mirrors 86

3.14 Microscope image of the final fabricated NRSEL devices, showing arrays of NRSELs with varying cavity widths and heights. The well-defined NRSEL cavities and side mirrors are clearly visible. . 87

4.1 Schematic of the micro-photoluminescence (μPL) setup used for characterizing the NRSEL devices. The pump laser (Nd:YAG, 532 nm, 7 ns pulse width, 10 kHz repetition rate) is focused onto the sample using a microscope objective (MO) with NA = 0.65. The emitted light is collected through the same MO and directed to a spectrometer (KYMERA-328I-D2-SIL, Oxford instruments, Andor) using a dichroic mirror (DM). A long-pass filter (LPF) is used to block any residual pump light before detection. The spectrometer is equipped with two detectors: a water-cooled InGaAs detector for near-infrared measurements and a visible range CCD sensor for shorter wavelengths. 92

4.2 a) Microscope image of the quasi-infinite array of nano-ridges under optical pumping above the lasing threshold. The pump spot diameter is 300 μm. b) Back focal plane image of the quasi-infinite array above the lasing threshold, showing an angular divergence of approximately 6.5°. 93

4.3 Lasing spectrum of a quasi-infinite array of period $\Lambda = 380$ nm, pumped with a spot size of 300 μm diameter at different pump power densities. Above the lasing threshold a narrow lasing peak appears at 984 nm. b) Integrated PL intensity showing a lasing threshold around 10 kW cm^{-2}. 94

4.4 (a) Measured lasing wavelength at different locations on the quasi-infinite array sample, showing a red-shift as we move from the center to the edge of the wafer. (b) The threshold pump power density for lasing at different locations in the sample. As we move from the edge to the center, the threshold decreases. 95

4.5 Room-temperature optical characterization. (a) PL spectra of a NRSEL with $W_{NRSEL} = 20\,\mu\mathrm{m}$ for different pump intensities. (b) Integrated PL and linewidth for a NRSEL with $W_{NRSEL} = 20\,\mu\mathrm{m}$ as a function of pump power. The linewidth reaches a minimum of 0.9 nm at threshold. (c) Measured lasing threshold versus cavity width for 31 devices within the same sample. Individual scatter points represent the threshold of each device, while the overlaid box plots summarize the statistical distribution of thresholds for each cavity width. The solid black line in each box represents the median value of the data. (d) Zoom-in on the integrated PL for a group of six NRSELs with different widths, showing the reduction of the threshold with increasing cavity width. (e) The threshold data is fitted using a reciprocal function, $a/W_{NRSEL} + b$. Scatter points (blue) represent the mean threshold values, and the calculated Q-factor (red) is plotted for comparison. 97

4.6 Polarization characterization of an NRSEL with $W_{NRSEL} = 20\,\mu\mathrm{m}$. The emitted light passes through a polarization analyser, and the intensity is recorded while rotating the analyser over a range of angles from 0° (analyser is perpendicular to the nano-ridge) to 180°. The fitted curve indicates strong polarization, with the electric field mostly aligned with the nano-ridges. 100

4.7 Mode identification for an NRSEL with W_{NRSEL} = 20 μm. (a) PL spectra for increasing pump power. For the highest pump power, three distinct peaks are visible. (b) Comparison between the experimental PL spectrum taken at 62.4 kW/cm^2 pump power density and the calculated wavelengths of the TE_{21L}, TE_{22L} and TE_{23L} modes, at the Γ point in the band diagrams for a nano-ridge array without photoresist and with photoresist. (c) Simulated band diagrams for nano-ridge arrays with and without photoresist. . . . 100

4.8 Lasing spectra of NRSELs with different cavity lengths: (a) 20 μm, (b) 25 μm, and (c) 35 μm. (d) Light-in vs. light-out curves for the three devices, showing the variation in lasing thresholds with cavity length. 101

4.9 Schematic of the far-field and near-field imaging setup. The emitted light from the NRSEL is collected by a microscope objective (MO) with NA = 0.65. For near-field imaging, the real-space image of the sample is formed at the image plane (blue rays) using a tube lens. For far-field imaging, the back-focal plane (BFP) of the MO is imaged onto the camera (red rays) using an additional lens. . . . 102

4.10 a) FDTD 3D band surface along kx and ky at TE_{21L} mode's resonance frequency. b) Top view of the band surface. c) 2D slice at the saddle point of the surface: 307 THz, showing the iso-frequency contour. The iso-frequency contour matches closely with the results obtained from the back-focal plane experimental images. 103

4.11 (a, b) Real-space images of devices with cavity sizes of 20 μm and 25 μm under optical pumping above the lasing threshold. In the 20 μm device, light is mostly confined to the cavity, although some emission extends into the photoresist mirror region on the right. In contrast, for the 25 μm device the emission is entirely localized within the cavity, with a clear reflection observed at the interface between the cavity and the photoresist side mirrors. (c) Real-space image of a quasi-infinite array under optical pumping above the lasing threshold, showing the emission from a large area of nano-ridges. (d) Back focal plane image for the 25 μm device above the lasing threshold, showing an angular divergence of approximately 6.5°. (e) Back focal plane image of the quasi-infinite array above the lasing threshold. 104

5.1 Schematic diagrams of the (a) angle-resolved cathodoluminescence (CL) setup and (b) angle-resolved photoluminescence (PL) setup used to probe the photonic band structure of the nano-ridge laser array. In both setups, the emitted light is collected and directed to an imaging spectrometer for angular and spectral resolution. reproduced from [1, 2] 109

5.2 (a) Cross-sectional SEM image of a cleaved array of nano-ridges with a period of 380 nm. (b) Cathodoluminescence (CL) emission spectrum from the array, showing broad band emission from the multi-quantum wells (MQWs) around 1000 nm and a smaller peak around 890 nm from the GaAs body. (c) Top-view SEM image of the nano-ridge array and the corresponding CL emission spatial map (950 to 1050 nm) integrated over the array. 111

5.3 (a,b) Angle-resolved photoluminescence (PL) along Γ-X and Γ-Y directions, respectively. FDTD band structures are overlaid in cyan. (c) Normalized angle-resolved reflection along Γ-X at different k_x values, showing a gradual increase in the absorption dip until it vanishes at the Γ point. 113

5.4 (a,b) Angle-resolved cathodoluminescence (CL) along Γ-X and Γ-Y, respectively. A sharp peak and enhanced spontaneous emission due to the BIC mode appear around 1.27 eV at the band edge. (c) A slice at $k_x = 0.11$ showing the CL intensity versus wavelength. The narrower peak corresponds to the BIC mode at 975 nm, while the broader peak arises from the first band TE_{21L}. 114

5.5 (a,b) Dispersion map using a slice at $k_x = 0.3$ with 500 nm steps along the nano-ridge's length. (c) Coarse dispersion map using a slice at $k_x = 0.3$ at different sample positions along the nano-ridge's length with a 50 μm step, reflecting changes in the nano-ridge geometry at these positions. (d) Cathodoluminescence peak at different positions with the corresponding nano-ridge width extracted from SEM images at those positions. 115

5.6 (a,b) Experimental angle-resolved white-light reflection measurements for the center and edge dies, respectively, showing good agreement with the simulated band diagram (cyan). (c) Cross-sections of the electric field distribution (E_y) for the first two BIC modes TE_{21L} and TE_{22L}, respectively. 116

5.7 (a) Lasing spectrum of the center die (TE_{21L}) with a narrow peak around 975 nm. (b) Integrated light input–output curve of the center die (TE_{21L}) at different pump fluences, showing a clear threshold around 0.56 mJ/cm^2. (c) Integrated light input–output curve of the edge die (TE_{22L}) at different pump fluences, showing a clear threshold around 0.4 mJ/cm^2. 118

5.8 (a) Angle-resolved photoluminescence at different pump fluences under pulsed femtosecond optical excitation for the center die, showing lasing at the band edge around 975 nm with a threshold pump fluence of 0.56 mJ/cm^2.(b) Angle-resolved photoluminescence at different pump fluences under pulsed femtosecond optical excitation for the edge die, showing lasing at the band edge around 920 nm with a threshold pump fluence of 0.4 mJ/cm^2. (c,d) Experimental back-focal-plane images (far-field) for the center and edge dies above their respective thresholds using a CMOS camera under nanosecond pulsed excitation. The far-field shows a lower divergence angle of around 3° for the edge die. 119

5.9 (a) 3D band diagram simulation using FDTD for the second TE band: TE_{22L}. (b) Iso-frequency contour at the band edge showing a small central BIC mode and modes from a higher-order band. . . 120

5.10 (a) 3D schematic of the nano-ridge cavity with photoresist side mirrors and the e-beam scan path from edge to center. (b) SEM of the 15 μm mirror-defined cavity. (c) Angle-resolved CL at three x-positions (0, 2, 7.5 μm) showing a dominant peak that shifts toward the band edge while multiple Fabry–Pérot modes remain visible. 121

5.11 (a) FDTD 3D TE_{21L} surface and iso-frequency contour with allowed longitudinal wavevectors marked as vertical lines at $k_x = m\pi/L$ (uniform spacing $\Delta k = \pi/L$), highlighting mirror-induced quantization. (b) 2D FDTD simulated E–k_x map resolving the same ladder of discrete cavity modes observed in CL and labeled by Γ indices. (c) Transverse electric field profiles of the first three discrete modes indicated in (b): $\Gamma_1(k_1)$ at 989.2 nm with one antinode, $\Gamma_2(k_2)$ at 989.8 nm with two antinodes, and $\Gamma_3(k_3)$ at 991.6 nm with three nodes, explaining the position-dependent excitation via local field overlap with the e-beam. 122

5.12 (a) Angle-resolved measurement with a wide iris collecting emission from both the cavity and mirror regions, showing two bands: one from the cavity region and a red-shifted band from the mirror region due to the photoresist. (b) Angle-resolved measurement with a narrow iris (≤ 15 μm) collecting emission only from the cavity region, showing only the first TE band from the cavity without any shift. 123

5.13 (a) Microscope image of the NRSEL array. (b) Angle-resolved E–k_x map for the 15 μm NRSEL under femtosecond pulsed excitation (0.19 mJ/cm^2), resolving two bands: the fundamental cavity band TE_{21L} near $\lambda \approx 975$ nm with clearly quantized modes (large Δk), and a red-shifted band near $\lambda \approx 1005$ nm from the photoresist side mirrors. (c) E–k_x at 0.4 mJ/cm^2 showing a narrow lasing peak at the band-edge BIC mode (1.27 eV, $\sim$ 975 nm). (d) E–k_x at 0.56 mJ/cm^2 revealing narrow emission at multiple Fabry–Pérot resonances and an additional line around 952 nm. 125

5.14 (a) E–k_y for the 15 μm device at 0.19 mJ/cm^2 exhibiting subtle, uniform quantization consistent with weaker longitudinal confinement along the ridge direction. (b) E–k_x for the 30 μm NRSEL at 0.16 mJ/cm^2, showing finer mode spacing Δk as expected from $\Delta k = \pi/L$. (c) Quantized mode momentum index m vs the in-plane wave vector $k_{//}$, for cavities of length 15 μm, 20 μm, 25 μm, and 30 μm; linear fits yield the average momentum step Δk (slope) and effective cavity length $L_{\text{eff}} = \pi/\text{slope}$. (d) L_{eff} versus design cavity length, highlighting that the 15 μm device shows the clearest spacing and best agreement with simulation; the simulated E–k map indicates $L_{\text{eff}} \approx 18$ μm for the nominal 15 μm design, consistent with field penetration into the mirror regions. 126

6.1 Bottom reflector to increase efficiency. (a) FDTD setup. (b) Simulated NRSEL mode profile without bottom reflector showing downward emission. (c) Simulated NRSEL mode profile with bottom reflector showing constructive interference and increased upward emission. (d) Simulated NRSEL mode profile with bottom reflector showing destructive interference and decreased upward emission. . 132

6.2 Different BIC modes with different farfield patterns. (a) Angle-resolved photoluminescence measurement showing TE_{21L} and TE_{21L} modes. (b) Simulated mode profiles of TE_{21L} and TE_{21L} modes. (c) Experimental farfield patterns of TE_{21L} and TE_{21L} modes. 134

6.3 Schematic of electrical injection for small NRSELs with contacts at the two ends of the nano-ridge array. 136

6.4 Spatial distribution of quantum well carrier density (along length of nano-ridge-bottom QW) for different doping concentrations. (courtesy of Andualem A. Yimam) 137

6.5 Schematic of electrical injection for large NRSELs with contacts placed at optical field nodes to minimize absorption losses. (a) Top view showing contact placement along the nano-ridge array at the ends for the cavity's fundamental mode. (b,c) contact placement for higher order modes. (The mode distribution in b,c is an illustration). 138

6.6 Schematic of a different nano-ridge shape for electrical injection, featuring a top hat of GaAs that pushes the optical mode down to the active region and avoids overlap with the top contact. 139

6.7 Electrical injection in large area PCSELs using a top grid electrode (reproduced from [5]). 140

6.8 Schematic of 2D NRSELs with square lattice. The second period is formed by silicon deposited between the nano-ridges then etched to form a square lattice. The periodicity in both directions creates a 2D BIC mode that can be used for lasing. This offers more control over the farfield pattern and beam shaping. It also allows to independently control the lasing mode post growth by choosing the second period of the silicon waveguides, enabling tuning the lasing wavelength post growth and more control over the process independently of the nano-ridge growth. 142

6.9 Simulated band structure of 2D NRSELs showing additional modes introduced by the second in-plane period. (a) $a_x = a_y = 400\,\mathrm{nm}$. (b) $a_x = 300\,\mathrm{nm}$, $a_y = 400\,\mathrm{nm}$. (c) $a_x = 400\,\mathrm{nm}$, $a_y = 300\,\mathrm{nm}$. In all cases, the silicon waveguide height equals the nano-ridge height. Varying either period modifies the band dispersion and shifts the resonant wavelengths, providing additional flexibility for future designs and post-growth wavelength control. 143

6.10 SEM images of amorphous silicon deposited between the nano-ridges ($\Lambda = 885nm$). The two images are using different growth conditions. The silicon doesn't fill the space between the nano-ridges completely. It starts accumulating on the sidewalls and top of the nano-ridges which prevents complete filling of the space between the nano-ridges. (courtsey of Zhongtao Oyuang) 144

6.11 Resonance of TE_{21L} changes with change in (a) width of the nano-ridge, (b) height, and (c) sensitivity of resonance wavelength to width ($nm\,nm^{-1}$). 145

A.1 (Left) Spin speed vs film thickness curves for AZ 5214 photoresist. (Right) Refractive index vs wavelength for AZ 5214 photoresist. . 151

A.2 ICP settings for etching GaAs/AlGaAs. 152

A.3 ARCL measurements for different periods. 154

A.4 White light reflection measurements for quasi infinite array with different polarizations. 155

A.5 Angle-resolved photoluminescence measurements at different locations on the sample. 156

A.6 Angle-resolved photoluminescence measurement for a device of 25 um cavity, showing four wave mixing peaks. 157

A.7 Angle-resolved photoluminescence measurement for a device of 15 um cavity, showing four wave mixing peaks. 157

A.8 Angle-resolved photoluminescence measurement for a device of 25 um cavity, showing four wave mixing peaks. 158

A.9 FDTD simulation results showing the effect of fabrication variability on the cavity mode localization for two different random seeds. 159

List of Tables

1.1 Qualitative comparison of EELs, VCSELs, and PCSELs (Part I). . 17
1.2 Qualitative comparison of EELs, VCSELs, and PCSELs (Part II, continued). 18
1.3 Qualitative comparison of EELs, VCSELs, and PCSELs (Part III, continued). 19

3.1 Summary of the different 300 mm wafers grown with varying growth conditions. The quantum well thickness and indium percentage in the InGaAs quantum wells are varied. 72
3.2 Measured nano-ridge widths (in nm) from SEM images for the center dies of the different wafers. 76
3.3 Measured nano-ridge Heights (in nm) from SEM images for the center dies of the different wafers. 76

List of Acronyms

CMOS	Complementary Metal-Oxide Semiconductor
VCSEL	Vertical-Cavity Surface Emitting Laser
NRSEL	Nano-Ridge Surface Emitting Laser
ART	Aspect Ratio Trapping
NRE	Nano-Ridge Engineering
BIC	Bound State in the Continuum
DBR	Distributed Bragg Reflector
PL	Photoluminescence
CL	Cathodoluminescence
PhC	Photonic Crystal
LED	Light Emitting Diode
QD	Quantum Dot
QW	Quantum Well
PCSEL	Photonic Crystal Surface Emitting Laser
FDTD	Finite-Difference Time-Domain
Si	Silicon
InP	Indium Phosphide

NR	Nano-Ridge
QW	Quantum Well
MQW	Multiple Quantum Well
TE	Transverse Electric
TM	Transverse Magnetic
FDTD	Finite-Difference Time-Domain
SPBIC	symmetry-protected bound state in the continuum
CW	Continuous-Wave
SEM	Scanning Electron Microscopy
STI	Shallow Trench Isolation
MOVPE	Metal-Organic Vapor Phase Epitaxy
SBM	slow bloch mode
ARPL	Angle-Resolved Photoluminescence
ARCL	Angle-Resolved Cathodoluminescence
LDOS	Local Density of Optical States
Q-factor	Quality factor
OCT	Optical Coherence Tomography
SOI	Silicon-On-Insulator
PIC	Photonic Integrated Circuit
DFB	Distributed Feedback
LED	Light Emitting Diode
SNR	Signal-to-Noise Ratio
PD	Photodetector

MBE	Molecular Beam Epitaxy
QD	Quantum Dot
TEM	Transmission Electron Microscopy
SWIR	Short-Wave Infrared
LDOS	Local Density of Optical States
GHz	GigaHertz
MHz	MegaHertz
WDM	Wavelength Division Multiplexing
AR	Angle-Resolved

Samenvatting

Vertical-cavity surface-emitting lasers (VCSELs) behoren tot de meest wijdverspreide halfgeleiderlasers, met een grote impact in datacom en in consumententoepassingen zoals optische muizen en smartphones (bv. voor gezichtsherkenning en afstandsmeting). Hun populariteit is te danken aan de mogelijkheid om ze te fabriceren en testen op waferschaal (typisch op GaAs-wafers), een compacte vormfactor en een lage kost. De VCSEL-architectuur steunt echter op een complexe verticale epitaxiale laagstapel met een onderste distributed Bragg reflector (DBR), een actieve winstlaag en een bovenste DBR, waarbij de spiegels (DBRs) doorgaans uit tientallen nauwkeurig gegroeide lagen bestaan. Deze complexiteit beperkt de toegankelijke golflengtegebieden, omdat DBR-spiegels met hoge reflectiviteit slechts voor enkele banden relatief eenvoudig te realiseren zijn (vaak rond 850 nm en 980 nm), terwijl uitbreiding naar andere golflengten (bv. 1300 nm, 1550 nm of het midden-infrarood) veel uitdagender is. Bovendien is de emissiegolflengte in grote mate bepaald door het epitaxiale ontwerp, waardoor goed gecontroleerde multi-golflengte VCSEL-arrays op één wafer en eenvoudige monolithische integratie met andere fotonische en elektronische componenten niet vanzelfsprekend zijn.

Aspect-ratio trapping (ART) en nano-ridge engineering (Nano-Ridge Engineering (NRE)) bieden een monolithische route om III–V actief materiaal van hoge kwaliteit rechtstreeks op silicium te groeien zonder dikke bufferlagen, door defecten op te sluiten in smalle, in oxide gedefinieerde sleuven en het materiaal te vormen tot nano-ridges die in periodieke arrays gerangschikt zijn. Deze nano-ridge matrices vormen een fotonisch kristal met hoog indexcontrast dat Bloch-modes ondersteunt, waardoor band-edge (slow-light) werking mogelijk wordt: staande-golven ondergaan voldoende terugkoppeling om lasing te bekomen terwijl het licht verticaal ten opzichte van het oppervlak wordt uitgekoppeld (zie figuur 5). Nano-ridge surface-emitting lasers (NRSELs) beloven daarom een lagere epitaxiale complexiteit dan VCSELs (geen micrometerdikke DBR-stapels), flexibiliteit in de keuze van de golflengte, via geometrische tuning (periode en ridge-dimensies) en post-processing (bv. diëlektrische depositie), en de mogelijkheid om multi-golflengte arrays te realizeren door lokaal de periode en/of de materiaalsamenstelling te variëren. In deze thesis leggen we de werkingsprincipes en ontwerpregels vast, beschrijven we wafermetrologie, epitaxie en fabricage van de lasercaviteit, en rapporteren we optische karakterisatie bij kamertemperatuur, trends in de drempelstroom en far-field emissie. Daarnaast gaan we verder dan een basale demonstratie door (i) de fotonische bandstructuur experimenteel te reconstrueren met hoek-geresolveerde Cathodoluminescence (CL) en Photoluminescence (PL) om Bound State in the Continuum (BIC)-gerelateerde band-edge lasing en modekwantisatie in eindige caviteiten experimenteel te bevestigen, en (ii) geavanceerde concepten uit te werken voor verbeterde extractie en bundelvorming (bv. toevoegen van spiegels onder de caviteit en engineering van de mode), realistische routes naar elektrische injectie, en strategieën voor additieve/post-growth golflengtetuning en meer flexibele 2D ontwerpconcepten.

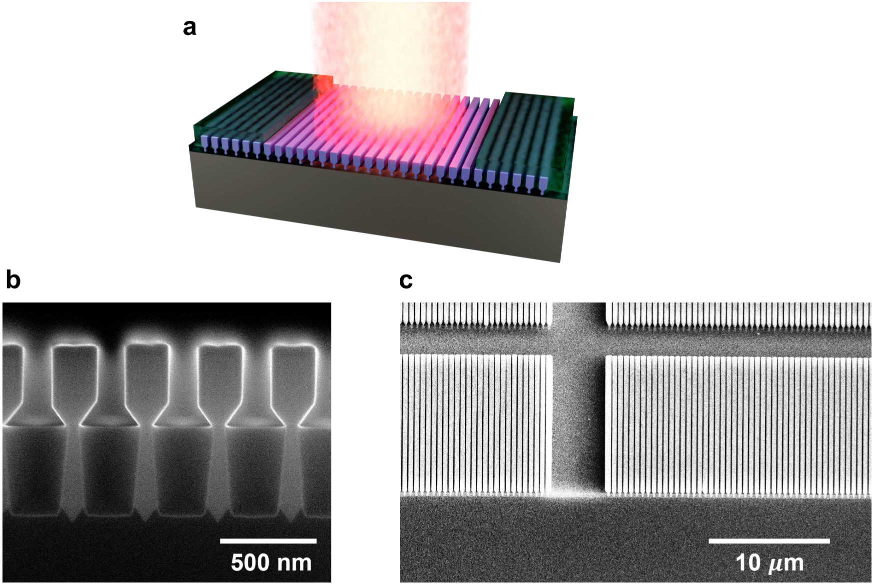

Figuur 1: Nano-ridge surface-emitting laser (NRSEL) op silicium. (a) Illustratie van de voorgestelde nano-ridge surface-emitting laser (NRSEL). (b) Scanning electron microscope (SEM) beeld van de dwarsdoorsnede van een gekliefde rij van nano-ridges. (c) Bovenaanzicht-SEM beeld van een rij van nano-ridges op een siliciumwafer.

Resultaten

In dit werk werden het theoretische kader en de ontwerpregels voor de realisatie van nano-ridge fotonisch-kristal caviteiten op silicium opgesteld door analyse van de fotonische banden, band-edge feedback en BIC-modes die high-Q oppervlakte-emissie mogelijk maken. Eerst werd met analytische schalingswetten en FDTD de benaderde periode voor emissie nabij 1 μm bepaald. Daarna werd het ontwerp verfijnd door verschillende kandidaatperiodes te vergelijken. Voor het geselecteerde veld met 380 nm periode (C13) bleek de gesimuleerde gevoeligheid van de resonantie voor variaties in de nano-ridge breedte lager te zijn ($\approx 2.3\,\mathrm{nm\,nm^{-1}}$) dan voor alternatieven met grotere periode. Ook de gevoeligheid voor de hoogte is kleiner ($\approx 0.7\,\mathrm{nm\,nm^{-1}}$). Dit motiveert zowel de keuze van het veld als de focus op breedtecontrole voor robuuste fabricage.

Groei op waferschaal met NRE, metrologie en een praktische fabricageflow worden aangetoond op zes 300 mm Si wafers (D02–D07). Door midddel van Scanning Electron Microscopy (SEM) en PL bij kamertemperatuur kwantificeerden we de nano-ridge dimensies, uniformiteit en optische kwaliteit, voor verschillende wafers en velden binnen de wafers. Wafer D03 werd geselecteerd voor device processing omdat deze in veld C13 geschikte dimensies combineert (centrale die: breedte $\approx$ 198 nm en hoogte $\approx$ 482 nm) met het sterkste PL signaal. Vervolgens werde micro-caviteiten gedefinieerd met optische lithografie en ICP-etsen, en als proof-of-principle werden side mirrors met lage index gerealiseerd via photoresist infill, waardoor arrays van devices met systematisch gevarieerde caviteitsgroottes ontstonden.

μPL metingen bij kamertemperatuur tonen oppervlakte-emitterende lasing aan, zowel voor quasi-oneindige arrays als voor micro-Nano-Ridge Surface Emitting Lasers (NRSELs). Voor een quasi-oneindig array met 380 nm periode verschijnt een smalle piek nabij 984 nm met een drempel van $\sim 10\,\mathrm{kW\,cm^{-2}}$, en back-focal-plane imaging toont een kleine divergentie van $\sim 6.5^\circ$ (zie figuur 7). Voor een representatieve micro-NRSEL met $W_{\mathrm{NRSEL}} = 20\,\mu\mathrm{m}$ is de gemeten drempel 10.8 $\mathrm{kW\,cm^{-2}}$ en de minimale lijnbreedte 0.9 nm net boven drempel, met sterk gepolariseerde emissie die vrijwel uitgelijnd is met de nano-ridge as. Een statistische studie van 31 devices toont een globale reductie van de drempel tot 5 $\mathrm{kW\,cm^{-2}}$ bij toenemende caviteitsbreedte tot een optimum rond 35 $\mu\mathrm{m}$, gevolgd door een beperkte toename bij grotere breedtes ($\sim 14\%$), consistent met het samenspel tussen toenemende Q en disorder-gerelateerde verliezen, weergegeven in figuur 6.

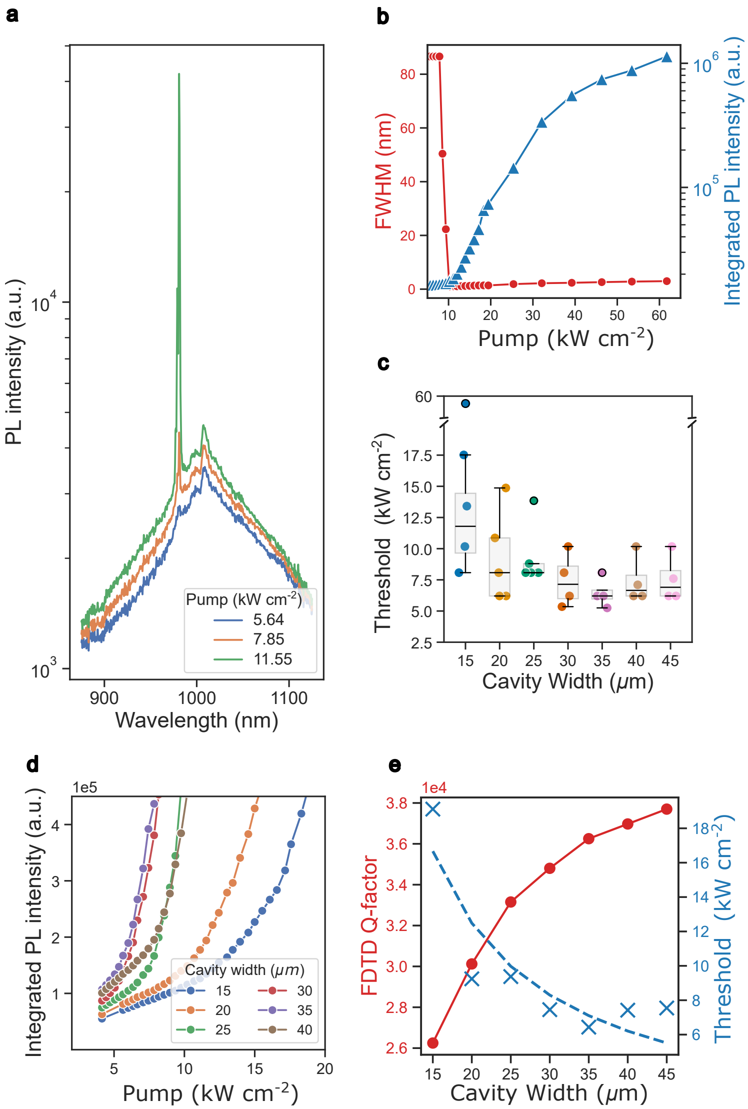

Figuur 2: Representatieve μPL spectra, lijnbreedte-vernauwing en statistische drempeltrends als functie van caviteitsbreedte.

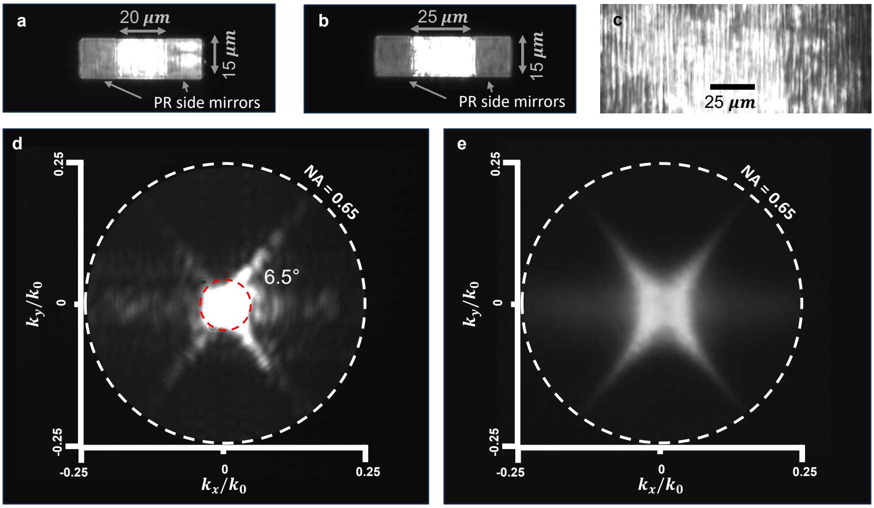

Figuur 3: (a, b) Real-space beelden van devices met caviteitsgroottes van 20 μm en 25 μm onder optische pumping boven de lasdrempel. In het 20 μm device is het licht voornamelijk in de caviteit geconcentreerd, hoewel er ook emissie uitbreidt in de photoresist mirror-regio rechts. In contrast is bij het 25 μm device de emissie volledig gelokaliseerd in de caviteit, met een duidelijke reflectie aan de interface tussen de caviteit en de photoresist side mirrors. (c) Real-space beeld van een quasi-oneindig array boven de lasdrempel, met emissie over een groot nano-ridge gebied. (d) Back-focal-plane beeld voor het 25 μm device boven drempel, met een hoekdivergentie van ongeveer 6.5°. (e) Back-focal-plane beeld van het quasi-oneindige array boven de lasdrempel.

Hoek-geresolveerde CL en PL metingen reconstrueren rechtstreeks de fotonische bandstructuur en bevestigen BIC-gerelateerde band-edge lasing. Hoek-geresolveerde reflectie van een breedbandige lichtbron resolveert de TE_{21L} en TE_{22L} banden en toont een vernauwing van de lijnbreedte naar Γ, waarbij de resonantie vernauwt van ~ 10 nm bij $k_x \approx 0.3$ tot onder de detectielimiet bij $k_x = 0$; dit is een duidelijke signatuur van een door symmetrie beschermde BIC (zie figuur 8). Complementaire hoek-geresolveerde CL reproduceert de dispersie en toont een scherpe band-edge piek met $Q > 300$. Onder femtoseconde-excitatie bevestigt hoek-geresolveerde PL lasing vanuit de TE_{21L} band edge nabij 975 nm met een drempel van 0.56 mJ/cm^2, terwijl een edge-die geometrie tweede orde band-edge laserwerking ondersteunt nabij 920 nm met een lagere drempel van 0.4 mJ/cm^2 en een kleinere verre veld divergentie van $\simeq 3°$. Voor eindige caviteiten die met photoresist zijspiegels worden gedefinieerd, worden discrete resonanties en modekwantisatie rechtstreeks waargenomen, consistent met $\Delta k \approx \pi/L$ en een effectieve caviteitslengte $L_{\mathrm{eff}} \approx 18\ \mu\mathrm{m}$ voor een nominaal $15\ \mu\mathrm{m}$ ontwerp als gevolg van veldpenetratie in de spiegels.

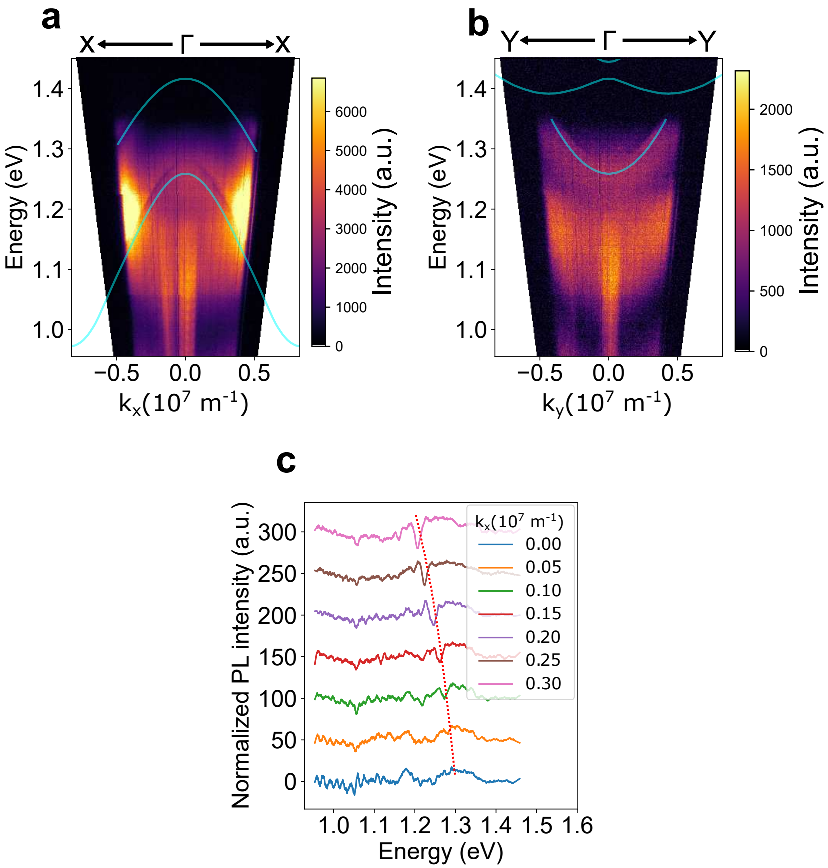

Figuur 4: Hoek-resolved metingen die de experimentele fotonische banden en de linewidth collapse naar Γ *tonen, consistent met een BIC.*

Ten slotte worden geavanceerde ontwerpconcepten onderzocht om de extractie-efficiëntie te verbeteren, bundelvorming mogelijk te maken en routes te openen naar elektrische injectie en spectrale controle. FDTD-simulaties tonen dat het toevoegen van een spiegel onder de caviteit de opwaartse emissie sterk kan verhogen via constructieve interferentie en de gesimuleerde Q kan verbeteren, met een opwaartse emissie die meer dan 73% bedraagt onder constructieve voorwaarden. Verder wordt verre veld optimalisatie via selectie van verschillende BIC modes besproken, elektrische-injectiestrategieën voor korte en lange caviteiten (inclusief contactplaatsing op knopen van het optisch veld en alternatieve nano-ridge doorsneden om modale overlap met contacten te reduceren), en additieve/post-groei golflengtetuning, waarbij simulaties aangeven dat een verandering van 1 nm in de nano-ridge breedte de resonantie met ~ 2.5 nm kan verschuiven.

Conclusie

Voor zover wij weten resulteerde dit werk in de eerste demonstratie van een optisch gepompte, oppervlakte-emitterende, epitaxiaal gegroeide III–V laser op een 300 mm siliciumwafer. Door BIC band-edge modes te benutten in een nano-ridge fotonisch-kristal platform realiseren we compacte oppervlakte-emitterende componenten die compatibel zijn met fabricage op waferschaal en standaard siliciumprocessen, en die over een wafer getuned kunnen worden via gecontroleerde variaties in geometrie en, in principe, materiaalsamenstelling.

Naast deze demonstratie legt deze thesis een directe link tussen de laserperformantie en de onderliggende bandstructuur. Groei op 300mm waferschaal met NRE, gecombineerd met metrologie en een praktische micro-fabricageflow, maakt micro-NRSELs mogelijk die bij kamertemperatuur lasen met een kleine divergentie. Hoek-geresolveerde PL en CL reconstrueren de fotonische dispersie en bevestigen dat de band-edge emissie geassocieerd is met BIC modes, terwijl studies van eindige caviteiten modekwantisatie tonen die kan worden benut voor verdere optimalisatie van het modeprofiel. De geavanceerde ontwerpconcepten in dit werk, waaronder verbeterde extractie via spiegels onder de caviteit, far-field shaping, strategieën voor elektrische injectie en additieve golflengtetuning, vormen een duidelijke roadmap naar schaalbare, elektrisch aangedreven en golflengte-afstembare NRSELs voor siliciumfotonica.

Summary

Vertical-cavity surface-emitting lasers (VCSELs) are among the most widely deployed semiconductor lasers, with major impact in datacom as well as consumer products such as optical mice and smartphones (e.g. face recognition and ranging). Their popularity is driven by wafer-scale fabrication and testing (typically on GaAs), compact form factor, and low cost. However, the VCSEL architecture relies on a complex vertical epitaxial stack consisting of a bottom distributed Bragg reflector (DBR), an active gain region, and a top DBR, where the mirrors typically require tens of precisely grown layers. This complexity constrains accessible wavelength ranges, since high-reflectivity DBRs are easiest to realize only for selected bands (commonly around 850 nm and 980 nm), while extending to other wavelengths (e.g. 1300 nm, 1550 nm, or the mid-infrared) is significantly more challenging. In addition, because the emission wavelength is largely set by epitaxial design, implementing well-controlled multi-wavelength VCSEL arrays on a single wafer and achieving straightforward monolithic integration with other photonic and electronic components remain non-trivial.

Aspect-ratio trapping (ART) and nano-ridge engineering (NRE) offer a monolithic route to grow high-quality III–V active material directly on silicon without thick buffer layers, by confining defects within narrow oxide-defined trenches and shaping the material into nano-ridges arranged in periodic arrays. These nano-ridge arrays form a high-index-contrast photonic crystal that supports Bloch modes, enabling band-edge (slow-light) operation where standing-wave resonances can provide sufficient in-plane feedback for lasing while emitting vertically from the surface (illustrated in figure 5). Nano-ridge surface-emitting lasers (NRSELs) therefore promise reduced epitaxial complexity compared to VCSELs (no micrometer-thick DBR stacks), broad wavelength agility through geometric tuning (period and ridge dimensions) and post-processing (e.g. dielectric deposition), and the prospect of multi-wavelength arrays on a single die by locally varying the photonic period and/or the material composition. In this thesis, we establish the operating principles and design rules, describe wafer metrology, epitaxy, and laser cavity fabrication, and report room-temperature optical characterization including threshold trends and far-field emission. In addition, we go beyond basic demonstration by (i) experimentally reconstructing the photonic band structure using angle-resolved CL and PL to directly confirm BIC-related band-edge lasing and finite-cavity mode quantization, and (ii) developing advanced concepts for improved extraction and beam shaping

(e.g. bottom reflectors and mode engineering), practical pathways toward electrical injection, and strategies for additive/post-growth wavelength tuning and more flexible 2D design concepts.

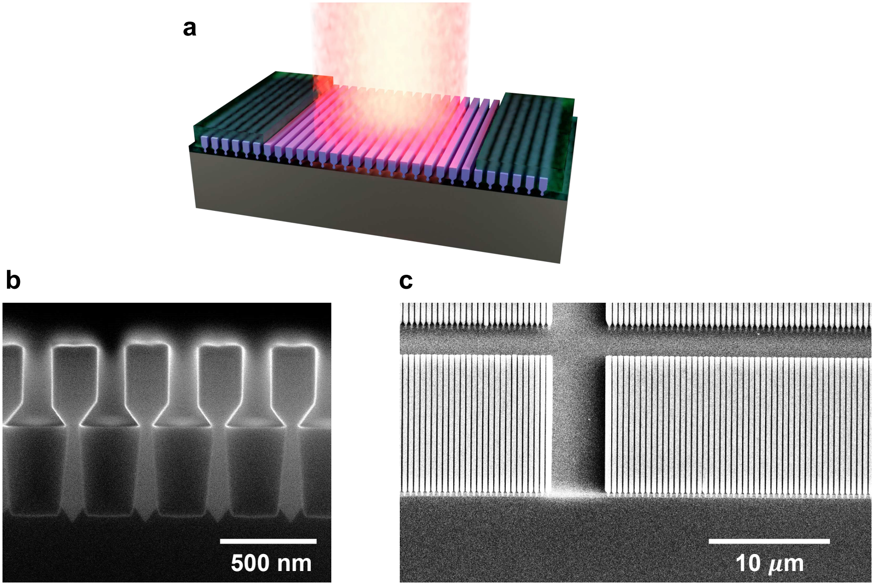

Figure 5: Nano-ridge surface emitting laser (NRSEL) on silicon. (a) Illustration of the proposed nano-ridge surface emitting laser (NRSEL). (b) Scanning electron microscope (SEM) image of the cross section of a cleaved array of nano-ridges. (c) Top-view SEM image of arrays of nano-ridges on a silicon wafer.

Results

The theoretical framework and design rules for nano-ridge photonic-crystal cavities on silicon are established by analyzing photonic bands, band-edge feedback, and BIC modes that enable high-Q surface emission. Using analytical scaling and FDTD, the target period for emission near 1 μm is identified to be on the order of 400 nm, and the design is refined by comparing candidate periods. For the selected 380 nm-period field (C13), the simulated resonance sensitivity to nano-ridge width variations is reduced ($\approx 2.3\ \mathrm{nm\,nm^{-1}}$) compared to larger-period alternatives, while the height sensitivity is smaller ($\approx 0.7\ \mathrm{nm\,nm^{-1}}$), motivating both the field choice and the focus on width control for robust fabrication.

Wafer-scale NRE growth, metrology, and a practical device fabrication flow are demonstrated on six 300 mm Si wafers (D02–D07). Cross-sectional SEM and room-temperature PL quantify nano-ridge dimensions, uniformity, and optical quality across wafers and fields. Wafer D03 is selected for device processing because it combines suitable dimensions in field C13 (center-die width $\approx$ 198 nm and height $\approx$ 482 nm) with the strongest PL signal. Micro-cavities are then defined by optical lithography and ICP etching, and low-index side mirrors are implemented as a proof of principle by photoresist infill, enabling arrays of devices with systematically varied cavity sizes.

Room-temperature μPL measurements demonstrate optically pumped surface-emitting lasing from both quasi-infinite arrays and micro-NRSELs. For a quasi-infinite 380 nm-period array, a narrow lasing peak near 984 nm appears with a threshold of $\sim$ 10 $\mathrm{kW\,cm^{-2}}$, and back-focal-plane imaging shows a narrow divergence of $\sim$ $6.5°$ (see figure 7). For a representative micro-NRSEL with $W_{\mathrm{NRSEL}} = 20$ μm, the measured threshold is 10.8 $\mathrm{kW\,cm^{-2}}$ and the minimum linewidth is 0.9 nm just above threshold, with strongly polarized emission aligned close to the nano-ridge axis. A statistical study of 31 devices shows an overall reduction of threshold to 5kW $\mathrm{cm^{-2}}$ with increasing cavity width up to an optimum around 35 μm, followed by a modest increase at larger widths ($\sim$ 14%), consistent with the interplay between increasing Q and disorder-related losses, shown in figure 6 .

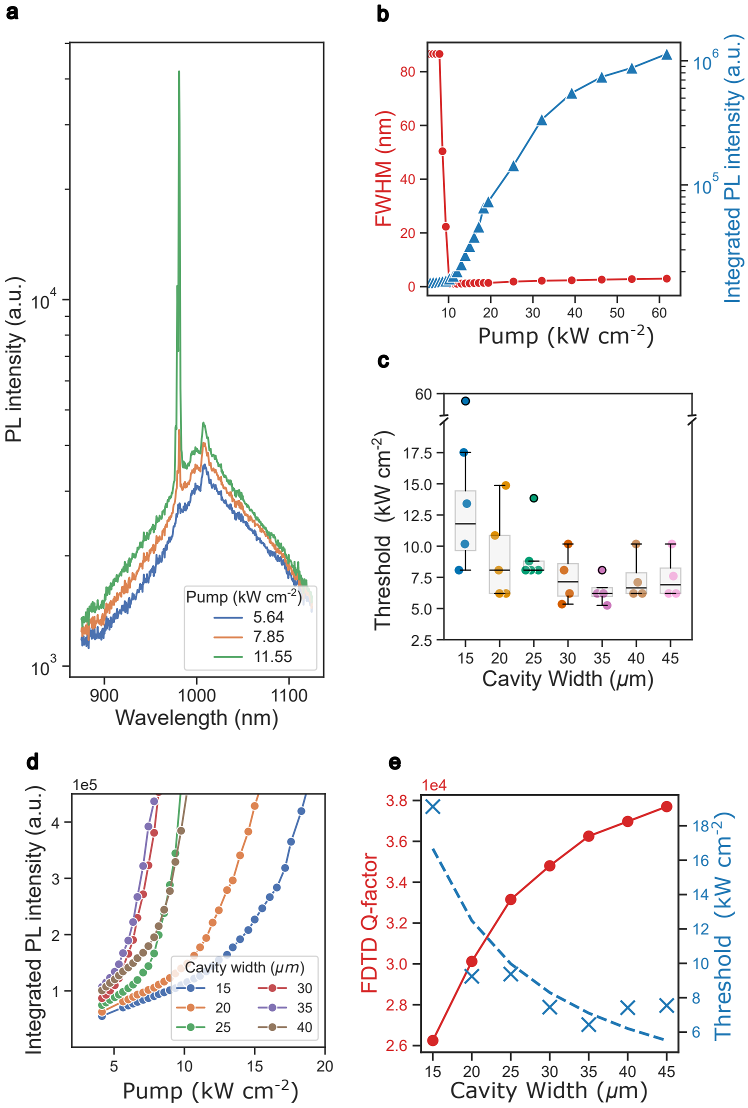

Figure 6: Representative μPL spectra, linewidth narrowing, and statistical threshold trends versus cavity width.

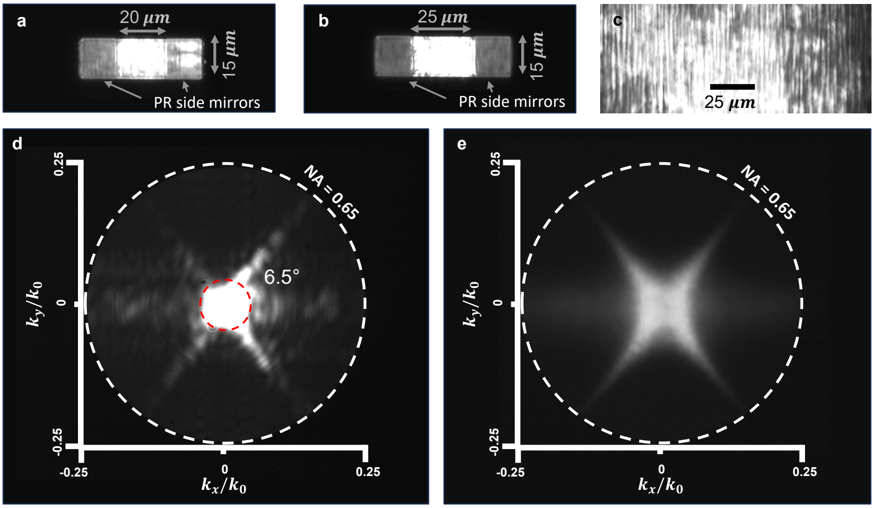

Figure 7: (a, b) Real-space images of devices with cavity sizes of 20 μm and 25 μm under optical pumping above the lasing threshold. In the 20 μm device, light is mostly confined to the cavity, although some emission extends into the photoresist mirror region on the right. In contrast, for the 25 μm device the emission is entirely localized within the cavity, with a clear reflection observed at the interface between the cavity and the photoresist side mirrors. (c) Real-space image of a quasi-infinite array under optical pumping above the lasing threshold, showing the emission from a large area of nano-ridges. (d) Back focal plane image for the 25 μm device above the lasing threshold, showing an angular divergence of approximately 6.5°. (e) Back focal plane image of the quasi-infinite array above the lasing threshold.

Angle-resolved CL and PL measurements directly reconstruct the photonic band structure and confirm BIC-related band-edge lasing. Angle-resolved white-light reflection resolves the TE_{21L} and TE_{22L} bands and shows a linewidth collapse toward Γ, with the resonance narrowing from $\sim$ 10 nm at $k_x \approx 0.3$ to below detection at $k_x = 0$, which is a clear signature of a symmetry-protected BIC (see figure 8). Complementary angle-resolved CL reproduces the dispersion and reveals a sharp band-edge peak with $Q > 300$. Under femtosecond excitation, angle-resolved PL confirms lasing from the TE_{21L} band edge near 975 nm with a threshold of 0.56 mJ/cm^2, while an edge-die geometry supports second-order band-edge lasing near 920 nm with a lower threshold of 0.4 mJ/cm^2 and a narrower far-field divergence of $\simeq 3°$. For finite cavities defined by photoresist side mirrors, discrete resonances and mode quantization are directly observed, consistent with $\Delta k \approx \pi/L$ and an effective cavity length $L_{\text{eff}} \approx 18\ \mu\text{m}$ for a nominal $15\ \mu\text{m}$ design due to field penetration into the mirrors.

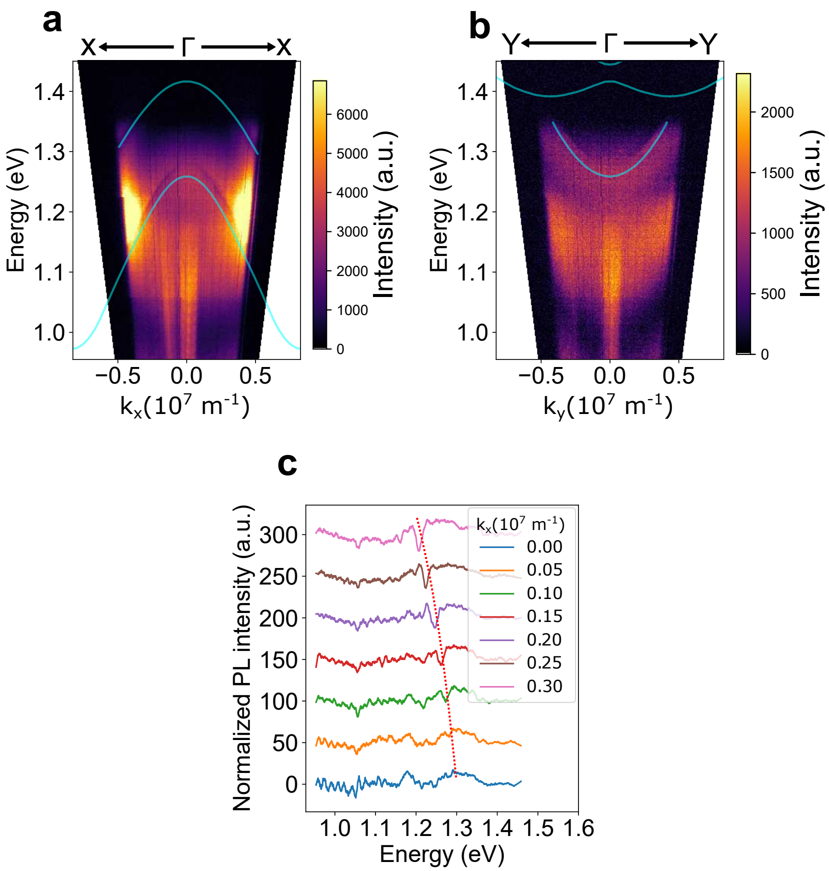

Figure 8: Angle-resolved measurements showing the experimental photonic bands and the linewidth collapse toward Γ*, consistent with a BIC.*

Finally, advanced design concepts are explored to improve extraction efficiency, enable beam shaping, and establish pathways to electrical injection and spectral control. FDTD simulations show that adding a bottom reflector can strongly enhance upward emission through constructive interference and can increase the simulated Q, with upward emission exceeding 73% under constructive conditions. The work further discusses far-field engineering via selection of different BIC modes, electrical injection strategies for short and long cavities (including contact placement at optical field nodes and alternative nano-ridge cross-sections to reduce modal overlap with contacts), and additive/post-growth wavelength tuning, where simulations indicate that a 1 nm change in nano-ridge width can shift the resonance by ~ 2.5 nm.

Conclusion

To the best of our knowledge, this work provides the first demonstration of an optically pumped, surface-emitting, epitaxially grown III–V laser realized on a 300 mm silicon wafer. By leveraging BIC band-edge modes in a nano-ridge photonic-crystal platform, we achieve compact surface-emitting devices that are inherently compatible with wafer-scale manufacturing and standard silicon processing tools, and that are tunable across a wafer through controlled variations in geometry and, in principle, material composition.

Beyond the device demonstration, the thesis establishes a direct connection between laser performance and the underlying band-structure physics. Wafer-scale NRE growth on 300 mm Si, combined with metrology and a practical micro-fabrication flow, enables micro-NRSELs that lase at room temperature with narrow divergence and systematic performance trends versus cavity geometry. Angle-resolved PL and CL reconstruct the photonic dispersion and confirm that band-edge emission is associated with BIC modes, while finite-cavity studies reveal mode quantization that can be exploited for mode engineering. Finally, the advanced design concepts proposed here, including improved extraction using bottom reflectors, far-field shaping, electrical injection strategies, and additive wavelength tuning, provide a clear roadmap toward scalable, electrically driven, and wavelength-controlled NRSELs for silicon photonics.

1

Introduction

1.1 Vertical-Cavity Surface-Emitting Lasers (VCSELs) 2
1.2 Recent Advances and Applications of VCSELs 5
1.3 Photonic-Crystal Surface-Emitting Lasers (PCSELs) . . . 8
1.4 Recent Advances and Applications of PCSELs 10
  1.4.1 Challenges and Ongoing Research 13
  1.4.2 Outlook and Future Directions 14
1.5 Comparison of EELs, VCSELs, and PCSELs 16
1.6 Silicon Photonics 20
1.7 Integration Techniques 20
  1.7.1 Heterogeneous Integration 21
  1.7.2 Monolithic Integration 23
  1.7.3 Monolithic III–V on Silicon via ART and NRE 24
1.8 Research Objectives and Thesis Outline 27
1.9 Publications and Patents 29
  1.9.1 Patent Application 29
  1.9.2 Publications in International Journals 29
  1.9.3 Publications in International Conferences 29
Bibliography 31

1.1 Vertical-Cavity Surface-Emitting Lasers (VCSELs)

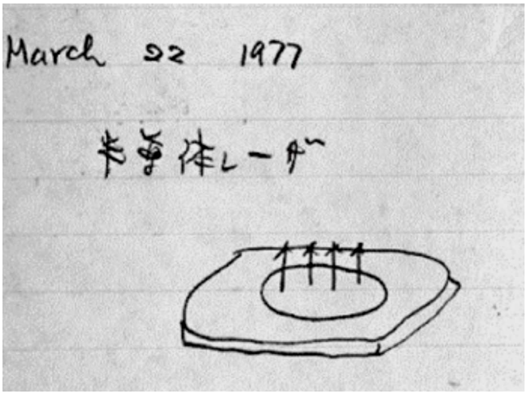

Figure 1.1: Sketch of the first VCSEL conceived in 1977 by Kenichi Iga [1].

Surface-emitting architectures enable wafer-level testing, dense 2D arrays, and straightforward free-space or fiber coupling, making them strong candidates for scalable optical I/O. The story of surface-emitting lasers began in 1977 when Kenichi Iga proposed the Vertical-Cavity Surface Emitting Laser (VCSEL) concept, as illustrated in figure 1.1 [1]. Since then, VCSELs have become the most widely deployed and successful lasers, particularly in short-reach data communications and consumer applications, due to their mature manufacturing process and low cost.

Kenichi Iga's push toward the VCSEL began with very practical frustrations about edge-emitting semiconductor lasers: their cavities were formed by cleaving wafers (early on, even using a "surgical knife"), which was inherently ill-suited to true mass production and also meant devices could only be fully characterized after cleaving, making wafer-scale testing and yield learning difficult. He also saw the edge-emitter geometry as a roadblock to 2D laser arrays. In parallel, he wanted more robust single-mode operationa as simulations suggested the cavity would need to be shorter than 50 µm to widen the free spectral range, and he worried about frequency reproducibility, since Fabry–Perot edge emitters (and cleave-length tolerances) made precise wavelength control difficult. Edge emitting lasers also suffer multimoding at higher powers due to their relatively large lateral dimensions, as shown in figure 1.2. Increasing the area of the cleaved facet to support higher power led to higher-order lateral modes, which complicated single-mode operation [1–5]. These considerations led him to the key conclusion: make the cavity vertical and build it from semiconductor/dielectric layers that can be fabricated with standard semiconductor processes rather than manual cleaving.

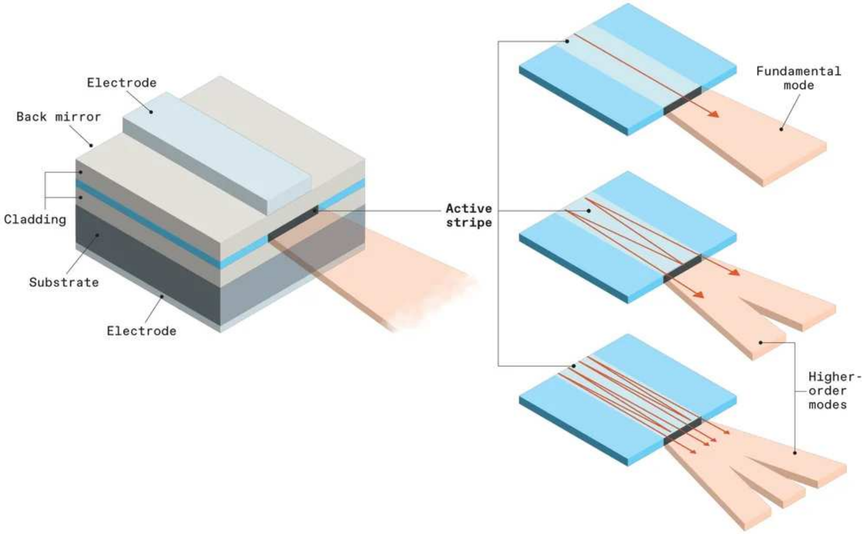

Figure 1.2: Schematic of a multimode edge-emitting laser due to the wide facet. (reproduced from [5])

This lead to the vertical-cavity surface-emitting laser (VCSEL) device, where the resonant cavity is formed vertically using Distributed Bragg Reflector (DBR) mirrors, as shown in figures 1.3 and 1.4, allowing the beam to exit from the surface rather than the chip edge [1, 6–8]. That geometry brings a set of practical advantages: low threshold currents, a near-circular output beam that couples well into optics/fibers, straightforward on-wafer testing before dicing, and, crucially, easy fabrication of 1D/2D emitter arrays for higher total power or structured illumination.

In 1982 Iga's group demonstrated one of the first practical surface-emitting injection lasers using a very short ($\approx 10\ \mu m$) GaInAsP/InP cavity emitting at 1.22 µm (tested at 77 K) and resulting in large mode separation. In subsequent GaAlAs/GaAs microcavity devices, they realized a circular buried cavity only a few micrometers in size, and also demonstrated Continuous-Wave (CW) operation at 77 K with even lower threshold (4.5 mA), establishing the microcavity VCSEL concept [1, 6–8].

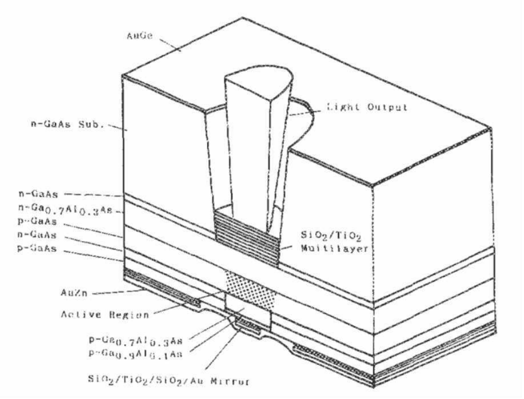

Figure 1.3: Schematic structure of a fabricated GaAlAs/GaAs vertical cavity surface-emitting laser (first room temperature VCSEL) reproduced from [8]).

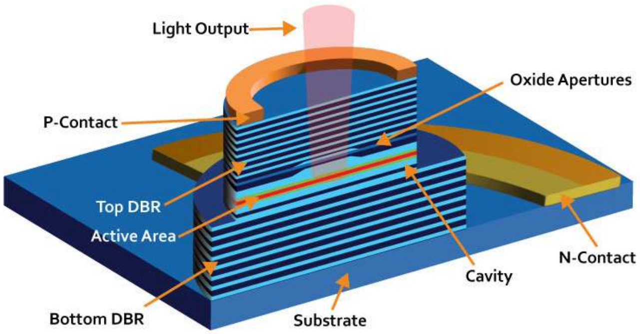

Figure 1.4: 3D Schematic structure of a modern vertical cavity surface-emitting laser (reproduced from [9]).

1.2 Recent Advances and Applications of VCSELs

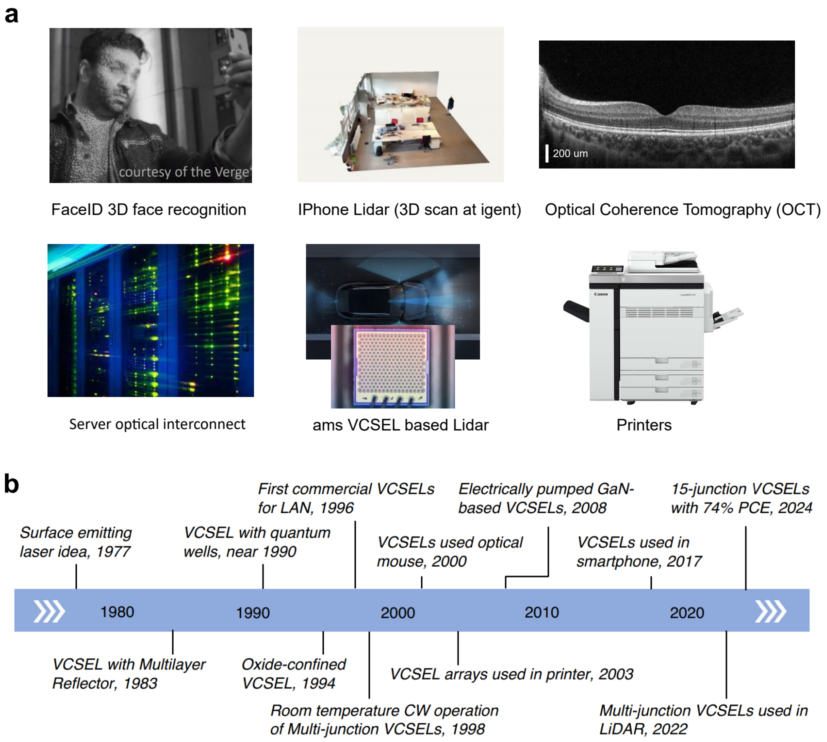

Figure 1.5: (a) Some applications of VCSELs. OCT figure reproduced from [10] (b) Timeline of VCSEL development (reproduced from [11]).

Building on decades of pioneering work by many researchers, VCSEL technology has advanced substantially in epitaxial material growth, device design, fabrication, and overall performance. As a result, VCSELs are now deployed across a wide range of applications, including short-reach optical communications, optical pointing and sensing (e.g., optical mice and face recognition), printing and storage technologies, and—most prominently in recent years—high-volume consumer and automotive platforms such as smartphones (3D sensing/illumination), AR/VR systems, and vehicle LiDAR. Figure 1.5 summarizes key milestones in the evolution of VCSEL development and presents some of the applications.

Over the past two decades, this maturation has consolidated into two dominant, high-volume pillars: short-reach optical interconnects (dominated by ∼850-nm links over multimode fiber) and illumination/sensing (notably ∼940-nm arrays for 3D sensing and emerging LiDAR transmitters). These deployments leverage

VCSEL advantages that are difficult to match with edge emitters; wafer-scale testability, dense 2D arrays, and fast direct modulation. Datacom adoption is driven by efficiency, reliability, and scalable manufacturing [1, 7, 12].

In data-center interconnects, the key challenge is no longer only bandwidth but energy per bit at scale. The rapid growth of AI workloads, expected to more than double global data center electricity demand by 2030, is pushing system bottlenecks from compute to communication and tightening interconnect energy and cost constraints [13–15]. Conventional electrical links face rising signal integrity and latency limits at high speeds and typically dissipate $\approx$ 1–15 $\mathrm{pJ/bit}$ at short reach and tens of $\mathrm{pJ/bit}$ over board/backplane distances [14–16]. Silicon photonics provides a strong system-level alternative: recent CMOS-compatible transmitters demonstrate sub-10 $\mathrm{pJ/bit}$ (down to $< 1\,\mathrm{pJ/bit}$) and multi-terabit capacities over data-center reaches, with studies projecting competitive cost per Gb/s as integration and co-packaging mature [12, 17–19]. Within this landscape, VCSEL-based links continue to advance toward $\sim$100-Gbps-per-lane through PAM4 and improved mode/parasitic control (oxide aperture engineering, mode filtering, etc.), with demonstrations steadily extending practical link speeds and distances [20, 21].

Long-wavelength VCSELs—typically O-band ($\sim$1310 nm) and C-band ($\sim$1550 nm)—target low-cost single-mode sources for short/medium-reach links with reduced dispersion. Here, the core device challenge is realizing low-loss, high-reflectivity mirrors and robust current confinement: monolithic InP-based DBRs have comparatively low index contrast, so many high-performance devices rely on hybrid/wafer-fused stacks pairing GaAs/AlGaAs DBRs with an InP-based active region. A recent review summarizes that wafer-fusion concepts have enabled long-time reliable long-wavelength VCSELs with $>$6 mW single-mode output, $\sim$13 GHz 3-dB bandwidth, and $\sim$37 Gb/s NRZ operation at 1550 nm [22]. Representative milestones include record fundamental-mode power (8 mW at $0\,^{\circ}\mathrm{C}$) in 1550-nm wafer-fused VCSELs [23], high-speed multilevel modulation such as 25 GBd 4-PAM (PAM4) links using a 1.5-μm VCSEL [24], and O-band results showing ($>$25) Gb/s direct modulation with 10 km SMF transmission at 1310 nm [25].

Alongside these performance-driven demonstrations, manufacturability and scale oriented mirror approaches are emerging, including nanoporous InP DBRs ($\Delta n \approx 1.0$) enabling VCSEL operation around 1380 nm and 1550 nm on InP substrates [26]. Long-wavelength (and SWIR) VCSEL families also extend into $\sim$1.3–2.3 μm regimes for spectroscopy and gas sensing, underscoring that state-of-the-art progress spans both high-speed datalinks and application-specific sources [22].

For illumination, sensing, and automotive LiDAR, the state of the art is increasingly defined by array-level power, brightness, divergence control, and wall-plug efficiency at 905/940 nm. A major device lever is the multi-junction (cascaded) VCSEL, which stacks multiple active regions interconnected by heavily doped tunnel junctions (typically $\gtrsim 10^{19}\ \mathrm{cm}^{-3}$) to enable carrier recycling between active regions while distributing current density and thermal load. This architecture is being pushed both for peak-power pulsed operation (e.g., $>$ 120 W peak power under pulsed current injection while retaining manufacturability advantages of surface emitters) [27] and importantly for record electro-optical efficiency: a recent Light: Science & Applications paper reports a 15-junction cascaded VCSEL achieving 74$\%$ power conversion efficiency at room temperature under nanosecond driving, with differential quantum efficiency ($>$ 1100$\%$) [28]. These devices stack multiple active regions (quantum wells) in series, with tunnel junctions between them. Carriers recombine in one active region to generate laser photons, and the tunnel junction then reinjects charge into the next stage, allowing the same injected current to drive photon generation again. Repeating this across several stages increases the optical output per unit current.

In parallel, these high-power/high-brightness arrays are increasingly central to automotive LiDAR , where improved brightness and reduced divergence can translate into longer range and better resolution; “anti-reflective VCSEL” concepts have also been proposed to mitigate optical feedback and support higher-brightness array operation relevant to LiDAR transmitter modules. A 6-junction AR-VCSEL array showcased a halved divergence and three times the brightness compared to its conventional counterpart [29, 30]

Finally, beyond fixed-wavelength emitters, another major trajectory is functional and wavelength expansion, exemplified by MEMS-tunable VCSELs in telecom-relevant bands (e.g., 1310 nm) for swept-source Optical Coherence Tomography (OCT), where the key figures of merit become tuning range, sweep rate, coherence, and sweep linearity rather than only static output power [31]. This direction is strategically important because it extends VCSELs from “illumination + interconnect” into compact swept sources for imaging and metrology.

Despite this broad progress, many of the hardest VCSEL challenges appear when one simultaneously demands large-area scaling, high single-mode beam quality, and high brightness (power in a diffraction-limited spot). This motivates alternative surface-emitting concepts, most notably Photonic Crystal Surface Emitting Lasers (PCSELs), which use photonic-crystal feedback to support intrinsically single-mode, high-brightness emission over larger apertures [5, 32].

1.3 Photonic-Crystal Surface-Emitting Lasers (PCSELs)

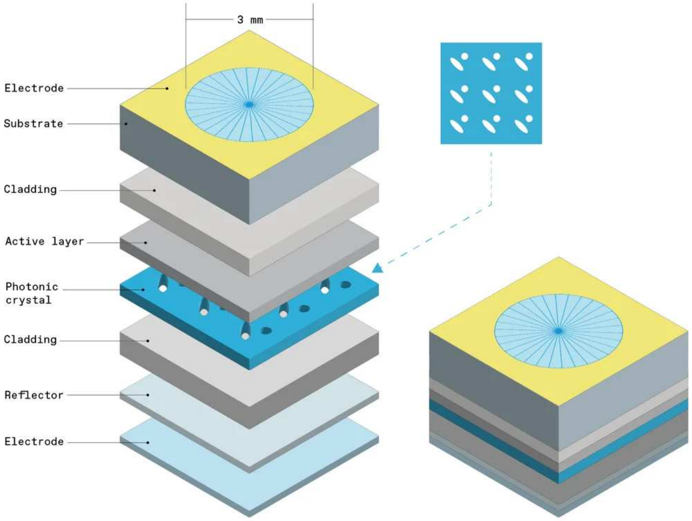

Figure 1.6: 3D Schematic structure of a photonic-crystal surface-emitting laser (reproduced from [5]).

Photonic crystal surface-emitting lasers (PCSELs) are semiconductor lasers that incorporate a 1D/2D dimensional photonic crystal (PhC) into the cavity to achieve large-area coherent oscillation and surface-normal emission. In a typical PCSEL, a periodic refractive-index modulation (often realized as a lattice of air holes in a semiconductor slab) is integrated with an active gain medium (e.g. multiple quantum wells) [33, 34]. The 2D photonic crystal provides in-plane distributed feedback and forms a band-edge resonance where the in-plane waves of the cavity modes form a 1D/2D standing wave. Lasing usually occurs at a high-symmetry point of the photonic band structure (most commonly the Γ point), and first-order Bragg diffraction couples a small fraction of the guided mode out of plane, producing a surface-emitted beam [33, 35–37].

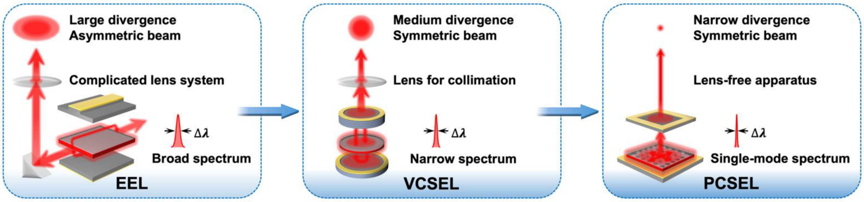

Figure 1.7: Comparison between edge-emitting lasers (EELs), vertical-cavity surface-emitting lasers (VCSELs), and photonic-crystal surface-emitting lasers (PCSELs) (reproduced from [38]).

PCSELs offer several advantages over traditional edge-emitting lasers and VCSELs. They can achieve high output power while maintaining single-mode operation due to the large-area coherent oscillation enabled by the photonic crystal feedback, as shown in figure 1.7. The surface-emission geometry simplifies packaging and testing, and the photonic crystal design allows for engineering of the far-field emission pattern, enabling low-divergence beams and tailored beam shapes [33, 36, 37].

Because the entire photonic crystal area acts as a coherent light aperture, PCSELs can exhibit extremely small beam divergence (down to $\sim 0.05^\circ$ in recent large-area devices) while maintaining single spatial mode operation even for millimetre-scale resonators [32]. This is in strong contrast to conventional edge-emitting lasers (EELs), which become highly multimode and astigmatic when their stripe width is increased, and to vertical-cavity surface-emitting lasers (VCSELs), which have good beam symmetry but typically require arrays to reach high power. PCSELs combine area-based power scaling (like EELs) with single-mode, narrow-divergence surface emission (like VCSELs), making them very attractive for high-brightness applications such as LiDAR, free-space optical communications, and materials processing [34, 38].

Figure 1.6 illustrates the basic structure of a PCSEL. It consists of a planar waveguide or resonator layer incorporating the 2D PhC pattern, sandwiched between cladding layers. The PhC lattice constant and filling factor are designed so that one of the band-edge frequencies overlaps the gain spectrum. At that band-edge the in-plane group velocity approaches zero, leading to strong field buildup over the entire device area [33]. The 2D Bragg scattering couples counter-propagating in-plane waves to form standing waves; at the same time, second-order Bragg diffraction extracts light vertically. When the out-of-plane scattering from all lattice sites interferes constructively, a highly directional surface-normal beam is produced. By tailoring the unit cell and lattice symmetry, one can control mode selection, polarization, radiation losses and the threshold separation between the fundamental and higher-order modes [34, 39].

The basic concept of a 2D photonic crystal laser and its surface-emitting implementation was pioneered by Noda and co-workers in the late 1990s [35]. Independently another group, Meier et al. reported lasing from a structure comprising a triangular-lattice photonic crystal and an organic gain medium [40]. Noda's group demonstrated coherent two-dimensional lasing in a surface-emitting laser with a triangular-lattice photonic crystal integrated with an InGaAsP/InP multiple-quantum-well slab by bonding two InP wafers (one for the active layer and another for the photonic crystal defined using electron bem lithography and reactive ion etching (RIE)), showing that a 2D PhC can serve as an efficient lateral resonator and outcoupler [35]. They also showed how important uniform current injection is for achieving large-area coherent oscillation. If injection is non-uniform, different parts of the Photonic Crystal (PhC) see different gain/index, as a result multiple locally favored oscillations happen instead of one coherent 2D mode. Subsequent work established systematic design rules for PCSELs, including polarization control, beam-pattern engineering, and large area (mm scale) high brightness [32–34].

1.4 Recent Advances and Applications of PCSELs

Large-area high-brightness PCSELs and Noda's group

A major research thrust since about 2015 has been scaling PCSELs to large apertures while retaining single-mode operation and diffraction-limited beams. Conventional semiconductor lasers become strongly multimode as the aperture grows, but PCSELs can circumvent this by engineering the Hermitian (energy-conserving) and non-Hermitian (radiative-loss) coupling coefficients of the PhC to favour a single band-edge mode over a wide area.

An important early milestone in power scaling was the demonstration of watt-class (0.5 W C.W. at room temperature), high-beam-quality photonic-crystal lasers by Hirose *et al.* [41]. Building on this, Yoshida *et al.* recently reported large-scale GaAs-based PCSELs with a resonator diameter of 3 mm, achieving continuous-wave (CW) output powers exceeding 50 W with purely single-mode operation and a beam divergence as small as 0.05° [32]. The brightness approaches $1\,\mathrm{GW\,cm^{-2}\,sr^{-1}}$, rivaling bulk solid-state and fiber lasers while maintaining a single monolithic semiconductor chip [32, 42]. The group also demonstated cutting steel using this high-power PCSEL, shown in figure 1.8, highlighting its potential for materials processing applications [5, 42].

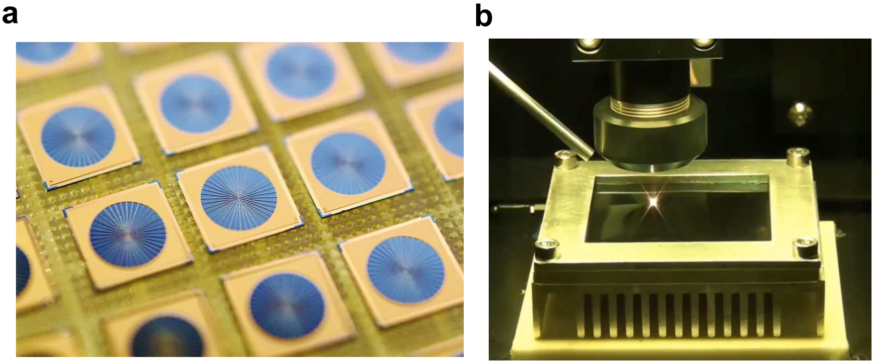

Figure 1.8: (a) A 3-millimeter-wide PCSELs on a wafer. (b) 50-watt PCSEL cutting steel (reproduced from [5]).

In parallel, Inoue *et al.* derived a general analytic "recipe" for ultra-large-area single-mode PCSELs by explicitly treating both Hermitian and non-Hermitian couplings in a double-lattice PhC [39]. Their theory clarifies how to design the PhC so that the fundamental Γ-point mode has much lower in-plane loss and properly tuned radiative loss compared to competing modes, enabling theoretical scaling to 3–10 mm diameter devices capable of 100 W–1 kW single-mode operation [39]. Experiments have since demonstrated 3 mm-diameter devices with tens of watts of CW single-mode output and even larger devices reaching hundreds of watts under pulsed drive [32, 42]. These results strongly suggest that one-chip, kW-class semiconductor PCSELs are feasible in the near future.

New wavelength regimes: telecom, visible, and deep-UV

Beyond GaAs-based near-infrared devices around 0.9–1.0 µm, PCSELs are now being realized across a wide spectral range. In the telecom bands, InP-based PCSELs have been developed for 1.3 and 1.55 µm, motivated by free-space optical communication and eye-safe LiDAR. Wang *et al.* demonstrated the first CW 1.55 µm PCSEL by introducing a "triple-lattice" photonic crystal resonator that superimposes three lattice point sets to boost in-plane feedback without requiring extremely high index contrast [43]. The device showed low threshold current density and stable single-mode CW operation, illustrating how sophisticated PhC designs can compensate for material limitations at longer wavelengths [43].

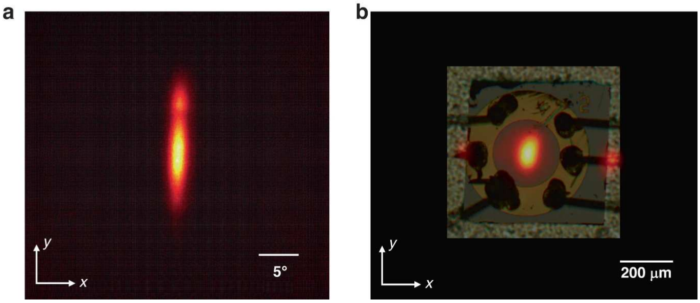

Figure 1.9: PCSEL at 1550 nm (reproduced from [43]). (a) Far-field pattern (b) Near-field pattern.

At shorter wavelengths, wide-bandgap III-nitride PCSELs have made notable progress. The first GaN PCSEL at blue-violet wavelengths was reported in 2008 [44], but only recently have watt-class, high-beam-quality GaN-based PCSELs been achieved. Emoto *et al.* realized blue PCSELs with output powers exceeding 0.32 W and circular single-lobed beams with $\sim 0.2^\circ$ divergence by carefully optimizing the layer structure and adopting a double-lattice PhC design [37]. This work demonstrated that robust 2D resonance and narrow-divergence beams are possible even in GaN, which has relatively low index contrast and demanding nanofabrication requirements. Continuous-wave operation with hundreds of milliwatts and $M^2 \approx 1$ has also been demonstrated [37].

Even the deep-ultraviolet regime has recently been reached. Apaydin *et al.* reported the first deep-UV PCSELs emitting around 279 nm under pulsed optical pumping, using carefully engineered AlGaN-based PhC structures to overcome the low-index-contrast and scattering challenges [45]. The devices exhibit single-mode emission with sub-degree beam divergence, highlighting the potential of PCSELs to provide high-beam-quality sources where conventional deep-UV edge emitters suffer from severe beam quality, multi-mode and mirror damage [45].

Beam control, steering, and functional PCSELs

The 2D nature of the PhC makes PCSELs an ideal platform for beam engineering. By spatially modulating the PhC parameters (hole size, position, or lattice constant), one can change the phase and amplitude distributions of the emitted beam. Sakata *et al.* introduced "dually modulated" photonic crystals that enable high-power, high-beam-quality 2D beam scanning without external optics [46]. They demonstrated on-chip PCSEL arrays with a 10×10 matrix of elemental emitters, each with slightly different modulation, achieving 100 resolvable beam directions in two dimensions [46]. More recently, Sakata *et al.* reviewed and extended the concept of modulated PCSELs, showing that a wide range of beam patterns can be realized simply by designing the PhC [47].

These developments effectively turn PCSELs into monolithic optical phased arrays, opening the door to compact, solid-state LiDAR transmitters with electronic beam steering. System-level analyses indicate that PCSEL-based LiDAR could enable lens-free, ultra-compact time-of-flight systems, with PCSEL arrays providing both illumination and scanning functionality [38, 42].

1.4.1 Challenges and Ongoing Research

Despite rapid progress, several key challenges remain before PCSELs can fully replace more established laser technologies in demanding applications.

Mode control, current spreading, and thermal management. Maintaining stable single-mode operation at high CW power requires excellent control of carrier and temperature distributions over a large area. Non-uniform current injection or thermal gradients can induce local changes in band-edge frequency and gain, allowing higher-order modes to appear at high drive currents [35]. Advanced electrode designs that selectively shape the current injection profile have been shown to suppress higher-order modes and enhance fundamental-mode operation in large-area PCSELs [48]. At the same time, high-power PCSELs require aggressive thermal management, such as bonding to high-thermal-conductivity submounts and carefully engineered heat spreaders, to avoid thermal lensing and maintain uniform operation [42].

Fabrication complexity and yield. Realizing high-quality 2D PhCs over millimetre-scale areas with nanometre-level precision is a nontrivial fabrication challenge. E-beam lithography remains the workhorse for research devices but is time-consuming for very large apertures and may suffer from stitching errors. Alternative patterning methods such as stepper lithography or nanoimprint are being explored to improve throughput and scalability [49–52]. Any disorder in the PhC (variations in lattice constant, hole size, or etch depth) can perturb the band-edge frequency and coupling strength, degrading performance. Hybrid cavity concepts, such as resonator-embedded PCSELs that combine a moderate-coupling PhC with auxiliary resonators, are being investigated to relax patterning tolerances while preserving mode control [42, 53].

Efficiency and reliability. Recent electrically pumped PCSEL demonstrations report wall-plug efficiencies in the *tens of percent* range in the best cases, but reported values vary widely by material system and design; overall, they remain below the highest-efficiency edge-emitting diode laser bars, which have demonstrated wall-plug efficiencies well above 50% (e.g., 73% at 70 W for 940 nm bars). [42, 54, 55]. Efficiency is limited by large active area, distributed radiation loss, and non-optimal current injection. Concepts such as multi-junction or multi-active-region PCSELs, improved PhC designs with reduced scattering loss, and optimized contact schemes are being pursued to push efficiency higher [42]. Long-term reliability under high current and high optical power also remains under active study; the complex epitaxial structures and regrowth steps introduce potential defect sites that must be controlled for thousands of hours of operation in industrial settings [38].

Dynamic characteristics and linewidth. Large-area PCSELs naturally raise questions about modulation bandwidth and spectral coherence. Although their large capacitance could, in principle, limit speed, several works have demonstrated that properly designed PCSELs can support multi-gigahertz modulation bandwidths and pulse operation, for example via gain switching or Q-switching mechanisms [56, 57]. Recent experiments and theory have analyzed intrinsic spectral linewidths of PCSELs in detail, revealing that very narrow linewidths can be obtained in PCSELs. According to the Schawlow-Townes theory, the laser linewidth is inversely proportional to the number of photons in the cavity. By scaling up the cavity area while maintaining a single mode, they significantly increased the photon count, which naturally compressed the linewidth to 35 kHz at powers 300 mW [58]. Understanding noise, coherence, and mode competition in these complex 2D cavities is an active research topic.

1.4.2 Outlook and Future Directions

The combination of high brightness, narrow divergence, and beam-shaping capability puts PCSELs in a strong position to impact several application areas. In LiDAR, PCSEL arrays offer a credible route to fully solid-state transmitters: large-area single-mode devices can provide the required peak power, while modulated or dually modulated PhCs enable electronic beam steering and pattern shaping [38, 46]. In industrial laser processing, kW-class PCSEL modules could eventually rival fiber and disk lasers, with the advantages of compactness and potentially higher electro-optic efficiency [32, 39].

On the scientific side, PCSELs provide a fertile platform for exploring non-Hermitian photonics, large-area coherence, and novel cavity dynamics, because the interplay of gain, loss and engineered band structure is highly tunable [39, 42]. Future directions include multi-wavelength PCSEL arrays (for RGB displays or spectroscopy), heterogeneous integration with silicon photonics for on-chip beam routing, and ultrafast PCSELs for coherent communications and LiDAR [59, 60].

Overall, PCSELs have evolved from a conceptual curiosity into a versatile laser platform spanning wavelengths from deep-UV to telecom bands and powers from milliwatts to tens of watts (and soon beyond). Continued advances in PhC design, materials growth, nanofabrication and packaging are expected to consolidate their position as a new class of high-brightness semiconductor lasers that can rival or even replace bulkier solid-state and fiber sources [42, 42].

1.5 Comparison of EELs, VCSELs, and PCSELs

Tables 1.1, 1.2, and 1.3 summarize a qualitative comparison of edge-emitting lasers (EELs), vertical-cavity surface-emitting lasers (VCSELs), and photonic-crystal surface-emitting lasers (PCSELs) across several key features, including emission geometry, typical single-emitter continuous-wave power, beam quality, direct modulation bandwidth, wavelength coverage, fabrication complexity, efficiency, and reliability.

Feature	**EELs**	**VCSELs**	**PCSELs**
Emission geometry	Edge emission from a Fabry–Pérot ridge or DFB/DBR cavity; output from chip facet.	Surface-normal emission from a short vertical cavity with DBR mirrors and an oxide (or implant) aperture.	**Surface-normal emission from a planar waveguide resonator with a 2D photonic crystal providing in-plane feedback and out-of-plane diffraction [33, 34].**
Typical single-emitter CW power (single-mode)	~ 0.1–1 W single-transverse-mode from ridge / tapered designs; tens of watts available in multimode high-power bars [61].	Single-mode: typically a few to ~ 10 mW (commercial) and up to ~ 50 mW in research devices; higher powers usually require arrays or multi-aperture designs [11].	**Single-mode: already demonstrated at tens of watts CW from a single 3 mm aperture device with > 50 W output [32, 42]; multi-watt-class devices in GaN and InP material systems have also been reported [37, 38].**
Beam divergence / beam quality (single device)	Good beam quality in one axis; typically strongly asymmetric and multimode for high-power devices (few to tens of degrees divergence) [61]. Beam shaping optics usually required.	Nearly circular, few-degree divergence for single-mode VCSELs; divergence increases and beam quality degrades for large-aperture multimode devices [11]. Well-suited for direct fiber coupling in short-reach links.	**Extremely narrow and circular beams; diffraction-limited operation with full-angle divergence down to $\sim 0.05^\circ$–0.1° reported for 3 mm devices [32, 42]. Very high brightness, attractive for LiDAR and free-space optics [38].**
Direct modulation bandwidth (3 dB)	Tens of GHz possible for optimized DFB/DBR or EAM-integrated devices; used in long-haul/coherent systems but often with external modulators rather than direct drive.	**Mature high-speed technology: 20–30 GHz 3 dB bandwidth in research devices; complex modulation formats beyond 100 Gb/s per lane demonstrated for 850 nm VCSELs [11]. Standard choice for short-reach datacom.**	Early devices: ~ 2–4 GHz 3 dB bandwidth [54, 62]. Recent photon–photon-resonance PCSELs show > 10 GHz bandwidth at ~ 1 W CW output in simulation/experiment [56]. Design studies suggest potential for 40 GHz-class bandwidths with strongly confined apertures, but this is not yet mainstream [39].

Table 1.1: Qualitative comparison of EELs, VCSELs, and PCSELs (Part I).

Feature	EELs	VCSELs	PCSELs
Wavelength coverage (mature technologies)	0.63–2 µm and beyond (InP, GaAs, GaN, etc.); telecom C-band DFBs are standard.	Most mature around 850 nm (datacom), 940 nm (3D sensing) and 1.3 µm; research VCSELs extend further into NIR [11].	**Demonstrated from deep-UV (**~ 279 **nm) through visible (GaN blue/violet) up to NIR and 1.55 µm (InP-based PCSELs) [37, 38, 43–45].**
Scalability and arrays	Power scaling via bars/stacks; coherent or spectral beam combining needed for diffraction-limited beams. Fabrication and packaging of high-fill-factor arrays is mature.	Very amenable to 1D/2D arrays on wafer; widely used in consumer depth cameras and sensing. Coherent combining is challenging due to cavity-to-cavity variation.	**Scalability is intrinsic: very large single apertures (mm-scale) can remain single-mode [32, 39]. Modulated photonic-crystal designs enable monolithic 2D beam-steering arrays without mechanical scanning [46, 47].**
Fabrication complexity	**Relatively simple epitaxy and processing (ridge/DFB structures, cleaved facets); very mature and low cost per watt.**	More complex epitaxy (thick DBR stacks, oxidation layers), but highly standardized and compatible with wafer-scale testing and packaging [11].	Highest structural complexity: requires high-quality epitaxy plus nanometre-precision 2D photonic-crystal patterning and, often, epitaxial regrowth over the PhC. Processing over millimetre-scale areas with tight tolerances is still a manufacturing challenge [34, 38].
Main strengths (for applications)	Very high power and electrical-to-optical efficiency; mature, robust technology for industrial processing, pumping and telecom.	High-speed, low-power, low-cost sources with easy array integration and direct fiber coupling; the workhorse for short-reach datacom and consumer 3D sensing [11].	Combines semiconductor compactness with solid-state/fiber-like brightness: ultra-narrow beams, large single-mode apertures, and monolithic beam steering. Particularly promising for LiDAR, high-brightness free-space links and compact projectors [38, 42, 46].
Key limitations (today)	Poor raw beam quality (especially in slow axis) and astigmatism; requires optics or beam combining for diffraction-limited beams at high power.	Single-emitter power limited compared to EELs/PCSELs; thermal management and modal control become difficult at high powers or long wavelengths.	Technology still emerging: lower wall-plug efficiency than best EELs, fabrication complexity, and relatively modest demonstrated modulation speeds compared to VCSELs [38, 42].

Table 1.2: Qualitative comparison of EELs, VCSELs, and PCSELs (Part II, continued).

Feature	**EELs**	**VCSELs**	**PCSELs**
Mode separation / mode discrimination	Single-mode operation typically achieved by index guiding, ridge width control, and/or DFB/DBR gratings; higher-order lateral modes appear as aperture increases unless special designs (e.g. tapered/antiguided) are used.	Fundamental transverse mode can be enforced with small oxide apertures; as aperture increases, transverse mode spacing shrinks and devices become multimode (often intentionally in high-power arrays) [11].	**Designed for large-area single-mode operation: band-edge mode selection and engineered coupling (including double-/multi-lattice and modulated PhC concepts) can maintain strong discrimination against higher-order modes even for mm-scale apertures [32–34, 39].**
Multi-wavelength on the same wafer	Common: arrays of DFB/DBR EELs at different wavelengths are routinely fabricated on the same wafer (e.g. WDM sources in InP platforms); wavelength selection via grating period and epitaxial design is mature.	Extremely difficult: wavelength is set by the vertical cavity resonance (DBR design and cavity thickness), so the cavity thickness must be precisely controlled along the growth direction. [11].	**Highly amenable: wavelength can be set lithographically by the photonic-crystal lattice constant/unit cell, enabling multi-wavelength arrays on a single wafer with otherwise similar epitaxy; this is attractive for integrated sources (e.g. multi-line illumination, spectroscopy, WDM-like arrays) [33, 34].**
Integration with silicon	Commonly integrated via hybrid approaches (e.g. flip-chip or butt-coupling to Si photonics); high-power EEL gain chips are frequently used as external or hybrid light sources for silicon photonic transceivers.	Typically used as discrete sources (fiber-coupled or free-space coupled); direct monolithic integration on silicon is non-trivial, but wafer-level packaging and co-packaged optics are mature for datacom modules [11].	Attractive for co-packaging / heterogeneous integration because of surface emission and potential for on-chip beam shaping/steering.

Table 1.3: Qualitative comparison of EELs, VCSELs, and PCSELs (Part III, continued).

1.6 Silicon Photonics

Silicon photonics leverages the mature Complementary Metal-Oxide Semiconductor (CMOS) manufacturing ecosystem, including large, low-cost silicon wafers, high-throughput lithography, and tight process control, to fabricate photonic components with scalability, yield, and repeatability comparable to microelectronics. This enables dense integration and co-design across devices, circuits, packaging, and electronics, and it supports wafer-scale fabrication and testing as well as co-packaging, for example fiber attach, thermal management, and high-density electrical and optical I/O, which ultimately determine system cost and performance. It enables compact and scalable transceivers for data communications and is increasingly relevant for sensing and emerging photonic computing platforms [63]. A central missing building block remains a low-cost, wafer-scale on-chip laser that is compatible with standard manufacturing flows.

Hybrid and heterogeneous integration of III–V gain media on silicon has made significant progress, achieving high-performance lasers via bonding or transfer printing [17, 18, 64]. These approaches, however, add assembly complexity and can limit throughput or cost targets for high-volume interconnects. As a result, monolithic routes that directly grow III–V materials on silicon substrates remain an active research direction [65, 66]. Within both heterogeneous and monolithic approaches, surface-emitting architectures are especially attractive because they simplify testing and packaging while enabling dense arrays.

1.7 Integration Techniques

Silicon has an indirect bandgap and cannot efficiently emit light, so integrating direct-bandgap III–V materials is essential for on-chip lasers. Lattice mismatch hampers integration of III/V materials on silicon substrates, as shown in figure 1.10. The lattice mismatch between III–V and group-IV materials (e.g., $\sim$4% between GaAs and Si) can generate a high density of threading dislocations (up to $\sim 10^{10}, \mathrm{cm}^{-2}$). These defects introduce dangling bonds and other nonradiative recombination centers, which degrade laser efficiency and reliability [67]. There are three main integration techniques: heterogeneous integration via wafer bonding, flip-chip, or transfer printing; planar monolithic growth of III–V materials on Si, for example by direct epitaxial growth on blanket silicon wafer using graded buffer layers or dislocation-filtering stacks; and selective-area monolithic integration of III–V on silicon in oxide-defined trenches/openings, for example using Aspect Ratio Trapping (ART), NRE. Each approach has its own technical trade-offs in terms of materials quality, scalability, cost, and compatibility with silicon photonics processes [17, 18, 64–66].

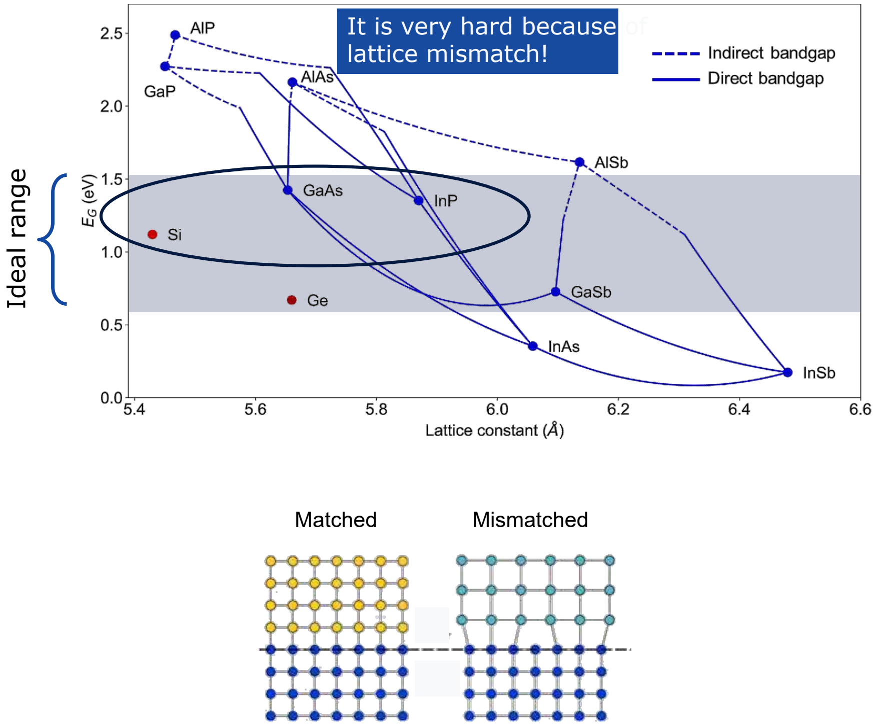
It is very hard because of lattice mismatch!

Figure 1.10: (a) Lattice constant vs bandgap energy for different semiconductor materials. (b) Diagram showing the lattice mismatch because of the different lattice constant of two materials.

1.7.1 Heterogeneous Integration

Wafer Bonding

Wafer bonding is the workhorse heterogeneous-integration route for silicon photonics when you want wafer-scale placement of a non-native thin film (most commonly III–V gain) onto processed SOI/SiN waveguide circuitry. In practice, “bonding” spans direct/molecular bonding (oxide-mediated or plasma-activated) as well as adhesive/polymer bonding; the shared idea is that the III–V epitaxial stack is attached first, then the native III–V substrate is removed and devices are fabricated (or completed) in the bonded film, enabling tight optical coupling (often evanescent) to the underlying silicon waveguides. Adhesive approaches such as ultra-thin divinylsiloxane-bis-benzocyclobutene (DVS-BCB) can relax surface/topography constraints and lower thermal budgets while still achieving very thin bonding layers needed for efficient coupling, at the cost of a weaker thermal path than metal/direct bonding in many designs. [68, 69]

An illustrative early example of this approach is the progression of InP-based photonic-crystal (PhC) lasers developed by researchers at Ecole Centrale de Lyon, aiming at silicon-compatible light sources. Starting from bonded InP multiple-quantum-well PhC membranes on silicon, they demonstrated room-temperature lasing near 1.5 μm using slow Bloch band-edge modes with mW-scale pulsed thresholds [70]. They then introduced graphite-like (honeycomb) PhC designs to enhance out-of-plane coupling and demonstrated compact surface-emitting Bloch-mode lasers on silicon [71]. Vertical feedback was later reinforced by combining the bonded PhC membrane with a high-index-contrast Si/SiO_2 Bragg reflector, pushing room-temperature surface-emitting microlasers toward sub-15 μW thresholds [72].

Flip-chip

Flip-chip integration instead treats the III–V element as a packaged-like, fully fabricated "known-good die" that is pick-and-placed onto the silicon photonics wafer/chip and then permanently attached (e.g., solder/metal bumps plus underfill/epoxy). This is attractive when you only need a modest number of active dies per PIC: you can test lasers before assembly, keep III–V processing largely on its native platform, and leverage high-throughput assembly tools. The core technical trade is that optical coupling (often butt-coupling into a facet or spot-size converter) becomes extremely alignment-sensitive and the thermal/mechanical design shifts toward packaging concerns (Coefficient of Thermal Expansion mismatch, heat extraction, and long-term reliability). [67, 73]

Transfer Printing

Transfer printing (often "micro-transfer printing") pushes heterogeneous integration toward massively parallel placement with high material utilization: micron-scale III–V coupons are released from a donor wafer, retrieved by a viscoelastic stamp, and printed onto predefined sites on the silicon photonics target. Because coupons can be small and placed selectively, transfer printing supports "mix-and-match" integration (different epitaxial stacks on the same SiPho wafer) and can enable wafer-level scaling without bonding an entire III–V die/wafer. Demonstrations include transfer-printed III–V emitters and DFB lasers integrated with silicon waveguide circuits; remaining challenges typically center on placement accuracy/overlay, designing alignment-tolerant couplers, interfacial adhesion/planarity, and establishing high-yield, high-reliability process flows. [74–76]

1.7.2 Monolithic Integration

Monolithic integration in silicon photonics refers to building multiple photonic (and electronic) functions directly on the same silicon wafer using CMOS-compatible deposition/epitaxy and lithography, rather than attaching pre-fabricated dies. In practice, the most mature “monolithic” path has been group-IV integration, where germanium (and SiGe/GeSn alloys) are grown on Si to add efficient near-IR absorption and electro-optic functionality while staying close to standard CMOS process modules. This has enabled wafer-scale Ge-on-Si photodetectors and co-integrated passive/active components (e.g., modulators + Ge PDs) with alignment set by lithography and without additional heterogenous integration steps [77–80]. The upside is scalability and tight co-integration with electronics; the core technical burden is materials quality and thermal-budget management (defects from lattice/thermal mismatch, strain engineering, and integration-friendly anneals) [78].

A major frontier for monolithic integration is the direct epitaxial growth of III–V gain media on Si/Silicon-On-Insulator (SOI) to realize on-chip lasers without bonding. This is difficult because heteroepitaxy must suppress threading dislocations, anti-phase boundaries, and thermal-stress defects; consequently, many approaches rely on selective-area growth (SAE), engineered buffers, and/or defect-tolerant active regions such as quantum dots [67, 81, 82]. Recent demonstrations highlight the momentum: electrically pumped InAs/GaAs quantum-dot lasers have been shown on 300 mm patterned Si photonic wafers, and embedded QD lasers have been directly grown inside trenched SOI and butt-coupled to silicon waveguides, both pointing toward foundry-relevant monolithic light sources [83, 84]. Remaining challenges are mainly around uniformity/yield at scale, thermal management, and co-optimizing epitaxy with back-end photonic/electronic process constraints [67].

1.7.3 Monolithic III–V on Silicon via ART and NRE

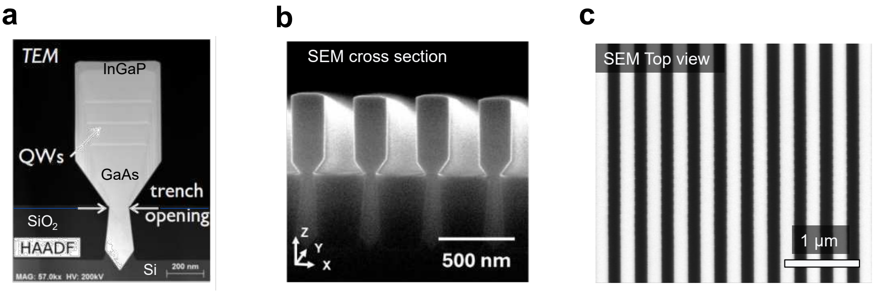

Figure 1.11: Nanoridges grown on silicon via ART and NRE. (a) TEM of single nanoridge [85]. (b) SEM of array of nanoridges [86]. (c) Top SEM view of nanoridge array [87].

As stated earlier, the monolithic integration of III–V gain media on silicon is fundamentally challenged by lattice and thermal mismatch. Aspect-ratio trapping (ART) and nano-ridge engineering (NRE) mitigate these issues by confining defects within narrow oxide trenches and shaping the overgrown material into high-quality nano-ridges, as shown in Fig. 1.11 [85]. This approach has enabled wafer-scale III–V nano-ridge optoelectronics on 300 mm silicon, including electrically injected nano-ridge lasers fabricated in a CMOS pilot line [87].

The epitaxial growth begins by preparing a patterned (001) Si wafer with oxide-defined trenches using a standard CMOS process known as shallow-trench isolation (STI). STI is normally used to electrically isolate neighbouring devices by means of narrow oxide-filled trenches. In a conventional STI flow, silicon is dry-etched to define the isolation trenches, which are then refilled with oxide and planarized. For nano-ridge epitaxy, this process is adapted so that narrow openings in the oxide expose the Si substrate and define the regions where selective III–V growth takes place. The ratio of exposed Si trench area to the total patterned area is typically kept around $9\text{–}10\%$, which helps control the selective-area-growth conditions and material loading effects [88].

The exposed silicon at the bottom of the trench is wet etched, commonly using tetramethylammonium hydroxide (TMAH), to expose $\{111\}$ Si facets in a V-shaped groove. This V-groove is important because nucleation on $\{111\}$ Si facets promotes anti-phase-domain-free growth of polar III–V material on non-polar silicon [88]. In addition, the oxide sidewalls of the trench provide the geometry required for ART. During the initial GaAs growth on Si, misfit dislocations are generated at the GaAs/Si interface due to the lattice mismatch, and some of these defects propagate as threading dislocations (TDs). In narrow trenches, TDs that glide along $\{111\}$ planes intersect the oxide sidewalls and terminate there instead of propagating into the upper device region. Since the $\{111\}$ glide planes are inclined by approximately 54.7° with respect to the (001) substrate surface, the ideal geometrical condition for trapping such dislocations corresponds to a trench aspect ratio $(AR = h/w)$ larger than about 1.4 [89]. Higher aspect ratios therefore provide more efficient dislocation trapping because the dislocations have a shorter lateral distance to travel before reaching an oxide sidewall. Experimentally, GaAs grown in 40 and 100 nm trenches shows efficient trapping, whereas many defects can reach the top surface in wider 300 nm trenches, as shown in figure 1.12. Thus, sufficiently narrow trenches strongly reduce the threading-dislocation density in the material that grows out of the trench. However, ART mainly traps dislocations that glide laterally along $\{111\}$ planes; dislocations that propagate nearly vertically, or that are pinned and cannot glide, may still escape the trapping region [85, 88, 90].

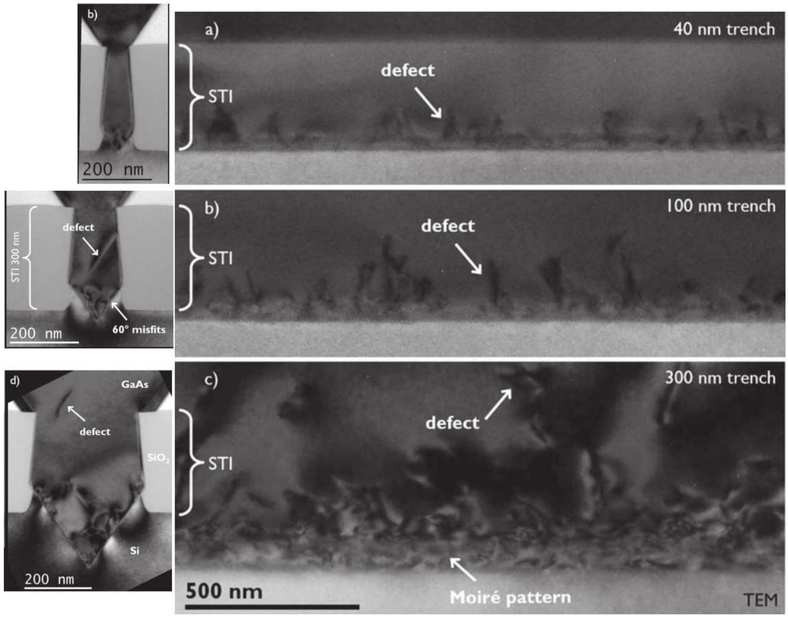

Figure 1.12: Cross-sectional and lateral TEM images of GaAs nano-ridges grown in 300 nm deep and a)40 nm, b)100 nm, c)300 nm, wide trenches. Higher aspect ratio trapping improves the defect trapping. Reproduced from [90].

The epitaxial growth is carried out by metal-organic vapor phase epitaxy (MOVPE) in a 300 mm chamber using group-III and group-V precursors such as tertiarybutyl arsine (TBAs), triethylgallium (TEGa), and trimethylgallium (TMGa) [86, 91].

Growth begins with GaAs nucleation on the exposed Si $\{111\}$ facets at the trench bottom. A low-temperature GaAs seed layer is then deposited, typically around $360\,^\circ\mathrm{C}$, to obtain continuous two-dimensional nucleation on the V-shaped Si surface. After this seed step, the temperature is increased to 500–$625\,^\circ\mathrm{C}$, for the main GaAs growth [88]. This step improves the crystal quality and allows strain relaxation through the formation of defects near the bottom of the trench, where they are subsequently confined by ART. Once the GaAs reaches the top of the trench, the epitaxy enters the nano-ridge engineering stage: instead of remaining confined inside the trench, the III–V crystal grows upward and laterally, forming a ridge above the oxide. The narrow trench therefore acts as the defect-filtering region, while the grown-out ridge provides the larger, relaxed III–V volume required for waveguiding and active-device integration.

The final nano-ridge geometry is governed by facet-dependent growth kinetics during MOVPE. Once the GaAs has grown out of the oxide trench, different crystallographic facets, such as the top (001) facet, the side $\{110\}$ facets, and the inclined $\{111\}_{\mathrm{Ga}}$ and $\{111\}_{\mathrm{As}}$ facets, grow at different rates. In general, fast-growing facets are rapidly consumed and disappear from the final morphology, whereas slow-growing facets remain visible and define the outer shape of the ridge. Therefore, by changing MOVPE parameters such as growth temperature, reactor pressure, precursor partial pressures, V/III ratio, and effective selective-area-growth rate, the relative growth-rate hierarchy of these facets can be modified. This enables the ridge shape to be tuned from triangular to broadened or rectangular box-like profiles, as illustrated in Fig. 1.13. For example, a rectangular nano-ridge can form when the $\{111\}_{\mathrm{Ga}}$ facets grow much faster than the (001) surface and are eliminated, while slower $\{110\}$ facets remain as nearly vertical sidewalls. The resulting flat (001) top surface is particularly important because it provides a suitable template for the subsequent pseudomorphic growth of quantum wells and other active III–V layers [88, 91, 92].

Recent device demonstrations show that nano-ridge technology has progressed from material growth to functional nano-ridge lasers. The first optically pumped InGaAs/GaAs nano-ridge DFB lasers used an etched grating on top of the ridge and showed single-mode room-temperature lasing with a threshold of approximately $37\ \mathrm{mW}$, corresponding to about $33.6\ \mathrm{kW/cm^2}$, for a $102\ \mu\mathrm{m}$-long device [93, 94]. To reduce fabrication-induced damage, Shi *et al.* later introduced a loss-coupled DFB cavity using a metallic grating deposited on top of the nano-ridge. This avoided etching into the III–V ridge and reduced the optically pumped threshold to approximately $10\ \mathrm{kW/cm^2}$ [95]. More recent work by Ouyang *et al.* replaced the metal or etched grating with amorphous-Si gratings. A top amorphous-Si grating DFB laser achieved a pulsed optical-pumping threshold of about $7.84\ \mathrm{kW/cm^2}$, while a sidewall amorphous-Si grating design enabled much stronger optical feedback and reduced the cavity length to about $16\ \mu\mathrm{m}$, with a threshold density of $9.9\ \mathrm{kW/cm^2}$ [96, 97]. Most importantly, the platform has recently reached electrical injection: De Koninck *et al.* demonstrated GaAs-based nano-ridge laser diodes fully fabricated on $300\ \mathrm{mm}$ Si wafers in a CMOS pilot line, showing room-temperature continuous-wave lasing around $1020\ \mathrm{nm}$ in more than 300 devices, with threshold currents as low as $5\ \mathrm{mA}$ and output powers exceeding $1\ \mathrm{mW}$ [87]. These demonstrations confirm that nano-ridge engineering is not only a material integration strategy but also a practical route toward scalable, CMOS-compatible III–V light sources on silicon.

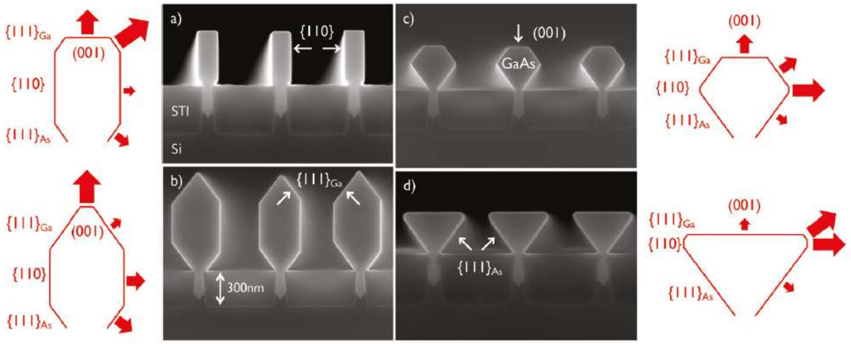

Figure 1.13: SEM images of GaAs ridges with different MOVPE growth conditions were applied. Reproduced from [92].

1.8 Research Objectives and Thesis Outline

The current state of the art still lacks a low-cost, wafer-scale, wavelength-tunable, monolithically integrated surface-emitting laser source. As we discussed earlier in section 1.5, PCSELs comes close to meeting these requirements, but their fabrication complexity and cost remain high due to the need for high-quality 2D photonic crystals over large areas, and active materials that usually require heterogeneous integration. Additionally, achieving precise wavelength control and scalability on standard silicon substrates is still a challenge which requries ebeam lithography and complex epitaxial regrowth steps. There's a pressing need for a new class of surface-emitting lasers that can be monolithically integrated on silicon wafers, offer lithographic wavelength control, and maintain high beam quality (single mode).

This thesis investigates whether nano-ridge technology can provide a feasible pathway toward compact surface-emitting lasers on silicon, and whether such devices can offer a credible alternative to conventional vertical-cavity surface-emitting lasers (VCSELs). The overarching research question is: can one-dimensional (1D) photonic-crystal nano-ridge surface-emitting lasers (NRSELs), epitaxially grown on 300 mm silicon wafers using aspect-ratio trapping (ART) and nano-ridge engineering (NRE), enable a competitive surface emitting laser on silicon? This question is addressed through several sub-questions. What theoretical framework is needed to describe NRSELs, including the photonic-crystal band picture, band-edge feedback, surface-emission mechanisms, and the role of symmetry-protected bound states in the continuum (BICs)? Can the strong refractive-index contrast between the III–V nano-ridge and its surrounding materials be exploited to form compact optical cavities with low-threshold lasing and directional surface emission? How do the actual nano-ridge geometry, lithographic constraints, and fabrication tolerances of 300 mm silicon processing influence the design and performance of NRSELs? Do the fabricated devices exhibit lasing, and how are the threshold, emission wavelength, polarization, and far-field behavior related to the designed photonic-crystal modes? Can angle-resolved photoluminescence (PL) and cathodoluminescence (CL) be used to experimentally reconstruct the photonic band structure, identify BIC-related modal features, and guide improved designs with lower threshold, enhanced directionality? Finally, how to improve the NRSELs in terms of threshold, directionality, fabrication robustness, and scalability, and what device-design strategies could enable future electrical injection?

The thesis is structured as follows:

- Chapter 2 develops the theoretical background and design framework for NRSELs, including the photonic-crystal band picture and the key mechanisms enabling surface emission.
- Chapter 3 describes the fabrication flow and metrology, including epitaxy on 300 mm silicon and dimensional characterization of the nano-ridge arrays.
- Chapter 4 presents optical characterization and lasing results, connecting device performance to the designed band-edge modes.
- Chapter 5 focuses on angle-resolved PL and CL measurements to experimentally reconstruct the photonic band structure and directly probe BIC-related features.
- Chapter 6 introduces advanced design concepts and simulations to improve the NRSELs and proposes methods for electrical injection.
- Chapter 7 summarizes the main conclusions and outlines future directions.

1.9 Publications and Patents

This work has led to a patent application and several publications in peer-reviewed journals and conferences, demonstrating the significance and impact of the research. The key publications are listed below:

1.9.1 Patent Application

- D. Van Thourhout, **E.M.B. Fahmy**, D. Colluci, B. Kunert, Surface emitting laser, EU-EP 24191605.5 (7/2024), US-US 19277838 (7/2025), published on January 29, 2026 under publication number US 2026 0031598 A1.

1.9.2 Publications in International Journals

- **E.M.B. Fahmy**, Z. Ouyang, D. Colucci, N. Le Thomas, J. Van Campenhout, B. Kunert, D. Van Thourhout, One-Dimensional Photonic Crystal Nano-Ridge Surface Emitting Lasers Epitaxially Grown on a Standard 300 mm Silicon Wafer, Light: Science & Applications (2026)
- **E.M.B. Fahmy**, T. Coenen, D. Van Thourhout, Probing Bound States in the Continuum in InGaAs/GaAs Photonic-Crystal Nano-ridge Lasers on 300 mm Silicon with Angle-Resolved Cathodoluminescence and Photoluminescence (In preparation, 2026)
- Z. Ouyang, **E.M.B. Fahmy**, D. Colucci, A. Yimam, J. Van Campenhout, B. Kunert, D. Van Thourhout, Ultra-compact InGaAs-GaAs nano-ridge laser monolithically grown on 300 mm silicon substrate, Optics Letters (2025)
- Z. Ouyang, D. Colucci, **E.M.B. Fahmy**, A. Yimam, J. Van Campenhout, B. Kunert, D. Van Thourhout, InGaAs/GaAs nano-ridge laser with an amorphous silicon grating monolithically grown on a 300mm Si wafer, Optics Letters (2024)

1.9.3 Publications in International Conferences

- **E.M.B. Fahmy**, T. Coenen, Z. Ouyang, D. Van Thourhout, A Novel Surface-Emitting Laser Using Coupled InGaAs/GaAs Nano-Ridges on Si: Insights from Cathodoluminescence, Conference on Lasers and Electro-Optics Europe, Germany, p.1 (2025).

- **E.M.B. Fahmy**, Z. Ouyang, D. Van Thourhout, InGaAs/GaAs Nano-Ridge Laser Based on Bound States in the Continuum Epitaxially Grown on a Si Wafer, IEEE Siphotonics, United Kingdom, p.paper WC6 (2025).
- **E.M.B. Fahmy**, Z. Ouyang, D. Van Thourhout, Slow-Light Lasing in 1D Photonic crystal InGaAs/GaAs Nano-Ridges Epitaxially Grown on a Si Wafer , Photonics West, 13371, United States, p.paper 133710V doi:10.1117/12.3043386 (2025).
- Z. Ouyang, D. Colucci, **E.M.B. Fahmy**, A. Yimam, J. Van Campenhout, B. Kunert, D. Van Thourhout, Compact 1.31 $\mu\mathrm{m}$-emission $In_{0.45}Ga_{0.55}As/In_{0.25}Ga_{0.75}As$ photonic crystal nano-ridge laser monolithically grown on a 300 mm silicon substrate, SPIE Europe, France, p. 130120D (2024).
- Z. Ouyang, **E.M.B. Fahmy**, D. Colucci, A. Yimam, B. Kunert, D. Van Thourhout, Side-amorphous-silicon-grating InGaAs/GaAs nano-ridge distributed feedback laser monolithically grown on a 300 mm silicon substrate, Asia Communications and Photonics Conference, China,(2023).
- Z. Ouyang, **E.M.B. Fahmy**, A. Yimam, B. Kunert, D. Van Thourhout, Low-optical-pumping-threshold InGaAs/GaAs nano-ridge laser monolithically grown on a 300 mm silicon substrate, Conference on Lasers and Electro-Optics, United States, p. paper STh3H.3 (2 pages) (2023).
- Z. Ouyang, **E.M.B. Fahmy** D. Colucci, A. Yimam, B. Kunert, D. Van Thourhout, Top-amorphous-silicon-grating InGaAs/GaAs nano-ridge distributed feedback laser monolithically grown on a 300 mm silicon substrate, IEEE Photonic Benelux Annual Symposium, Netherlands (2022).
- **E.M.B. Fahmy**, Z. Ouyang, D. Van Thourhout, Amorphous Silicon side-wall grating DFB InGaAs/GaAs nano-ridge laser epitaxially grown on a Si wafer, IEEE Benelux Photonics Chapter - Annual Symposium 2022, Netherlands, p.poster 19 (2022).

Bibliography

[1] K. Iga, “Vertical-cavity surface-emitting laser: Its conception and evolution,” *Japanese Journal of Applied Physics*, vol. 47, p. 1, 2008. [Online]. Available: https://iopscience.iop.org/article/10.1143/JJAP.47.1

[2] L. A. Coldren, S. W. Corzine, and M. L. Mashanovitch, *Diode Lasers and Photonic Integrated Circuits*, 2nd ed. Hoboken, NJ: Wiley, 2012.

[3] G. Yuan, J. Mu, Y. Zhou, J. Zhang, C. Chen, Y. Zhou, Z. Zhang, T. Liu, T. Zhang, X. Gao, Y. Cao, Y. Ning, and L. Wang, “Beam control of broad-area semiconductor lasers using high-order sidewall gratings,” *Applied Physics B*, vol. 131, no. 10, p. 190, 2025. [Online]. Available: https://link.springer.com/10.1007/s00340-025-08555-3

[4] R. Hülsewede, J. Sebastian, H. Wenzel, G. Beister, A. Knauer, and G. Erbert, “Beam quality of high power 800 nm broad-area laser diodes with 1 and 2 µm large optical cavity structures,” *Optics Communications*, vol. 192, no. 1–2, pp. 69–75, 2001. [Online]. Available: https://linkinghub.elsevier.com/retrieve/pii/S0030401801011476

[5] S. Noda, M. Yoshida, and T. Inoue, “The tiny ultrabright laser that can melt steel,” Apr. 2024. [Online]. Available: https://spectrum.ieee.org/pcsel

[6] Y. Motegi, H. Soda, and K. Iga, “Surface-emitting gainasp/inp injection laser with short cavity length,” *Electronics Letters*, vol. 18, no. 11, pp. 461–463, 1982. [Online]. Available: http://digital-library.theiet.org/doi/10.1049/el%3A19820314

[7] K. Iga, “Surface-emitting laser-its birth and generation of new optoelectronics field,” *IEEE Journal of Selected Topics in Quantum Electronics*, vol. 6, no. 6, pp. 1201–1215, 2000. [Online]. Available: http://ieeexplore.ieee.org/document/902168/

[8] F. Koyama, S. Kinoshita, and K. Iga, “Room-temperature continuous wave lasing characteristics of a GaAs vertical cavity surface-emitting laser,” *Applied Physics Letters*, vol. 55, no. 3, pp. 221–222, 1989. [Online]. Available: https://pubs.aip.org/apl/article/55/3/221/56826/Room-temperature-continuous-wave-lasing

[9] D. Douglass, “Vertical cavity surface emitting lasers (vcsels) and their applications,” https://www.dentonvacuum.com/blog/vertical-cavity-surface-emitting-lasers-vcsels-and-their-applications/, Mar. 2024, accessed: 2026-1-9.

[10] I. Leandro, B. Lorenzo, M. Aleksandar, M. Dario, G. Rosa, A. Agostino, and T. Daniele, "OCT-based deep-learning models for the identification of retinal key signs," *Scientific Reports*, vol. 13, no. 1, p. 14628, Sep. 2023.

[11] G. Pan, M. Xun, X. Zhou, Y. Sun, Y. Dong, and D. Wu, "Harnessing the capabilities of vcsels: Unlocking the potential for advanced integrated photonic devices and systems," *Light: Science & Applications*, vol. 13, no. 1, p. 229, 2024. [Online]. Available: https://www.nature.com/articles/s41377-024-01561-8

[12] Q. Cheng, M. Bahadori, M. Glick, S. Rumley, and K. Bergman, "Recent advances in optical technologies for data centers: A review," *Optica*, vol. 5, no. 11, p. 1354, 2018. [Online]. Available: https://opg.optica.org/abstract.cfm?URI=optica-5-11-1354

[13] S. Chen, "Data centres will use twice as much energy by 2030 — driven by AI," *Nature*, pp. d41 586–025–01 113–z, 2025. [Online]. Available: https://www.nature.com/articles/d41586-025-01113-z

[14] A. Ghiasi, "Large data centers interconnect bottlenecks," *Optics Express*, vol. 23, no. 3, p. 2085, 2015. [Online]. Available: https://opg.optica.org/abstract.cfm?URI=oe-23-3-2085

[15] J. Krause Perin, A. Shastri, and J. M. Kahn, "Data center links beyond 100 Gbit/s per wavelength," *Optical Fiber Technology*, vol. 44, pp. 69–85, 2018. [Online]. Available: https://linkinghub.elsevier.com/retrieve/pii/S1068520017302183

[16] C. A. Thraskias, E. N. Lallas, N. Neumann, L. Schares, B. J. Offrein, R. Henker, D. Plettemeier, F. Ellinger, J. Leuthold, and I. Tomkos, "Survey of Photonic and Plasmonic Interconnect Technologies for Intra-Datacenter and High-Performance Computing Communications," *IEEE Communications Surveys & Tutorials*, vol. 20, no. 4, pp. 2758–2783, 2018. [Online]. Available: https://ieeexplore.ieee.org/document/8367741/

[17] K. Li, D. J. Thomson, S. Liu, W. Zhang, W. Cao, C. G. Littlejohns, X. Yan, M. Ebert, M. Banakar, D. Tran, F. Meng, H. Du, and G. T. Reed, "An integrated CMOS–silicon photonics transmitter with a 112 gigabaud transmission and picojoule per bit energy efficiency," *Nature Electronics*, vol. 6, no. 11, pp. 910–921, 2023. [Online]. Available: https://www.nature.com/articles/s41928-023-01048-1

[18] T. Baehr-Jones, S. Ardalan, M. Chang, S. Jafarlou, X. Serey, G. Zarris, G. Thompson, A. Darbinian, B. West, B. Behnia, V. Velev, Y. Z. Li, K. Roelofs, W. Wu, J. Mali, J. Zhan, N. Ophir, C. Horng, R. Narevich,

F. Guan, J. Yang, H. Wu, P. Maupin, R. Manley, Y. Ahuja, A. Novack, L. Wang, and M. Streshinsky, “Monolithically integrated 112 Gbps PAM4 optical transmitter and receiver in a 45 nm CMOS-silicon photonics process,” *Optics Express*, vol. 31, no. 15, p. 24926, 2023. [Online]. Available: https://opg.optica.org/abstract.cfm?URI=oe-31-15-24926

[19] S. Bernal, M. Dumont, E. Berikaa, C. St-Arnault, Y. Hu, R. G. Castrejon, W. Li, Z. Wei, B. Krueger, F. Pittalà, J. Bowers, and D. V. Plant, “12.1 terabit/second data center interconnects using O-band coherent transmission with QD-MLL frequency combs,” *Nature Communications*, vol. 15, no. 1, p. 7741, 2024. [Online]. Available: https://www.nature.com/articles/s41467-024-51682-2

[20] S. Hu, X. Zhang, C. Li, H. Yin, X. Li, and X. Xin, “Latest advances in vcsel technology for next-generation data center network [invited],” *Chinese Optics Letters*, vol. 22, no. 11, p. 111401, 2024. [Online]. Available: https://www.researching.cn/articles/OJff0183d301780311

[21] A. Liu, B. Tang, Z. Li, and W. Zheng, “70 Gbps PAM-4 850-nm oxide-confined VCSEL without equalization and pre-emphasis,” *Journal of Semiconductors*, vol. 45, no. 5, p. 050501, 2024. [Online]. Available: https://iopscience.iop.org/article/10.1088/1674-4926/45/5/050501

[22] A. Babichev, S. Blokhin, E. Kolodeznyi, L. Karachinsky, I. Novikov, A. Egorov, S.-C. Tian, and D. Bimberg, “Long-wavelength vcsels: Status and prospects,” *Photonics*, vol. 10, no. 3, p. 268. [Online]. Available: https://www.mdpi.com/2304-6732/10/3/268

[23] A. Caliman, A. Mereuta, G. Suruceanu, V. Iakovlev, A. Sirbu, and E. Kapon, “8 mW fundamental mode output of wafer-fused VCSELs emitting in the 1550-nm band,” *Optics Express*, vol. 19, no. 18, p. 16996, 2011. [Online]. Available: https://opg.optica.org/oe/abstract.cfm?uri=oe-19-18-16996

[24] R. Rodes, M. Mueller, B. Li, J. Estaran, J. B. Jensen, T. Gruendl, M. Ortsiefer, C. Neumeyr, J. Rosskopf, K. J. Larsen, M.-C. Amann, and I. T. Monroy, “High-Speed 1550 nm VCSEL Data Transmission Link Employing 25 GBd 4-PAM Modulation and Hard Decision Forward Error Correction,” *Journal of Lightwave Technology*, vol. 31, no. 4, pp. 689–695, 2013. [Online]. Available: http://ieeexplore.ieee.org/document/6338991/

[25] A. Caliman, A. Mereuta, P. Wolf, A. Sirbu, V. Iakovlev, D. Bimberg, and E. Kapon, “25 Gbps direct modulation and 10 km data transmission with 1310 nm waveband wafer fused VCSELs,” *Optics Express*, vol. 24, no. 15, p. 16329, 2016. [Online]. Available: https://opg.optica.org/abstract.cfm?URI=oe-24-15-16329

[26] B. Li, C. Mi, J.-H. Kang, H. Li, R. T. Elafandy, W.-C. Lai, J.-K. Sheu, and J. Han, “Photonic engineering of inp towards homoepitaxial short-wavelength infrared vcsels,” *Optica*, vol. 11, no. 1, p. 113, 2024. [Online]. Available: https://opg.optica.org/abstract.cfm?URI=optica-11-1-113

[27] W.-H. Huang, C.-Y. Shan, K.-L. Chi, Y.-J. Xu, and T.-C. Lu, “Study of far-field reduction in high power 940 nm vertical-cavity surface-emitting lasers cascaded by tunnel junctions,” *Scientific Reports*, vol. 15, no. 1, p. 32037, 2025. [Online]. Available: https://www.nature.com/articles/s41598-025-17744-1

[28] Y. Xiao, J. Wang, H. Liu, P. Miao, Y. Gou, Z. Zhang, G. Deng, S. Zhou *et al.*, “Multi-junction cascaded vertical-cavity surface-emitting laser with a high power conversion efficiency of 74%,” *Light: Science & Applications*, vol. 13, p. 60, 2024.

[29] D. Liang, C. Zhang, P. Zhang, S. Liu, H. Li, S. Niu, R. Z. Rao, L. Zhao, X. Chen, H. Li, and Y. Huo, “Evolution of laser technology for automotive LiDAR, an industrial viewpoint,” *Nature Communications*, vol. 15, no. 1, p. 7660, 2024. [Online]. Available: https://www.nature.com/articles/s41467-024-51975-6

[30] C. Zhang, H. Li, and D. Liang, “Antireflective vertical-cavity surface-emitting laser for LiDAR,” *Nature Communications*, vol. 15, no. 1, p. 1105, 2024. [Online]. Available: https://www.nature.com/articles/s41467-024-44754-w

[31] M. Payandeh, H. K. Sahoo, A. Simonsen, M. Janka, J. Viheriälä, M. Guina, E. Semenova, and K. Yvind, “High-speed, widely tunable bidirectional 1310 nm mems vcsels for oct imaging,” *Optics Express*, vol. 33, no. 23, p. 47692, 2025. [Online]. Available: https://opg.optica.org/abstract.cfm?URI=oe-33-23-47692

[32] M. Yoshida, S. Katsuno, T. Inoue, J. Gelleta, K. Izumi, M. De Zoysa, K. Ishizaki, and S. Noda, “High-brightness scalable continuous-wave single-mode photonic-crystal laser,” *Nature*, vol. 618, no. 7966, pp. 727–732, 2023. [Online]. Available: https://www.nature.com/articles/s41586-023-06059-8

[33] S. Noda, K. Kitamura, T. Okino, D. Yasuda, and Y. Tanaka, “Photonic-Crystal Surface-Emitting Lasers: Review and Introduction of Modulated-Photonic Crystals,” *IEEE Journal of Selected Topics in Quantum Electronics*, vol. 23, no. 6, pp. 1–7. [Online]. Available: http://ieeexplore.ieee.org/document/7907235/

[34] K. Ishizaki, M. D. Zoysa, and S. Noda, “Progress in photonic-crystal surface-emitting lasers,” *Photonics*, vol. 6, no. 3, pp. 1–15, 2019.

[35] M. Imada, S. Noda, A. Chutinan, T. Tokuda, M. Murata, and G. Sasaki, “Coherent two-dimensional lasing action in surface-emitting laser with triangular-lattice photonic crystal structure,” *Applied Physics Letters*, vol. 75, no. 3, pp. 316–318, 1999. [Online]. Available: https://pubs.aip.org/apl/article/75/3/316/108652/Coherent-two-dimensional-lasing-action-in-surface

[36] L. Ferrier, P. Rojo-Romeo, E. Drouard, X. Letatre, and P. Viktorovitch, “Slow bloch mode confinement in 2d photonic crystals for surface operating devices,” *Optics Express*, vol. 16, no. 5, p. 3136, 2008.

[37] K. Emoto, T. Koizumi, M. Hirose, M. Jutori, T. Inoue, K. Ishizaki, M. De Zoysa, H. Togawa, and S. Noda, “Wide-bandgap gan-basedwatt-class photonic-crystal lasers,” *Communications Materials*, vol. 3, no. 1, p. 72, 2022. [Online]. Available: https://www.nature.com/articles/s43246-022-00288-6

[38] Y.-H. Hong, W.-C. Miao, W.-C. Hsu, K.-B. Hong, C.-L. Lin, C. Lin, S.-C. Chen, and H.-C. Kuo, “Progress of photonic-crystal surface-emitting lasers: A paradigm shift in lidar application,” *Crystals*, vol. 12, no. 6, p. 800. [Online]. Available: https://www.mdpi.com/2073-4352/12/6/800

[39] T. Inoue, M. Yoshida, J. Gelleta, K. Izumi, K. Yoshida, K. Ishizaki, M. D. Zoysa, and S. Noda, “General recipe to realize photonic-crystal surface-emitting lasers with 100-W-to-1-kW single-mode operation,” *Nature Communications*, vol. 13, no. 1, pp. 1–10, 2022.

[40] M. Meier, A. Mekis, A. Dodabalapur, A. Timko, R. E. Slusher, J. D. Joannopoulos, and O. Nalamasu, “Laser action from two-dimensional distributed feedback in photonic crystals,” *Applied Physics Letters*, vol. 74, no. 1, pp. 7–9, 1999. [Online]. Available: https://pubs.aip.org/apl/article/74/1/7/519872/Laser-action-from-two-dimensional-distributed

[41] K. Hirose, Y. Liang, Y. Kurosaka, A. Watanabe, T. Sugiyama, and S. Noda, “Watt-class high-power, high-beam-quality photonic-crystal lasers,” *Nature Photonics*, vol. 8, no. 5, pp. 406–411, 2014.

[42] S. Noda, T. Inoue, M. Yoshida, J. Gelleta, M. D. Zoysa, and K. Ishizaki, “High-power and high-beam-quality photonic-crystal surface-emitting lasers: A tutorial,” *Advances in Optics and Photonics*, vol. 15, no. 4, p. 977, 2023. [Online]. Available: https://opg.optica.org/abstract.cfm?URI=aop-15-4-977

[43] Z. Wang, X. Liu, P. Wang, H. Lu, B. Meng, W. Zhang, L. Wang, and Y. Wang, “Continuous-wave operation of 1550 nm surface-emitting lasers,” 2024.

[44] H. Matsubara, S. Yoshimoto, H. Saito, Y. Jianglin, Y. Tanaka, and S. Noda, “Gan photonic-crystal surface-emitting laser at blue-violet wavelengths,”

Science, vol. 319, no. 5862, pp. 445–447, 2008. [Online]. Available: https://www.science.org/doi/10.1126/science.1150413

[45] D. apaydin, H. Andersson, L. Uhlig, S. Graupeter, J. Ciers, G. Cardinali, E. Strandberg, T. Wernicke, M. Kneissl, U. T. Schwarz, P. Tassin, and A. Haglund, "Deep-uv photonic crystal surface-emitting lasers," *Laser & Photonics Reviews*, p. e00271, 2025. [Online]. Available: https://onlinelibrary.wiley.com/doi/10.1002/lpor.202500271

[46] R. Sakata, K. Ishizaki, M. De Zoysa, S. Fukuhara, T. Inoue, Y. Tanaka, K. Iwata, R. Hatsuda, M. Yoshida, J. Gelleta, and S. Noda, "Dually modulated photonic crystals enabling high-power high-beam-quality two-dimensional beam scanning lasers," *Nature Communications*, vol. 11, no. 1, p. 3487. [Online]. Available: https://www.nature.com/articles/s41467-020-17092-w

[47] R. Sakata, K. Ishizaki, M. D. Zoysa, K. Kitamura, T. Inoue, J. Gelleta, and S. Noda, "Photonic-crystal surface-emitting lasers with modulated photonic crystals enabling 2D beam scanning and various beam pattern emission," *Applied Physics Letters*, vol. 122, no. 13, 2023.

[48] C. Gautam, M. Pan, S. Seth, T. J. Rotter, M. Zhou, B. J. Thompson, R. Gibson, S. Fan, G. Balakrishnan, and W. Zhou, "Mode distribution impact on photonic crystal surface emitting laser performance," *APL Photonics*, vol. 9, no. 7, p. 076113, 2024. [Online]. Available: https://pubs.aip.org/app/article/9/7/076113/3303934/Mode-distribution-impact-on-photonic-crystal

[49] S. T. Ha, Q. Li, J. K. W. Yang, H. V. Demir, M. L. Brongersma, and A. I. Kuznetsov, "Optoelectronic metadevices," *Science*, vol. 386, no. 6725, p. eadm7442, 2024. [Online]. Available: https://www.science.org/doi/10.1126/science.adm7442

[50] S. Selvaraja, P. Jaenen, W. Bogaerts, D. Van Thourhout, P. Dumon, and R. Baets, "Fabrication of Photonic Wire and Crystal Circuits in Silicon-on-Insulator Using 193-nm Optical Lithography," *Journal of Lightwave Technology*, vol. 27, no. 18, pp. 4076–4083, 2009. [Online]. Available: http://ieeexplore.ieee.org/document/4909149/

[51] G. Calafiore, Q. Fillot, S. Dhuey, S. Sassolini, F. Salvadori, C. A. Mejia, K. Munechika, C. Peroz, S. Cabrini, and C. Piña-Hernandez, "Printable photonic crystals with high refractive index for applications in visible light," *Nanotechnology*, vol. 27, no. 11, p. 115303, 2016. [Online]. Available: https://iopscience.iop.org/article/10.1088/0957-4484/27/11/115303

[52] C. Pina-Hernandez, A. Koshelev, S. Dhuey, S. Sassolini, M. Sainato, S. Cabrini, and K. Munechika, "Nanoimprinted High-Refractive Index Active

Photonic Nanostructures Based on Quantum Dots for Visible Light," *Scientific Reports*, vol. 7, no. 1, 2017.

[53] Z. Bian, X. Zhao, J. Liu, D. Kim, A. F. McKenzie, S. Thoms, P. Reynolds, N. D. Gerrard, A. S. M. Kyaw, J. Grant, K. Rae, J. R. Orchard, C. H. Hill, C. W. Munro, P. Ivanov, D. T. D. Childs, R. J. E. Taylor, and R. A. Hogg, "Resonator embedded photonic crystal surface emitting lasers," *npj Nanophotonics*, vol. 1, no. 1, p. 13. [Online]. Available: https://www.nature.com/articles/s44310-024-00014-9

[54] J. R. Orchard, P. Ivanov, A. F. McKenzie, C. H. Hill, I. Javed, C. W. Munro, J. Kettle, R. A. Hogg, D. T. D. Childs, and R. J. E. Taylor, "Small signal modulation of photonic crystal surface emitting lasers," *Scientific Reports*, vol. 13, no. 1, p. 19019. [Online]. Available: https://www.nature.com/articles/s41598-023-45414-7

[55] A. Knigge, G. Erbert, J. Jönsson, W. Pittroff, R. Staske, B. Sumpf, M. Weyers, and G. Tränkle, "Passively cooled 940 nm laser bars with 73% wall-plug efficiency at 70 W and 25°C," *Electronics Letters*, vol. 41, no. 5, pp. 250–251, 2005. [Online]. Available: http://digital-library.theiet.org/doi/10.1049/el%3A20058180

[56] R. Morita, T. Inoue, T. Ueda, M. Masuda, K. Nigo, M. Yoshida, M. D. Zoysa, K. Ishizaki, J. Gelleta, and S. Noda, "200-w short-pulse operation of photonic-crystal lasers based on simultaneous absorptive and radiative q-switching," *Optics Express*, vol. 31, no. 19, p. 31116. [Online]. Available: https://opg.optica.org/abstract.cfm?URI=oe-31-19-31116

[57] R. Morita, T. Inoue, S. Nakano, S. Ishimura, H. Takahashi, T. Tsuritani, M. De Zoysa, K. Ishizaki, M. Suzuki, and S. Noda, "High-Power and High-Speed Photonic-Crystal Surface-Emitting Lasers (PCSELs) Based on Photon-Photon Resonance," in *2024 IEEE 29th International Semiconductor Laser Conference (ISLC)*. Orlando, FL, USA: IEEE, 2024, pp. 1–2. [Online]. Available: https://ieeexplore.ieee.org/document/10717341/

[58] T. Aoki, Y. Itoh, M. Ogasawara, K. Fujii, S. Kimura, Y. Sawada, H. Yoshinaga, N. Fujiwara, H. Yagi, M. Yanagisawa, M. Yoshida, T. Inoue, M. D. Zoysa, K. Ishizaki, and S. Noda, "Narrow-linewidth 1.55-µm-wavelength InP-based photonic-crystal surface-emitting lasers with near-diffraction-limited beam quality," *Optics Express*, vol. 33, no. 20, p. 42480, 2025. [Online]. Available: https://opg.optica.org/abstract.cfm?URI=oe-33-20-42480

[59] A. S. M. Kyaw, B. C. King, A. F. McKenzie, Z. Bian, D. Kim, N. D. Gerrard, K. Nishi, K. Takemasa, M. Sugawara, D. T. D. Childs, C. H. Hill, R. J. E.

Taylor, and R. A. Hogg, "Epitaxially regrown quantum dot photonic crystal surface emitting lasers," *Applied Physics Letters*, vol. 124, no. 22, p. 221101, May 2024.

[60] T. Inoue, T. Kim, S. Katsuno, R. Morita, M. Yoshida, M. De Zoysa, K. Ishizaki, and S. Noda, "Measurement and numerical analysis of intrinsic spectral linewidths of photonic-crystal surface-emitting lasers," *Applied Physics Letters*, vol. 122, no. 5, p. 051101, 2023. [Online]. Available: https://pubs.aip.org/apl/article/122/5/051101/2874749/Measurement-and-numerical-analysis-of-intrinsic

[61] M. J. Miah, S. Strohmaier, G. Urban, and D. Bimberg, "Beam quality improvement of high-power semiconductor lasers using laterally inhomogeneous waveguides," *Applied Physics Letters*, vol. 113, no. 22, p. 221107, 2018. [Online]. Available: https://pubs.aip.org/apl/article/113/22/221107/36568/Beam-quality-improvement-of-high-power

[62] C.-Y. Peng, H.-T. Cheng, Y.-H. Hong, W.-C. Hsu, F.-H. Hsiao, T.-C. Lu, S.-W. Chang, S.-C. Chen, C.-H. Wu, and H.-C. Kuo, "Performance Analyses of Photonic-Crystal Surface-Emitting Laser: Toward High-Speed Optical Communication," *Nanoscale Research Letters*, vol. 17, no. 1, p. 90. [Online]. Available: https://link.springer.com/10.1186/s11671-022-03728-x

[63] S. L. Chuang, *Physics of Photonic Devices*. John Wiley & Sons.

[64] S. Shekhar, W. Bogaerts, L. Chrostowski, J. E. Bowers, M. Hochberg, R. Soref, and B. J. Shastri, "Roadmapping the next generation of silicon photonics," *Nature Communications*, vol. 15, no. 1, p. 751, 2024. [Online]. Available: https://www.nature.com/articles/s41467-024-44750-0

[65] Z. Zhou, B. Yin, and J. Michel, "On-chip light sources for silicon photonics," *Light: Science & Applications*, vol. 4, no. 11, pp. e358–e358, 2015. [Online]. Available: https://www.nature.com/articles/lsa2015131

[66] Z. Zhou, X. Ou, Y. Fang, E. Alkhazraji, R. Xu, Y. Wan, and J. E. Bowers, "Prospects and applications of on-chip lasers," *eLight*, vol. 3, no. 1, p. 1, 2023. [Online]. Available: https://elight.springeropen.com/articles/10.1186/s43593-022-00027-x

[67] M. Tang, J.-S. Park, Z. Wang, S. Chen, P. Jurczak, A. Seeds, and H. Liu, "Integration of iii-v lasers on si for si photonics," *Progress in Quantum Electronics*, vol. 66, pp. 1–18, 2019.

[68] D. Liang and J. E. Bowers, "Recent progress in heterogeneous iii-v-on-silicon photonic integration," *Light: Advanced Manufacturing*, vol. 2, no. 1, pp. 59–83, 2021.

[69] S. Keyvaninia, M. Muneeb, S. Stanković, P. J. Van Veldhoven, D. Van Thourhout, and G. Roelkens, "Ultra-thin dvs-bcb adhesive bonding of iii-v wafers, dies and multiple dies to a patterned silicon-on-insulator substrate," *Optical Materials Express*, vol. 3, no. 1, pp. 35–46, 2013.

[70] C. Monat, C. Seassal, X. Letartre, P. Regreny, P. Rojo-Romeo, P. Viktorovitch, M. Le Vassor d'Yerville, D. Cassagne, J. P. Albert, E. Jalaguier, S. Pocas, and B. Aspar, "Inp-based two-dimensional photonic crystal on silicon: In-plane bloch mode laser," *Applied Physics Letters*, vol. 81, no. 27, pp. 5102–5104, 2002. [Online]. Available: https://pubs.aip.org/apl/article/81/27/5102/513833/InP-based-two-dimensional-photonic-crystal-on

[71] J. Mouette, C. Seassal, X. Letartre, P. Rojo-Romeo, J.-L. Leclercq, P. Regreny, P. Viktorovitch, E. Jalaguier, P. Perreau, and H. Moriceau, "Very low threshold vertical emitting laser operation in inp graphite photonic crystal slab on silicon," *Electronics Letters*, vol. 39, no. 6, pp. 526–528, 2003. [Online]. Available: http://digital-library.theiet.org/doi/10.1049/el%3A20030371

[72] B. Ben Bakir, family=Seassal, X. Letartre, P. Viktorovitch, M. Zussy, L. Di Cioccio, and J. M. Fedeli, "Surface-emitting microlaser combining two-dimensional photonic crystal membrane and vertical bragg mirror," *Applied Physics Letters*, vol. 88, no. 8, p. 081113, 2006. [Online]. Available: https://pubs.aip.org/apl/article/88/8/081113/331285/Surface-emitting-microlaser-combining-two

[73] A. Marinins, S. Hänsch, H. Sar, F. Chancerel, N. Golshani, H.-L. Wang, A. Tsiara, D. Coenen, P. Verheyen, G. Capuz, Y. De Koninck, O. Yilmaz, G. Morthier, F. Schleicher, G. Jamieson, S. Smyth, A. McKee, Y. Ban, M. Pantouvaki, D. C. La Tulipe, and J. Van Campenhout, "Wafer-scale hybrid integration of inp dfb lasers on si photonics by flip-chip bonding with sub-300 nm alignment precision," *IEEE Journal of Selected Topics in Quantum Electronics*, vol. 29, no. 3, p. 8200311, 2023.

[74] J. Zhang, B. Haq, J. O'Callaghan, A. Gocalinska, E. Pelucchi, Trindade, B. Corbett, G. Morthier, and G. Roelkens, "Transfer-printing-based integration of a iii-v-on-silicon distributed feedback laser," *Optics Express*, vol. 26, no. 7, pp. 8821–8830, 2018.

[75] A. De Groote, P. Cardile, A. Subramanian, A. M. Fecioru, C. Bower, Delbeke, R. Baets, and G. Roelkens, "Transfer-printing-based integration of single-mode waveguide-coupled iii-v-on-silicon broadband light emitters," *Optics Express*, vol. 24, no. 13, pp. 13 754–13 762, 2016.

[76] C. Yu, M. Zhang, L. Liang, L. Qin, Y. Chen, Y. Lei, Y. Wang, Y. Song, C. Qiu, P. Jia, D. Li, and L. Wang, "Advancements in transfer printing techniques

and their applications in photonic integrated circuits," *Light: Science & Applications*, vol. 14, p. 396, 2025.

[77] Y. Ishikawa and K. Wada, "Germanium for silicon photonics," *Thin Solid Films*, vol. 518, no. 6, pp. S83–S87, 2010.

[78] J. Liu, "Monolithically integrated ge-on-si active photonics," *Photonics*, vol. 1, no. 3, pp. 162–197, 2014.

[79] T.-Y. Liow, K.-W. Ang, Q. Fang, J.-F. Song, Y.-Z. Xiong, M.-B. Yu, G.-Q. Lo, and D.-L. Kwong, "Silicon modulators and germanium photodetectors on soi: Monolithic integration, compatibility, and performance optimization," *IEEE Journal of Selected Topics in Quantum Electronics*, vol. 16, no. 1, pp. 307–315, 2010.

[80] S. Park, T. Tsuchizawa, T. Watanabe, H. Shinojima, H. Nishi, K. Yamada, Y. Ishikawa, K. Wada, and S. Itabashi, "Monolithic integration and synchronous operation of germanium photodetectors and silicon variable optical attenuators," *Optics Express*, vol. 18, no. 8, pp. 8412–8421, 2010.

[81] Y. Han, W. K. Ng, Y. Xue, Q. Li, K. S. Wong, and K. M. Lau, "Telecom inp/ingaas nanolaser array directly grown on (001) silicon-on-insulator," *Optics Letters*, vol. 44, no. 4, p. 767, 2019. [Online]. Available: https://opg.optica.org/abstract.cfm?URI=ol-44-4-767

[82] Z. Wang, B. Tian, M. Pantouvaki, W. Guo, P. Absil, J. Van Campenhout, C. Merckling, and D. Van Thourhout, "Room-temperature inp distributed feedback laser array directly grown on silicon," *Nature Photonics*, vol. 9, no. 12, pp. 837–842, 2015. [Online]. Available: https://www.nature.com/articles/nphoton.2015.199

[83] C. Shang, K. Feng, E. T. Hughes, A. Clark, M. Debnath, R. Koscica *et al.*, "Electrically pumped quantum-dot lasers grown on 300 mm patterned si photonic wafers," *Light: Science & Applications*, vol. 11, p. 299, 2022.

[84] W.-Q. Wei, A. He, B. Yang, Z.-H. Wang, J.-Z. Huang, D. Han, M. Ming, X. Guo, Y. Su, J.-J. Zhang, and T. Wang, "Monolithic integration of embedded iii-v lasers on soi," *Light: Science & Applications*, vol. 12, no. 1, p. 84. [Online]. Available: https://www.nature.com/articles/s41377-023-01128-z

[85] B. Kunert, W. Guo, Y. Mols, B. Tian, Z. Wang, Y. Shi, D. Van Thourhout, M. Pantouvaki, J. Van Campenhout, R. Langer, and K. Barla, "III/V nano ridge structures for optical applications on patterned 300 mm silicon substrate," *Applied Physics Letters*, vol. 109, no. 9, p. 091101, 2016.

[86] E. M. B. Fahmy, Z. Ouyang, D. Colucci, N. Le Thomas, J. Van Campenhout, B. Kunert, and D. Van Thourhout, "One-dimensional photonic crystal nano-ridge surface emitting lasers epitaxially grown on a standard 300 mm silicon wafer," *Light: Science & Applications*, vol. 15, no. 1, p. 120, 2026. [Online]. Available: https://www.nature.com/articles/s41377-025-02061-z

[87] Y. De Koninck, C. Caer, D. Yudistira, M. Baryshnikova, H. Sar, P.-Y. Hsieh, C. I. Özdemir, S. K. Patra, N. Kuznetsova, D. Colucci, A. Milenin, A. A. Yimam, G. Morthier, D. Van Thourhout, P. Verheyen, M. Pantouvaki, B. Kunert, and J. Van Campenhout, "GaAs nano-ridge laser diodes fully fabricated in a 300-mm CMOS pilot line," *Nature*, vol. 637, no. 8044, pp. 63–69, 2025. [Online]. Available: https://doi.org/10.1038/s41586-024-08364-2

[88] B. Kunert, W. Guo, Y. Mols, R. Langer, and K. Barla, "(Invited) Integration of III/V Hetero-Structures By Selective Area Growth on Si for Nano- and Optoelectronics," *ECS Transactions*, vol. 75, no. 8, p. 409, 2016.

[89] Q. Li and K. M. Lau, "Epitaxial growth of highly mismatched III-V materials on (001) silicon for electronics and optoelectronics," *Progress in Crystal Growth and Characterization of Materials*, vol. 63, no. 4, pp. 105–120, 2017.

[90] B. Kunert, Y. Mols, M. Baryshniskova, N. Waldron, A. Schulze, and R. Langer, "How to control defect formation in monolithic III/V hetero-epitaxy on (100) Si? A critical review on current approaches," *Semiconductor Science and Technology*, vol. 33, no. 9, p. 093002, Sep. 2018.

[91] Özdemir, Cenk Ibrahim, "III-V photodetectors monolithically integrated on silicon for interconnect applications," Ph.D. dissertation, Ghent University, 2024.

[92] Kunert, B. and Langer, R. and Pantouvaki, M. and Van Campenhout, J. and Van Thourhout, Dries, "Gaining an edge with nano-ridges," *COMPOUND SEMICONDUCTOR*, vol. 24, no. 5, pp. 36–41, 2018.

[93] Shi, Yuting, "GaAs nano-ridge lasers epitaxially grown on silicon," Ph.D. dissertation, Ghent University, 2020.

[94] Y. Shi, Z. Wang, J. V. Campenhout, M. Pantouvaki, W. Guo, B. Kunert, and D. V. Thourhout, "Optical pumped InGaAs/GaAs nano-ridge laser epitaxially grown on a standard 300-mm Si wafer," *Optica*, vol. 4, no. 12, pp. 1468–1473, 2017.

[95] Y. Shi, M. Pantouvaki, J. V. Campenhout, D. Colucci, M. Baryshnikova, B. Kunert, and D. V. Thourhout, "Loss-coupled DFB nano-ridge laser monolithically grown on a standard 300-mm Si wafer," *Opt.*

Express, vol. 29, no. 10, pp. 14 649–14 657, 2021. [Online]. Available: https://opg.optica.org/oe/abstract.cfm?URI=oe-29-10-14649

[96] Z. Ouyang, D. Colucci, E. M. B. Fahmy, A. A. Yimam, J. V. Campernhout, B. Kunert, and D. V. Thourhout, "Ingaas/gaas nano-ridge laser with an amorphous silicon grating monolithically grown on a 300mm si wafer," *Opt. Lett.*, vol. 49, no. 16, pp. 4741–4744, Aug 2024. [Online]. Available: https://opg.optica.org/ol/abstract.cfm?URI=ol-49-16-4741

[97] Z. Ouyang, E. M. B. Fahmy, D. Colucci, A. A. Yimam, J. V. Campenhout, B. Kunert, and D. V. Thourhout, "Ultra-compact ingaas/gaas nano-ridge laser monolithically grown on 300mm silicon substrate," *Opt. Lett.*, vol. 50, no. 7, pp. 2358–2361, Apr 2025. [Online]. Available: https://opg.optica.org/ol/abstract.cfm?URI=ol-50-7-2358

2

Theory and Design of Nano-Ridge Surface-Emitting Lasers

2.1 Photonic Crystal Foundations 44
2.2 Bound States in the Continuum 49
  2.2.1 Symmetry-Protected BICs in 1D Photonic Crystal Slabs 51
  2.2.2 BICs for Lasers 51
2.3 Design of Nano-Ridge Surface-Emitting Lasers 53
2.4 Effect of Nano-Ridge Dimensions for Infinite Arrays . . . 56
  2.4.1 Effect of Geometry on Resonance Frequency 56
  2.4.2 Effect of Nano-ridge's width on Q-factor 57
2.5 Design of NRSEL With Finite Dimensions 60
2.6 Summary 62
Bibliography 64

This chapter develops the theoretical and design framework for NRSELs epitaxially grown on silicon. It consolidates the physics of PhCs, bound states in the continuum (BICs), and practical design rules including finite-cavity engineering, and robustness to dimensional variability. These concepts underpin the devices and measurements presented in later chapters.

2.1 Photonic Crystal Foundations

The Nano-Ridge (NR) arrays act simultaneously as the gain medium and as a one-dimensional PhC that supplies in-plane optical feedback and vertical out-coupling. In order to understand their operation, it is important to understand the underlying PhC physics. The physics of periodic structures was initially studied in quantum mechanics, where electrons in crystalline solids experience a periodic potential, leading to the formation of electronic band structures, which dictate the material's electronic properties. Similarly, in photonic crystals, the spatially periodic dielectric function $\varepsilon(\mathbf{r})$ acts for photons as the periodic potential does for electrons, resulting in photonic band structures. This analogy allows us to apply the same mathematical formalism, solving wave equations in a periodic medium, to both electrons and photons, so that band theory governs the propagation of light in photonic crystals just as it does for electrons in solids [1].

A PhC is defined by a spatially periodic permittivity, where $\mathbf{r}$ is the position vector in space and $\mathbf{R}$ is a lattice translation vector that describes the periodicity of the structure:

$$\varepsilon(\mathbf{r}+\mathbf{R}) = \varepsilon(\mathbf{r}). \tag{2.1}$$

For a 1D PhC aligned along x with period Λ, the direct and reciprocal lattice vectors are

$$\mathbf{R} = m\,\Lambda\,\hat{\mathbf{x}}, \qquad \mathbf{G} = \frac{2\pi m}{\Lambda}\,\hat{\mathbf{x}}, \quad m \in \mathbb{Z}. \tag{2.2}$$

In our case, high-index GaAs ridges (with InGaAs quantum wells) alternate with air gaps, yielding strong index contrast. Time-harmonic Maxwell equations in such periodic media reduce to the eigenproblem (for uniform μ)

$$\nabla \times \left[\frac{1}{\varepsilon(\mathbf{r})}\,\nabla \times \mathbf{H}(\mathbf{r})\right] = \frac{\omega^2}{c^2}\,\mathbf{H}(\mathbf{r}), \tag{2.3}$$

whose mode solutions are Bloch waves with a periodic envelope:

$$\mathbf{H}_{n\mathbf{k}}(\mathbf{r}) = \mathbf{u}_{n\mathbf{k}}(\mathbf{r})\,e^{i\mathbf{k}\cdot\mathbf{r}}, \qquad \mathbf{u}_{n\mathbf{k}}(\mathbf{r}+\mathbf{R}) = \mathbf{u}_{n\mathbf{k}}(\mathbf{r}). \tag{2.4}$$

where $\mathbf{H}_{n\mathbf{k}}$ is the magnetic-field eigenmode in band n with crystal momentum $\mathbf{k}$, and $\mathbf{u}_{n\mathbf{k}}$ is a function with the same periodicty as the crystal.

The Bloch dispersions $\omega_n(\mathbf{k})$ define photonic bands over the first Brillouin zone. At symmetry points, counter-propagating spatial harmonics that differ by a reciprocal lattice vector $\mathbf{G}$ become degenerate and hybridize; the periodic index then couples them and lifts the degeneracy, shown in figure 2.1a,b, opening a stop band (Bragg scattering in the band picture). For a 1D grating, first-order Bragg coupling ($m{=}1$) produces a gap at the zone edge $k_x = \pi/\Lambda$; for second-order Bragg coupling

(m=2), the same degeneracy appears at the Γ point after folding[1]. This Bragg splitting and its real-space interpretation are illustrated schematically in Fig. 2.1 taken from [joannopoulos2008].

At the Bragg condition, the same degeneracy of counter-propagating waves appears at $k = \pm\pi/a$ in a uniform medium, and the periodic dielectric modulation lifts this degeneracy by coupling the two plane waves $\mathrm{e}^{\pm i\pi x/a}$. In the presence of a weak index modulation with period a, the true eigenmodes at the band edge are no longer the individual travelling waves, but their symmetric and antisymmetric superpositions:

$$\psi_+(x) \propto \mathrm{e}^{i\pi x/a} + \mathrm{e}^{-i\pi x/a} \propto \cos\left(\frac{\pi x}{a}\right), \tag{2.5}$$

$$\psi_-(x) \propto \mathrm{e}^{i\pi x/a} - \mathrm{e}^{-i\pi x/a} \propto \sin\left(\frac{\pi x}{a}\right). \tag{2.6}$$

These are standing waves with fixed nodes and antinodes relative to the index profile. If the high-index regions are centered at the maxima of $\cos(\pi x/a)$, then ψ_+ has its electric-field antinodes in the high-permittivity material, shown in figure 2.2, with the larger ε. This increases the effective refractive index n_{eff} seen by this mode and therefore pushes its eigenfrequency down, making $\cos(\pi x/a)$ the lower band-edge mode. Conversely, $\psi_- \propto \sin(\pi x/a)$ has nodes (or reduced field) in the high-index regions and antinodes in the low-index regions, so it samples a lower average permittivity, has a smaller n_{eff}, and consequently lies at a higher frequency. In this way, the original degeneracy at $k = \pm\pi/a$ is split into a lower band edge (field concentrated in n_{high}) and an upper band edge (field concentrated in n_{low}), with the frequency separation defining the photonic band gap. The bigger the index contrast, the larger the band gap, as can be seen in figure 2.1c [1].

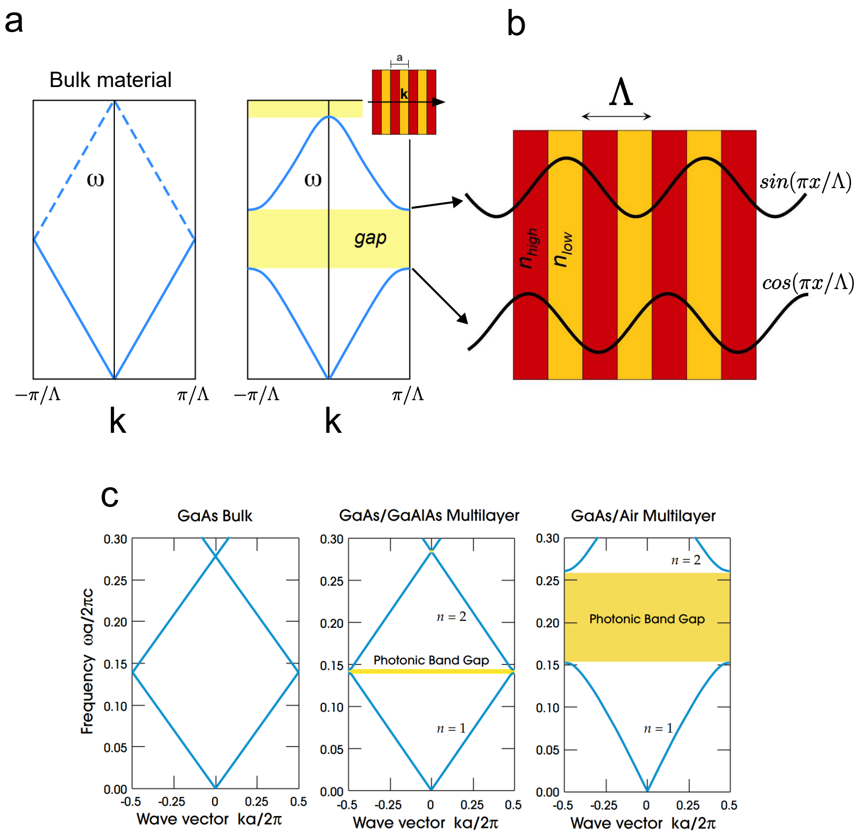

Figure 2.1: (a) Dispersion relation (band diagram), frequency ω versus Bloch wavenumber k_x, of a uniform bulk material, where the dashed lines indicate the apparent "folding" produced by applying Bloch's theorem with an artificial periodicity Λ. A physical periodic modulation of the dielectric function (inset) lifts the degeneracies at the Brillouin-zone boundaries and opens a band gap at $k_x = \pm\pi/\Lambda$, as well as a higher-order gap at $k_x = 0$. (b) Electic field of the corresponding band-edge modes. The degenerate $k_x = \pm\pi/\Lambda$ plane waves of the uniform medium are split into standing waves $\cos(\pi x/\Lambda)$ and $\sin(\pi x/\Lambda)$ by the dielectric periodicity, forming the lower and upper edges of the band gap, respectively. The $\cos(\pi x/\Lambda)$ mode has electric-field peaks in the high-index regions (n_{high}) and therefore lies at a lower frequency than the $\sin(\pi x/\Lambda)$ mode, which peaks in the low-index regions. c) the band diagram caluclated for three different cases with a fill-factor of 50%. Left: Bulk GaAs, Center: periodic structure of two materials with dielectric constants 13 and 12. Right: periodic structure of GaAs and air.[reproduced from [1]]

Whether a Bloch mode is guided or radiative depends on its position relative to the light line (air light cone), $\omega = c\,|\mathbf{k}_{||}|/n_{\text{air}}$. A more detailed discussion of this concept is discussed in the coming sections.

To estimate the grating period we use the Bragg relation from coupled-mode theory (CMT), shown in Fig. 2.2. This relation assumes a weak, sinusoidal perturbation and uses the unperturbed guided mode with $k = n_{\text{eff}} k_0$, so it offers a quick first calculation rather than an exact solution.

$$k_{//} = k + mG, \qquad m \in \mathbb{Z}, \tag{2.7}$$

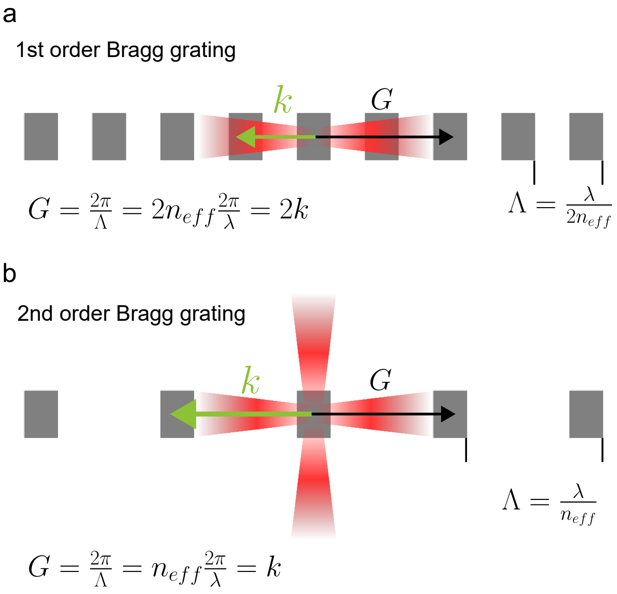

Figure 2.2: Schematic of first- and second-order Bragg gratings. (a) First-order (m=1) Bragg provides strong in-plane feedback (gap near $k \approx G/2$) but does not by itself give near-normal out-coupling. (b) Second-order uses the same period to realize both in-plane feedback and vertical out-coupling: feedback via m=2 ($2k \approx 2G \Rightarrow k \approx G$) and near-normal emission via the m=1 harmonic ($k \approx G$). The green arrows indicates the light propagating wave vector. Black arrows are the corresponding reciprocal lattice vector G(reproduced from [2])

A second-order surface-emitting design uses the same period for feedback and vertical emission ($m = 2$), which places the Bragg degeneracy at Γ in the folded band structure,

$$G \approx k \quad \Longrightarrow \quad n_{\text{eff}} \frac{2\pi}{\lambda_0} \approx \frac{2\pi}{\Lambda} \;\Rightarrow\; \boxed{\Lambda \approx \frac{\lambda_0}{n_{\text{eff}}}}. \tag{2.8}$$

In our case, the Quantum Wells (QWs) emit around $\lambda_0 \approx 1000$ nm (InGaAs gain), GaAs has $n \approx 3.4$–3.6 at 1 μm, but the effective index of a GaAs/air nano-ridge mode is markedly lower due to field penetration into air. First, we estimate n_{eff} using effective mode theory:

$$\varepsilon_{\text{eff,TE}} \;\approx\; f\,\varepsilon_{\text{GaAs}} + (1-f)\,\varepsilon_{\text{air}}, \qquad n_{\text{eff}} \;\approx\; \sqrt{\varepsilon_{\text{eff,TE}}}. \tag{2.9}$$

Around $\lambda_0 \approx 1000$ nm we take $n_{\text{GaAs}} \approx 3.45$ so that $\varepsilon_{\text{GaAs}} \approx 11.9$, and $n_{\text{air}} = 1$. This yields, for representative duty cycles f,

$$\begin{aligned} f &= 0.40: \;\; n_{\text{eff}} \approx \sqrt{0.4 \cdot 11.9 + 0.6 \cdot 1} \approx 2.32, \\ f &= 0.50: \;\; n_{\text{eff}} \approx \sqrt{0.5 \cdot 11.9 + 0.5 \cdot 1} \approx 2.54, \\ f &= 0.60: \;\; n_{\text{eff}} \approx \sqrt{0.6 \cdot 11.9 + 0.4 \cdot 1} \approx 2.75. \end{aligned} \tag{2.10}$$

$$\Lambda \approx \frac{1000\text{ nm}}{2.3\text{–}2.7} \;\approx\; 370\text{–}435\text{ nm}, \tag{2.11}$$

and a representative $n_{\text{eff}} \approx 2.5$ yields

$$\Lambda \approx \frac{1000\text{ nm}}{2.5} \approx 400\text{ nm}, \tag{2.12}$$

A period of 400 nm is a good starting point for FDTD simulations. These period estimates are close to the values found later using FDTD simulations.

2.2 Bound States in the Continuum

Open wave systems generally support (i) extended radiating states forming a continuum and (ii) localized bound states trapped by an effective confining potential (figure 2.3a). When a discrete state spectrally overlaps the continuum, it typically hybridizes with radiation channels and becomes a leaky resonance with a finite linewidth. A BIC is the counterintuitive exception: it is spatially localized while its eigenfrequency lies inside the radiation continuum, yet the state remains perfectly non-radiating and produces no outgoing flux [3].

In photonics, BICs appear naturally in guided-wave structures patterned periodically in-plane, most notably PhC slabs. A PhC slab consists of a dielectric guiding layer with a one- or two-dimensional periodic modulation. For each in-plane Bloch wavevector $k_{||}$, there exist radiation channels in the claddings; in dispersion diagrams these channels are bounded by the *light cone*. Ordinary guided modes exist below the light line, whereas above the light line modes can generally couple to outgoing plane waves and radiate. A photonic BIC is a truly guided eigenmode that lies above the light line, i.e., within the continuum of radiating states, but nevertheless has vanishing radiative loss [3, 4].

The defining feature of a BIC is a vanishing coupling amplitude into all available radiation channels. Equivalently, its radiative decay rate $\gamma_{\text{rad}} \to 0$ and radiative quality factor $Q_{\text{rad}} = \omega_0/(2\gamma_{\text{rad}}) \to \infty$. In practice, measured resonances are *quasi-BICs* with very large but finite Q due to absorption, finite-size effects, and fabrication imperfections.

Two mechanisms dominate in PhC slabs [3, 4]:

Symmetry-protected BICs. When the structure has a symmetry (e.g. a mirror plane or C_2 rotation) the eigenmodes can be classified by parity/representation. At high-symmetry k-points such as the Γ point ($k_{||} = 0$), the outgoing plane-wave channels have a fixed symmetry. If a slab mode has the opposite symmetry, radiation coupling is forbidden, leading to a symmetry-protected BIC, as sketched in 2.3b.

Resonance-trapped (*Friedrich–Wintgen*) BICs. Even when symmetry allows radiation, leakage can cancel by destructive interference between two (or more) radiating pathways. In dispersion diagrams this often occurs near avoided crossings of leaky resonances, where parameters can be tuned to drive the net far-field amplitude to zero.

These two mechanisms can coexist within the same platform, enabling both Γ-point symmetry-protected bound state in the continuum (SPBIC) and off-Γ accidental/interference BICs, as sketched in 2.3d.

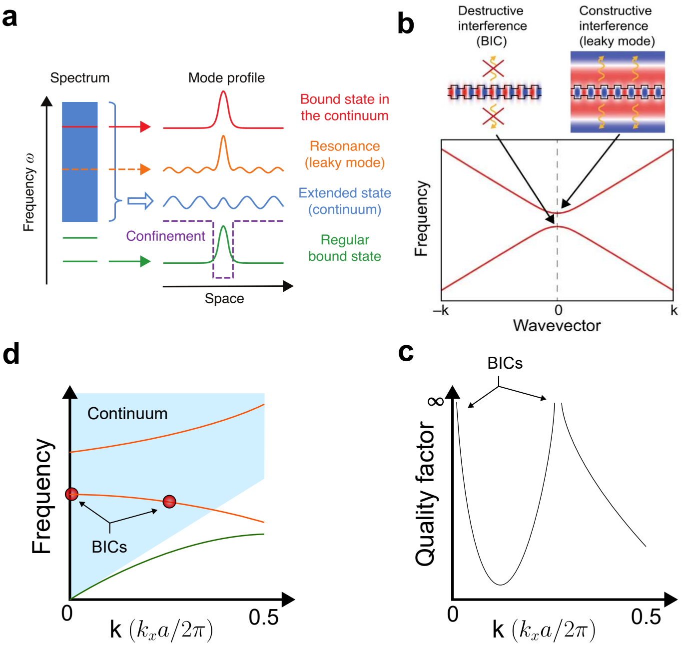

Figure 2.3: Bound states in the continuum. (a) Schematic Illustration explaining BIC modes: Open systems have two main kinds of states: extended "continuum" waves (blue) and localized bound states trapped by a confining potential (green). Normally, any state that sits in the continuum couples to extended waves and leaks energy (orange), becoming a radiating resonance. Bound states in the continuum (BICs) (red) are the exception: they exist within the continuum's frequency range yet stay localized and non-radiating, producing no outgoing flux [reproduced from [3]]. (b) Schematic illustration of a symmetry protected bound state in the continuum (BIC) in a photonic crystal slab. In periodic structure the modes at the band edge couple and form a band gap. the mode at the lower band edge is odd with respect to the mirror symmetry plane of the slab, while the radiating channel is even. Due to this symmetry mismatch, the mode cannot couple to the radiating channel and becomes a BIC. (c) A schematic illustration showing the band structure of a photonic crystal slab with a symmetry-protected BIC at the Γ *point. The BIC lies above the light line (dashed), within the radiation continuum, yet remains perfectly confined due to symmetry protection. a second BIC could also exist away from the* Γ *point, arising from destructive interference (parameter tuning or accidental) between leaky modes [reproduced from [3]]. (d) the corresponding quality factor (Q) plot showing the diverging Q at the BIC points.*

2.2.1 Symmetry-Protected BICs in 1D Photonic Crystal Slabs

For a symmetric 1D PhC slab (periodic along x, invariant along y), a particularly important SPBIC appears at $k_x = 0$ (Γ point). At normal incidence and below the diffraction threshold, the only radiation channel is the zeroth-order symmetric plane wave, which is even with respect to $x \to -x$. If the slab eigenmode is odd under this symmetry operation, the overlap integral between the slab mode and the outgoing plane wave vanishes, and the mode cannot radiate. This parity-based decoupling is the canonical SPBIC mechanism in PhC slabs [3, 4].

A useful modeling perspective treats leaky PhC slab modes as a transverse Fabry–Perot resonance composed of a small number of propagative Bloch waves bouncing vertically inside the slab. Within this multimode Fabry–Perot picture, BICs correspond to points where the net outgoing amplitude cancels exactly. The analysis also reveals a practical constraint: below a cutoff frequency (related to the existence of a higher-order Bloch wave), BICs cannot exist regardless of slab thickness [4]. Consequently, the slab thickness and the set of propagating Bloch-wave orders strongly influence where BICs occur and how they evolve under perturbations.

2.2.2 BICs for Lasers

Lasers require optical feedback and sufficiently low cavity loss. Because an ideal BIC has $\gamma_{\mathrm{rad}} = 0$, BIC-hosting structures provide a natural route to extremely large Q_{rad}, enhancing light–matter interaction and enabling narrow-linewidth lasing. In realistic devices, the lasing mode is typically a quasi-BIC: Q is finite due to nonradiative loss, finite device size, and/or intentional symmetry breaking that enables useful outcoupling.

A landmark demonstration of lasing from photonic BICs was reported by Kodigala *et al.*, who realized room-temperature lasing from an optically pumped nanoresonator array designed to support a resonance-trapped (interference-based) BIC [5]. Their results also highlight an important theme: BIC lasers can combine high Q with engineered far-field patterns and robustness associated with underlying mode structure.

Symmetry-protected BICs in 1D PhC slabs are especially attractive for surface-emitting laser architectures: periodicity supplies in-plane feedback (band-edge/slow-light behavior near Γ), while symmetry protection suppresses out-of-plane radiation loss at $k_x = 0$. To realize a practical laser, the design goal is typically to (i) place the SPBIC (or a nearby quasi-BIC) within the gain bandwidth and (ii) allow controlled leakage for vertical emission.

A representative implementation is the GaN ultraviolet BIC laser demonstrated by Chen *et al.*, which uses a 1D resist line-and-space periodic structure fabricated directly on a GaN film to support a symmetry-protected BIC mode [6]. By avoiding etching into the GaN gain layer, the approach preserves material quality while still enabling directional, narrow-linewidth lasing. The work reports single-mode UV lasing with a linewidth on the order of 0.10 nm and a beam divergence of $\sim 1.5°$, and shows that lasing can occur for device sizes on the order of several micrometers [6]. Importantly, the SPBIC signature appears in the strong angular dependence of the cavity Q, which increases rapidly as the incidence angle approaches zero (the Γ point).

In the next section, we build on these concepts to introduce our BIC PhC laser design implemented using the nano-ridge technology. We focus on a symmetry-protected 1D PhC slab platform, where the Γ-point parity mismatch provides a high-Q state suitable for low-threshold lasing, while controlled symmetry breaking and finite device size enable efficient surface emission.

2.3 Design of Nano-Ridge Surface-Emitting Lasers

As discussed earlier, The array of nano-ridges, shown in figure 2.4, can be considered as a high-index contrast one-dimensional PhC, inherently supporting multiple optical modes. The refractive index of the material and the index contrast play a crucial role in determining the band-gap[1, 7]. Additionally, the height of the nano-ridge structure determines the number of supported modes. An increase in height results in the emergence of more bands, adding complexity to the band diagram. The periodicity and fill factor of the PhC also influence the frequency of the modes. Notably, decreasing the period shifts the bands towards higher frequencies[1].

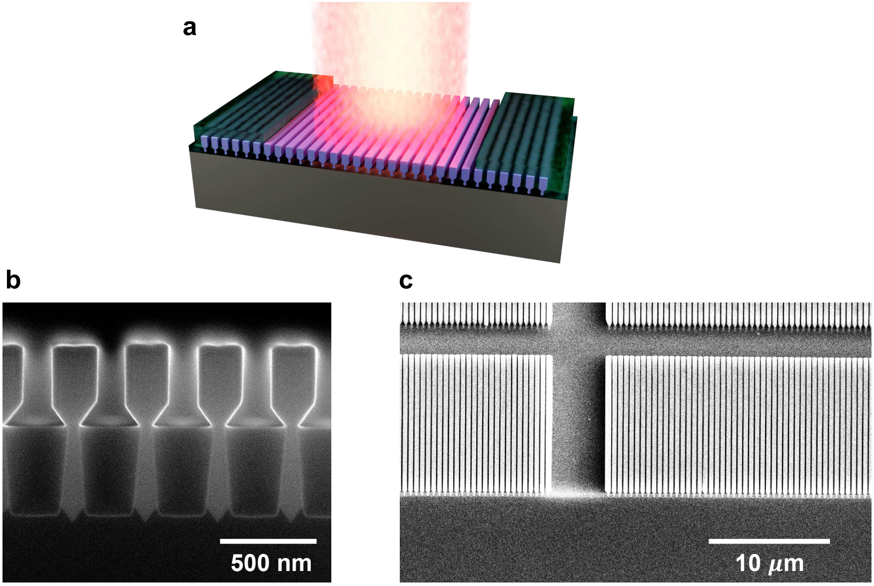

Figure 2.4: Nano-ridge surface emitting laser (NRSEL) on silicon. (a) Illustration of the proposed nano-ridge surface emitting laser (NRSEL). (b) Scanning electron microscope (SEM) image of the cross section of a cleaved array of nano-ridges. (c) Top-view SEM image of arrays of nano-ridges on a silicon wafer.

To systematically track the optical modes of interest, a structured naming convention was employed. The modes appearing at the band-edge (band-edge modes) are denoted as TE_{xyz} and categorized based on the Bragg order (x), band number (y), and their position relative to the band gap (z), indicating whether they are predominantly confined in the dielectric region (lower band (L)) or the air region (higher band (H)). We focus on quasi Transverse Electric (TE)-modes, having their electric field predominantly oriented along the nano-ridges, and hence within the plane of the QWs. It is well-known that the compressively strained InGaAs

QWs embedded within the GaAs nano-ridges provide the highest gain for this polarization[8, 9]. Figure 2.5a,b shows a schematic representation of the nano-ridge array and the band diagram calculated for an array of nano-ridges with period Λ = 380 nm, height H = 410 nm and width W = 197 nm. These dimensions were chosen to match the average dimensions of the waveguides in our fabricated sample, measured using SEM. The band diagram was calculated using a 2D finite difference time domain (Finite-Difference Time-Domain (FDTD)) simulation with Bloch boundary conditions. The band diagram demonstrates significant mode separation, which arises from the substantial contrast in refractive index between the air and dielectric sections of the PhC[1]. Another result of the high index contrast is the flattening of the bands (reduced dispersion curvature) near the band edges[10, 11]. At the band-edges, a slow-light Bloch mode (SBM) propagates inside the structure with group velocity $d\omega/dk$ approaching zero due to the flat dispersion curvature. This phenomenon can be attributed to the superposition of reflected waves resulting from the index modulation - GaAs and air - at the symmetry points within the structure[1, 12–15].

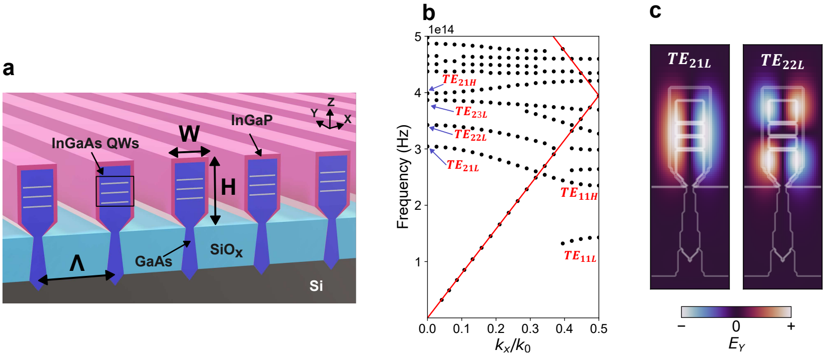

Figure 2.5: Nano-ridge 1D photonic crystal (a) Schematic representation showing an array of nano-ridges with the most relevant dimensional parameters. (b) Dispersion diagram for an array of nano-ridges calculated using 2D-FDTD. The radiation continuum lies above the light line (red). (c) Calculated electric field for the first two band edge modes at the Γ *point* $k_x/k_0 = 0$.

We are interested in the modes at the high symmetry Γ point $k_x = 0$ as these might couple to vertically emitting radiating modes. In Figure 2.5c, the mode profiles for the first two band-edge modes at the Γ point, TE_{21L}, and TE_{22L}, are shown. Both modes are predominantly confined within the high-index dielectric region and are commonly referred to as dielectric modes.

As discussed in Sec. 2.2, modes above the light line are generally expected to radiate. At high-symmetry points such as Γ, however, symmetry can forbid coupling to the available far-field channels, yielding a BIC (or, in finite structures, a high-Q quasi-BIC). This is crucial for interpreting Fig. 2.5: even when band-edge modes lie within the radiation continuum, their radiation loss is primarily governed by symmetry (field parity) at Γ, not solely by their position relative to the light line. In the following, we use the mode symmetry at Γ to identify which band-edge mode can retain a very high Q while remaining accessible for surface emission [3, 16, 17].

In an ideal, infinite nano-ridge PhC, TE_{21L} is symmetry-protected and does not couple to radiating channels despite being above the light line [6]. Its electric field is antisymmetric and exhibits a node at the center of the nano-ridge, as shown in Fig. 2.5c. Realistically, the PhC is finite, leading to uncertainty in the in-plane wave vectors and hence symmetry breaking, allowing vertical emission[14]. For our nano-ridge height of 410 nm, two higher-order BIC modes[6], TE_{22L} and TE_{23L} are also supported. They appear at higher energies and share the field antisymmetry that renders TE_{21L} a BIC. Since this symmetry protection only holds strictly at the Γ point, even a small shift of the in-plane wave vector degrades the confinement of all three modes. Consequently, these BIC modes exhibit a pronounced dependence on the in-plane wave vector: as one moves away from the Γ point, their Q-factor drops steeply, whereas the Q-factor of the first lossy (symmetric) mode shows only weak dependence on the in-plane wave vector[5, 6, 12, 18]. A side-by-side comparison of the Q-factor dispersion and corresponding mode profiles for the first three BIC modes (TE_{21L}, TE_{22L}, and TE_{23L}) and the first lossy mode (TE_{21H}) is presented in figure 2.6. In figure 2.6a, the Q-factor dispersion for an array of nano-ridges without a silicon substrate is shown. The BIC modes TE_{21L}, TE_{22L}, and TE_{23L} exhibit a significant drop in Q-factor as the in-plane wave vector shifts away from the Γ point, while the leaky symmetric mode TE_{21H} has a low Q-factor with only weak dependence on the in-plane wave vector. In figure 2.6b, the Q-factor dispersion for an array of nano-ridges with a silicon substrate is shown. The presence of the substrate limits the maximum achievable Q-factor due to leakage into the substrate, but the BIC modes still show a significant drop in Q-factor as the in-plane wave vector shifts away from the Γ point.

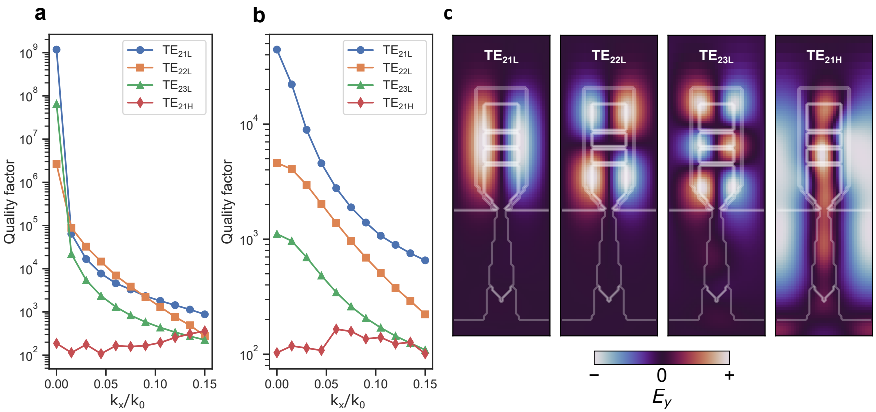

Figure 2.6: Quality factor for BIC mode vs leaky mode. (a) Quality factor for an array of nano-ridges without a silicon substrate using bloch boundary conditions calculated for different k values. For the asymmetric BIC modes TE_{21L}, TE_{22L}, and TE_{23L} the quality factor drops significantly off-gamma $k_x = 0$. The leaky symmetric mode TE_{21H} has a low quality factor and a weak dependence of the quality factor on the k value. (b) Quality factor for an array of nano-ridges with a silicon substrate using bloch boundary conditions calculated for different k values. For the asymmetric BIC modes TE_{21L}, TE_{22L}, and TE_{23L} the quality factor drops significantly off-gamma $k_x = 0$. The substrate limits the maximum achievable quality factor as it allows leakage. (c) Mode profiles for the TE_{21L}, TE_{22L}, and TE_{23L} modes at the Γ point, showing the antisymmetric field distribution that leads to the BIC behavior. The TE_{21H} mode shows a symmetric field distribution, which allows coupling to radiating channels and results in a low quality factor.

2.4 Effect of Nano-Ridge Dimensions for Infinite Arrays

2.4.1 Effect of Geometry on Resonance Frequency

As stated earlier, for optimising the design of the nano-ridges, we focused on the TE_{21L} mode, operating at the Γ point, as it provides the highest overlap with the QWs in the nano-ridge. Second, the nano-ridge dimensions and the period need to be chosen such that the resonance frequency of this mode matches the QW gain peak, around 1000 nm. Figure 2.7a shows how the resonance frequency of this mode is varying as function of period, fill factor and height. The fill factor is defined as the ratio of the nano-ridge width and the periodicity $FF = W/\Lambda$. The resonance frequency of the band-edge mode is extracted from the band diagram. The simulations were carried out using 2D-FDTD with Bloch boundary conditions. The period of the array obviously has the biggest impact on the resonance frequency.

Also the nano-ridge width, and hence the fill factor have a strong influence. The effect of the nano-ridge height is less important. Height variations of 0.4–0.6 µm shift the resonance by only ≈25–30 nm, whereas sweeping the width from 152 nm to 304 nm changes the resonance by roughly 375 nm, about an order of magnitude larger, making the nano-ridge width together with the periodicity the dominant parameters. The available mask (see section: 3.1) provided only a fixed number of array designs, of which the one with a period of Λ= 380 nm provides the best match for our device design. Figure 2.7b shows that, with this period, the emission wavelength can be varied anywhere within the gain bandwidth of the QW's, which ranges approximately from 980 nm to 1060 nm, by controlling the nano-ridge height and width.

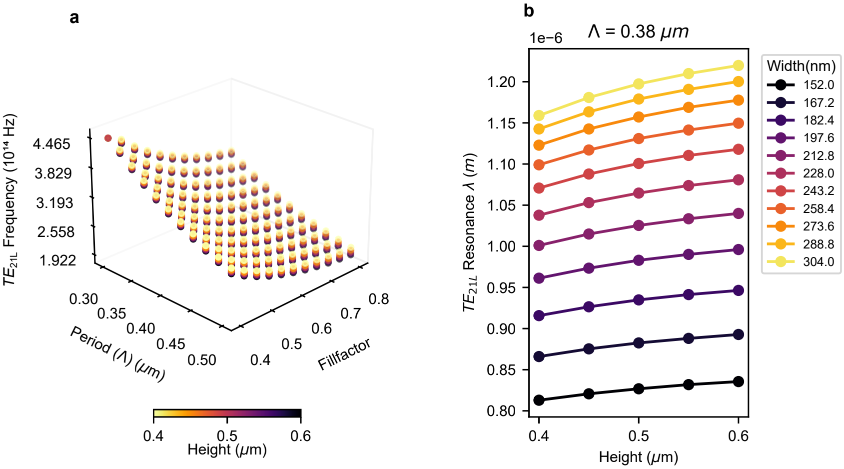

Figure 2.7: Geometry dependent resonance frequency shift. (a) Sweep of the resonance frequency of the TE_{21L} mode, as function of nano-ridge array period ($Lambda$) and fill factor, for varying nano-ridge heights (H). b) Resonance wavelength (λ) for the chosen design period $Lambda$ = 0.38 μm, as function of height (H), for different widths (W).

2.4.2 Effect of Nano-ridge's width on Q-factor

In theory, the BIC mode at the Γ point has an infinite Q-factor for ideal infinite PhC. However, in practice, several factors limit the achievable Q-factor. One of these factors is the presence of a silicon substrate below the nano-ridge array, which breaks the vertical symmetry of the structure and allows leakage into the substrate due to its proximity from the optical mode[6]. This makes the width of the nano-ridge an important parameter, as it determines the confinement of the mode within the nano-ridge. Figure 2.8 shows that the calculated Q-factor of the TE_{21L} mode at the Γ point as function of the nano-ridge width, without a substrate (a) and with a silicon substrate (b). In the absence of a substrate, the Q-factor barely depends on the width, as the mode is well confined within the nano-ridge for all widths. However, when a substrate is present below the nano-ridge array, the Q-factor shows a strong dependence on the nano-ridge geometry especially the width due to the close proximity of the optical mode to the silicon substrate. In the presence of a substrate The Q-factor increases with increasing width, as the mode becomes better confined within the nano-ridge, reducing leakage into the substrate. However, for widths larger than 220 nm, the Q-factor saturates around 1e7, as further increases in width do not significantly improve confinement. The simulations were carried out using 2D FDTD with Bloch boundary conditions to simulate an infinite sturcture.

For a finite NR array with 42 NRs or a cavity width of $15\mu m$ ($H = 480$ nm, $\Lambda = 380$ nm), this trend does not hold as can be seen in figure 2.9. The Q-factor increases with increasing width up to 250 nm, after which it starts to decrease again. This can be explained by the fact that for narrow nano-ridges, the mode is less confined and more prone to leaking to the substrate, resulting in a lower Q-factor. As the width increases, the mode becomes better confined, leading to an increase in Q-factor. However, beyond a certain width (250 nm), the mode starts to leaking to the sides, increasing lateral leakage and reducing the Q-factor. Therefore, there is an optimal width (250 nm) that balances confinement and lateral leakage, resulting in the highest Q-factor for the finite nano-ridge array. As discussed earlier, the resonance frequency of the TE_{21L} mode depends significantly on the nano-ridge width. Therefore, when choosing the optimal width for a specific design, one must also consider the desired resonance frequency. The effect of width on lasing threshold is experimentally investigated later in section 4.2.1. Additionally, random variations in the width were investigated. Simulations show that random variations in nano-ridge width, even with a standard deviation as small as 5 nm, can lead to significant Q factor fluctuations and mode distortions caused by Anderson localization [19, 20]. A discussion on how this structural disorder impacts cavity performance and efficiency can be found in the appendix A.6.

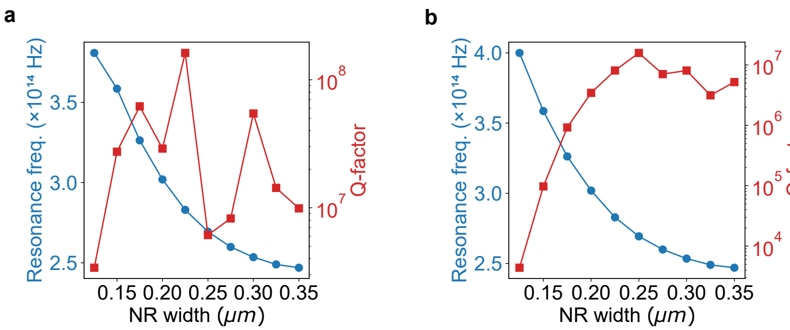

Figure 2.8: Q-factor dependence on nano-ridge width with bloch boundary conditions to simulate an infinite structure. (a) Calculated Q-factor and resonance frequency for the TE_{21L} *mode at the* Γ *point as function of the nano-ridge width without a substrate. (b) Calculated Q-factor and resonance frequency for the* TE_{21L} *mode at the* Γ *point as function of the nano-ridge width with a silicon substrate below the nano-ridge array.*

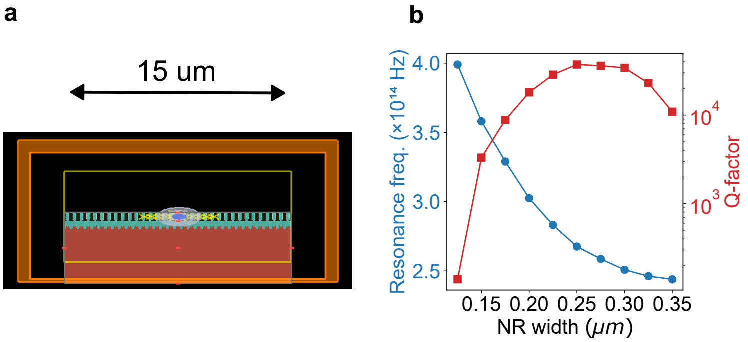

Figure 2.9: Q-factor dependence on nano-ridge width for a finite array. (a) schematic showing a 2d FDTD simulation for a 15 μm *wide array. (b) Calculated Q-factor and resonance frequencyfor the* TE_{21L} *mode at the* Γ *point as function of the nano-ridge width for a finite array of 42 nano-ridges (*$H = 480nm, \Lambda = 380nm$*) with a silicon substrate below the nano-ridge array.*

2.5 Design of NRSEL With Finite Dimensions

In the previous section we considered a nano-ridge array with infinite dimensions. Although we did obtain laser operation of quasi-infinite arrays as we will show later in the experimental results (4.2.1), in practice we desire to keep the dimensions more restricted. Reducing the dimensions of the NRSEL array adversely impacts the device performance however. A reduction in the number of periods results in decreased confinement and in-plane light leakage. This is clearly visible from figure 2.10b, which shows a 2D FDTD simulation of the TE_{21L} mode for an array of 40 nano-ridges with Λ = 380 nm, H = 410 nm and W = 197 nm. Figure 4c shows how the Q-factor of this mode increases with an increasing number of nano-ridge periods, and saturates for more than 90 periods, when the in-plane losses become negligible. As the modal gain threshold is inversely proportional to the Q-factor $G_{th} \propto 1/Q$, reaching a low threshold requires a relatively large device. This trade-off can be overcome by introducing suitable mirrors at both sides of the cavity. A possible approach consists of forming a heterostructure from two PhCs with shifted bandgap, as shown schematically in figure 2.10a. If one ensures that the frequency of the targeted band-edge mode of the central PhC falls within the bandgap of the surrounding PhC, the latter acts as a mirror and reduces in-plane losses.

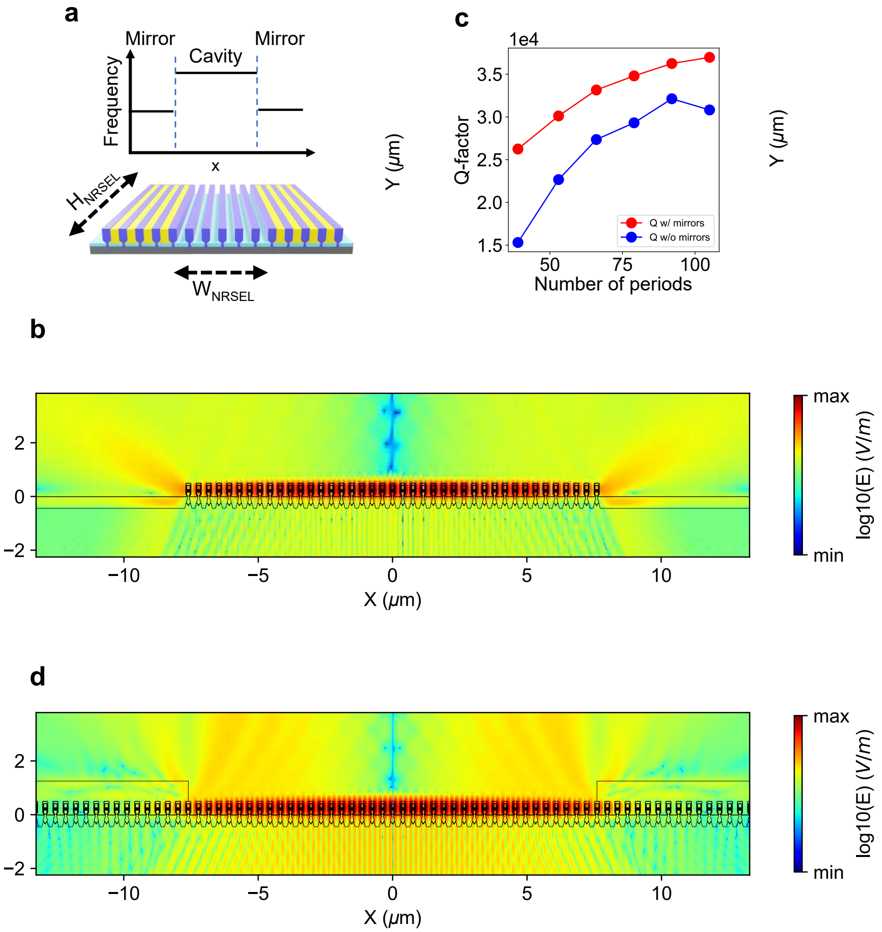

Figure 2.10: Bloch mode confinement with side mirrors. (a) Side mirrors defined by locally shifting the slow Bloch mode to a longer wavelength. This forms a barrier around the middle cavity, enhancing the electric field in the cavity, and reducing the lateral losses. (b, d) A 2D FDTD simulation of a finite nano-ridge crystal without and with mirrors, showing a cross-section of the TE_{21L} *mode. The side mirror is formed by adding photoresist of index 1.6 between and on top of the nano-ridges. (c) Calculated Q-factor for the* TE_{21L} *mode without and with side mirrors, as function of the number of periods.*

This approach allows to localize the mode while keeping the Q-factor sufficiently high, thereby allowing for low threshold lasing[21–23]. The standard approach to shift the bandgap of a PhC is to change its period. However, due to a limitation in the available mask used for patterning the nano-ridge we choose a different approach here. Specifically, depositing a material with refractive index higher than air, such as SiO2, between the nano-ridges shifts the bandgap frequency downwards, as illustrated in Figure 2.10a. Simulations show that embedding an array of nano-ridges within a 1.5 µm thick photoresist layer with refractive index 1.6, shifts the resonance wavelength of the TE_{21L} mode from 984 nm to 1012 nm. Figure 2.10d shows the simulated mode profile for a cavity formed by a central array of 40 uncovered nano-ridges and mirrors of 15 nano-ridges embedded within SiO2. The reduced lateral leakage, increased confinement and reflection at the boundaries is clearly visible. Adding the mirror increases the Q-factor from 15000 to 26000 for the 40 periods device. The vertical emission increases to 20.7% compared to around 14.3% without the side oxide mirrors. Adding a bottom mirror could further increase the vertically coupled power, as will be discussed later in chapter 6.1.

Note that the upward-radiated field shows a node at the cavity center, which directly reflects the antisymmetric field parity of the TE_{21L} quasi-BIC. In future designs, this double-lobed emission can be mitigated by deliberately engineering the out-coupling phase so that the radiation from adjacent periods adds constructively at normal incidence. Reported strategies include introducing a localized phase-shift/defect section in the grating (e.g., a π-phase shift or an equivalent half-period offset) to break the odd symmetry at the cavity center and form a single-lobed surface-emitting mode [24]; and applying controlled symmetry breaking (geometric asymmetry or asymmetric cladding) to weakly hybridize the symmetry-protected mode with an even, radiative component, thereby lifting the far-field node while maintaining a high (but finite) Q [25, 26]. In practice, however, lattice imperfections and other fabrication nonidealities tend to relax the ideal symmetry and partially wash out the central far-field node, so the distinctly double-lobed pattern is not always observed in our far-field measurements, as discussed in Chapter 5. Moreover, the finite device size and additional scattering from the lateral mirrors complicate the phase relations required for clean period-to-period interference, further reducing the visibility of the ideal interference-induced node.

2.6 Summary

We established the theoretical basis and design methodology for NRSELs:

- 1D nano-ridge PhCs support high-Q BICs at Γ, allowing both confinement and surface emission.
- Ridge width and fill factor dominate wavelength tuning.
- Finite cavities with index-shift mirrors provide robust lateral confinement and controlled vertical extraction.

These principles guide the epitaxy, metrology, and device demonstrations in the following chapters.

Bibliography

[1] J. D. Joannopoulos, *Photonic Crystals: Molding the Flow of Light*. Princeton University Press.

[2] X. Chen, R. Su, J. Liu, J. Li, and X.-H. Wang, “Scalable and highly efficient approach for an on-chip single-photon source,” *Photonics Research*, vol. 10, no. 9, p. 2066, Sep. 2022.

[3] C. W. Hsu, B. Zhen, A. D. Stone, J. D. Joannopoulos, and M. Soljacic, “Bound states in the continuum,” *Nature Reviews Materials*, vol. 1, no. 9, 2016.

[4] A. I. Ovcharenko, C. Blanchard, J.-P. Hugonin, and C. Sauvan, “Bound states in the continuum in symmetric and asymmetric photonic crystal slabs,” *Physical Review B*, vol. 101, no. 15, p. 155303, 2020. [Online]. Available: https://link.aps.org/doi/10.1103/PhysRevB.101.155303

[5] A. Kodigala, T. Lepetit, Q. Gu, B. Bahari, Y. Fainman, and B. Kanté, “Lasing action from photonic bound states in continuum,” *Nature*, vol. 541, no. 7636, pp. 196–199, 2017.

[6] M. H. Chen, D. Xing, V. C. Su, Y. C. Lee, Y. L. Ho, and J. J. Delaunay, “GaN Ultraviolet Laser based on Bound States in the Continuum (BIC),” *Advanced Optical Materials*, vol. 11, no. 6, pp. 1–8, 2023.

[7] S. B. Cavalcanti, M. De Dios-Leyva, E. Reyes-Gómez, and L. E. Oliveira, “Band structure and band-gap control in photonic superlattices,” *Physical Review B - Condensed Matter and Materials Physics*, vol. 74, no. 15, 2006.

[8] Y. Shi, Z. Wang, J. V. Campenhout, M. Pantouvaki, W. Guo, B. Kunert, and D. V. Thourhout, “Optical pumped InGaAs/GaAs nano-ridge laser epitaxially grown on a standard 300-mm Si wafer,” *Optica*, vol. 4, no. 12, pp. 1468–1473, 2017.

[9] S. L. Chuang, *Physics of Photonic Devices*. John Wiley & Sons.

[10] S. Nojima, “Optical-gain enhancement in two-dimensional active photonic crystals,” *Journal of Applied Physics*, vol. 90, no. 2, pp. 545–551, 2001.

[11] S. Droulias, C. Fietz, P. Zhang, T. Koschny, and C. M. Soukoulis, “Lasing threshold control in two-dimensional photonic crystals with gain,” *Optics Express*, vol. 22, no. 16, p. 19242, 2014.

[12] N. D. Le, P. Bouteyre, A. Kheir-Aldine, F. Dubois, S. Cueff, L. Berguiga, X. Letartre, P. Viktorovitch, T. Benyattou, and H. S. Nguyen, “Super

Bound States in the Continuum on a Photonic Flatband: Concept, Experimental Realization, and Optical Trapping Demonstration," *Phys. Rev. Lett.*, vol. 132, no. 17, p. 173802, 2024. [Online]. Available: https://link.aps.org/doi/10.1103/PhysRevLett.132.173802

[13] K. Sakai, E. Miyai, T. Sakaguchi, D. Ohnishi, T. Okano, and S. Noda, "Lasing band-edge identification for a surface-emitting photonic crystal laser," *IEEE Journal on Selected Areas in Communications*, vol. 23, no. 7, pp. 1335–1340, 2005.

[14] S. H. Kwon and Y. H. Lee, "High Index-Contrast 2D Photonic Band-Edge Laser," *IEICE Transactions on Electronics*, vol. E87-C, no. 3, pp. 308–315, 2004.

[15] P. Viktorovitch, E. Drouard, M. Garrigues, J. L. Leclercq, X. Letartre, P. R. Romeo, and C. Seassal, "Photonic crystals: Basic concepts and devices," *Comptes Rendus Physique*, vol. 8, no. 2, pp. 253–266, 2007.

[16] B. Zhen, C. W. Hsu, L. Lu, A. D. Stone, and M. Soljaıfmmode \checkc\else č\fiıifmmode \acutec\else ć\fi, "Topological Nature of Optical Bound States in the Continuum," *Phys. Rev. Lett.*, vol. 113, no. 25, p. 257401, 2014.

[17] M.-S. Hwang, H.-C. Lee, K.-H. Kim, K.-Y. Jeong, S.-H. Kwon, K. Koshelev, Y. Kivshar, and H.-G. Park, "Ultralow-threshold laser using super-bound states in the continuum," *Nature communications*, vol. 12, no. 1, p. 4135, 2021.

[18] N. D. Le, F. Dubois, X. Letartre, P. Viktorovitch, and H. S. Nguyen, "Extended Bound states In the Continuum for ultraheavy photons in photonic lattice," pp. 1–8, 2019. [Online]. Available: http://arxiv.org/abs/1905.00215

[19] B. Kumar, R. Homri, Priyanka, S. K. Maurya, M. Lebental, and P. Sebbah, "Localized modes revealed in random lasers," *Optica*, vol. 8, no. 8, p. 1033, 2021.

[20] A. Mafi, "Transverse Anderson localization of light: A tutorial," *Advances in Optics and Photonics*, vol. 7, no. 3, p. 459, 2015.

[21] T. Inoue, M. Yoshida, M. D. Zoysa, K. Ishizaki, and S. Noda, "Design of photonic-crystal surface-emitting lasers with enhanced in-plane optical feedback for high-speed operation," *Optics Express*, vol. 28, no. 4, p. 5050, 2020.

[22] L. Ferrier, P. Rojo-Romeo, E. Drouard, X. Letatre, and P. Viktorovitch, "Slow bloch mode confinement in 2d photonic crystals for surface operating devices," *Optics Express*, vol. 16, no. 5, p. 3136, 2008.

[23] P. Viktorovitch, C. Sciancalepore, B. B. Bakir, X. Letartre, and C. Seassal, “Double photonic crystal vertical-cavity surface-emitting lasers,” *High Contrast Metastructures II*, vol. 8633, p. 863302, 2013.

[24] S. Li, G. Witjaksono, S. Macomber, and D. Botez, “Analysis of Surface-Emitting Second-Order Distributed Feedback Lasers With Central Grating Phaseshift,” *IEEE Journal on Selected Topics in Quantum Electronics*, vol. 9, no. 5, pp. 1153–1165, 2003.

[25] “High power surface emitting terahertz laser with hybrid second- and fourth-order Bragg gratings,” *Nature Communications*, vol. 9, no. 1, pp. 1–7, 2018.

[26] S. Biasco, A. Ciavatti, L. Li, A. G. Davies, E. H. Linfield, H. Beere, D. Ritchie, and M. S. Vitiello, “Highly efficient surface-emitting semiconductor lasers exploiting quasi-crystalline distributed feedback photonic patterns,” *Light: Science and Applications*, vol. 9, no. 1, pp. 1–11, 2020.

3

Metrology and Fabrication of NRSELs

3.1 Wafers Overview **68**
3.2 Nano-Ridge Epitaxy **71**
3.3 Wafer Metrology **72**
3.3.1 Measuring Dimensions Using SEM 73
3.3.2 PL Characterization Using CW Excitation 78
3.3.3 PL characterization Using Pulsed Excitation 80
3.4 NRSEL Definition **80**
3.4.1 Optical Lithography Mask Design 80
3.4.2 NRSEL Fabrication Process 83
3.5 Summary **87**
Bibliography **89**

In this chapter we focus on the wafer metrology and fabrication process of the NRSEL devices. First, we describe the epitaxial growth of the InGaAs/GaAs nano-ridges on patterned silicon wafers using NRE. Next, we present SEM and PL metrology for different wafers to assess the material quality and uniformity of the nano-ridges and to pick the optimal wafer for device fabrication. Lastly, we detail the fabrication steps involved in defining micro NRSEL devices, including the optical lithography mask design and the etching and patterning processes used to create the NRSEL cavities and side mirrors.

3.1 Wafers Overview

Six 300 mm wafers were grown with varying growth conditions to optimize the nano-ridge dimensions and quantum well gain of the InGaAs/GaAs nano-ridges. The wafers differed in terms of growth temperature, V/III ratio, and quantum well thickness. PL measurements were performed at room temperature to evaluate the optical quality of the nano-ridges on each wafer.

In figure 3.1, we show photographs and SEM images of a 300 mm silicon wafer after the epitaxial growth of InGaAs/GaAs nano-ridges using NRE. The wafer contains multiple fields of nano-ridge arrays with varying trench periods and widths, as defined by the Tower35 mask design illustrated in figure 3.2. Each field has a specific trench period and width, allowing us to study their influence on the nano-ridge dimensions and accordingly the optical properties. A zoomed-in SEM image of the nano-ridge array in field C13, which has a trench period of 380 nm, is shown in figure 3.1c. A cross-sectional SEM image of the nano-ridge array, in figure 3.1d, reveals the box-like shape of the nano-ridges, which forms a 1D photonic crystal.

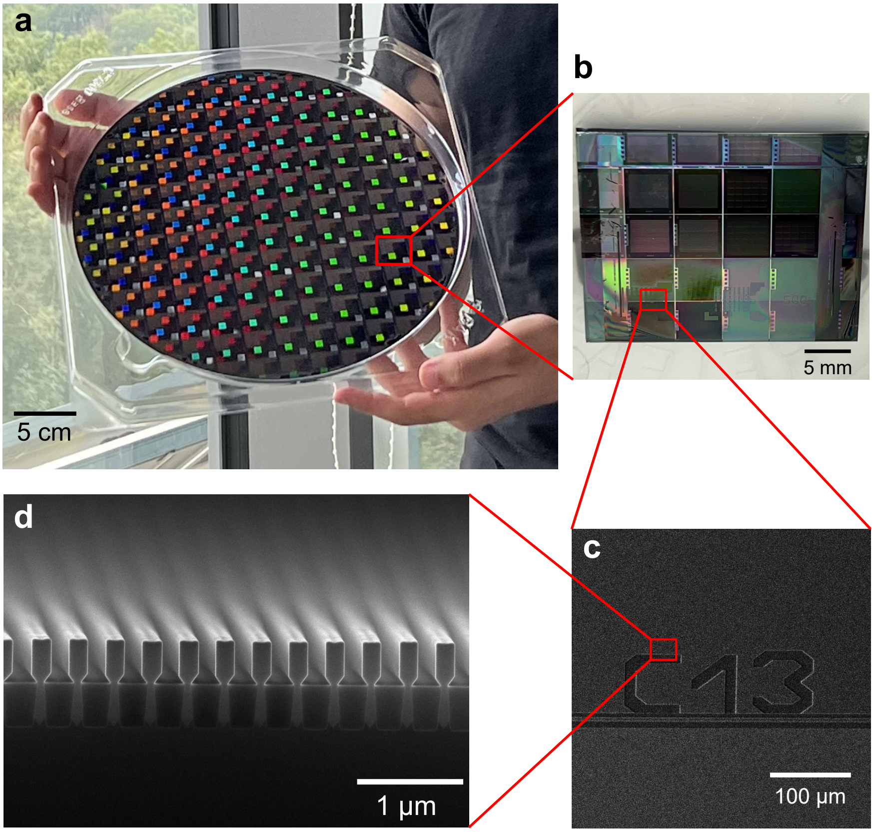

Figure 3.1: (a) Photograph of a 300 mm silicon wafer after the epitaxial growth of InGaAs/GaAs nano-ridges using NRE. (b) Optical microscope image of a die from the wafer, showing the patterned trenches filled with nano-ridges. c) Zoomed-in view of the nano-ridge array in field C13 using SEM, which has a trench period of 380 nm. d) Cross-sectional SEM image of the nano-ridge array in field C13, showing the box-like shape of the nano-ridges.

The mask (Tower35), shown in figure 3.2, contains 20 fields of 5 mm x (3.5 or 5 mm) nano-ridge arrays numbered (C1 to C20). The trench size and period is held constant, ensuring good uniformity, as illustrated in figure 3.2. Although the Tower35 mask was not originally intended for the NRSEL project, it was the only available option and nevertheless offers a useful variety of trench parameters. The trench period ranges from 100 nm to 800 nm and the trench widths from 80 nm to 100 nm, enabling a systematic study of their influence on the nano-ridge dimensions. With appropriate growth optimization, several fields on this mask can be tuned to match the target geometries predicted by our simulations. As we discussed earlier in chapter 2, from the basic analytical equations we expect a period of around 400 nm to match the lasing wavelength of around 1000 nm. We found three fields: C13, C18, and C8 of periods 380, 400, and 480 nm respectively to be a close match. According to FDTD simulations, C13 field ($\Lambda = 380\,\mathrm{nm}$) had the least sensitivity ($\approx 2.3\,\mathrm{nm\,nm^{-1}}$) to the nano-ridge's width variations compared to C18 ($\approx 3\,\mathrm{nm\,nm^{-1}}$) and C8 ($\approx 3.6\,\mathrm{nm\,nm^{-1}}$), as shown in figure 3.3. Therefore, we focused our metrology and fabrication efforts on the field C13, which has a trench period of 380 nm and a trench width of 80 nm, giving us a periodic array of nano-ridges with $\Lambda = 380\,\mathrm{nm}$.

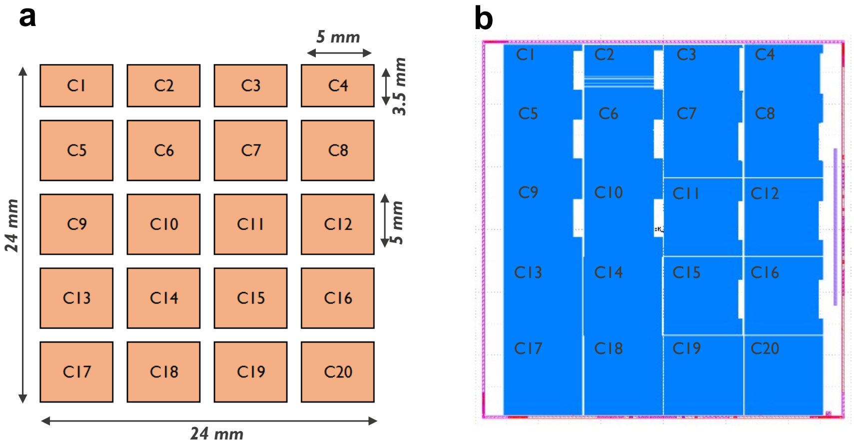

Figure 3.2: a) Schematic illustration of the Tower35 mask design used for the epitaxial growth of InGaAs/GaAs nano-ridges. The mask contains 20 fields of nano-ridge arrays with varying trench periods and widths. b) Picture from the GDS layout of the Tower35 mask, showing the different fields and their respective trench dimensions.

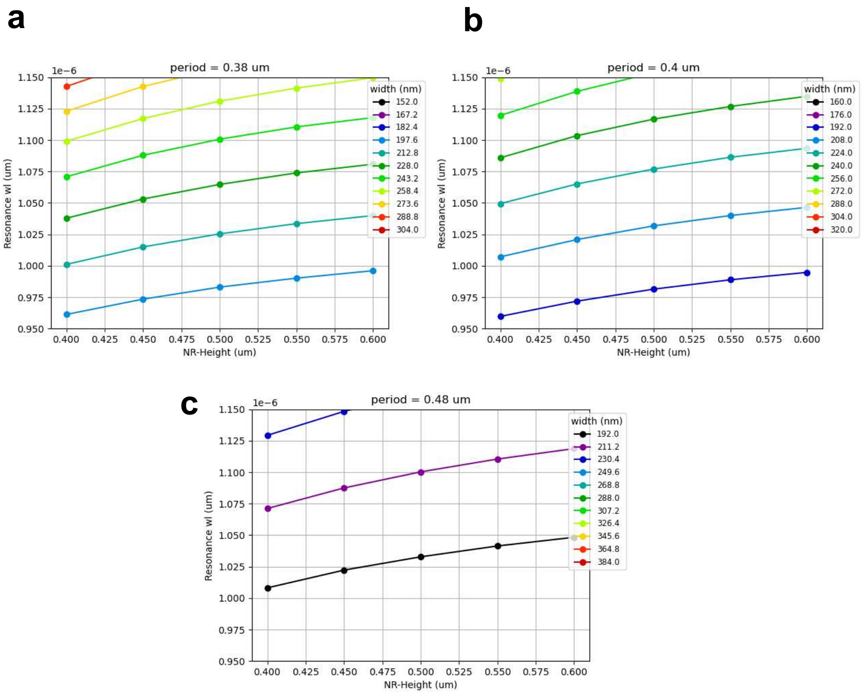

Figure 3.3: Simulated photonic band structures (resonance frequency of TE_{21L} mode) for InGaAs/GaAs nano-ridge arrays with trench periods of (a) 380 nm (C13), (b) 400 nm (C18), and (c) 480 nm (C8). The change in nano-ridge width has the biggest influence on the resonance frequency for TE_{21L} mode for the 480 nm period, while the 380 nm period shows the least sensitivity to width variations. This means that fabrication tolerances will have less impact on the lasing wavelength for the 380 nm period.

3.2 Nano-Ridge Epitaxy

The InGaAs/GaAs nano-ridges were epitaxially grown on 300 mm patterned silicon wafers using NRE[1–4]. This involves a combination of selective area growth in narrow trenches to confine relaxation defects arising from the large lattice mismatch via aspect ratio trapping (ART), and nano-ridge shape engineering during the growth out of the trench, to control the final shape of the nano-ridges. The process starts with the formation of Si fins embedded in SiO_2, which are realized via a shallow trench isolation (STI) process on (001) Si, a common approach in CMOS fabrication. These Si fins are then wet-etched with tetramethylammonium hydroxide to expose two 111 Si facets required for subsequent III-V growth without antiphase disorder. Then MOVPE is used to grow the InGaAs/GaAs nano-ridges. The application of very narrow trenches prevents threading dislocations from protruding into the active InGaAs QW layers. Once the material extends above the SiO_2 mask, careful control of the growth parameters allows to obtain the box-like shape visible in figure 3.1d with dimensions as obtained from simulations. For wafer D03, used in fabrication of NRSELs, which will is discussed later. Three $In_{0.23}Ga_{0.77}As$ QWs are embedded in the GaAs nano-ridges for providing optical gain. We estimated an indium content of $23 \pm 1\%$ and a quantum well thickness of 11 ± 1 nm.The nano-ridges are expected to provide a material gain of approximately ($5000\ \mathrm{cm}^{-1}$) [5], corresponding to a modal gain of about ($250\ \mathrm{cm}^{-1}$) for an optical confinement factor of ($\Gamma = 5\%$). To improve the carrier confinement and to reduce surface recombination, the InGaAs/GaAs nano-ridges were capped with a lattice matched InGaP layer. The indium content and quantum well thickness are different from wafer to another as the growth conditions were varied. The data for the different wafers is summarized in table 3.1. The indium composition and thickness estimations are based on X-Ray Diffraction (XRD) measurements of the nano-ridge sample. The indium composition is an important parameter as it determines the bandgap of the quantum wells and accordingly the gain spectrum. However, the resonance wavelength of the cavity modes is mainly determined by the nano-ridge dimensions, which are controlled by the trench geometry defined in the mask and the growth conditions of the nano-ridges. Therefore, by varying both the trench geometry, nano-ridge geometry, and the quantum well composition/thickness, we can optimize the overlap between the gain spectrum and the cavity modes to achieve lasing.

	D02	D03	D04	D05	D06	D07
Quantum well thickness (nm)	13	12	-	-	-	-
Indium percentage in QW	20	25	19-21	19-21	19-21	14-16

Table 3.1: Summary of the different 300 mm wafers grown with varying growth conditions. The quantum well thickness and indium percentage in the InGaAs quantum wells are varied.

3.3 Wafer Metrology

Before proceeding with the fabrication of NRSEL devices, we first study the quality, uniformity and dimensions of the nano-ridges. We employed a combination of SEM and PL spectroscopy to evaluate the structural and optical properties of the nano-ridges across different wafers. SEM imaging was used to examine the morphology and dimensions of the nano-ridges, ensuring that they conform to the desired deisgn specifications. PL measurements provided insights into the optical quality of the material.

3.3.1 Measuring Dimensions Using SEM

In order to measure the nano-ridge dimensions, we acquired ross-sectional SEM images of the nano-ridge arrays in fields C8, C13, and C18 for all six wafers. We cleaved the wafers to expose the cross-sections and took images at multiple locations across each field to assess uniformity. This process was repeated for center and edge dies of each wafer to evaluate the uniformity across the 300 mm wafer. For some wafer, we were able to do the measurements from center to edge dies. From the cross-sectional images, we determined the nano-ridge widths and heights. The wafers were cleaved to expose the cross-sections, and the images were taken at multiple locations across each field to assess uniformity. This process was repeated for center and edge dies of each wafer to evaluate the uniformity across the 300 mm wafer.

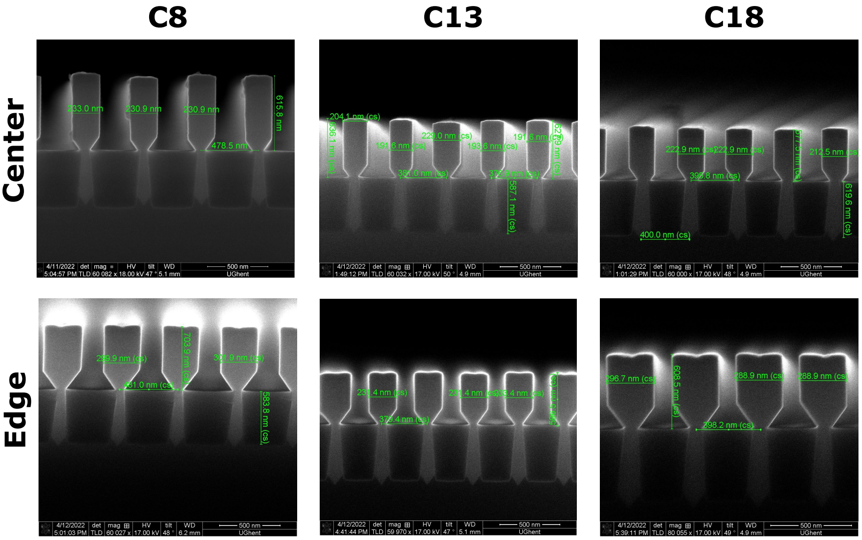

Figure 3.4: Cross-sectional SEM images of InGaAs/GaAs nano-ridge arrays in fields C8 ($\Lambda = 480\ \mathrm{nm}$*), C13 (*$\Lambda = 380\ \mathrm{nm}$*) and C18 (*$\Lambda = 400\ \mathrm{nm}$*) for wafer D03. The images show the nano-ridge dimensions for both center and edge dies of each field.*

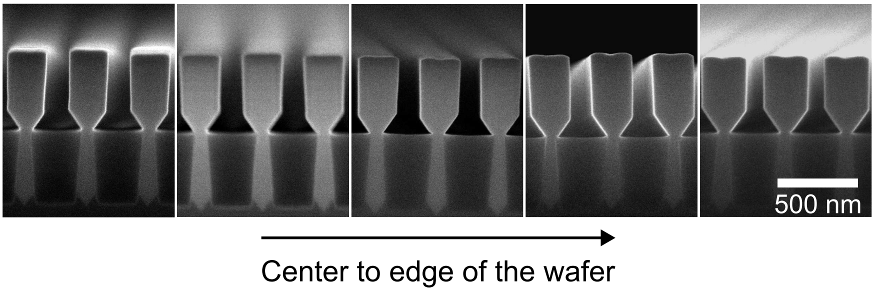

Figure 3.5: Cross-sectional SEM images of InGaAs/GaAs nano-ridge arrays in field C13 ($\Lambda = 380$ nm*) for wafer D04, showing the nano-ridge dimensions from center to edge dies. The images demonstrate the uniformity of the nano-ridge dimensions across the 300 mm wafer.*

In the center-die SEM tables, the largest-period field C8 ($\Lambda = 480$ nm) systematically yields the largest nano-ridges (widths 224–316 nm; heights 452–750 nm), while C13 ($\Lambda = 380$ nm) gives the smallest widths (187–254 nm) and intermediate heights (430–660 nm). C18 ($\Lambda = 400$ nm) falls between these two where data is available (widths 203–288 nm; heights 352–609 nm). This ordering indicates that the trench period/field choice strongly influences the effective mass transport and facet evolution during selective-area growth, providing a predictable "geometric lever" to coarse-tune the nano-ridge size before any process optimization.

Wafer-to-wafer (process) variations then shift these baselines substantially, especially in height, showing that growth conditions can outweigh mask geometry in setting the final aspect ratio. For example, wafer D02 produces markedly larger ridges in every field than the other wafers (e.g., C13: 254 nm width and 660 nm height; C8: 316 nm and 750 nm), whereas wafers D03–D07 cluster much more tightly in C13 width (187–198 nm) and show a smaller—but still meaningful—height spread (430–496 nm). The strongest wafer-to-wafer separation appears in height rather than width, suggesting that vertical growth rate (and/or the duration of the "growth-out-of-trench" regime) is more sensitive to run conditions than the lateral footprint for these structures.

Finally, die-to-die (within-wafer) non-uniformity captures how reproducible the process is across the 300 mm wafer and is most clearly seen in the center-to-edge data for D04–D07 (Fig 3.7). Some wafers show relatively stable widths across dies (e.g., D05/D06 in C13 stay near 190 nm), while others exhibit localized excursions (e.g., D04 shows a strong width increase toward one extreme die, and D07 shows a peak width at an intermediate die). Heights typically vary more than widths across dies and do not necessarily follow a simple monotonic center-to-edge trend, consistent with competing spatial effects (temperature gradients, flow/boundary-layer variations, and pattern-density/loading effects) that can change local growth rates differently across the wafer.

Wafer-to-wafer shifts usually reflect drift in global MOVPE conditions and precursor delivery (e.g., temperature calibration, pressure/total flow and thus precursor mole fractions/V/III), while die-to-die variations more often come from within-wafer transport non-uniformity (temperature/flow fields, boundary-layer effects and reactant depletion) plus pattern-density micro-loading that changes local precursor availability [6–8]

Luckily, the height has a smaller influence on the resonance frequency compared to the width as discussed earlier in chapter 2. The width has a sensitivity of around 2.3 nm/nm for the 380 nm period while the height has a sensitivity of only 0.7 nm/nm, so even with the observed height variations across the wafer, the impact on the resonance wavelength will be less significant compared to width variations. For the device demonstration wafer D03 was selected as we said earlier due to; (i) it provides nano-ridge dimensions closest to our target design in field C13 (width = 198 nm, height = 482 nm), (ii) it exhibits a big variation of the dimensions from the center to the edge, and (iii) it shows the highest PL intensity among all wafers, indicating superior optical quality as we will see in the next section.

In future work, a tight process-control strategy should be implemented to reduce both wafer-to-wafer and die-to-die variability and thereby achieve more uniform nano-ridge dimensions across the wafer. The die-averaged SEM data show that width control can already be very good on some wafers, with D05 and D06 exhibiting relatively small die-to-die width spreads (D05: 189–194 nm, mean $\approx$ 191 nm with $\sigma \approx 3$ nm; D06: 186–196 nm, mean $\approx$ 190 nm with $\sigma \approx 4$ nm). The measured dimensions for the center dies for each wafer are summarized in tables 3.2 and 3.3.

Another approach is to control nano-ridge uniformity by lithographically defining the ridge width with an oxide template: a narrow trench seeds the ridge, while a wider oxide opening above it caps lateral expansion. During epitaxy the ridge grows until it meets the oxide sidewalls, which then act as a geometrical stop that stabilizes the final ridge width and suppresses further sidewall growth, as shown in figure 3.6. This template-limited, self-stopping width control has already been demonstrated for nano-ridge HBT structures, where the oxide boundary is used to lock in the ridge width for reproducible transistor geometry across a 300 mm wafer [9]. It remains to be seen if this process maintains the optical quality of the material.

	D02	D03	D04	D05	D06	D07
C8 (Λ) = 480 nm	316	227	277	232	224	224
C13 (Λ) = 380 nm	254	198	236	189	193	187
C18 (Λ) = 400 nm	288	216	-	209	210	203

Table 3.2: Measured nano-ridge widths (in nm) from SEM images for the center dies of the different wafers.

	D02	D03	D04	D05	D06	D07
C8 (Λ) = 480 nm	750	452	611	576	527	556
C13 (Λ) = 380 nm	660	482	496	439	430	449
C18 (Λ) = 400 nm	609	434	-	395	352	391

Table 3.3: Measured nano-ridge Heights (in nm) from SEM images for the center dies of the different wafers.

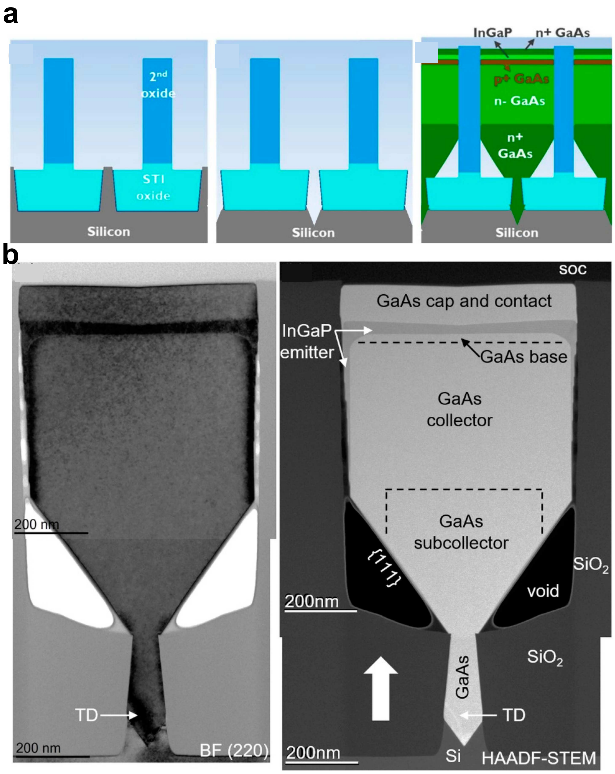

Figure 3.6: (a) Schematic of the double trench-patterned oxide template (left) after opening the wide trench in the second oxide, (center) after silicon recess etch to create a 111-faceted V-groove at the bottom of the narrow trench and (right) after epitaxial deposition of a HBT layer stack. (b)Cross-section (stitched) TEM images of a HBT layer stack viewed under (left) two-beam BF (220) and (right) HAADF-STEM conditions with all device layers indicated. (reproduced from [9])

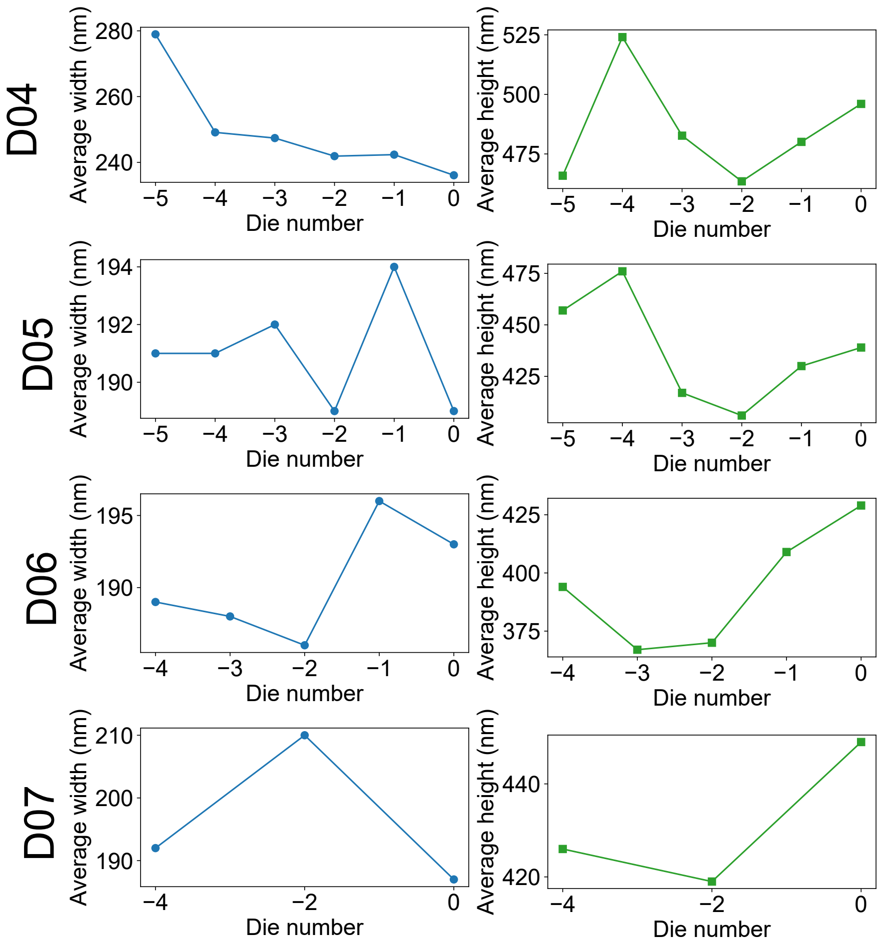

Figure 3.7: Cross-sectional SEM images of InGaAs/GaAs nano-ridge arrays in field C13 ($\Lambda = 380$ nm) for wafers D04, D05, D06 and D07.

3.3.2 PL Characterization Using CW Excitation

Room-temperature PL measurements were performed on all six wafers to evaluate the optical quality of the nano-ridges. A continuous-wave (CW) laser with a wavelength of 532 nm was used to excite the nano-ridges, and the emitted PL signal was collected and analyzed using a spectrometer. The measurements were conducted at multiple locations across each field to assess uniformity. The PL spectra for the center dies of each wafer in field C13 are shown in figure 3.8.

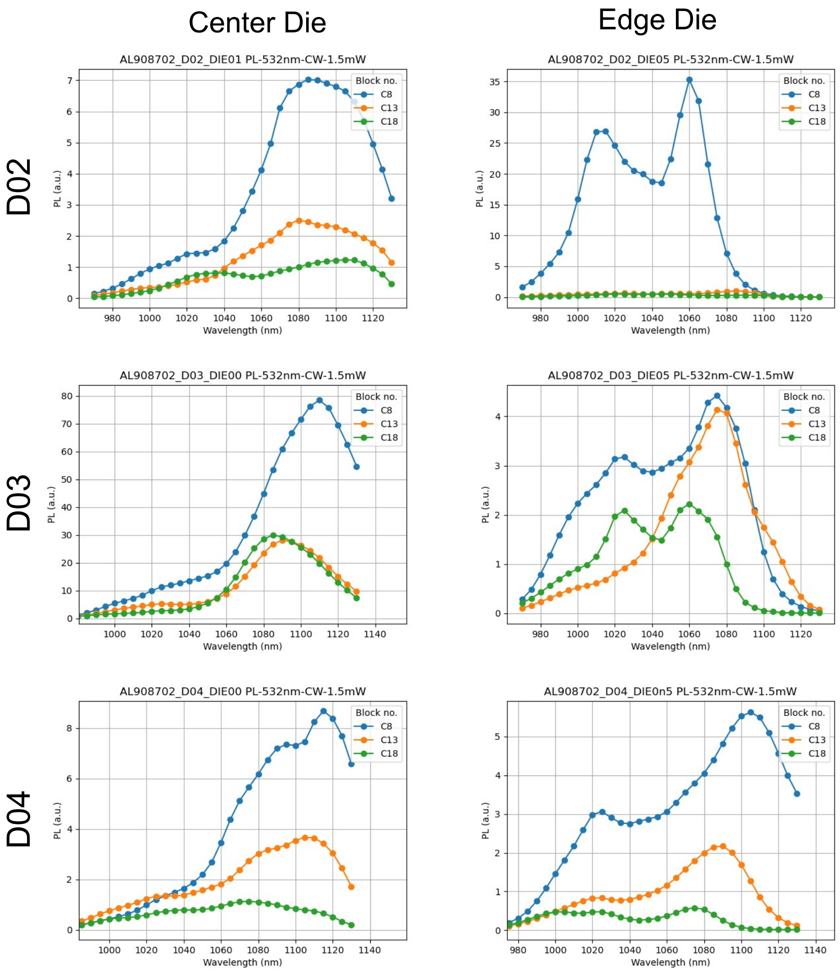

Figure 3.8: Room-temperature PL spectra for the center dies of wafers D02 to D04 in fields: C8 ($\Lambda = 480$ nm*), C13 (*$\Lambda = 380$ nm*) and C18 (*$\Lambda = 400$ nm*). The spectra show the peak emission wavelength and intensity for each wafer, with wafer D03 exhibiting the highest peak intensity.*

The peak wavelength is around 1100 nm for all samples, although the indium content and quantum well thickness are different for each wafer. This is due to the strong dispersion from the grating (periodic structure) dominating the spectral response as discussed earlier. More on the experimental dispersion and band diagram measurements are discussed later in chapter 5. From the PL measurements, we observed that wafer D03 exhibited the highest PL intensity among all wafers, indicating superior optical quality. Additionally, the edge die for wafer D03 shows a relatively stronger PL signal for all fields, making it a promising candidate for fabricating our devices.

3.3.3 PL characterization Using Pulsed Excitation

Based on the combined SEM and PL results, we selected wafer D03 for the fabrication of NRSEL devices. This wafer demonstrated optimal nano-ridge dimensions and superior optical quality, making it the most suitable choice for our intended applications. Detailed results from the pulsed PL measurements on wafer D03 will be discussed in chapter 4 when we present the lasing results from the fabricated NRSEL devices.

3.4 NRSEL Definition

3.4.1 Optical Lithography Mask Design

Now that we picked the optimal wafer, we can proceed to fabricate NRSEL devices. To define localized NRSEL devices, we designed an optical lithography mask that allows to pattern both the NRSEL cavities and their side mirrors in a two-step process. The mask includes arrays of NRSEL devices with varying cavity widths (W_{NRSEL}) and heights (H_{NRSEL}) to study their influence on the lasing characteristics. The side mirrors are formed by filling the space between the nano-ridges with a low refractive index material, creating a high refractive index contrast that provides strong optical feedback. The design of the mask is illustrated in 3.9.

The lithography mask for the NRSEL fabrication was designed to cover fields C13 and C18 on the Tower35 mask, which have trench periods of 380 nm and 400 nm, respectively. Five different designs were created (see Figure 3.9). Each design consists of arrays of NRSEL devices with varying cavity widths (W_{NRSEL}) and heights (H_{NRSEL}). Some designs contain repeated NRSEL cavities of the same dimensions and side mirrors formed by filling the space between the nano-ridges with a low-refractive-index material. To cover both diagonal fields we placed 2×2 copies of each design so they span C13 (380 nm) and C18 (400 nm).

Because there were no sufficiently large optical alignment marks on the wafer, we added a dedicated alignment frame around fields C13 and C18 and used the frame corners as reliable references for overlay. In addition, markers for aligning the mirror mask were defined during the ICP etch step used to form the NRSEL cavities. For experiments reported here we focused on the first design, which was replicated 25 times (a 5×5 array) across the wafer to increase the chance of finding functioning devices despite process non-uniformity. In this design (1), a parameter sweep is included: the cavity width varies from $15\,\mu\mathrm{m}$ to $60\,\mu\mathrm{m}$ and the cavity height from $5\,\mu\mathrm{m}$ to $95\,\mu\mathrm{m}$.

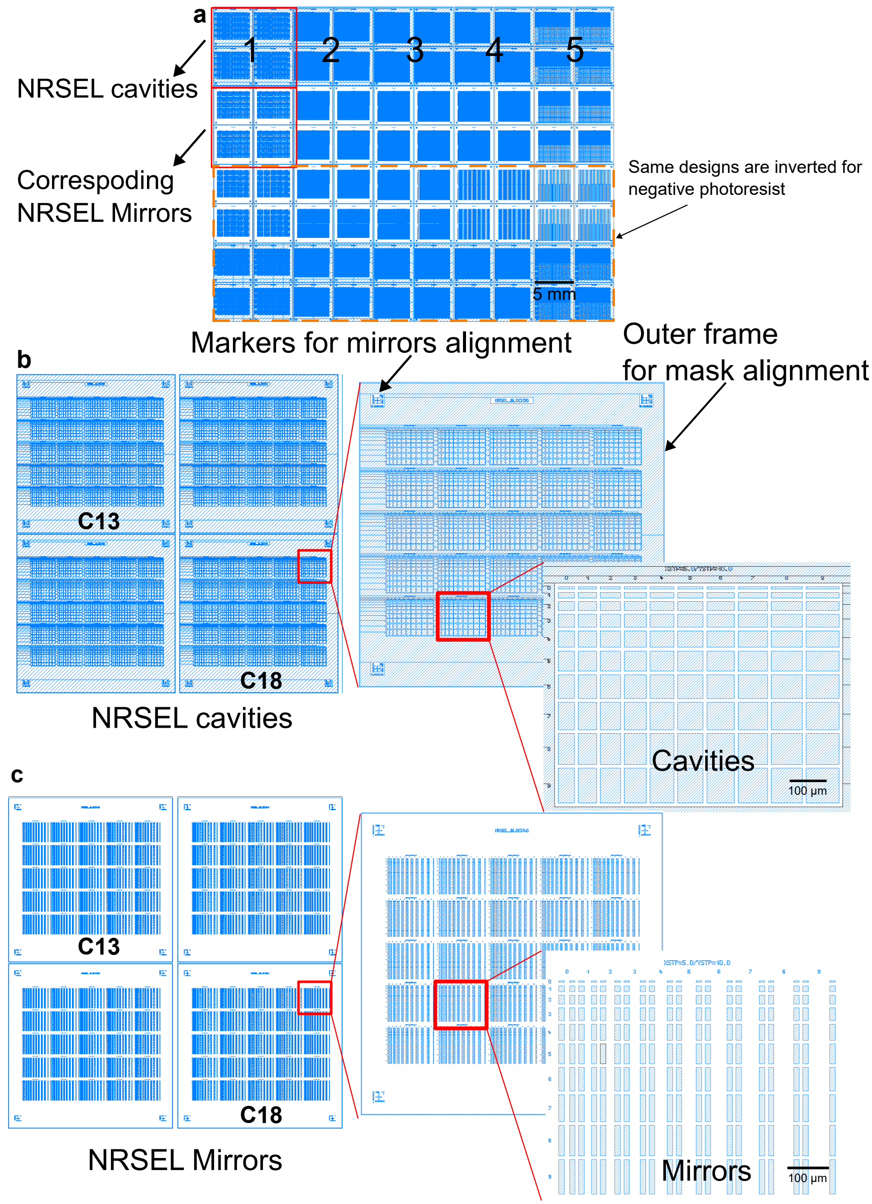

Figure 3.9: Optical lithography mask design for NRSEL fabrication. (a) GDS layout of the whole lithography mask. it consists of 5 different designs each spanning 4 fields to cover C13 and C18 (diagonal fields). for each design there's a corresponding mirror mask that aligns via the markers defined in ICP at the same time as the cavities. The lower half of the mask is the same design inverted for negative photoresist. (b) A zoom in on design 1: it includes arrays of NRSEL devices with varying cavity widths (W_{NRSEL}) and heights (H_{NRSEL}), as well as side mirrors formed by filling the space between the nano-ridges with a low refractive index material (c).

3.4.2 NRSEL Fabrication Process

The goal is to define localized nano-ridge surface-emitting lasers (NRSELs) with controlled dimensions. To simplify the process and as a proof-of-principle, we used photoresist (AZ 5214, $n \approx 1.6$) instead of SiO2 to form the mirrors. Arrays of NRSEL cavities were patterned in AZ5214 by optical lithography, followed by selective removal of the surrounding nano-ridge material using a SiCl4/N2 ICP-RIE step. Mirrors were then formed by spin-coating AZ5214 and patterning it to fill the inter-ridge gaps. For the reported design the mirror width was kept at 15 μm, the cavity width W_{NRSEL} was varied from 15–40 μm and the cavity height H_{NRSEL} from 5–45 μm, as shown in Figure 3.9.

Figure 3.10 summarizes the intended flow and device geometry. AZ 5214 is not the usual mask choice for ICP etching. In early trials the resist did not survive the etching process and was burned. After some process optimizations (RF power reduction), we managed to etch without damage to the resist (Figure 3.11). Although the etching was a success, incomplete resist removal after ICP was observed (Figure 3.12a–b); an optimized heated solvent (AZ100 at 80°C) improved development and revealed the patterned cavities (Figure 3.12c–d). Successful definitions are confirmed by SEM and FIB cross-sections (Figure 3.13a–b), and the false-coloured cross-section and optical image demonstrate effective photoresist infill ($\approx$ 900 nm) forming the low-index mirrors (Figure 3.13c–d). The final microscope overview is shown in Figure 3.14. More infrmation about the fabrication process can be found in appendix A.

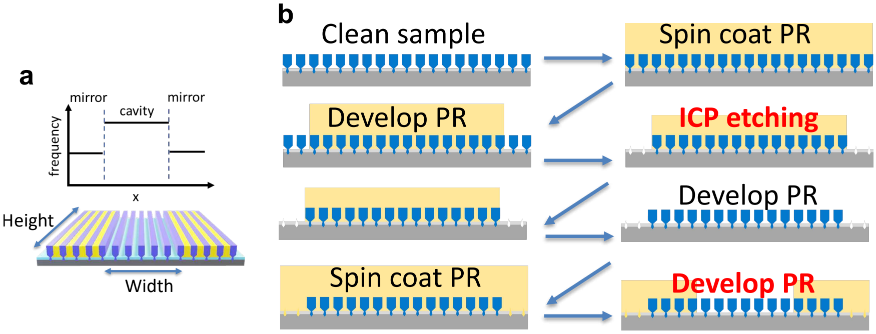

Figure 3.10: Fabrication steps. (a) Schematic illustration of the NRSEL. (b) Schematic illustration of the NRSEL fabrication process, including photoresist patterning to define the NRSEL devices, ICP RIE etching to remove the nano-ridge material outside the NRSELs, and photoresist spin coating and patterning to define the side mirrors.

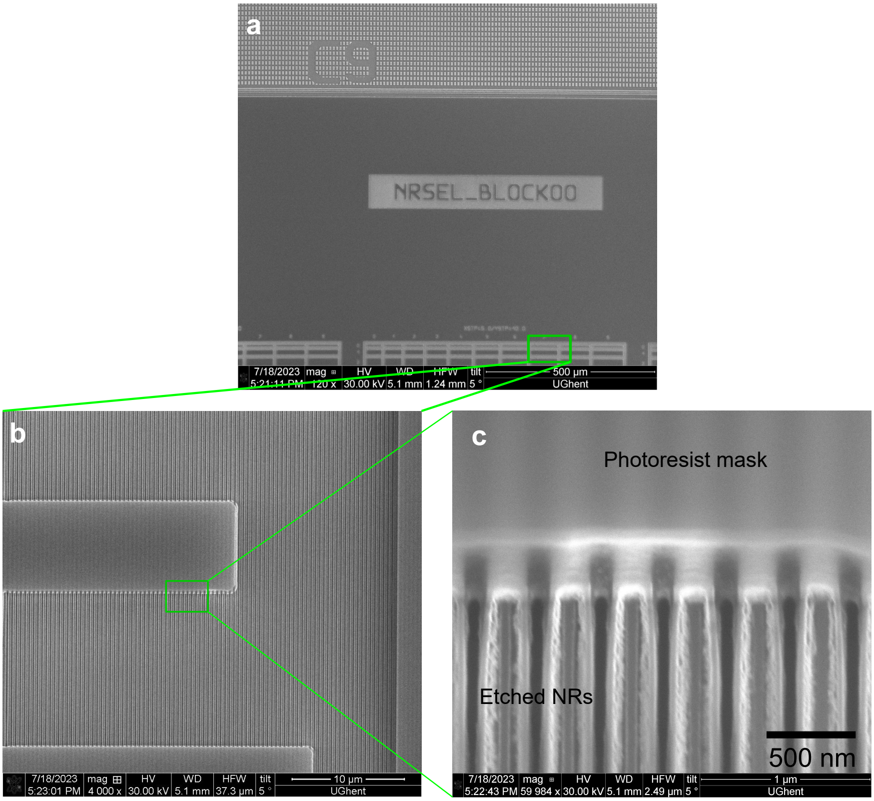

Figure 3.11: (a,b) SEM image showing the definition of the NRSEL array after ICP etching of the nano-ridge material using SiCl4/N2 chemistry. The photoresist mask remains intact after etching, indicating successful process optimization. (c) SEM of a single NRSEL cavity after ICP etching, showing the successful removal of the nano-ridge material outside the NRSEL cavity while preserving the integrity of the photoresist mask.

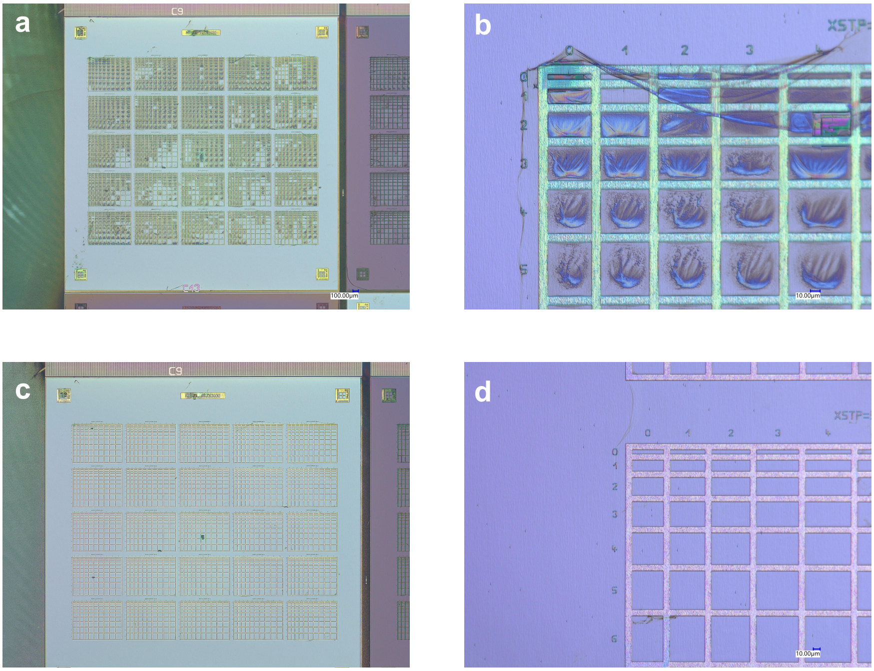

Figure 3.12: (a,b) Microscope image of NRSEL fabrication, showing incomplete removal of the photoresist after ICP etching and development in acetone. (c,d) Microscope image of the same sample, Using AZ100 at 80° C for 10 mins the resist was almost removed completely, revealing the well-defined NRSEL cavities.

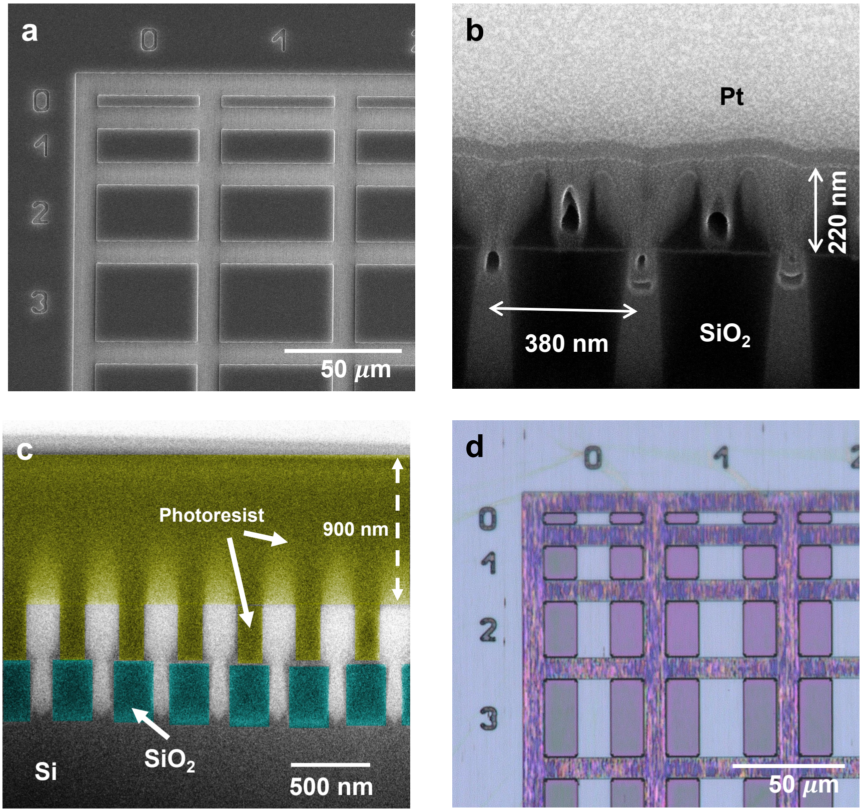

Figure 3.13: (a) SEM image showing definition of the NRSEL array after successful etching of the nano-ridge material using ICP. (b) FIB cross-section image of a single NRSEL cavity after ICP etching, showing the successful removal of the nano-ridge material outside the NRSEL cavity. (c) False coloured cross-section SEM image after defining the side mirrors using photoresist, showing successful infilling and coverage with a height of 900 nm on top of the nano-ridges. (d) Optical image after NRSEL definition and development of the side mirrors

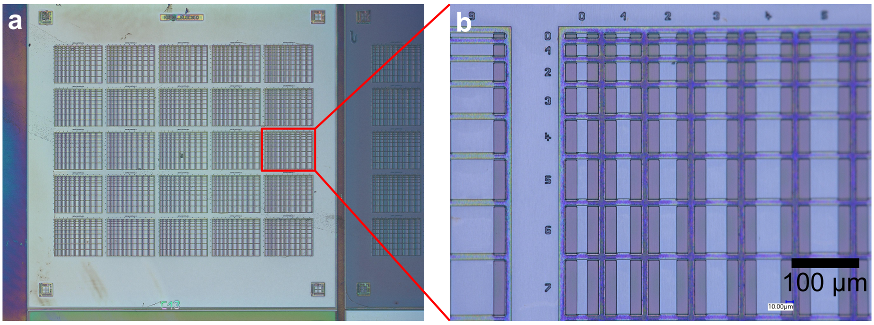

Figure 3.14: Microscope image of the final fabricated NRSEL devices, showing arrays of NRSELs with varying cavity widths and heights. The well-defined NRSEL cavities and side mirrors are clearly visible.

3.5 Summary

This chapter describes the metrology and fabrication route used to realize nano-ridge surface-emitting lasers (NRSELs) on 300 mm patterned silicon. InGaAs/GaAs nano-ridge arrays were grown by NRE, combining selective-area growth in narrow trenches (to confine relaxation defects via aspect-ratio trapping) with shape engineering after growth-out-of-trench to obtain box-like ridges that act as a 1D photonic crystal. Six wafers (D02–D07) were produced under different growth conditions, while the Tower35 pattern provided multiple trench periods and widths to tune the nano-ridge geometry. Guided by the analytical design rules and FDTD results, the work focused on fields close to the targeted photonic period—especially C13 ($\Lambda = 380$ nm), which shows the lowest resonance sensitivity to nano-ridge width variations and is therefore the most robust to fabrication tolerances.

Cross-sectional SEM and PL metrology measurements was then used to quantify nano-ridge dimensions, assess across-wafer uniformity, and compare optical material quality among wafers and fields. Cross-sectional SEM established how both mask period and wafer-to-wafer process variations impact ridge width/height, while room-temperature PL revealed that the spectral response is strongly influenced by the grating dispersion, with wafer D03 providing the highest intensity and suitable dimensions for device processing. Based on these results, D03 was selected for NRSEL fabrication, and an optical lithography mask was designed to define cavity and mirror regions (covering C13 and C18) with a parameter sweep in cavity width and height, including an added alignment frame and overlay markers. NRSELs were realized by patterning AZ5214 photoresist, using $SiCl_4/N_2$ ICP-RIE to remove nano-ridges outside the cavities, and then forming low-index side mirrors by photoresist infill; process optimizations (notably reduced RF power and improved resist stripping using heated AZ100) enabled clean cavity definition and successful mirror formation confirmed by microscopy, SEM, and FIB cross-sections. The successful fabrication of NRSEL devices was confirmed through SEM and FIB cross-sectional imaging. In the next chapter, we will present the lasing results from the fabricated NRSEL devices and discuss their performance characteristics.

Bibliography

[1] B. Kunert, W. Guo, Y. Mols, B. Tian, Z. Wang, Y. Shi, D. Van Thourhout, M. Pantouvaki, J. Van Campenhout, R. Langer, and K. Barla, “III/V nano ridge structures for optical applications on patterned 300 mm silicon substrate,” *Applied Physics Letters*, vol. 109, no. 9, p. 091101, 2016.

[2] B. Kunert, W. Guo, Y. Mols, R. Langer, and K. Barla, “(Invited) Integration of III/V Hetero-Structures By Selective Area Growth on Si for Nano- and Optoelectronics,” *ECS Transactions*, vol. 75, no. 8, p. 409, 2016.

[3] Y. Shi, Z. Wang, J. V. Campenhout, M. Pantouvaki, W. Guo, B. Kunert, and D. V. Thourhout, “Optical pumped InGaAs/GaAs nano-ridge laser epitaxially grown on a standard 300-mm Si wafer,” *Optica*, vol. 4, no. 12, pp. 1468–1473, 2017.

[4] D. Colucci, M. Baryshnikova, Y. Shi, Y. Mols, M. Muneeb, Y. D. Koninck, D. Yudistira, M. Pantouvaki, J. V. Campenhout, R. Langer, D. V. Thourhout, and B. Kunert, “Unique design approach to realize an O-band laser monolithically integrated on 300 mm Si substrate by nano-ridge engineering,” *Opt. Express*, vol. 30, no. 8, pp. 13 510–13 521, 2022.

[5] Shi, Yuting, “GaAs nano-ridge lasers epitaxially grown on silicon,” Ph.D. dissertation, Ghent University, 2020.

[6] M. A. Tischler, “Advances in metalorganic vapor-phase epitaxy,” *IBM Journal of Research and Development*, vol. 34, no. 6, pp. 828–848, 1990. [Online]. Available: http://ieeexplore.ieee.org/lpdocs/epic03/wrapper.htm?arnumber=5389787

[7] D. Koleske, R. M. Biefeld, and J. G. Cederberg, “The science and practice of metal-organic vapor phase epitaxy (movpe).” Sandia National Laboratories (SNL-NM), Albuquerque, NM (United States), 06 2014. [Online]. Available: https://www.osti.gov/biblio/1714519

[8] J. Li, P. Brabant, D. Hannan, T. Vasen, S. Afroz, K. Nagamatsu, J. Chang, P. Shea, D. Lawson, and R. Howell, “Ultra-low resistance n+GaN contacts for GaN HEMT applications using MOCVD selective area epitaxy in N2 carrier gas,” *AIP Advances*, vol. 12, no. 3, p. 035201, 2022. [Online]. Available: https://pubs.aip.org/adv/article/12/3/035201/2819406/Ultra-low-resistance-n-GaN-contacts-for-GaN-HEMT

[9] Y. Mols, A. Vais, S. Yadav, L. Witters, K. Vondkar, R. Alcotte, M. Baryshnikova, G. Boccardi, N. Waldron, B. Parvais, N. Collaert, R. Langer,

and B. Kunert, “Monolithic integration of nano-ridge engineered ingap/gaas hbts on 300 mm si substrate,” *Materials*, vol. 14, no. 5682, 2021. [Online]. Available: https://www.mdpi.com/1996-1944/14/19/5682

4

Laser Characterization

4.1 Introduction **91**
4.2 Laser Characterization **93**
    4.2.1 Lasing from Quasi-Infinite Arrays 93
    4.2.2 Lasing from Micro NRSELs 95
4.3 Farfield Imaging **101**
4.4 Summary **105**
Bibliography **106**

4.1 Introduction

The fabricated samples were measured using micro-photoluminescence (μPL) spectroscopy (figure 4.1 at room temperature with a 532-nm nanosecond pulsed Nd:YAG laser as the pump source [1]. The laser was focused into a 300 μm diameter spot using a microscope objective with NA = 0.65. The emission from the devices was collected through the same microscope objective with the help of a dichroic mirror, and detected with a spectrometer (KYMERA-328I-D2-SIL, Oxford instruments, Andor) that has two sensors attached: a water-cooled InGaAs detector (iDus,

---

[1] The results in this chapter were (partly) published in [1].

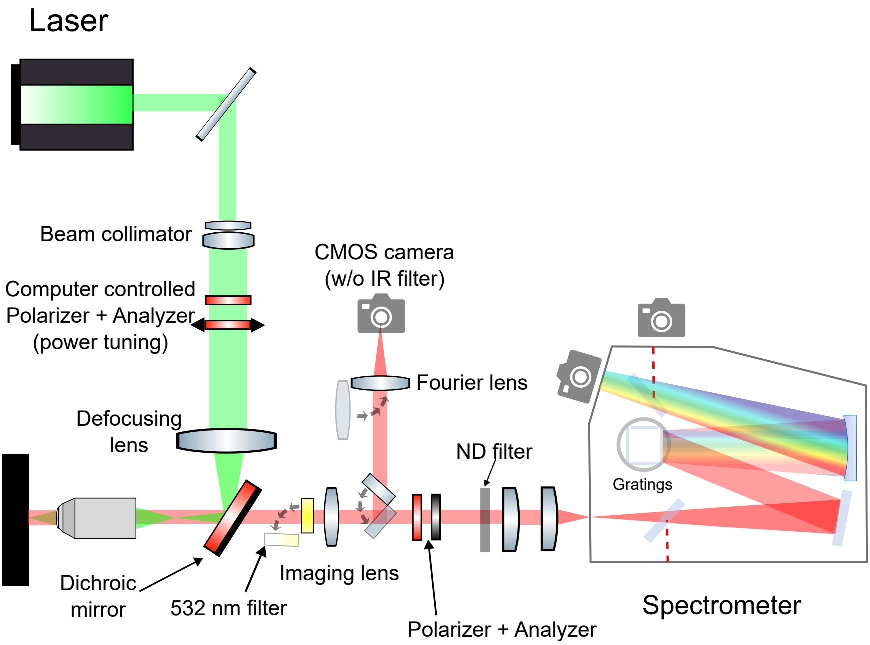

Figure 4.1: Schematic of the micro-photoluminescence (μPL) setup used for characterizing the NRSEL devices. The pump laser (Nd:YAG, 532 nm, 7 ns pulse width, 10 kHz repetition rate) is focused onto the sample using a microscope objective (MO) with NA = 0.65. The emitted light is collected through the same MO and directed to a spectrometer (KYMERA-328I-D2-SIL, Oxford instruments, Andor) using a dichroic mirror (DM). A long-pass filter (LPF) is used to block any residual pump light before detection. The spectrometer is equipped with two detectors: a water-cooled InGaAs detector for near-infrared measurements and a visible range CCD sensor for shorter wavelengths.

DU490A-1.7 Model, Oxford Instruments, Andor) and a visible range CCD sensor (iDus 401, DU401A). First, we characterized a NRSEL device of width W_{NRSEL} = 20 μm and height H_{NRSEL} = 15 μm in detail, measuring its PL spectra under different pumping conditions, from which we determined its threshold pump density and its linewidth. Then, 31 devices with varying cavity widths were characterized to explore the effect of cavity width on the lasing threshold and to compare the results with the simulated Q-factors presented earlier. Finally, a NRSEL device of width W_{NRSEL} = 35 μm and an unpatterned region, which can be considered as a quasi-infinite array of nano-ridges, were further investigated using back focal plane (BFP) imaging, a technique also known as fourier plane imaging.

4.2 Laser Characterization

4.2.1 Lasing from Quasi-Infinite Arrays

To begin, we investigated the lasing spectrum of a quasi-infinite array of nano-ridges, which can be considered as a large area of unpatterned nano-ridges without any cavity mirrors. An array of period $\Lambda = 380$ nm was optically pumped at different pump powers (figure 4.2). The pump laser was focused into a pump spot with a diameter of 300 μm. As shown in figure 4.3, upon reaching a pump power density of 10 kW/cm^2, a sharp peak appears at 986 nm, corresponding to the BIC TE_{21L} mode of interest. The lasing threshold is determined by finding the intersection point between the linear fit of the integrated PL signal and the lower axis (pump power). Using an additional lens to image the back-focal plane of the microscope objective onto a camera[2–5], we captured the far-field emission pattern of the quasi-infinite array above the lasing threshold (figure 4.2b). The emission exhibits a narrow angular divergence of approximately 6.5°. More details on the far-field imaging and the explanation for the farfield pattern are provided later in the section 4.3.

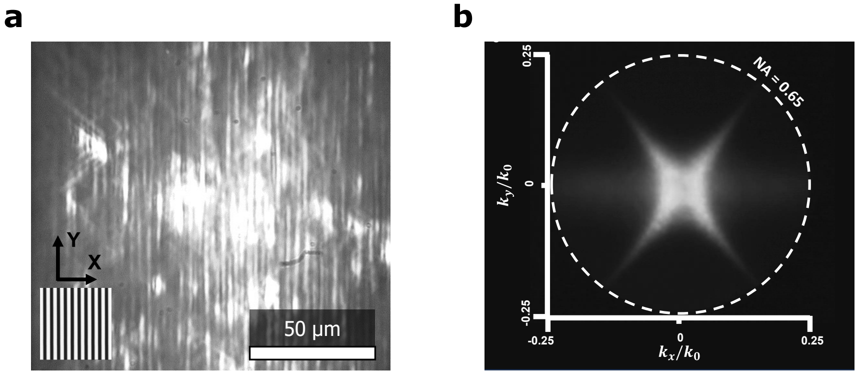

Microscope image

Farfield image

Figure 4.2: a) Microscope image of the quasi-infinite array of nano-ridges under optical pumping above the lasing threshold. The pump spot diameter is 300 μm. b) Back focal plane image of the quasi-infinite array above the lasing threshold, showing an angular divergence of approximately 6.5°.

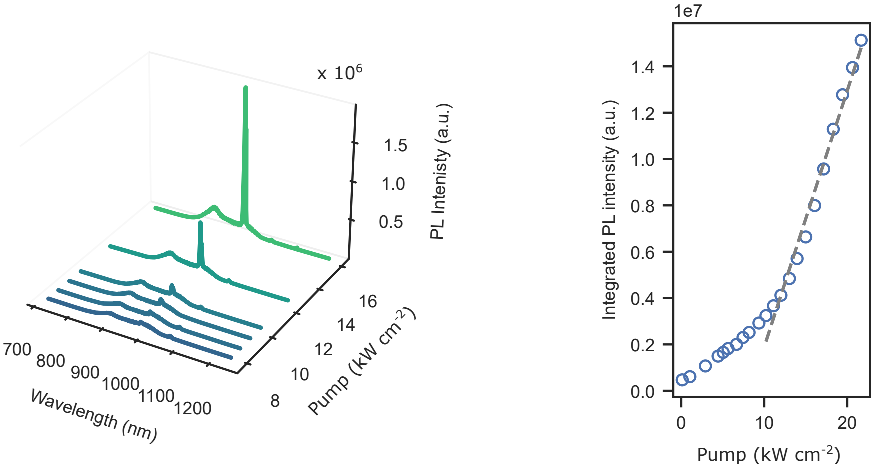

Figure 4.3: Lasing spectrum of a quasi-infinite array of period $\Lambda = 380$ nm, *pumped with a spot size of 300* μ*m diameter at different pump power densities. Above the lasing threshold a narrow lasing peak appears at 984 nm. b) Integrated PL intensity showing a lasing threshold around 10 kW cm*$^{-2}$.

Effect of Nano-ridge Width on Lasing

To study the effect of the nano-ridge width on the lasing wavelength, we measured the lasing spectra from different locations on a quasi-infinite array sample. The results are shown in figure 4.4. The measurements reveal a clear decrease in the lasing wavelength as we move from the edge to the center of the field (C13 $\Lambda = 380nm$). This shift is attributed to the variation in the nano-ridge width across the field, which shifts the photonic band structure and consequently the lasing wavelength. The observed trend is consistent with our earlier simulations, which predicted that increasing the nano-ridge width leads to a an increase in the wavelength of the resonant mode.Separate SEM measurements confirmed that the nano-ridge width varies from approximately 225 nm at the edge to 215 nm at the center of the field, confirming the correlation between width variation and lasing wavelength shift and the lasing threshold variation.

The decrease in width from edge to center is also reflected in the lasing threshold, which increases from approximately 5 kW/cm^2 at the edge to around 10 kW/cm^2 at the center (figure 4.4). This finding highlights the importance of precise control over nano-ridge dimensions during fabrication to achieve desired lasing characteristics.

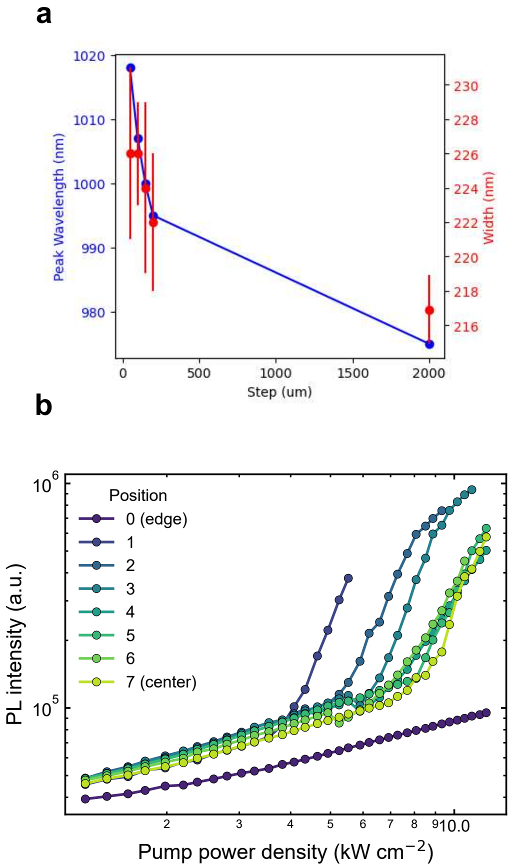

Figure 4.4: (a) Measured lasing wavelength at different locations on the quasi-infinite array sample, showing a red-shift as we move from the center to the edge of the wafer. (b) The threshold pump power density for lasing at different locations in the sample. As we move from the edge to the center, the threshold decreases.

4.2.2 Lasing from Micro NRSELs

We measured lasing threshold versus cavity width for 31 devices within the same sample. Figure 4.5a shows the measured spectra under various pumping conditions for an NRSEL with W_{NRSEL} = 20 μm. At low pump intensities, a broad spontaneous emission spectrum is observed. When increasing the pump power, a lasing peak emerges (λ = 984 nm). Figure 4.5b, shows the measured linewidth and the integrated PL intensity around the lasing peak as function of the pump power. The lasing threshold is calculated by taking the intersection point between the fit of the linear region of the integrated PL signal and the lower axis (pump power). For this device, the threshold pump density is 10.8 kW/cm^2. The narrowest linewidth is obtained just above threshold and is measured to be 0.9 nm. We believe the linewidth to be limited by the pulsed optical pumping.

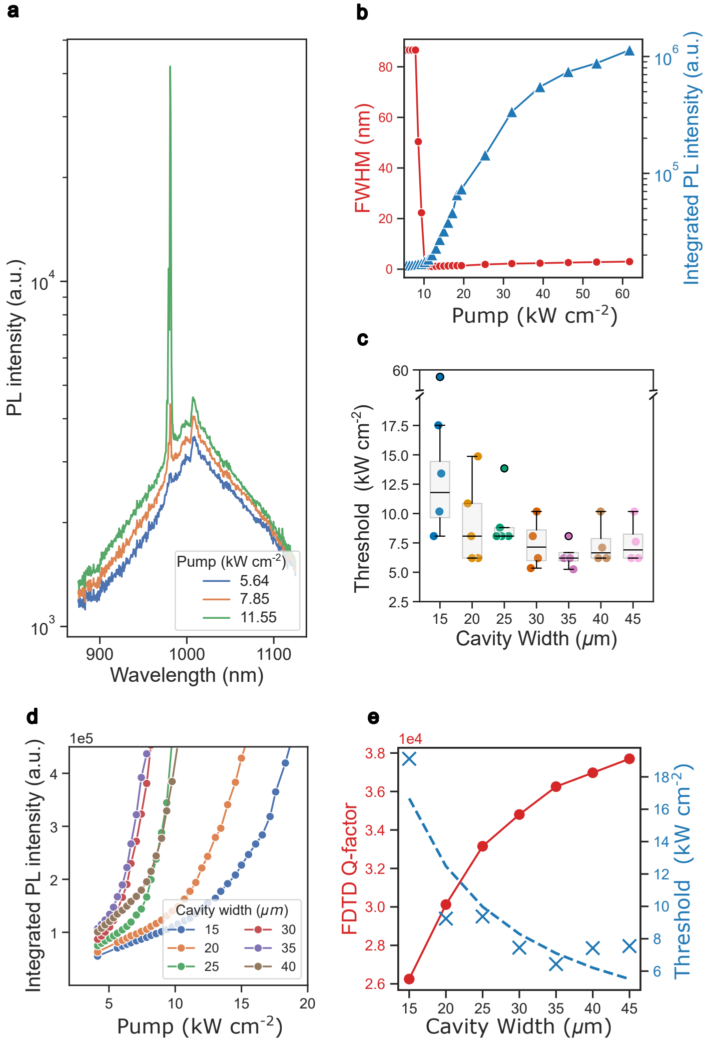

Figure 4.5: Room-temperature optical characterization. (a) PL spectra of a NRSEL with $W_{NRSEL} = 20\,\mu\mathrm{m}$ *for different pump intensities. (b) Integrated PL and linewidth for a NRSEL with* $W_{NRSEL} = 20\,\mu\mathrm{m}$ *as a function of pump power. The linewidth reaches a minimum of 0.9 nm at threshold. (c) Measured lasing threshold versus cavity width for 31 devices within the same sample. Individual scatter points represent the threshold of each device, while the overlaid box plots summarize the statistical distribution of thresholds for each cavity width. The solid black line in each box represents the median value of the data. (d) Zoom-in on the integrated PL for a group of six NRSELs with different widths, showing the reduction of the threshold with increasing cavity width. (e) The threshold data is fitted using a reciprocal function,* $a/W_{NRSEL} + b$*. Scatter points (blue) represent the mean threshold values, and the calculated Q-factor (red) is plotted for comparison.*

Figure 4.11a shows a microscope image of the NRSEL with W_{NRSEL} = 20 μm under optical pumping above the lasing threshold. The pump light is filtered out using a dichroic mirror. Note that the pump spot is much larger than the cavity size. The picture shows clear confinement of the optical mode within the central cavity as defined by the photoresist mirrors, indicating successful fabrication. The emission is highly polarized, with the electric field aligned within 20° of the nano-ridge axis.

We characterised the polarization of an NRSEL with W_{NRSEL} = 20 μm by passing the emitted light through a polarization analyser and recording the intensity while it was rotated over a range of angles (typically) from 0° (analyser is perpendicular to the nano-ridge) to 180°. The results are shown in figure 4.6 together with a fitted curve. This shows the device is strongly polarized, with the electrical field mostly aligned with the nano-ridges. The difficulty in perfectly aligning both the sample and the analyser, combined with the fact that the field is not strictly TE-polarized, results in a significant shift of the peak from 90°.

This confirms the mode is traveling perpendicular to the nano-ridges and does not simply originate from reflections at the top and bottom facets of the nano-ridge. For this device, also localised light emission from the mirror region can be seen. This emission appears at higher pump powers and is not expected, as the mirror regions have a lower index contrast and a smaller width compared to the central cavity, which should lead to higher losses and a lower Q-factor. This effect is not observed for all cavities: e.g. for the device with W_{NRSEL} = 25 μm, shown in figure 4.11b, only emission from the central cavity is observed. Therefore, we believe it is associated with variations in the nano-ridge's dimensions and imperfections that can lead to the localization of light emission in some parts of the array. The nature of this emission and the associated slow bloch mode (SBM) will be discussed in more detail below.

To evaluate the effect of the cavity width on the devices' lasing threshold, we compared a group of devices with W_{NRSEL} varying from 15 to 45 μm. Figure 4.5d shows the associated light-in vs. light-out curves for a group of six devices and figure 4.5c shows how the threshold pump density varies with the cavity width for all the measured devices. In total 31 devices were measured. The experimental data reveals an inverse relationship: as the cavity width increases from 15 to 35 μm, there is a sharp reduction in the threshold (up to a 63$\%$ drop). Beyond 35 μm, however, the trend reverses slightly: the lasing thresholds increase by approximately 14$\%$. This inflection appears to coincide with a regime where the simulated Q-factor—although still rising from about 36,300 to 37,700 as shown in figure 4.5e, starts to saturate. In this regime, further widening of the cavity yields only marginal improvements in the Q-factor (roughly an additional 4$\%$). The saturation of the threshold might indicate the influence of random disorder effects, as longer cavity PhC lasers tend to suffer higher losses (often referred to as slow-light induced losses[6]) when operating near the band-edge. Notably, the minimum lasing threshold was found for devices with a 35 μm cavity, which also exhibited the smallest spread in threshold values, suggesting that the optimal cavity dimension minimizes the impact of fabrication-induced disorder. The spread in threshold for devices of the same cavity size can be attributed to disorder and slight changes in dimensions. Overall, while increasing the cavity width leads to lower lasing thresholds due to improved Q-factors, the practical realization of these benefits is highly sensitive to fabrication tolerances and disorder.

To unambiguously match the peaks visible in the laser spectrum with the modes found in the simulated band-diagram, the NRSEL with W_{NRSEL} = 20 μm was characterised again, now using the visible range CCD sensor to be able to measure wavelengths shorter than 900 nm. The result is shown in figure 4.7. As discussed above, this device shows emission from both the mirror region and the cavity region (see figure 4.11a) and the spectra shown here include light from both regions. With increasing pump power, first a peak at 985 nm starts to appear, then a second one at 1010 nm, and lastly a third one around 890 nm. In figure 4.7b and c, these experimental results are compared with FDTD simulations of the band diagram for nano-ridge arrays with and without photoresist. Figure 4.7b shows the measured spectrum at high pump power (62.4 kW/cm^2) and figure 4.7c shows the wavelength of the TE_{21L}, TE_{22L} and TE_{23L} modes, at the Γ point. The first peak in the lasing spectrum, at 985 nm, matches the TE_{21L} mode of the array without PR. The calculated Q-factor of this mode is 26053 (for a cavity size of 40 nano-ridges with mirrors). The second peak, at 1010 nm, matches the TE_{21L} mode for a nano-ridge array with photoresist. Using a diaphragm, we could indeed associate this mode in the spectrum with emission coming from the photoresist region. Given this mode's lower Q-factor (9200) it shows up at higher pump powers. The third peak (890 nm) matches the higher order TE22L mode. This mode has a relatively low Q-factor of 4056. Additionally, its wavelength lies outside the quantum well gain region. Therefore, we suspect that the gain experienced by this mode originates from the GaAs nano-ridge itself. Note that the small deviation between the measured and simulated wavelengths can be explained by small deviations in the nano-ridge dimensions or values of the refractive index. Measuring the band diagram experimentally would provide a more concrete proof of the mode identification but it requires more advanced techniques such as angle-resolved spectroscopy[7, 8]. We carried out extensive angle resolved experiments in chapter 5.

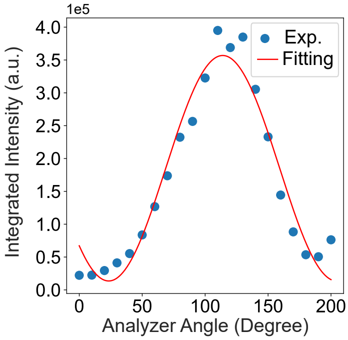

Figure 4.6: Polarization characterization of an NRSEL with $W_{NRSEL} = 20\,\mu\mathrm{m}$*. The emitted light passes through a polarization analyser, and the intensity is recorded while rotating the analyser over a range of angles from 0°* *(analyser is perpendicular to the nano-ridge) to 180°. The fitted curve indicates strong polarization, with the electric field mostly aligned with the nano-ridges.*

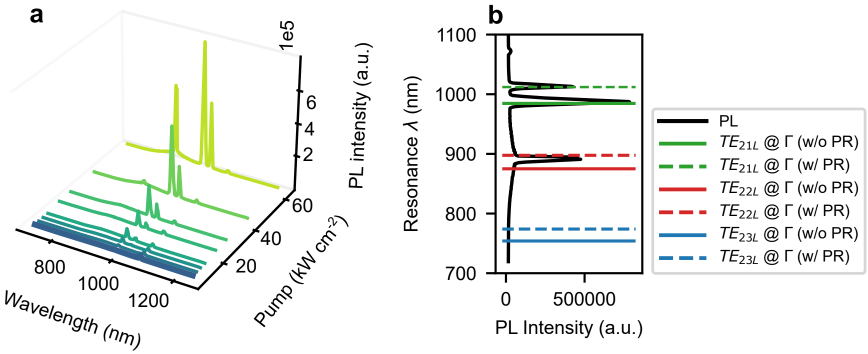

Figure 4.7: Mode identification for an NRSEL with W_{NRSEL} *= 20 µm. (a) PL spectra for increasing pump power. For the highest pump power, three distinct peaks are visible. (b) Comparison between the experimental PL spectrum taken at 62.4* kW/cm^2 *pump power density and the calculated wavelengths of the* TE_{21L}*,* TE_{22L} *and* TE_{23L} *modes, at the* Γ *point in the band diagrams for a nano-ridge array without photoresist and with photoresist. (c) Simulated band diagrams for nano-ridge arrays with and without photoresist.*

We also managed to measure lasing from devices with shorter nano-ridge lengths (5 μm), as shown in figure 4.8. However, these devices exhibited inconsistent lasing behaviour This is likely due to fabrication imperfections having a more pronounced effect on the Q-factor in shorter cavities. Further optimization of the fabrication process is needed to achieve reliable lasing in these smaller devices. The minimum lasing threshold observed in these devices was 6 kW/cm^2, which is around the same as the longer devices of the same cavity widths.

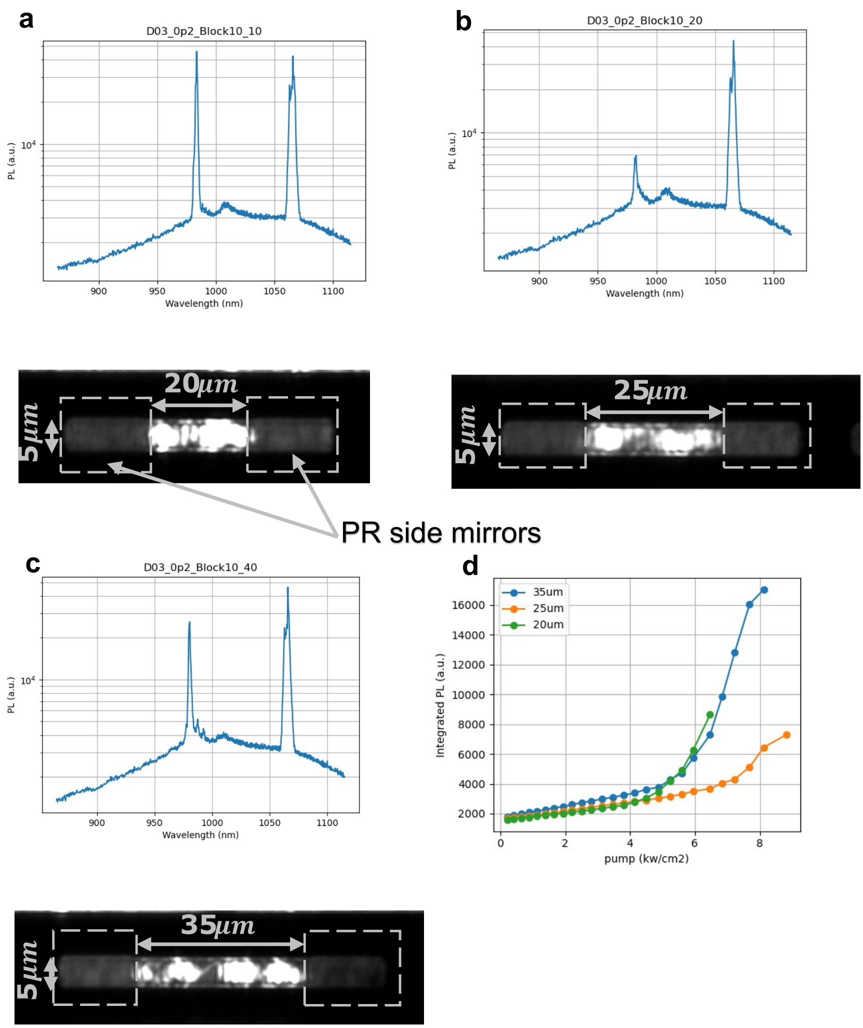

Figure 4.8: Lasing spectra of NRSELs with different cavity lengths: (a) 20 µm, (b) 25 µm, and (c) 35 µm. (d) Light-in vs. light-out curves for the three devices, showing the variation in lasing thresholds with cavity length.

4.3 Farfield Imaging

The devices were studied further using back-focal plane (BFP) imaging (figure 4.9). The BFP of an objective lens contains information about the angular spectrum of the light emitted from the sample plane. By imaging the BFP, the angular distribution of light emitted from the PhC can be mapped to momentum space using the formula:

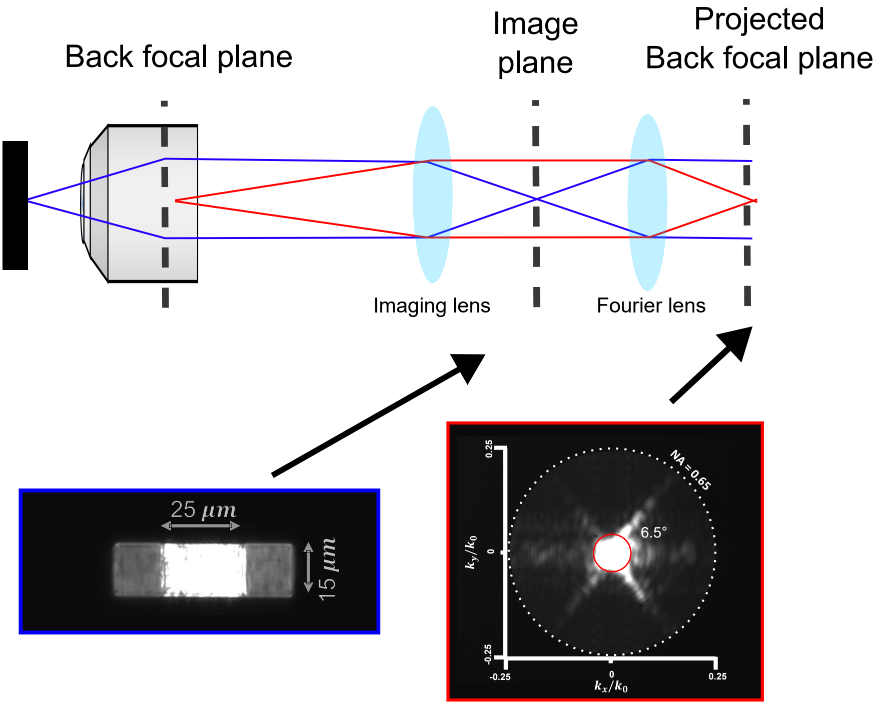

Figure 4.9: Schematic of the far-field and near-field imaging setup. The emitted light from the NRSEL is collected by a microscope objective (MO) with NA = 0.65. For near-field imaging, the real-space image of the sample is formed at the image plane (blue rays) using a tube lens. For far-field imaging, the back-focal plane (BFP) of the MO is imaged onto the camera (red rays) using an additional lens.

$k_{//} = k_0 sin(\theta)$. Hence, the in-plane k-vector ($k//$) can be evaluated knowing the emission wavelength ($k_0 = 2\pi/\lambda$) and the emission angle (θ), theta is the angle between the normal to the surface and the propagation direction of the emitted light. This mapping is crucial for understanding the dispersion relations in PhCs[4, 5]. Figure 4.11d and e, show the back-focal plane image of the NRSEL with W_{NRSEL} = 25 μm and the quasi-infinite array shown in figure 4.11b and c respectively, above their respective lasing threshold. Both devices show an angle of divergence lower than 10°, reflecting relatively tight beam confinement.

The unique emission patterns shown in figure 4.11d, e represent iso-frequency contours of the three-dimensional dispersion surface[9] (figure 4.10). The 3D band structure was simulated using the FDTD (Finite-Difference Time-Domain) method by calculating the resonant modes for each k-vector. A 3D representation of the first TE band is shown in figure 4.10a,b. The band shows a saddle point at Γ. Figure 4.10c shows an iso-frequency contour obtained by taking a plane intersection of the 3D band at the band-edge frequency. Above the lasing threshold, the intense monochromatic emission at the Γ point couples to modes at the same frequency within the band diagram, resulting in the distinctive star-shaped emission pattern observed. For the quasi-infinite array, the emission pattern clearly shows the characteristic star-shaped pattern also found from the 3D band structure calculations. For the finite size cavity, this pattern is still visible but now additional k-vector components are added, due to the scattering induced by the mirrors. Some components are also missing due to the finite size of the device which is discussed in more detail in chapter 5.

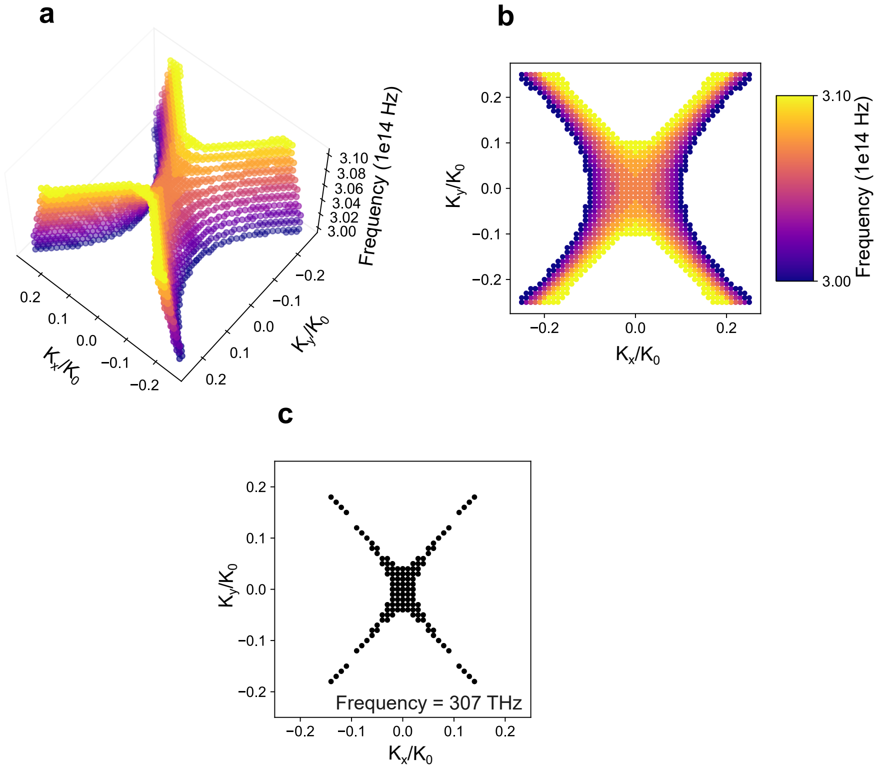

Figure 4.10: a) FDTD 3D band surface along kx and ky at TE_{21L} mode's resonance frequency. b) Top view of the band surface. c) 2D slice at the saddle point of the surface: 307 THz, showing the iso-frequency contour. The iso-frequency contour matches closely with the results obtained from the back-focal plane experimental images.

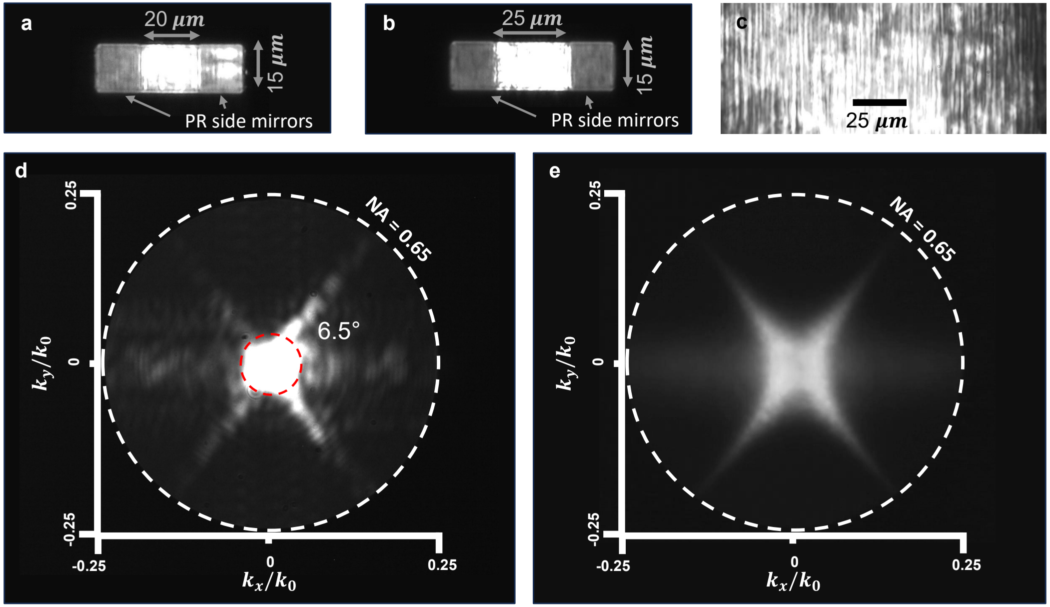

Figure 4.11: (a, b) Real-space images of devices with cavity sizes of 20 µm and 25 µm under optical pumping above the lasing threshold. In the 20 µm device, light is mostly confined to the cavity, although some emission extends into the photoresist mirror region on the right. In contrast, for the 25 µm device the emission is entirely localized within the cavity, with a clear reflection observed at the interface between the cavity and the photoresist side mirrors. (c) Real-space image of a quasi-infinite array under optical pumping above the lasing threshold, showing the emission from a large area of nano-ridges. (d) Back focal plane image for the 25 µm device above the lasing threshold, showing an angular divergence of approximately 6.5°. (e) Back focal plane image of the quasi-infinite array above the lasing threshold.

4.4 Summary

This chapter presents the room-temperature optical characterization of the fabricated NRSELs using a micro-photoluminescence (μPL) setup with 532-nm nanosecond pulsed pumping and spectrally resolved detection, complemented by back-focal-plane (BFP) imaging. Lasing is first demonstrated from a quasi-infinite nano-ridge array ($\Lambda = 380\ \mathrm{nm}$), where a narrow peak near 985 nm emerges at a threshold of $\sim 10\ \mathrm{kW\,cm^{-2}}$ and the far-field shows a small angular divergence ($\sim 6.5°$); spatial scans further reveal that nano-ridge width non-uniformity across the field shifts the lasing wavelength and modifies the threshold. Micro-NRSEL cavities are then analyzed in detail: a representative device ($W_{\mathrm{NRSEL}} = 20\,\mu\mathrm{m}$) shows lasing at 984 nm with a threshold of $10.8\ \mathrm{kW\,cm^{-2}}$ and a minimum linewidth of 0.9 nm (likely limited by pulsed pumping), and polarization measurements confirm strongly polarized emission aligned close to the nano-ridge axis. A statistical study of 31 devices establishes an overall inverse trend between threshold and cavity width up to $\sim 35\,\mu\mathrm{m}$ (minimum threshold of $5\ \mathrm{kW\,cm^{-2}}$ and smallest spread), followed by slight threshold saturation/increase consistent with Q-factor saturation and disorder/slow-light losses. Finally, multiple spectral peaks are matched to simulated band-diagram modes (including TE_{21L} with and without photoresist and a higher-order TE mode), and BFP imaging links the observed narrow-divergence, star-shaped emission patterns to iso-frequency contours of the simulated 3D dispersion surface near a saddle point at Γ.

Bibliography

[1] E. M. B. Fahmy, Z. Ouyang, D. Colucci, N. Le Thomas, J. Van Campenhout, B. Kunert, and D. Van Thourhout, “One-dimensional photonic crystal nano-ridge surface emitting lasers epitaxially grown on a standard 300 mm silicon wafer,” *Light: Science & Applications*, vol. 15, no. 1, p. 120, 2026. [Online]. Available: https://www.nature.com/articles/s41377-025-02061-z

[2] V. A. Nguyen, V. H. Le, E. Sarelli, L. Malgrey, D. K. Luu, H. L. Chu, T. T. Vu, C. Q. Tong, D. L. Vu, C. Seassal, Q. Le-Van, and H. S. Nguyen, “Direct observation of exceptional points in photonic crystal by cross-polarization imaging in momentum space,” *Applied Physics Letters*, vol. 123, 11 2023.

[3] S. Cueff, L. Berguiga, and H. S. Nguyen, “Fourier imaging for nanophotonics,” *Nanophotonics*, vol. 13, no. 6, pp. 841–858, 2024. [Online]. Available: https://www.degruyter.com/document/doi/10.1515/nanoph-2023-0887/html

[4] N. Le Thomas, R. Houdré, M. V. Kotlyar, D. O’Brien, and T. F. Krauss, “Exploring light propagating in photonic crystals with Fourier optics,” *Journal of the Optical Society of America B*, vol. 24, no. 12, p. 2964, 2007.

[5] N. Le Thomas, R. Houdré, D. M. Beggs, and T. F. Krauss, “Fourier space imaging of light localization at a photonic band-edge located below the light cone,” *Physical Review B - Condensed Matter and Materials Physics*, vol. 79, no. 3, pp. 1–4, 2009.

[6] W. Xue, Y. Yu, L. Ottaviano, Y. Chen, E. Semenova, K. Yvind, and J. Mork, “Threshold characteristics of slow-light photonic crystal lasers,” *Physical Review Letters*, vol. 116, no. 6, 2016.

[7] T. Coenen, *Angle-Resolved Cathodoluminescence Nanoscopy*, 2014.

[8] T. Coenen, B. J. Brenny, E. J. Vesseur, and A. Polman, “Cathodoluminescence microscopy: Optical imaging and spectroscopy with deep-subwavelength resolution,” *MRS Bulletin*, vol. 40, no. 4, pp. 359–365, 2015. [Online]. Available: http://link.springer.com/10.1557/mrs.2015.64

[9] E. C. Regan, Y. Igarashi, B. Zhen, I. Kaminer, C. W. Hsu, Y. Shen, J. D. Joannopoulos, and M. Soljačić, “Direct imaging of isofrequency contours in photonic structures,” *Science Advances*, vol. 2, no. 11, p. e1601591, 2016.

5

Probing BIC in NRSELs with Angle-Resolved CL and PL

5.1 Measurement Techniques 108
5.2 Angle-Resolved Measurements of Nano-Ridge Laser Photonic Bands 110
5.3 Effect of NR Dimensions on Band Structure and BIC Resonance 112
5.4 BIC Lasing Confirmation via Angle-Resolved Photoluminescence 117
5.5 Finite Cavity and Quantization Effects 118
5.6 Summary 124
Bibliography 127

In this chapter we unfold the underlying physics of the lasing mechanism using a combination of angle resolved (AR) PL and CL. Angle-resolved measurements provide the experimental photonic band structure, allowing us to visualize the cavity modes, directly confirm the BIC mode, and clearly show that band-edge lasing originates from BIC modes. Additionally, we explore finite-cavity NRSELs using ARCL and ARPL setups, providing an experimental demonstration of mode quantization resulting from the finite size of the devices. By restricting the dimensions of the cavity, we observe a transition from a continuous band-edge resonance to a series of discrete, quantized cavity modes.

5.1 Measurement Techniques

To experimentally map the photonic bands of the nano-ridge laser structure, we employ two complementary angle-resolved techniques: cathodoluminescence (CL) spectroscopy and photoluminescence (PL) spectroscopy. Both methods enable us to probe the dispersion relations of the optical modes supported by the nano-ridge array, providing insights into their confinement and radiative properties. The measurements were done in the Netherlands at Delmic[1] and in France at Ecole Central de Lyon[2] using two different setups, as illustrated in Figure 5.1.

In the angle-resolved CL setup (developed by Delmic) (Fig. 5.1a), the sample is mounted inside a scanning electron microscope (SEM) and excited by a tightly focused electron beam. The electron beam excites the active region (the quantum wells), thereby locally exciting the nano-ridge optical modes; the coupling efficiency at a given position is governed by the local density of optical states (LDOS) at the beam excitation point[3]. The excited modes then radiate light into the far field (the CL signal). A parabolic mirror inside the SEM collects the emitted light and sends it to an imaging spectrometer. By projecting the far-field (Fourier-plane) distribution onto the spectrometer entrance slit, the signal can be recorded on a 2D camera, with the wavelength (energy) dispersed along one axis and the emission angle (momentum) encoded along the other. Converting emission angle to in-plane wavevector allows us to reconstruct the photonic band structure. Because the excitation spot is on the order of a few nanometers, AR-CL offers high spatial resolution, enabling measurements on individual nano-ridges or selected regions of the array.

Observing the band dispersion when exciting a single ridge of the nano-ridge array supports the interpretation that the relevant modes are delocalized Bloch modes extending over many periods. The appearance of the band structure under localized excitation indicates that emission from the excited ridge couples to neighboring ridges, allowing the optical field to propagate across the array and sample the periodic structure. This also enables a spatial assessment of fabrication uniformity by scanning across the sample.

In the angle-resolved PL setup (developed by EC Lyon) (5.1b), we use an optical excitation source, such as a pulsed laser or broadband white light, to uniformly illuminate the nano-ridge array. The emitted light is collected and sent to an imaging spectrometer in a manner similar to the CL setup. By analyzing the angular distribution of the emitted photons as a function of wavelength, we can reconstruct the photonic band structure and identify resonant modes[2]. This technique is particularly useful for studying lasing behavior under optical pumping conditions. Using white light reflection measurements, we can also probe the absorption features of the nano-ridge array, providing complementary information about the photonic bands.

Python scripts were developed with the help of Delmic and the university of Lyon to process the raw data from both setups, converting camera pixel coordinates to physical quantities such as wavelength and in-plane wavevector. This involved calibrating the spectrometer and accounting for the optical geometry of the collection system. The processed data yield two-dimensional maps of intensity versus wavelength and wavevector, revealing the dispersion relations of the nano-ridge laser modes.

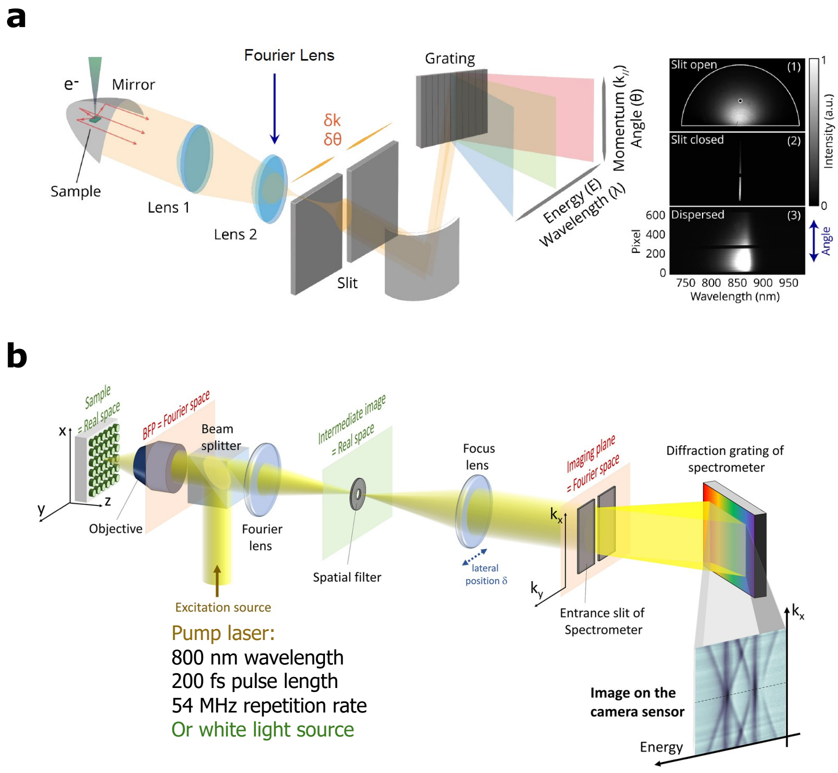

Figure 5.1: Schematic diagrams of the (a) angle-resolved cathodoluminescence (CL) setup and (b) angle-resolved photoluminescence (PL) setup used to probe the photonic band structure of the nano-ridge laser array. In both setups, the emitted light is collected and directed to an imaging spectrometer for angular and spectral resolution. reproduced from [1, 2]

5.2 Angle-Resolved Measurements of Nano-Ridge Laser Photonic Bands

To directly map the dispersion and verify band-edge BIC lasing, we first use angle resolved cathodoluminescence (AR-CL) spectroscopy[4–6]. In this cathodoluminescence (CL) setup, the sample (5.2a) sits inside a scanning electron microscope (SEM) and is excited from above by a tightly focused ($\approx$ 10 nm) 20 kV electron beam. Figure 5.2b presents a CL spectrum obtained using a 10 kV, 340 pA electron beam scanned across an array of nano-ridges. The spectrum spans a broad wavelength range from 800 nm to 1100 nm, with contributions from both the GaAs body and the embedded InGaAs MQWs. The broad luminescence provides a wide spectral window over which guided modes can be engineered. Figure 5.2c shows a spatial emission map of the nano-ridge array integrated over 950–1050 nm. All nano-ridges contribute within this band, but the emission intensity varies across the array, consistent with modest fabrication-induced variations in geometry or material quality.

For angle-resolved photoluminescence (ARPL) measurements, we use a separate optical setup that allows flexible source options, such as broadband white-light illumination (for reflection measurements) or a pulsed laser beam (for excitation). The emitted light is then collected and sent to an imaging spectrometer in a manner analogous to the CL configuration, enabling simultaneous recording of wavelength on one camera axis and far-field emission angle on the other. White light reflection from a quasi-infinite nano-ridge array (field 5 mm, 13150 periods), measured along Γ-X and Γ-Y (Figures 5.3a,b), clearly resolves two dispersive bands that match the overlaid FDTD calculations (cyan). Nano-ridges of 380 nm period, 197 nm width and 480 nm height were used for the simulations to reflect the average dimensions obtained using a scanning electron microscope (SEM). The lower-energy TE_{21L} band exhibits opposite curvature along Γ-X versus Γ-Y, whereas the higher-energy TE_{22L} band maintains the same-sign curvature near Γ, enabling unambiguous band assignment consistent with FDTD. A normalized cut along Γ-X at several k_x values (Fig. 5.3c) shows the absorption dip gradually narrowing and then vanishing at Γ: the linewidth contracts from 10 nm at $k_x \approx 0.3$ to below detection at $k_x = 0$, signaling a bound-state-in-the-continuum (BIC) with high Q factor and a narrow linewidth[7, 8]. BIC modes do not interact with free-space radiation at normal incidence due to symmetry mismatch, which makes them harder to excite and detect using white light. However, their presence can be inferred from the vanishing linewidth as the mode approaches Γ[7, 9]. Complementary angle-resolved cathodoluminescence (CL) along Γ-X and Γ-Y (Figures 5.4a,b) reproduces these dispersions and reveals a sharp band-edge peak near 1.27 eV due to the BIC-enhanced emission. A representative slice at $k_x = 0.11$ (Figure

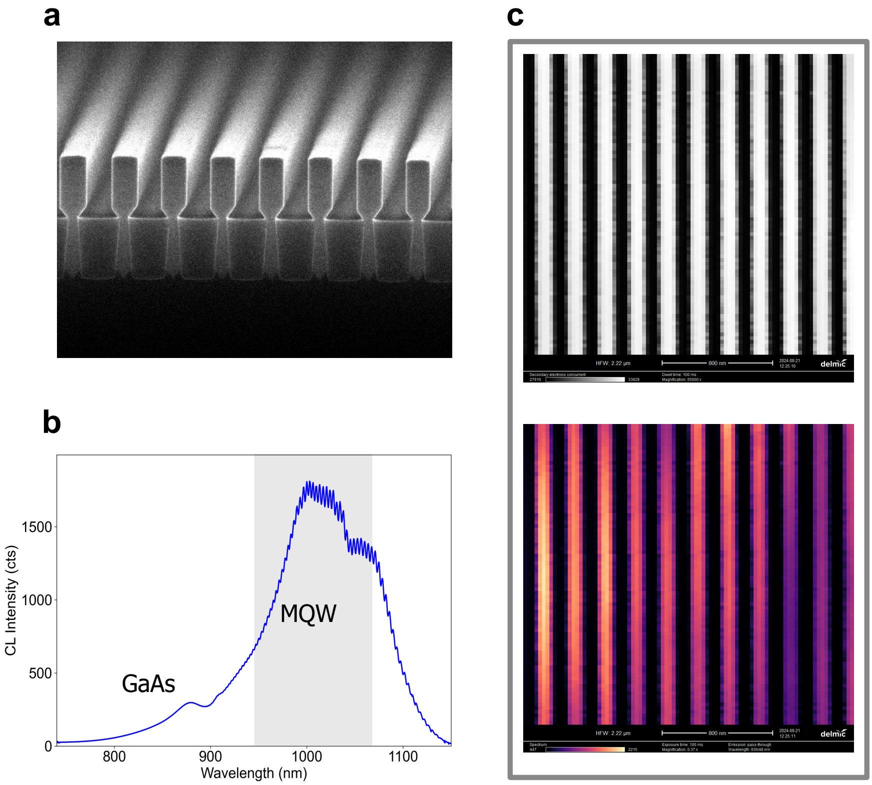

Figure 5.2: (a) Cross-sectional SEM image of a cleaved array of nano-ridges with a period of 380 nm. (b) Cathodoluminescence (CL) emission spectrum from the array, showing broad band emission from the multi-quantum wells (MQWs) around 1000 nm and a smaller peak around 890 nm from the GaAs body. (c) Top-view SEM image of the nano-ridge array and the corresponding CL emission spatial map (950 to 1050 nm) integrated over the array.

5.4c) further resolves a narrow peak at 975 nm corresponding to the BIC on the first band TE_{21L} with a high Q factor (> 300), alongside a broader feature from the underlying TE_{21L} band. Unlike the PL, in which multiple ridges are excited simultaneously, for the CL measurements a single ridge is initially excited by placing the beam in the center of one ridge. Yet, the behavior that is observed in the dispersion maps is similar which is a testament to the delocalized nature of these optical modes. This enhancement being visible even under nanoampere-scale CL excitation speaks to the strength of the photonic confinement. The high Q-factor indicates that photons dwell in the cavity for many optical cycles, while the nearly flat dispersion (i.e. low group velocity) at the band edge maximizes the local density of optical states. Together, these factors amplify the spontaneous emission rate via the Purcell effect, funnelling more of the MQW gain into the desired cavity mode[10, 11].

5.3 Effect of NR Dimensions on Band Structure and BIC Resonance

The nano-ridges measure on average 198 nm in width and 482 nm in height for this sample. Figure 5.5d shows that, within the 380-nm-pitch field, the nano-ridge width decreases by approximately 10 nm from the field edge toward the center, as revealed by SEM inspection. From this we learn that a systematic within-field width gradient is present, which can shift the local resonance frequency across the field. To see the effect of variability in the geometric dimensions on the band structure and the BIC mode resonance frequency, we perform a series of angle-resolved measurements. In Figure 5.5a, a scan of the CL intensity at a fixed in-plane wavevector ($k_x = 0.3$) forms a nanoscale dispersion map with 500 nm steps. The map reveals a dispersion of $\approx 0.2\ \mathrm{nm}/\mu\mathrm{m}$ of displacement along the nano-ridge's length, yielding a total peak redshift of 4.5 nm over 20 $\mu\mathrm{m}$, as shown in Figure 5.5b. In figures 5.5c and 5.5d, we acquired a coarser dispersion map at the same in-plane wavevector ($k_x = 0.3$) using 50 $\mu\mathrm{m}$ scan increments. Over the full scan, the nano-ridge width increased by approximately $10\ \mathrm{nm}$, producing a systematic band-edge redshift of $\approx 30\ \mathrm{nm}$. This agrees well with our FDTD simulations, which predict a wavelength sensitivity of $\approx 2.5\ \mathrm{nm}/\mathrm{nm}$ to changes in nano-ridge width [12]. These findings indicate that the lasing wavelength can be precisely set by tailoring the nanoridge dimensions, and that further post-fabrication fine-tuning can be achieved via dielectric deposition to adjust ridge width or height without the need for additional etching. They also underscore the importance of tightly controlling dimensional variability during fabrication to hit the target design parameters.

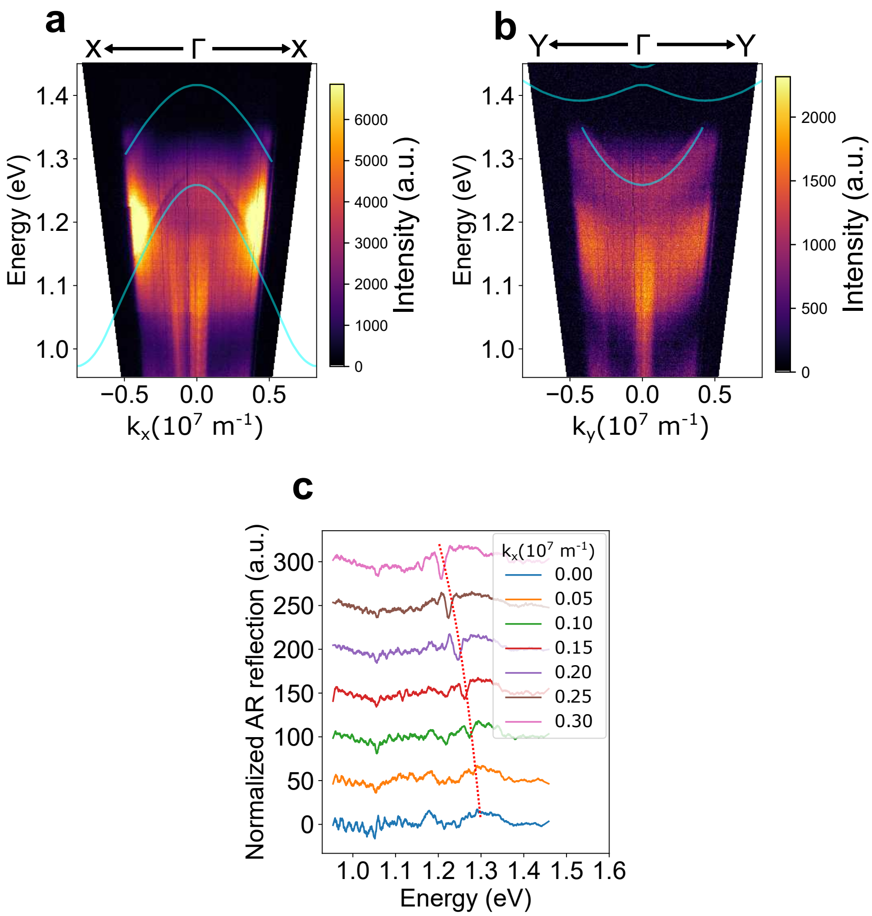

Figure 5.3: (a,b) Angle-resolved photoluminescence (PL) along Γ-X and Γ-Y directions, respectively. FDTD band structures are overlaid in cyan. (c) Normalized angle-resolved reflection along Γ-X at different k_x values, showing a gradual increase in the absorption dip until it vanishes at the Γ point.

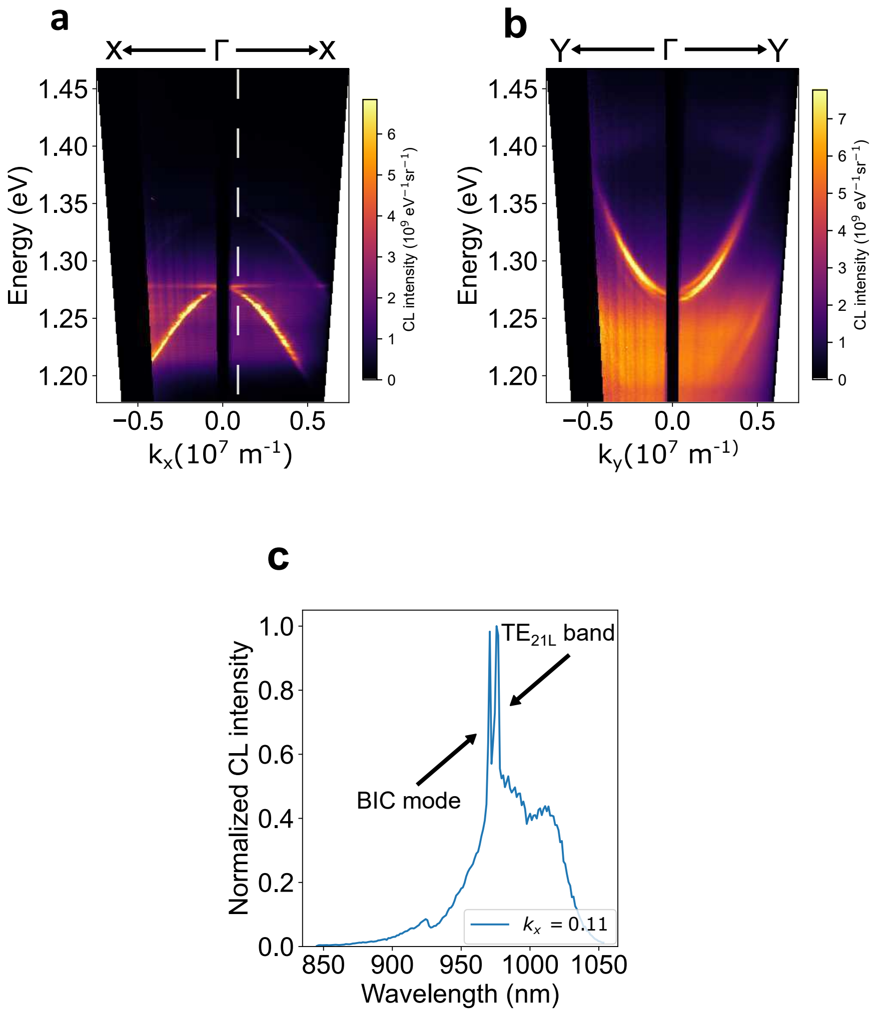

Figure 5.4: (a,b) Angle-resolved cathodoluminescence (CL) along Γ*-X and* Γ*-Y, respectively. A sharp peak and enhanced spontaneous emission due to the BIC mode appear around 1.27 eV at the band edge. (c) A slice at* $k_x = 0.11$ *showing the CL intensity versus wavelength. The narrower peak corresponds to the BIC mode at 975 nm, while the broader peak arises from the first band* TE_{21L}.

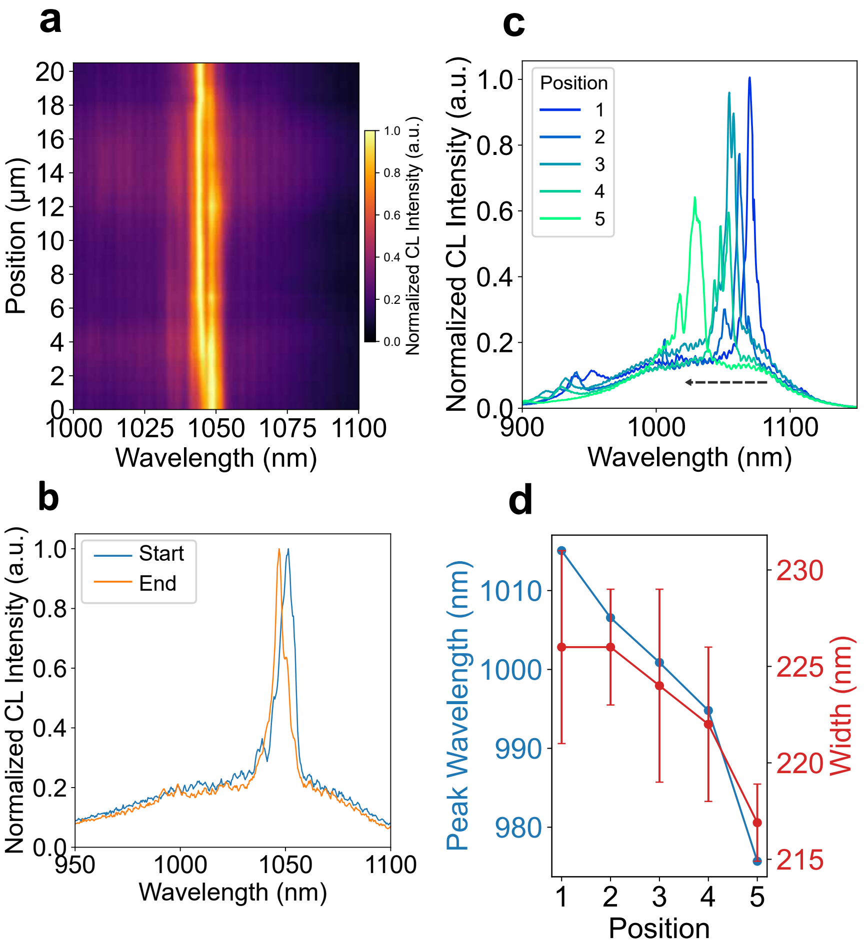

Figure 5.5: (a,b) Dispersion map using a slice at $k_x = 0.3$ with 500 nm steps along the nano-ridge's length. (c) Coarse dispersion map using a slice at $k_x = 0.3$ at different sample positions along the nano-ridge's length with a 50 μm step, reflecting changes in the nano-ridge geometry at these positions. (d) Cathodoluminescence peak at different positions with the corresponding nano-ridge width extracted from SEM images at those positions.

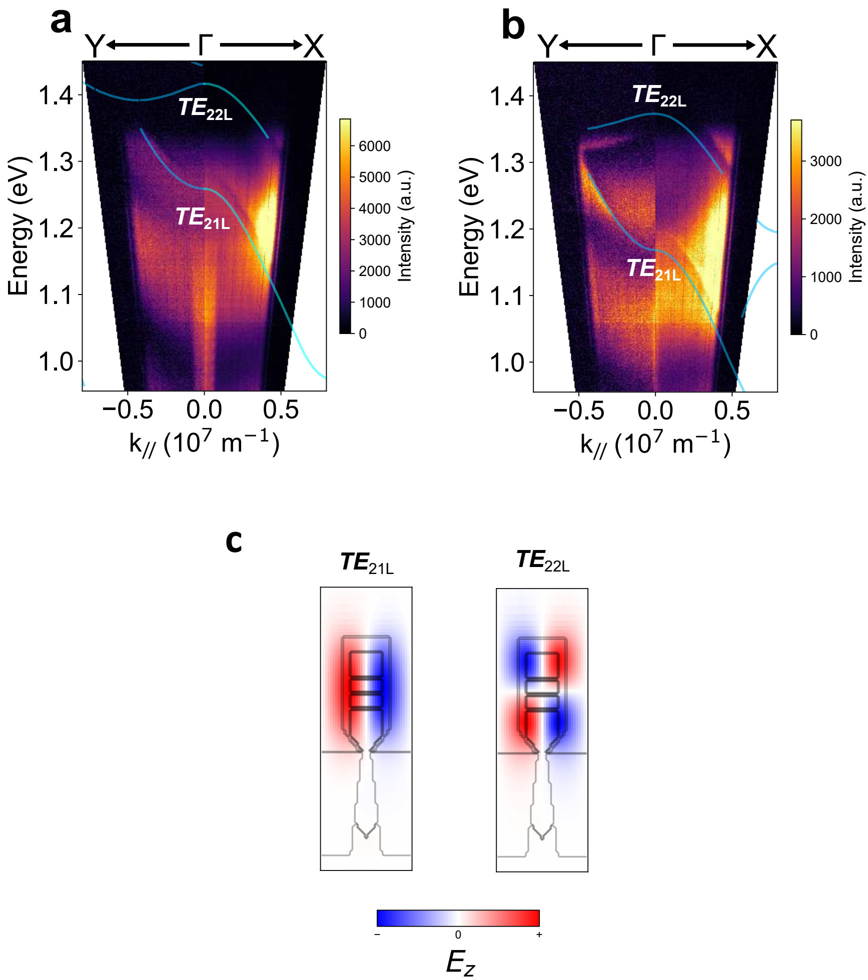

Figure 5.6: (a,b) Experimental angle-resolved white-light reflection measurements for the center and edge dies, respectively, showing good agreement with the simulated band diagram (cyan). (c) Cross-sections of the electric field distribution (E_y) for the first two BIC modes TE_{21L} and TE_{22L}, respectively.

Fabrication variability spans both within-field gradients and die-to-die shifts across the 300 mm wafer. At 380 nm period, the center die holds ~ 197.5 nm width and 482 nm height, while edge dies average 232.4 nm width and 427 nm height. This center–edge contrast, driven by global loading and flux non-uniformities in SAE, effectively yields two designs on one wafer: a "center" geometry (197.5 $\times$ 482 nm) and an "edge" geometry (232.4 $\times$ 427 nm), differing by $\sim$ 35 nm in width and $\sim$ 55 nm in height, enough to shift the photonic bands by tens of nanometers. Because the edge geometry brings the second-order band-edge mode TE_{22L} into the MQW emission window, it supports second-order lasing near 920 nm, whereas the center die lases on the first-order mode TE_{21L} at $\sim$ 975 nm. Figure 5.6c shows the mode profiles for the first-order mode and the second-order mode, respectively. These results nicely demonstrate the platform's wavelength-tuning capability, but they also highlight the need for improved process control: the emission is highly sensitive to small fabrication variations, so greater uniformity will be required for consistent performance across the wafer. Figures 5.6a and 5.6b show the white-light reflection measurements using the μPL setup, illustrating the shift in the band diagram from the wafer's center to edge overlaid with the FDTD band diagrams using the respective average dimensions, showing very good agreement. There is a slight misalignment in wavelength between the experimental bands along k_x and k_y due to the physical limitations of the setup: rotating the sample by hand to perform the measurement along different directions causes us to probe different locations on the sample and hence the shift in the bands.

5.4 BIC Lasing Confirmation via Angle-Resolved Photoluminescence

In Figure 5.8a, the angle-resolved photoluminescence under pulsed femtosecond excitation for the center die is shown. Below threshold, the emission follows the broad spontaneous-emission profile of the MQWs modulated by the fundamental band of the structure; above a critical fluence of 0.56 mJ/cm^2, a sharp peak emerges at 975 nm. The input–output curve, in figure 5.7, shows a clear knee at 0.56 mJ/cm^2, confirming the lasing threshold, and the emission linewidth collapses to $\simeq 1$ nm at threshold, signalling coherent stimulated emission.

The edge–die lases from its second-order band-edge mode near 920 nm (figure 5.8b) with a lower threshold fluence of 0.4 mJ/cm^2. The physical origin of this reduced threshold remains under investigation, but one plausible factor is that the second-order band exhibits similar curvature along both k_x and k_y (i.e. an isotropic flatness), which may trap photons more effectively than the saddle-shaped first-order band (opposite curvature) and thus enhance light–matter interaction (figures

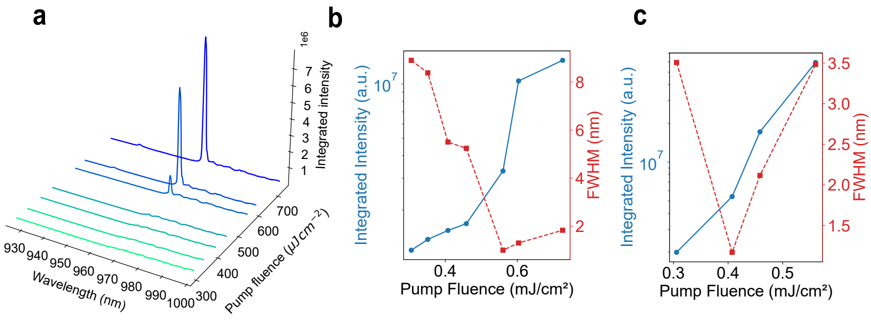

Figure 5.7: (a) Lasing spectrum of the center die (TE_{21L}) with a narrow peak around 975 nm. (b) Integrated light input–output curve of the center die (TE_{21L}) at different pump fluences, showing a clear threshold around 0.56 mJ/cm^2. (c) Integrated light input–output curve of the edge die (TE_{22L}) at different pump fluences, showing a clear threshold around 0.4 mJ/cm^2.

5.6a,b). In Figures 5.8c and 5.8d, far-field (back-focal-plane) images for both designs were acquired on a separate nanosecond-excitation setup using a CMOS camera. These images confirm narrow, surface-emitting beams from both devices, with the edge–die laser showing a smaller divergence angle of $\simeq 3°$, consistent with its isotropic dispersion and matching the iso-frequency contours obtained from the band diagram simulations, as shown in figure 5.9.

5.5 Finite Cavity and Quantization Effects

So far, we have been focusing on quasi-infinite arrays of nano-ridges. However, we have previously shown (chapter 4) that it is possible to make smaller micro lasers with lower lasing thresholds and as small as 15 $\mu\mathrm{m}$ or around 40 nano-ridge-wide cavities with the help of side mirrors[12, 13]. To quantify the impact of the photoresist mirrors, we performed angle-resolved CL on a finite 15 $\mu\mathrm{m}$ cavity. This measurement revealed discrete bright spots along each branch of the first Bloch band TE_{21L}, indicating mode discretization in the mirror-defined cavity, as shown in Figure 5.10c. In the device schematic and SEM pictures, shown in figures 5.10a and 5.10b, we indicate the photoresist mirror and scan trajectory. We scan the electron beam from the mirror edge toward the cavity center in 150-nm steps, covering half the cavity. In Figure 5.10c, angle-resolved CL maps at different cavity positions show discrete bright spots along each branch of the cavity Bloch band; the dominant peak shifts toward the band-edge wavelength as the beam approaches the center, while secondary Fabry–Pérot (FP) modes remain visible. Another band arising from the photoresist mirrors at smaller energy can also be seen. These

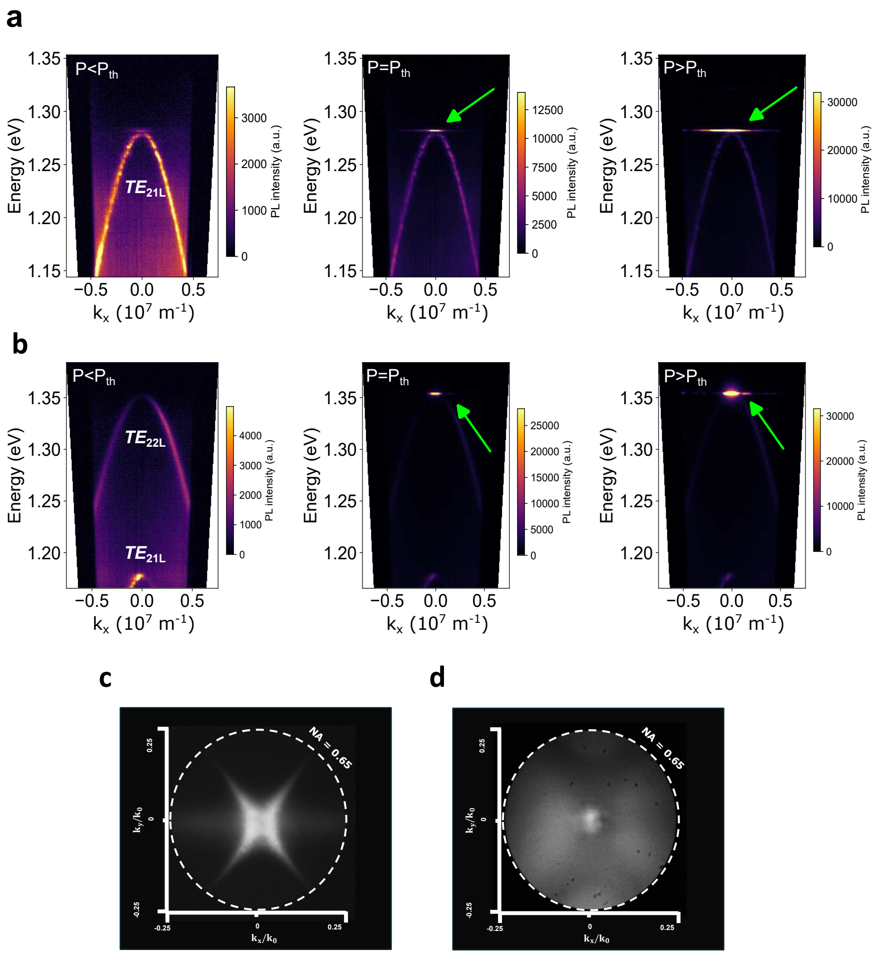

Figure 5.8: (a) Angle-resolved photoluminescence at different pump fluences under pulsed femtosecond optical excitation for the center die, showing lasing at the band edge around 975 nm with a threshold pump fluence of 0.56 mJ/cm^2.(b) Angle-resolved photoluminescence at different pump fluences under pulsed femtosecond optical excitation for the edge die, showing lasing at the band edge around 920 nm with a threshold pump fluence of 0.4 mJ/cm^2. (c,d) Experimental back-focal-plane images (far-field) for the center and edge dies above their respective thresholds using a CMOS camera under nanosecond pulsed excitation. The far-field shows a lower divergence angle of around 3° for the edge die.

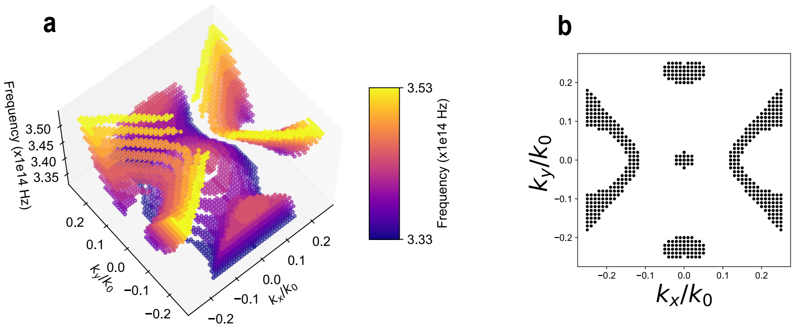

Figure 5.9: (a) 3D band diagram simulation using FDTD for the second TE band: TE_{22L}*. (b) Iso-frequency contour at the band edge showing a small central BIC mode and modes from a higher-order band.*

discrete spots arise from longitudinal quantization in a finite cavity of length L, where $k_m = m\pi/L$ imposes a uniform spacing $\Delta k = \pi/L$; consequently, reducing L increases mode spacing and accentuates the band discretization[14, 15]. In figure 5.11a, a 3D field–band diagram rendering and the iso-frequency contour visualize the modal envelope and the allowed analytically calculated k_x values (vertical lines at $k_x = m\pi/L$, spaced by Δk). Consistent with this picture, the CL maxima cluster around these allowed k_x values, indicating that the mirror-defined finite length sets the mode spacing.

FDTD simulations reinforce this picture: The simulated E–k_x map, shown in figure 5.11b, resolves the same ladder of discrete cavity modes observed in CL, and the corresponding transverse cross-sections of the cavity mode profiles (figure 5.11c) explain the position-dependent excitation. We highlight the first three discrete modes at k_1, k_2, k_3, labeled Γ_1, Γ_2, Γ_3 in figure 5.11b: Γ_1 exhibits one antinode, Γ_2 has two antinodes, and Γ_3 has three. These spatial field distributions align with the expected Fabry–Perot standing waves in a 15 μm cavity and illustrate how each resonance corresponds to a different number of field antinodes between the side mirrors. Because the real-space field maxima occur at different locations for the Γ-point modes ($\Gamma_1 \rightarrow \Gamma_3$), the e-beam preferentially excites the mode with the largest local field overlap at the chosen excitation position.

We now move from local CL excitation to uniform pumping of the entire cavity using an angle-resolved micro-PL (μPL) setup with a femtosecond laser. A microscope image of the NRSEL array is shown in figure 5.13a. Under pulsed excitation at 0.19 mJ/cm^2, the 15 μm cavity's E–k_x map (figure 5.13b) resolves two bands: the central fundamental TE cavity band (TE_{21L}, $\lambda \approx 975$ nm) with clearly quantized modes as seen earlier in the CL maps, and a red-shifted band ($\lambda \approx 1005$ nm) originating from the photoresist side mirrors. By narrowing down

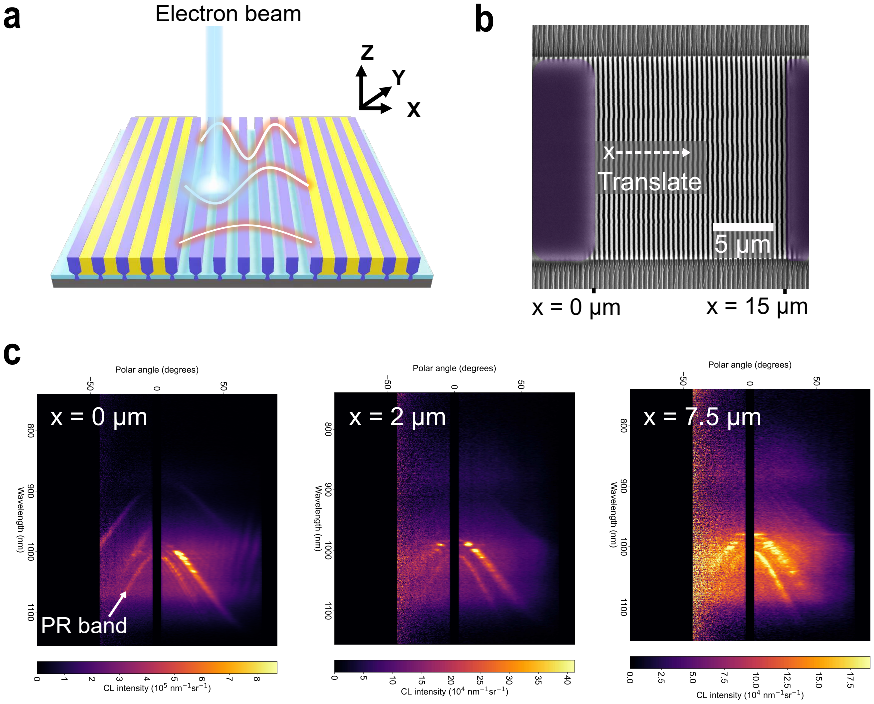

Figure 5.10: (a) 3D schematic of the nano-ridge cavity with photoresist side mirrors and the e-beam scan path from edge to center. (b) SEM of the $15\ \mu\mathrm{m}$ *mirror-defined cavity. (c) Angle-resolved CL at three* x*-positions (0, 2,* $7.5\ \mu\mathrm{m}$*) showing a dominant peak that shifts toward the band edge while multiple Fabry–Pérot modes remain visible.*

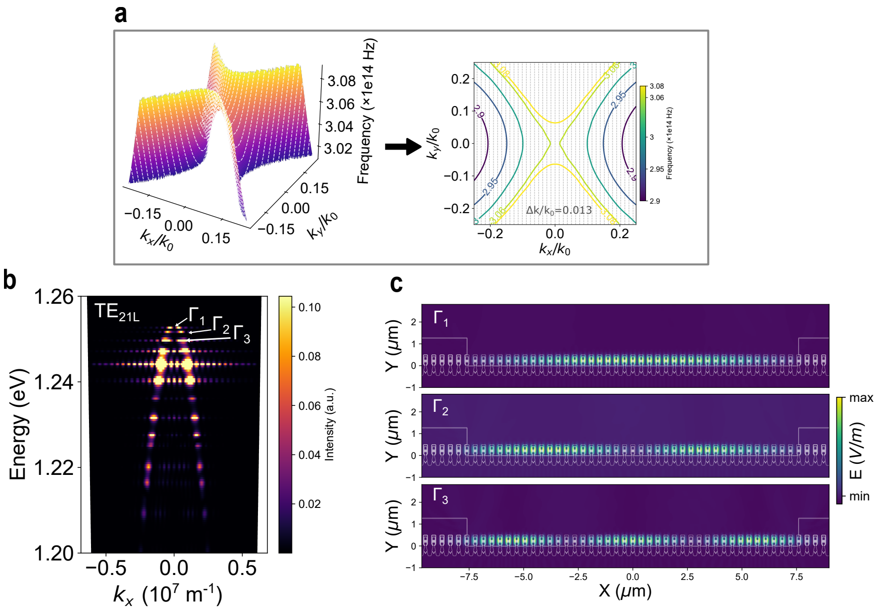

Figure 5.11: (a) FDTD 3D TE_{21L} surface and iso-frequency contour with allowed longitudinal wavevectors marked as vertical lines at $k_x = m\pi/L$ (uniform spacing $\Delta k = \pi/L$), highlighting mirror-induced quantization. (b) 2D FDTD simulated E–k_x map resolving the same ladder of discrete cavity modes observed in CL and labeled by Γ indices. (c) Transverse electric field profiles of the first three discrete modes indicated in (b): $\Gamma_1(k_1)$ at 989.2 nm with one antinode, $\Gamma_2(k_2)$ at 989.8 nm with two antinodes, and $\Gamma_3(k_3)$ at 991.6 nm with three nodes, explaining the position-dependent excitation via local field overlap with the e-beam.

the collection iris, we selectively suppress emission from the mirror regions and confirm this second band's PR-mirror origin, consistent with our FDTD predictions (see figure 5.12). The 30 μm device measured at 0.16 mJ/cm^2 (figure 5.13b) shows discrete modes but with a finer Δk, as expected from $\Delta k = \pi/L$. Angle-resolved PL taken along k_y for the 15 μm cavity at 0.19 mJ/cm^2 (figure 5.13a) shows only subtle, uniform quantization as the cavity is also finite along the ridge direction due to etching, but weaker reflectivity and facet imperfections reduce the visibility of Fabry–Pérot steps compared to k_x.

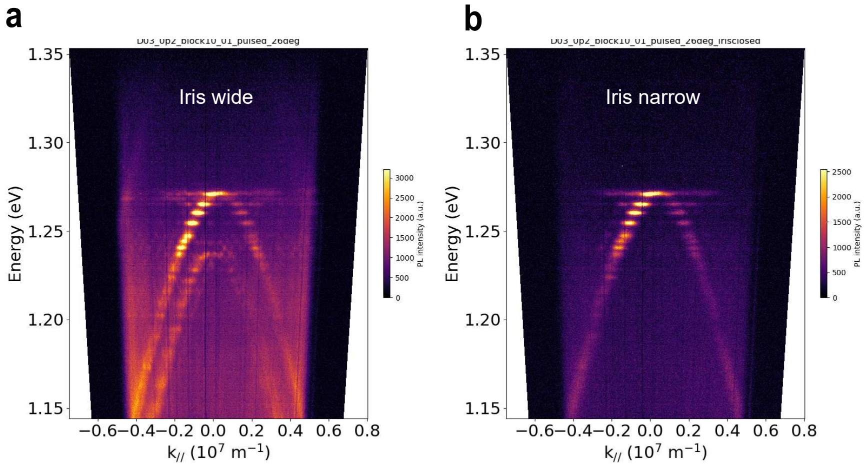

Figure 5.12: (a) Angle-resolved measurement with a wide iris collecting emission from both the cavity and mirror regions, showing two bands: one from the cavity region and a red-shifted band from the mirror region due to the photoresist. (b) Angle-resolved measurement with a narrow iris ($\leq$ *15* μm*) collecting emission only from the cavity region, showing only the first TE band from the cavity without any shift.*

Power-dependent maps along k_x highlight the transition to lasing and the evolution of discrete resonances. At 0.4 mJ/cm^2 (figure 5.13c), the 15 μm NRSEL displays a narrow lasing peak at the band-edge BIC mode (1.27 eV, $\sim$ 975 nm). Increasing the fluence to 0.56 mJ/cm^2 (figure 5.13d) brings out additional narrow emissions at multiple Fabry–Pérot resonances and an extra line near 952 nm, which might be a result of a nonlinear process due to the high excitation power. To quantify the mode quantization, we plot the mode number m versus the in-plane k-vector k_x for cavities of length 15 μm, 20 μm, 25 μm, and 30 μm (Fig. 6g). Linear fits yield the average momentum step and hence the effective cavity length $L_{\text{eff}} = \pi/\Delta k_x$. figure 5.14d summarizes L_{eff} versus design length: the 15 μm device with nano-ridge length of 5 μm shows the clearest mode separation and the closest agreement with simulation, whereas larger cavities exhibit noisier spacing. The nano-ridge length should not influence the quantization in the Γ-X direction. The difference arising from the two 15 μm devices with different nano-ridge length could arise due to either imperfect measurement alignment from sample rotation or fabrication disorder in the device. From the simulated E–k map we extract $L_{\text{eff}} \approx 18\ \mu\text{m}$ for the nominal 15 μm design, consistent with field penetration into the mirror regions on both sides, as expected for finite-reflectivity PR mirrors.

The quantization along the Γ-Y direction could be used in the future for electrical injection of the NRSEL devices. Using reflective end facets with high reflection will allow stronger quantization of the longitudinal modes, which in turn causes the formation of optical field nodes along the nano-ridge's length with uniform separation. By placing the electrical plugs (contacts) at the locations of field nodes, the device can be uniformly injected with minimum losses to the optical fields.

5.6 Summary

In this chapter, we explain the lasing mechanism in NRSELs by experimentally reconstructing the photonic band structure using angle-resolved (Angle-Resolved (AR)) PL and CL. Angle-resolved white-light reflection and Angle-Resolved Photoluminescence (ARPL) measurements on quasi-infinite nano-ridge arrays reveal dispersive TE_{21L} and TE_{22L} bands in good agreement with FDTD, while the progressive narrowing and eventual disappearance of the resonance linewidth at Γ provides a direct signature of a symmetry-protected BIC. Complementary Angle-Resolved Cathodoluminescence (ARCL) reproduces the same dispersions with nanoscale excitation and shows enhanced band-edge emission near the BIC, consistent with a high-Q mode and increased LDOS near a flat band edge. We then quantify how fabrication-induced variations in nano-ridge dimensions (within-field gradients and center-to-edge die shifts) translate into systematic band shifts and changes in the band-edge lasing wavelength, demonstrating wavelength tunability but also highlighting the need for improved uniformity. Finally, by introducing photoresist side mirrors to form finite cavities, we observe a transition from a continuous band-edge resonance to a ladder of discrete, quantized cavity modes with spacing $\Delta k \approx \pi/L$, confirmed by both ARCL/ARPL maps and FDTD, and we show that lasing in these mirror-defined cavities still originates from the band-edge BIC while exhibiting clear finite-size (Fabry perot) quantization effects.

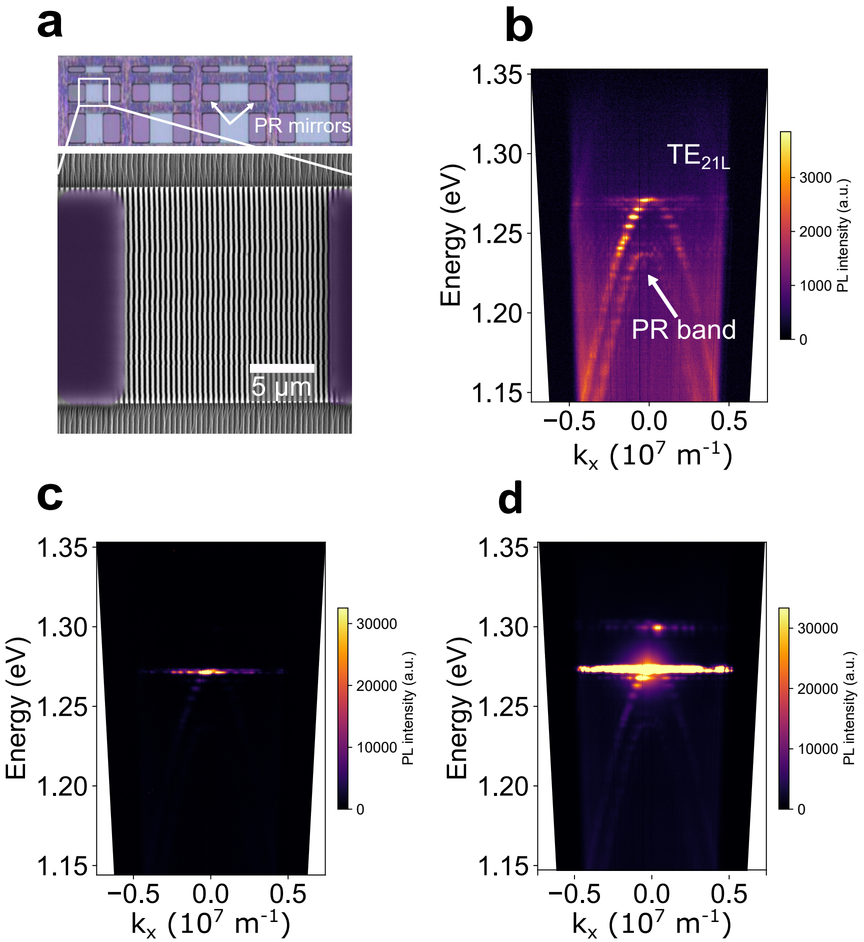

Figure 5.13: (a) Microscope image of the NRSEL array. (b) Angle-resolved E–k_x map for the $15\ \mu\mathrm{m}$ *NRSEL under femtosecond pulsed excitation (0.19 mJ/cm^2), resolving two bands: the fundamental cavity band* TE_{21L} *near* $\lambda \approx 975$ nm *with clearly quantized modes (large* Δk*), and a red-shifted band near* $\lambda \approx 1005$ nm *from the photoresist side mirrors. (c) E–k_x at 0.4 mJ/cm^2 showing a narrow lasing peak at the band-edge BIC mode (1.27 eV,* ~ 975 nm*). (d) E–k_x at 0.56 mJ/cm^2 revealing narrow emission at multiple Fabry–Pérot resonances and an additional line around 952 nm.*

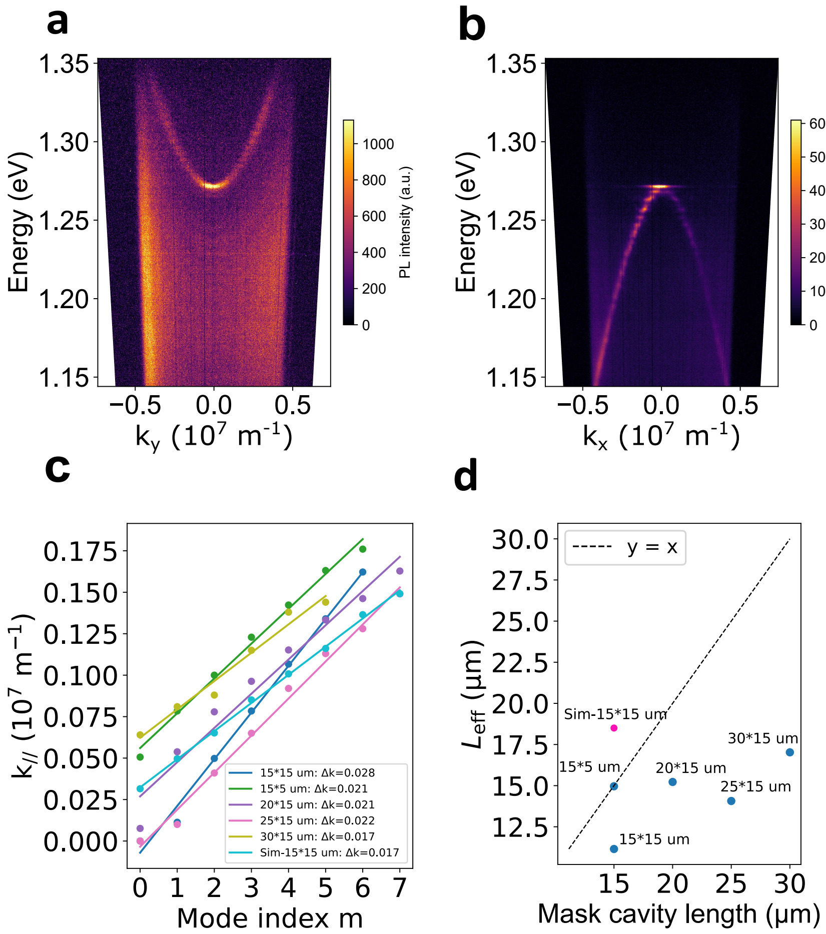

Figure 5.14: (a) E–k_y for the 15 μm device at 0.19 mJ/cm^2 exhibiting subtle, uniform quantization consistent with weaker longitudinal confinement along the ridge direction. (b) E–k_x for the 30 μm NRSEL at 0.16 mJ/cm^2, showing finer mode spacing Δk as expected from $\Delta k = \pi/L$. (c) Quantized mode momentum index m vs the in-plane wave vector $k_{//}$, for cavities of length 15 μm, 20 μm, 25 μm, and 30 μm; linear fits yield the average momentum step Δk (slope) and effective cavity length $L_{\text{eff}} = \pi/\text{slope}$. (d) L_{eff} versus design cavity length, highlighting that the 15 μm device shows the clearest spacing and best agreement with simulation; the simulated E–k map indicates $L_{\text{eff}} \approx 18$ μm for the nominal 15 μm design, consistent with field penetration into the mirror regions.

Bibliography

[1] T. Coenen, B. J. Brenny, E. J. Vesseur, and A. Polman, “Cathodoluminescence microscopy: Optical imaging and spectroscopy with deep-subwavelength resolution,” *MRS Bulletin*, vol. 40, no. 4, pp. 359–365, 2015. [Online]. Available: http://link.springer.com/10.1557/mrs.2015.64

[2] S. Cueff, L. Berguiga, and H. S. Nguyen, “Fourier imaging for nanophotonics,” *Nanophotonics*, vol. 13, no. 6, pp. 841–858, 2024. [Online]. Available: https://www.degruyter.com/document/doi/10.1515/nanoph-2023-0887/html

[3] E. J. R. Vesseur, T. Coenen, H. Caglayan, N. Engheta, and A. Polman, “Experimental Verification of n = 0 Structures for Visible Light,” *Physical Review Letters*, vol. 110, no. 1, p. 013902, 2013. [Online]. Available: https://link.aps.org/doi/10.1103/PhysRevLett.110.013902

[4] T. Coenen, E. J. R. Vesseur, and A. Polman, “Angle-resolved cathodoluminescence spectroscopy,” *Applied Physics Letters*, vol. 99, no. 14, 2011.

[5] T. Coenen, *Angle-Resolved Cathodoluminescence Nanoscopy*, 2014.

[6] S. Mignuzzi, M. Mota, T. Coenen, Y. Li, A. P. Mihai, P. K. Petrov, R. F. M. Oulton, S. A. Maier, and R. Sapienza, “Energy-Momentum Cathodoluminescence Spectroscopy of Dielectric Nanostructures,” *ACS Photonics*, vol. 5, no. 4, pp. 1381–1387, 2018.

[7] A. Kodigala, T. Lepetit, Q. Gu, B. Bahari, Y. Fainman, and B. Kanté, “Lasing action from photonic bound states in continuum,” *Nature*, vol. 541, no. 7636, pp. 196–199, 2017.

[8] M. H. Chen, D. Xing, V. C. Su, Y. C. Lee, Y. L. Ho, and J. J. Delaunay, “GaN Ultraviolet Laser based on Bound States in the Continuum (BIC),” *Advanced Optical Materials*, vol. 11, no. 6, pp. 1–8, 2023.

[9] B. Duan, S. Liu, X. Liu, X. chong Yu, C. Wang, and D. Yang, “High-Q quasi-BIC in photonic crystal nanobeam for ultrahigh sensitivity refractive index sensing,” *Results in Physics*, vol. 47, Apr. 2023.

[10] S. Joseph, S. Pandey, S. Sarkar, and J. Joseph, “Bound states in the continuum in resonant nanostructures: An overview of engineered materials for tailored applications,” *Nanophotonics*, vol. 10, no. 17, pp. 4175–4207, 2021.

[11] Z. Dong, Z. Mahfoud, R. Paniagua-Domínguez, H. Wang, A. I. Fernández-Domínguez, S. Gorelik, S. T. Ha, F. Tjiptoharsono, A. I. Kuznetsov, M. Bosman, and J. K. W. Yang, “Nanoscale mapping of optically inaccessible

bound-states-in-the-continuum," *Light: Science and Applications*, vol. 11, no. 1, 2022.

[12] E. M. B. Fahmy, Z. Ouyang, D. Colucci, N. Le Thomas, J. Van Campenhout, B. Kunert, and D. Van Thourhout, "One-dimensional photonic crystal nano-ridge surface emitting lasers epitaxially grown on a standard 300 mm silicon wafer," *Light: Science & Applications*, vol. 15, no. 1, p. 120, 2026. [Online]. Available: https://www.nature.com/articles/s41377-025-02061-z

[13] E. M. B. Fahmy, T. Coenen, and D. Van Thourhout, "Probing bound states in the continuum in ingaas/gaas photonic-crystal nano-ridge lasers on 300 mm silicon with angle-resolved cathodoluminescence and photoluminescence," 2026, submitted.

[14] J. Si, M. Wang, Z. Chen, Y. Xu, J. Chen, Z. Zhang, W. Liu, C. Peng, and W. Zheng, "Active beam steering enabled by photonic crystal surface emitting laser," *2023 Opto-Electronics and Communications Conference, OECC 2023*, 2023.

[15] Z. Chen, X. Yin, J. Jin, Z. Zheng, Z. Zhang, F. Wang, L. He, B. Zhen, and C. Peng, "Observation of miniaturized bound states in the continuum with ultra-high quality factors," *Science Bulletin*, vol. 67, no. 4, pp. 359–366, 2022. [Online]. Available: https://linkinghub.elsevier.com/retrieve/pii/S2095927321006769

6

Advanced Design Concepts

6.1 Increasing Efficiency Using Bottom Reflector 130
6.2 Shaping Output Field 132
6.3 Electrical Injection 135
6.3.1 Strategy for Small NRSELs 135
6.3.2 Strategy for Large NRSELs 137
6.4 Alternative Nano-Ridge Shape for Electrical Injection . . 138
6.5 2D NRSELs 140
6.6 Additive/Post-Growth Wavelength Tuning 144
6.7 Summary 145
Bibliography 146

This chapter explores advanced design concepts and simulations aimed at enhancing the laser's overall performance. We investigate methods to increase the device's efficiency and tailor the output field shape through refined photonic crystal engineering. Additionally, we outline a strategic approach for achieving effective electrical injection and present a method for additive wavelength tuning to provide precise spectral control.

6.1 Increasing Efficiency Using Bottom Reflector

To increase the efficiency of NRSELs, a bottom reflector can be added below the nano-ridge array to reflect downward emitted light back upwards. Due to the assymetry of the nano-ridge structure, a significant portion of the emitted light is directed downwards into the substrate. By incorporating a bottom reflector, this downward emission can be redirected upwards, enhancing the overall upward emission efficiency.

This can be achieved by incorporating a distributed Bragg reflector (DBR) or a metal mirror beneath the nano-ridge array during the fabrication process. Figure 6.1 illustrates the concept of adding a bottom reflector to the NRSEL structure.

The separation (d) between the nano-ridge array and the bottom reflector sets the relative phase between the directly upward-emitted field and the field that is emitted downward, reflected by Au, and returns upward. Using a simple interference model,

$$E_{\uparrow,\mathrm{tot}} = E_{\uparrow} + Ae^{i(2\beta d+\phi_{\mathrm{eff}})}, \tag{6.1}$$

where $\beta = 2\pi n_s/\lambda$ is the propagation constant in the spacer (effective index n_s), and ϕ_{eff} is an effective phase term that includes the Au reflection phase and any additional phase offsets of the structure. Constructive interference (maximum upward emission) occurs when

$$2\beta d + \phi_{\mathrm{eff}} = 2\pi m, \tag{6.2}$$

and destructive interference (minimum upward emission) occurs when

$$2\beta d + \phi_{\mathrm{eff}} = (2m+1)\pi, \tag{6.3}$$

with $m \in \mathbb{Z}$. The spacing between a constructive and a destructive condition is therefore

$$\Delta d = \frac{\pi}{2\beta} = \frac{\lambda}{4n_s}. \tag{6.4}$$

Since n_s (and ϕ_{eff}) is not known exactly, we scan d in simulation. The simulation mesh ($20\,\mathrm{nm}$) also limits the spacing resolution. We started the sweep at an arbitrary separation of $d = 2\,\mu\mathrm{m}$ to keep the Au mirror sufficiently far from the cavity mode and reduce near-field interaction with the metal. From the sweep, we find a maximum around $d = 2.07\,\mu\mathrm{m}$ with $Q = 319{,}404$, compared to $Q \approx 20{,}000$ without the bottom Au mirror. At $d = 2.00\,\mu\mathrm{m}$, we obtain $Q = 28{,}000$, which is consistent with a constructive-interference condition. The difference between these two points is $\sim 70\,\mathrm{nm}$, comparable to the analytical estimate $\Delta d = \lambda/(4n_s) = 982.6\,\mathrm{nm}/(4 \times 3.57) \approx 69\,\mathrm{nm}$.

Simulations show an increase in upward emission intensity to more than 73% when a bottom reflector is used combined constructively with the side mirrors (compared to 70% with destructive condition), as shown in figures 6.1c,d. The emission directed upward is enhanced due to constructive interference between the directly emitted upward field and the reflected downward field, as shown in figure 6.1c. Conversely, when the bottom reflector is positioned to create destructive interference, the upward emission is reduced as shown in figure 6.1d. Overall, incorporating a bottom reflector can significantly enhance the upward emission of NRSELs. This enhancement in efficiency can lead to lower lasing thresholds and improved overall performance of the NRSEL devices.

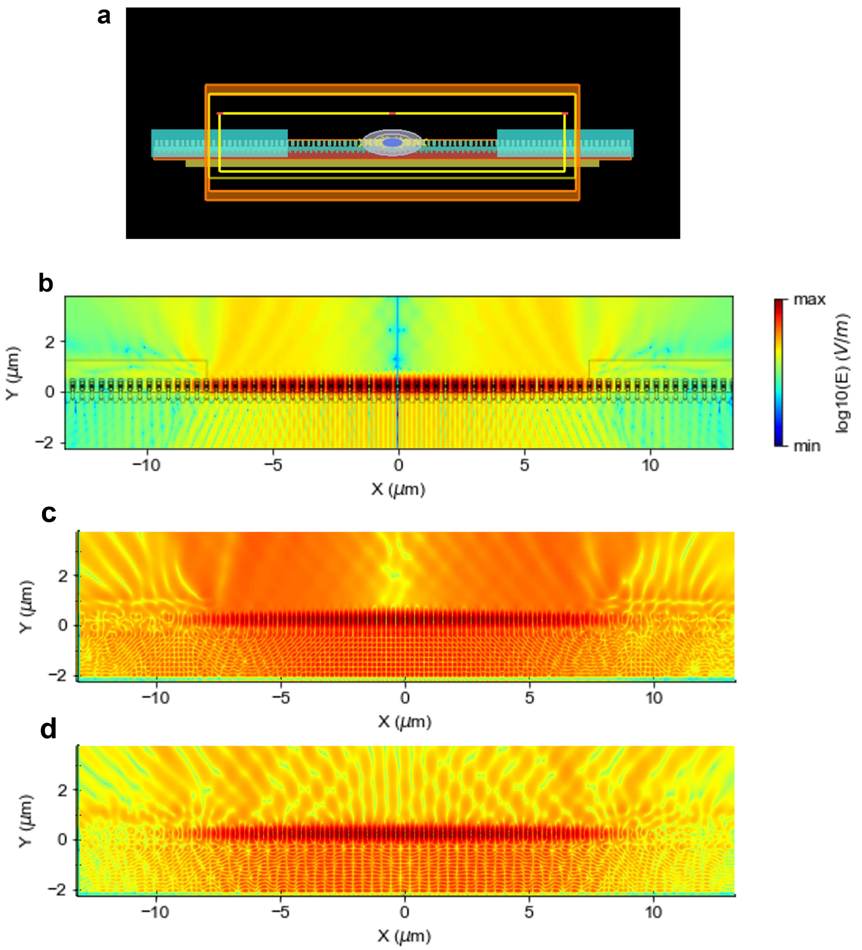

Figure 6.1: Bottom reflector to increase efficiency. (a) FDTD setup. (b) Simulated NRSEL mode profile without bottom reflector showing downward emission. (c) Simulated NRSEL mode profile with bottom reflector showing constructive interference and increased upward emission. (d) Simulated NRSEL mode profile with bottom reflector showing destructive interference and decreased upward emission.

6.2 Shaping Output Field

Shaping the output field of NRSELs can be achieved by exploiting the unique properties of the BIC mode and the finite cavity effects. By tailoring the nano-ridge array geometry and leveraging the mode quantization due to the finite cavity size, we can manipulate the far-field emission pattern to achieve desired beam profiles.

This is useful for applications requiring specific beam shapes or directions.

The BIC mode in NRSELs offers a unique opportunity to engineer the far-field emission pattern by tailoring the nano-ridge array geometry. By modifying parameters such as the nano-ridge width, height, and periodicity, we can influence the photonic band structure and the associated BIC characteristics. This enables control over the directionality, divergence, and polarization of the emitted beam. As we have previously shown, modes TE_{21L} and TE_{22L} can be excited by changing the nano-ridge width and periodicity. Each has a different field distribution and farfield pattern, as shown in figure 6.2. By carefully designing the nano-ridge geometry, we can selectively excite these modes to achieve desired emission properties. This level of control opens up possibilities for customizing NRSEL emission characteristics for specific applications, such as on-chip optical interconnects or sensing.

The choice of BIC mode can be guided by the intended application. For optical interconnects, a near-circular far-field with low divergence, as observed for TE_{22L}, is generally preferred because it concentrates power into a single on-axis lobe and improves overlap with standard coupling optics (e.g., lenses or single-mode fibers), thereby relaxing alignment and packaging tolerances. In contrast, the star-shaped, higher-divergence far field of TE_{21L} distributes power among multiple angular lobes, which can reduce single-aperture coupling efficiency but may be advantageous for applications that benefit from non-Gaussian emission. The structured, multi-lobed emission of TE_{21L} can also be attractive for structured illumination, where the far-field pattern itself serves as a projected intensity distribution without additional diffractive optics. Consequently, TE_{22L} is more attractive when efficient, well-collimated emission is required (e.g., interconnects), whereas TE_{21L} can be beneficial when the sensing metric or illumination function leverages far-field pattern structure and its perturbation-induced changes.

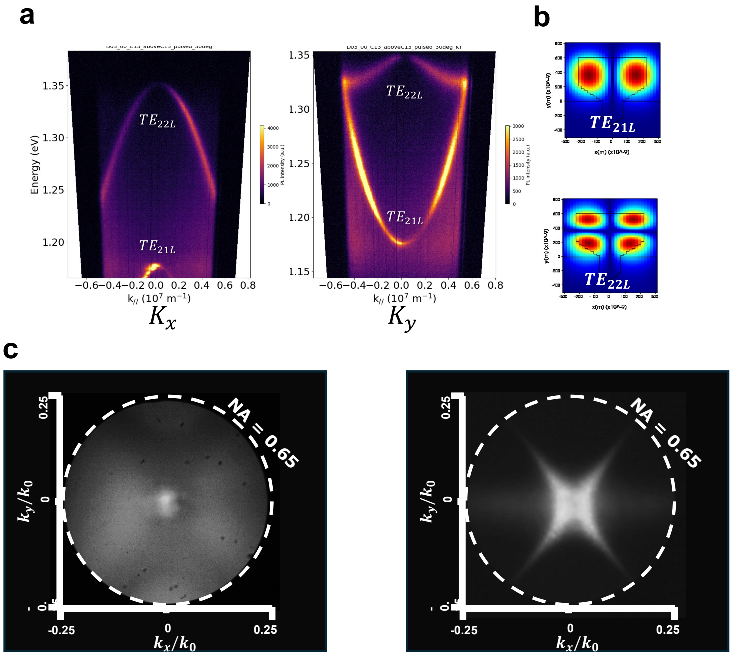

Figure 6.2: Different BIC modes with different farfield patterns. (a) Angle-resolved photoluminescence measurement showing TE_{21L} and TE_{21L} modes. (b) Simulated mode profiles of TE_{21L} and TE_{21L} modes. (c) Experimental farfield patterns of TE_{21L} and TE_{21L} modes.

6.3 Electrical Injection

PCSELs have been electrically injected for a long time [1–3]. Similarly, single nano-ridge lasers have also been electrically injected [4]. However, electrical injection for NRSELs has not been demonstrated yet. We could not get doped wafers to test electrical injection in this thesis. However, we discuss strategies for implementing electrical injection in future work.

6.3.1 Strategy for Small NRSELs

To achieve electrical injection in small NRSELs, such as devices of 5 μm length, a viable approach involves the use of electrodes at the ends of the nano-ridge array, as shown in figure 6.3. This configuration allows for efficient current injection while minimizing interference with the optical mode and preserving vertical emission. A key challenge with placing the electrodes at the two ends is the non-uniform current distribution that can occur due to the carriers recombining before reaching the center of the active region. The silicon substrate serves as the n-type contact, while the p-type contact is made through the top of the nano-ridge [4]. To address this, the doping profile within the nano-ridge can be engineered to facilitate better carrier transport towards the center of the active region. Additionally, the doping profile of the substrate below the nano-ridge can be optimized as well, through splitting the substrate in 3 regions with different doping as shown in figure 6.4.

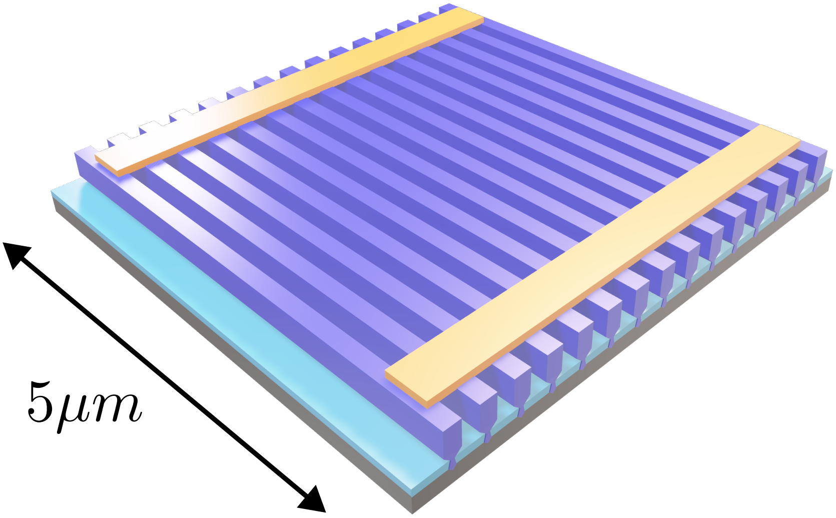

Figure 6.3: Schematic of electrical injection for small NRSELs with contacts at the two ends of the nano-ridge array.

Prelimenary TCAD simulations were carried out to study the current distribution in small NRSELs with contacts at the two ends. The results, shown in figure 6.4, indicate that by increasing the doping concentration in the p-GaAs decreases the variation in carrier density in the QW's along the nano-ridge length. This leads to a more uniform current distribution across the active region, which is crucial for achieving efficient lasing. However, increasing the doping concentration also poses challenges, such as potential changes in the nano-ridge shape during growth and increased optical losses due to free carrier absorption. Therefore, a balance must be struck between achieving uniform current injection and maintaining optimal optical properties. Using a doping concentration of $5 \times 10^{19}\ \mathrm{cm}^{-3}$ along with a thin layer of heavily doped p++ layer ($1 \times 10^{20}\ \mathrm{cm}^{-3}$) on top of the p-GaAs region can help improve carrier uniformity while mitigating some of these challenges. FDTD simulations show a approximately 5% decrease (from 30000 to 27000) in the Q factor due to the increased doping concentration, which is a reasonable trade-off for achieving more uniform current injection and improved lasing performance. Further optimization of the doping profile and device geometry may be necessary to fully realize the benefits of this approach while minimizing any adverse effects on the optical properties of the NRSEL.

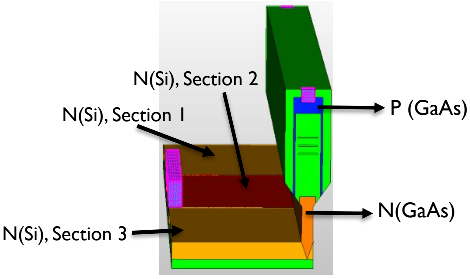

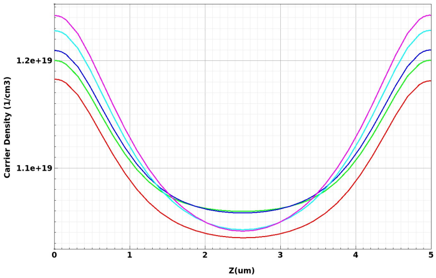

No	P (GaAs) (1/cm³)	N(GaAs) (1/cm³)	N(Si) Section 1(1/cm³)	N(Si) Section 2 (1/cm³)	N(Si) Section 3 (1/cm³)
1	1E20	1E19	1E17	1E19	1E17
2	1E20	5E18	1E17	1E19	1E17
3	1E20	1E18	1E17	1E19	1E17
4	1E20	5E17	1E17	1E19	1E17
5	1E20	1E17	1E17	1E19	1E17

Figure 6.4: Spatial distribution of quantum well carrier density (along length of nano-ridge-bottom QW) for different doping concentrations. (courtesy of Andualem A. Yimam)

6.3.2 Strategy for Large NRSELs

We discussed in chapter 5 section 5.5 that larger NRSELs exhibit mode quantization due to the finite cavity size. This leads to distinct field distributions with nodes and antinodes. By placing electrical contacts at the optical field nodes, we can minimize absorption losses while still achieving efficient current injection. This approach leverages the spatial distribution of the optical mode within the cavity, allowing for effective current injection while preserving the quality factor of the resonant mode. By carefully designing the contact geometry and placement, it might be possible to achieve efficient electrical injection without significantly perturbing the optical properties of the NRSEL. This strategy is particularly advantageous for larger NRSELs, where the mode structure is more complex and the impact of contact placement on the optical mode can be more pronounced. Overall, this node-based contact placement approach provides a promising pathway for implementing electrical injection in large NRSELs while maintaining their desirable optical characteristics. Figure 6.5 illustrates this concept, showing contacts strategically positioned at the optical field nodes along the nano-ridge array.

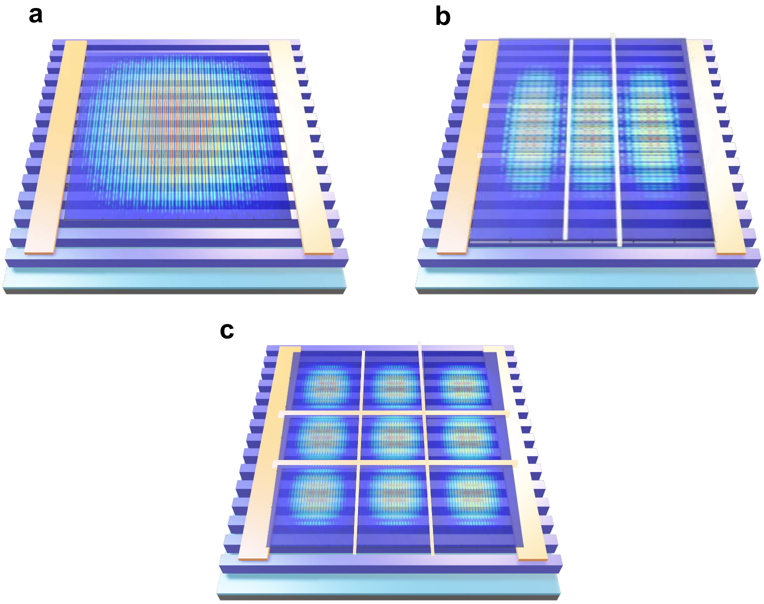

Figure 6.5: Schematic of electrical injection for large NRSELs with contacts placed at optical field nodes to minimize absorption losses. (a) Top view showing contact placement along the nano-ridge array at the ends for the cavity's fundamental mode. (b,c) contact placement for higher order modes. (The mode distribution in b,c is an illustration).

6.4 Alternative Nano-Ridge Shape for Electrical Injection

Another approach for electrical injection in large NRSELs could involve using a different shaped nano-ridge. Using a nano-ridge shape that has a top hat of GaAs, as shown in figure 6.6, would push the optical mode down to the active region and avoid overlap with the top contact. This design is feasible within the NRE growth technique. Using this approach, We would not suffer from non-uniform current injection as the contacts could be distributed along the length of the nano-ridge, ensuring a more uniform carrier distribution across the active region without complex doping profiles. This method would allow the flexibility of contact placement to optimize both electrical and optical performance. Any farfield shape (allowed by the BIC mode) can be achieved without worrying about the placement of the contacts as they will be far away from the optical mode. This would be applicable for both small and large NRSELs and is the most promising approach for electrical injection in NRSELs. Wang et al. have demonstrated electrical injection in large area photonic crystal surface-emitting lasers (1.5 mm x 1.5 mm) using a top grid electrode [5], as shown in figure 6.7. The downside of this approach is the blocking of some of the emitted light by the top contact grid. However, this can be minimized by optimizing the grid design to balance electrical injection uniformity and optical transmission. They also showed minimal impact on the farfield pattern and beam quality. A similar approach can be used for NRSELs using the nano-ridge shape shown in figure 6.6. Alternatively, light can be extracted from the bottom of the nano-ridge exploiting silicon's transparency window at longer wavelengths (e.g. 1500 nm), which would completely eliminate any overlap between the optical mode and the top contact.

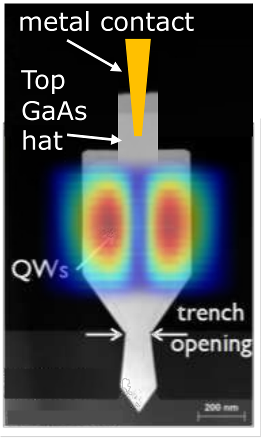

Figure 6.6: Schematic of a different nano-ridge shape for electrical injection, featuring a top hat of GaAs that pushes the optical mode down to the active region and avoids overlap with the top contact.

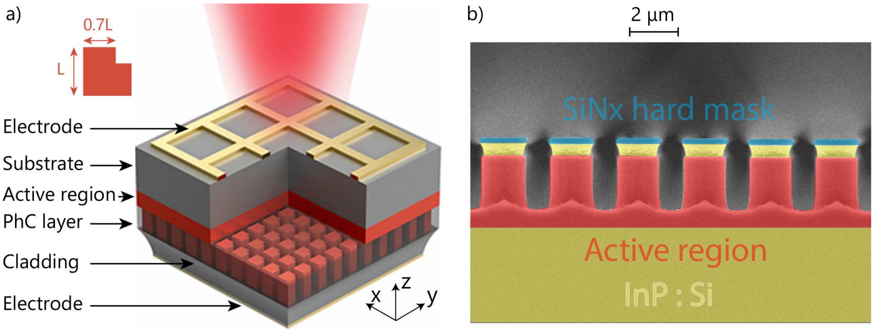

Figure 6.7: Electrical injection in large area PCSELs using a top grid electrode (reproduced from [5]).

6.5 2D NRSELs

Full control over the period of the grown nano-ridges is difficult. The choice of the period could be limited by the growth conditions and the loading effects during the MOCVD growth. To overcome this limitation, 2D NRSELs can be designed by introducing a second period in the direction perpendicular to the nano-ridges. This can be achieved by depositing silicon between the nano-ridges and etching it to form a square lattice, as shown in figure 6.8. The periodicity in both directions creates a 2D BIC mode that can be used for lasing. This offers more control over the farfield pattern and beam shaping. It also allows to independently control the lasing mode post growth by choosing the second period of the silicon waveguides. This could allow tuning the lasing wavelength post growth and more control over the process independently of the nano-ridge growth.

Preliminary simulations show the existence of additional modes in the band structure due to the second period, as shown in figure 6.8. The simulations were done for a fillfactor = 0.5 for both the nano-ridges and the silicon waveguides. These modes can be engineered to achieve desired lasing characteristics. The resonance wavelength can be tuned by changing the second period of the silicon waveguides, allowing for post-growth wavelength control as shown in figure 6.9. Further simulations are needed to understand the complex bandstructure of these 2D NRSELs and calculate the mode profiles and the farfield patterns.

We carried out preliminary experiments to deposit amorphous silicon between nano-ridges of large periods as a first test ($\Lambda = 885nm$). however, the silicon did not fill the space between the nano-ridges completely. it started accumulating on the sidewalls and top of the nano-ridges which prevents complete filling of the space between the nano-ridges, as shown in figure 6.10. Further optimization of the deposition conditions is needed to achieve complete filling of the space between the nano-ridges.

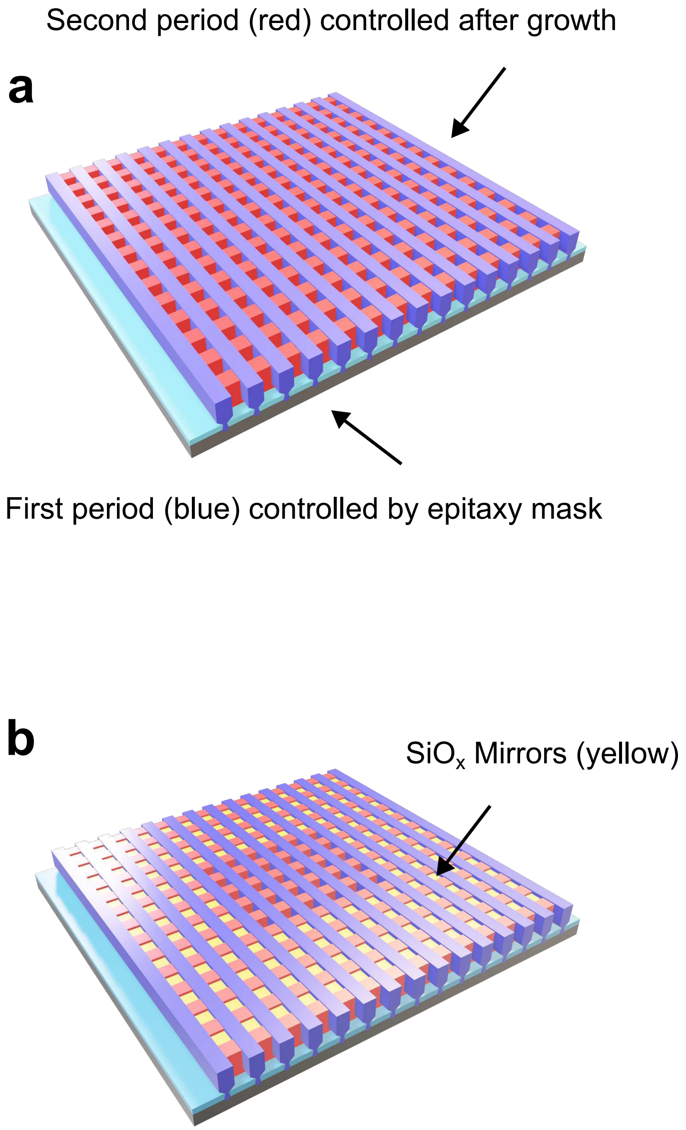

Figure 6.8: Schematic of 2D NRSELs with square lattice. The second period is formed by silicon deposited between the nano-ridges then etched to form a square lattice. The periodicity in both directions creates a 2D BIC mode that can be used for lasing. This offers more control over the farfield pattern and beam shaping. It also allows to independently control the lasing mode post growth by choosing the second period of the silicon waveguides, enabling tuning the lasing wavelength post growth and more control over the process independently of the nano-ridge growth.

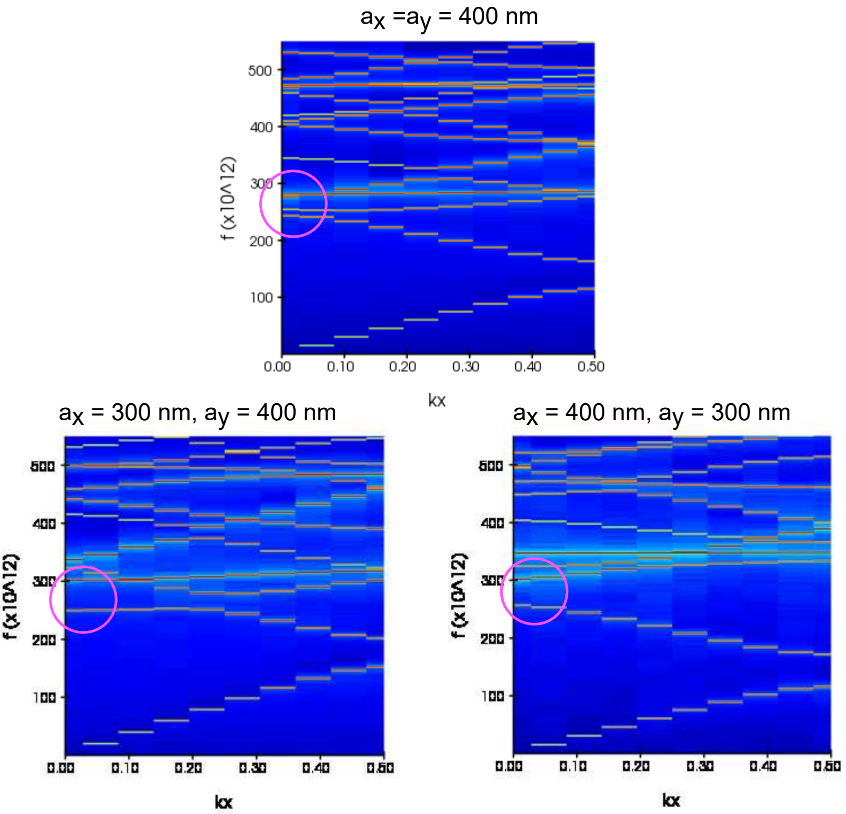

Figure 6.9: Simulated band structure of 2D NRSELs showing additional modes introduced by the second in-plane period. (a) $a_x = a_y = 400\,\mathrm{nm}$. *(b)* $a_x = 300\,\mathrm{nm}$, $a_y = 400\,\mathrm{nm}$. *(c)* $a_x = 400\,\mathrm{nm}$, $a_y = 300\,\mathrm{nm}$. *In all cases, the silicon waveguide height equals the nano-ridge height. Varying either period modifies the band dispersion and shifts the resonant wavelengths, providing additional flexibility for future designs and post-growth wavelength control.*

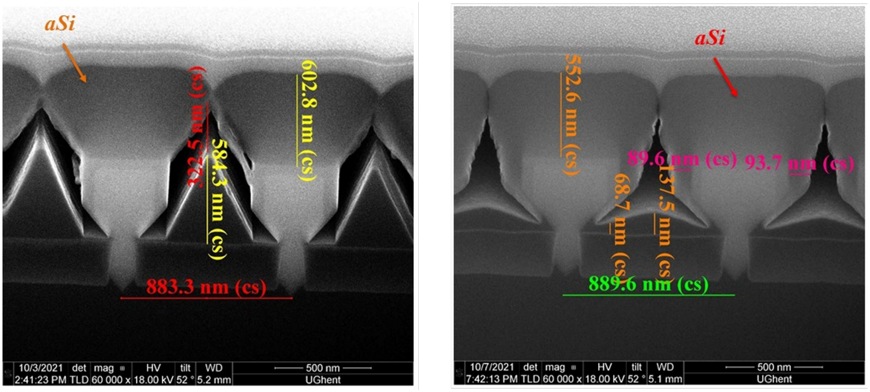

Figure 6.10: SEM images of amorphous silicon deposited between the nano-ridges ($\Lambda = 885nm$). The two images are using different growth conditions. The silicon doesn't fill the space between the nano-ridges completely. It starts accumulating on the sidewalls and top of the nano-ridges which prevents complete filling of the space between the nano-ridges. (courtsey of Zhongtao Oyuang)

6.6 Additive/Post-Growth Wavelength Tuning

As we discussed in chapter 2, the resonance wavelength of NRSELs is highly dependent on the nano-ridge width and period. However, once the nano-ridges are grown, these parameters are fixed. To achieve post-growth wavelength tuning, we can explore additive manufacturing techniques to modify the effective refractive index of the nano-ridge array. One approach could involve depositing a thin layer of high-index material on top of the nano-ridges, effectively increasing the overall refractive index and shifting the resonance wavelength. By carefully selecting the thickness and refractive index of the added layers, we can achieve the desired wavelength tuning while maintaining the integrity of the nano-ridge structure. This post-growth modification strategy opens up new possibilities for tailoring the emission properties of NRSELs. Simulations show that a change of just 1 nm in nano-ridge's width can result in a shift of approximately 2.5 nm in the resonance wavelength, for a period of 380 nm and a height of 500 nm as shown in figure 6.11. This sensitivity highlights the potential for fine-tuning the resonance wavelength through precise control of the nano-ridge dimensions via additive manufacturing techniques.

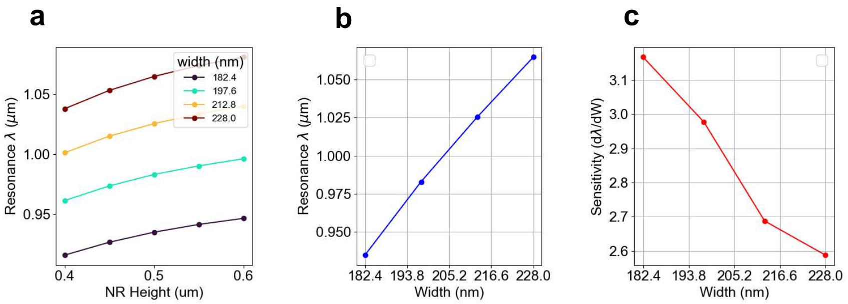

Figure 6.11: Resonance of TE_{21L} *changes with change in (a) width of the nano-ridge, (b) height, and (c) sensitivity of resonance wavelength to width* ($nm\,nm^{-1}$)*.*

6.7 Summary

This chapter presents advanced design concepts and simulations to further improve NRSEL performance beyond the baseline devices. First, a bottom reflector (e.g., Au or a DBR) is introduced to recycle downward emission and enhance upward extraction through controlled interference, yielding a strong increase in upward emission and a substantial improvement in the simulated Q factor. Next, we discuss output-field engineering by tailoring the nano-ridge geometry to selectively access different BIC modes (e.g., TE_{21L} and TE_{22L}) with distinct far-field patterns, enabling beam shaping through photonic-crystal design. We then outline practical routes toward electrical injection, including contact strategies for short and long cavities, supported by preliminary TCAD simulations indicating that appropriate p-doping profiles can improve carrier uniformity, and we discuss an alternative nano-ridge cross-section that pushes the optical mode away from the top contact to reduce absorption while allowing distributed contacting. Finally, we propose 2D NRSEL concepts that add a second in-plane period using silicon structuring for increased control of the band structure, and we describe additive or post-growth wavelength tuning via dielectric deposition or regrowth to adjust the effective index and shift the resonance with fine spectral control.

Bibliography

[1] M. Imada, S. Noda, A. Chutinan, T. Tokuda, M. Murata, and G. Sasaki, "Coherent two-dimensional lasing action in surface-emitting laser with triangular-lattice photonic crystal structure," *Applied Physics Letters*, vol. 75, no. 3, pp. 316–318, 1999. [Online]. Available: https://pubs.aip.org/apl/article/75/3/316/108652/Coherent-two-dimensional-lasing-action-in-surface

[2] K. Hirose, Y. Liang, Y. Kurosaka, A. Watanabe, T. Sugiyama, and S. Noda, "Watt-class high-power, high-beam-quality photonic-crystal lasers," *Nature Photonics*, vol. 8, no. 5, pp. 406–411, 2014.

[3] S. Noda, T. Inoue, M. Yoshida, J. Gelleta, M. D. Zoysa, and K. Ishizaki, "High-power and high-beam-quality photonic-crystal surface-emitting lasers: A tutorial," *Advances in Optics and Photonics*, vol. 15, no. 4, p. 977, 2023. [Online]. Available: https://opg.optica.org/abstract.cfm?URI=aop-15-4-977

[4] Y. De Koninck, C. Caer, D. Yudistira, M. Baryshnikova, H. Sar, P.-Y. Hsieh, C. I. Özdemir, S. K. Patra, N. Kuznetsova, D. Colucci, A. Milenin, A. A. Yimam, G. Morthier, D. Van Thourhout, P. Verheyen, M. Pantouvaki, B. Kunert, and J. Van Campenhout, "GaAs nano-ridge laser diodes fully fabricated in a 300-mm CMOS pilot line," *Nature*, vol. 637, no. 8044, pp. 63–69, 2025. [Online]. Available: https://doi.org/10.1038/s41586-024-08364-2

[5] Z. Wang, Y. Liang, B. Meng, Y.-T. Sun, G. Omanakuttan, E. Gini, M. Beck, I. Sergachev, S. Lourdudoss, J. Faist, and G. Scalari, "Large area photonic crystal quantum cascade laser with 5 w surface-emitting power," *Optics Express*, vol. 27, no. 16, p. 22708, 2019. [Online]. Available: https://opg.optica.org/abstract.cfm?URI=oe-27-16-22708

7

Conclusion and outlook

7.1 Conclusions 147
7.2 Outlook 149
Bibliography 150

7.1 Conclusions

This thesis introduced the first nano-ridge surface-emitting laser (NRSEL) epitaxially grown on a trench-patterned 300 mm silicon wafer. Experimentally, the devices show stimulated emission with thresholds as low as $5\ \mathrm{kW/cm^2}$ and single-mode operation, demonstrating that a compact, lithographically defined, CMOS-compatible surface-emitting laser can be realized through monolithic III–V nano-ridge epitaxy on 300 mm silicon wafers.

A central result is that the emission originates from a band-edge, BIC-mediated mode of the nano-ridge array. Angle-resolved spectroscopy reveals the associated photonic dispersion and the strong suppression of radiative leakage at the Γ point, consistent with the BIC picture. The pronounced spontaneous-emission enhancement observed even under nanoampere-level cathodoluminescence excitation further supports the presence of a high-Q, Γ-point band-edge resonance. These ingredients explain the low lasing threshold and the directional, surface-emitting far-field patterns that make NRSELs attractive for scalable on-chip light sources.

We further showed that the NRSEL wavelength can be tuned via geometry. FDTD simulations predict a sensitivity of 2.5 $\mathrm{nm\,nm^{-1}}$ to the nano-ridge width. In line with this trend, photoluminescence and SEM metrology reveal a 35 nm shift in peak wavelength accompanied by a 10 ± 5 nm change in nano-ridge width from wafer edge to center, corresponding to an effective sensitivity of 3.5 $\mathrm{nm\,nm^{-1}}$. More broadly, within-field loading effects introduce a $\simeq 10$ nm width gradient, while wafer-scale nonuniformity between center and edge dies yields a ~ 35 nm width difference, shifting the band-edge resonance by $\simeq 20$ nm. Exploiting these dimensional variations enables two distinct laser designs on the same 300 mm substrate, highlighting multi-wavelength potential within a CMOS-compatible process flow.

Looking forward, a tighter process-control strategy should reduce both wafer-to-wafer and die-to-die variability and thereby improve wafer-level uniformity of the nano-ridge dimensions. The die-averaged SEM data already indicate that excellent width control is achievable on some wafers, with D05 and D06 exhibiting relatively small die-to-die width spreads (D05: 189–194 nm, mean ≈ 191 nm with $\sigma \approx 3$ nm; D06: 186–196 nm, mean ≈ 190 nm with $\sigma \approx 4$ nm). The measured dimensions for the center dies for each wafer are summarized in Tables 3.2 and 3.3.

Beyond process tuning, nano-ridge uniformity can be strengthened by lithographically defining the ridge width with an oxide template: a narrow trench seeds the ridge, while a second, wider oxide opening above it defines the maximum allowable lateral expansion, as shown in Fig. 3.6. During epitaxy the ridge expands until it meets the oxide sidewalls, which then act as a geometric stop that stabilizes the final ridge width and suppresses further sidewall growth. This template-limited, self-stopping width control has already been demonstrated for nano-ridge HBT structures, where the oxide boundary is used to lock in the ridge width for realizing reproducible transistor geometries across a 300 mm wafer [1].

Finally, we discussed pathways to extend both functionality and wavelength coverage. By adapting material composition, a wide spectral range should be addressable; for example, O-band operation around 1.3 μm has been demonstrated in InGaAs/GaAs nano-ridge lasers by tuning indium content [2]. Extending nano-ridge engineering to alternative material systems such as GaSb opens prospects for wavelengths beyond 1.5 μm [3]. We also outlined a route toward electrical injection, motivated by prior demonstrations of electrically injected nano-ridge lasers using a p–i–n junction and damascene-fabricated tungsten plug contacts [4]. For NRSELs, electrode placement must preserve the optical mode profile and keep the surface-emitted beam unobstructed; for larger devices, placing contacts at optical-field nodes (informed by the observed mode quantization in finite cavities) provides a practical strategy to minimize optical loss.

7.2 Outlook

Future work could focus on experimentally demonstrating electrically injected NRSEL devices, building upon earlier electrically injected nano-ridge lasers [4]. A key near-term task is to implement an injection geometry that preserves vertical emission: tungsten plugs (or alternative contacts) should be positioned to minimize overlap with the optical mode and to avoid blocking the emitted beam. For larger cavities, contact placement at optical-field nodes provides a natural strategy to reduce absorption loss while maintaining uniform current injection.

At the platform level, improving dimensional uniformity (within-field and across-wafer) will be important to tighten wavelength control and device-to-device reproducibility. In parallel, integrating NRSELs with passive silicon photonics, electronic drivers, and on-chip micro-optics can translate the demonstrated directionality and low-threshold operation into practical systems.

Finally, extending the accessible wavelength range remains a compelling direction: alloy and heterostructure engineering in InGaAs-based nano-ridges can address the O-band [2], while GaSb-based nano-ridge engineering offers a route toward longer infrared wavelengths [3]. Together, these efforts can broaden the NRSEL technology toward applications in telecommunications, LiDAR, environmental sensing, and spectroscopy.

Bibliography

[1] Y. Mols, A. Vais, S. Yadav, L. Witters, K. Vondkar, R. Alcotte, M. Baryshnikova, G. Boccardi, N. Waldron, B. Parvais, N. Collaert, R. Langer, and B. Kunert, "Monolithic integration of nano-ridge engineered ingap/gaas hbts on 300 mm si substrate," *Materials*, vol. 14, no. 5682, 2021. [Online]. Available: https://www.mdpi.com/1996-1944/14/19/5682

[2] D. Colucci, M. Baryshnikova, Y. Shi, Y. Mols, M. Muneeb, Y. D. Koninck, D. Yudistira, M. Pantouvaki, J. V. Campenhout, R. Langer, D. V. Thourhout, and B. Kunert, "Unique design approach to realize an O-band laser monolithically integrated on 300 mm Si substrate by nano-ridge engineering," *Opt. Express*, vol. 30, no. 8, pp. 13 510–13 521, 2022.

[3] M. Baryshnikova, Y. Mols, Y. Ishii, R. Alcotte, H. Han, T. Hantschel, O. Richard, M. Pantouvaki, J. Van Campenhout, D. Van Thourhout, R. Langer, and B. Kunert, "Nano-Ridge Engineering of GaSb for the Integration of InAs/GaSb Heterostructures on 300 mm (001) Si," *Crystals*, vol. 10, no. 4, 2020. [Online]. Available: https://www.mdpi.com/2073-4352/10/4/330

[4] Y. De Koninck, C. Caer, D. Yudistira, M. Baryshnikova, H. Sar, P.-Y. Hsieh, C. I. Özdemir, S. K. Patra, N. Kuznetsova, D. Colucci, A. Milenin, A. A. Yimam, G. Morthier, D. Van Thourhout, P. Verheyen, M. Pantouvaki, B. Kunert, and J. Van Campenhout, "GaAs nano-ridge laser diodes fully fabricated in a 300-mm CMOS pilot line," *Nature*, vol. 637, no. 8044, pp. 63–69, 2025. [Online]. Available: https://doi.org/10.1038/s41586-024-08364-2

A

Appendix A

A.1 NRSEL Fabrication Process Flow

Photoresist AZ 5214 used as a mask for etching GaAs/AlGaAs nano-ridges using ICP. It was also used for defining side mirrors.

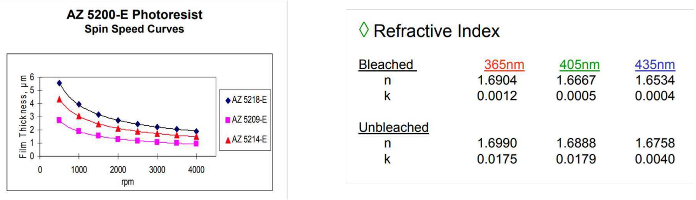

◊ Refractive Index

Bleached	365nm	405nm	435nm
n	1.6904	1.6667	1.6534
k	0.0012	0.0005	0.0004
Unbleached			
n	1.6990	1.6888	1.6758
k	0.0175	0.0179	0.0040

Figure A.1: (Left) Spin speed vs film thickness curves for AZ 5214 photoresist. (Right) Refractive index vs wavelength for AZ 5214 photoresist.

- **Spin coat Photoresist AZ 5214:** Acc: 1000, RPM: 4000, $t = 40\,\mathrm{s}$
- **Bake:** 3 mins at 100°C
- **Exposure:** 30 s (dependent on UV lamp intensity)
- **Development:** AZ400k:H_2O (1:3) for 20 s

- **Etching:** ICP (Inductively Coupled Plasma) etching for III–V recipe or stop after development for side mirrors.
- **ICP Settings for GaAs/AlGaAs:**
    - RF power: 50 W
    - Plasma forward power (ICP): 200 W
- **Resist Removal:** Using AZ100 at 80°C for 10 mins; resist was almost completely removed.

Figure A.2: ICP settings for etching GaAs/AlGaAs.

- **Characterization (Filmetrics and Dektak):**
    - Before ICP: PR film thickness = 1373 nm
    - After ICP (1 min): PR film thickness = 1270 nm
- **GaAs Etch Rate:**
    - 340 nm etched in 1 m 18 s.
    - Target 600 nm etch requires approximately 2 m 18 s (dependent on ICP settings).

A.2 ARCL Measurements for Different Periods

ARCL measurements for different periods are shown in figure A.3. The results show a good agreement with the simulated band structures and indicate that the resonance wavelength is period dependent as expected. The bigger periods have larger nano-ridges which allow the existence of many resonances and the band structure becomes more complex.

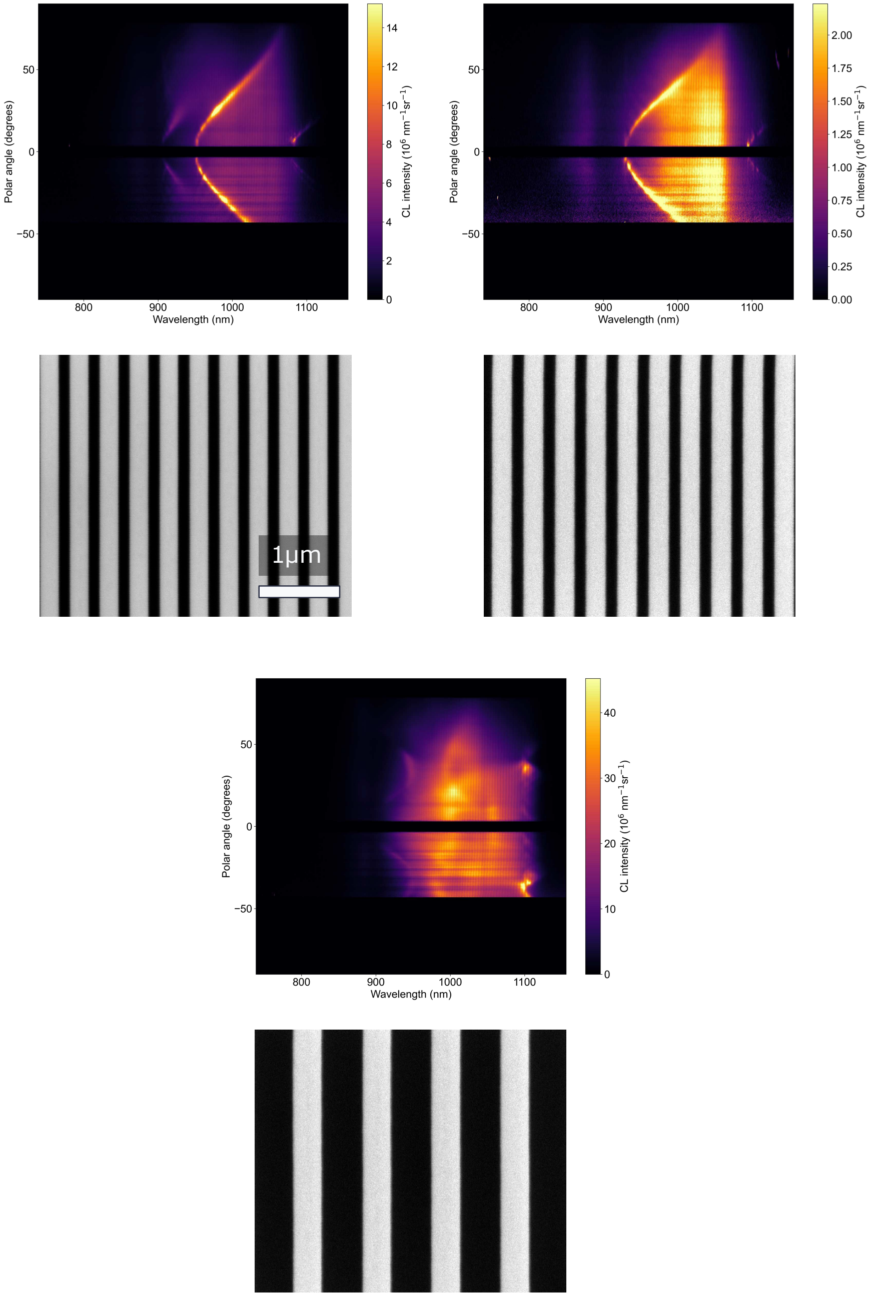

Figure A.3: ARCL measurements for different periods.

A.3 Polarized AR Reflection Measurements

White light reflection measurements for quasi infinite array with different polarizations are shown in figure A.4. The results show a good agreement with the simulated band structures and indicate that the resonance is polarization dependent as expected. the electric field is mostly polarized along the length of the nanoridges.

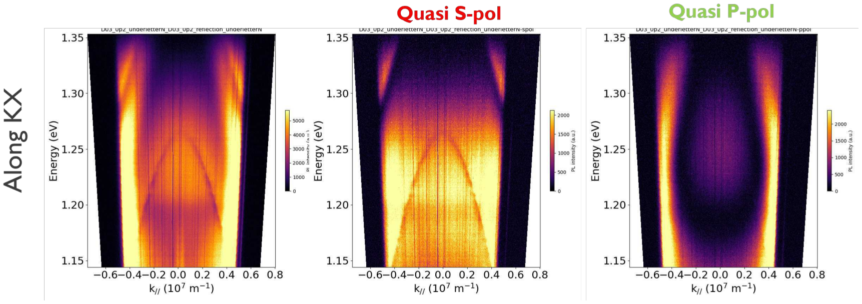

Figure A.4: White light reflection measurements for quasi infinite array with different polarizations.

A.4 ARPL Scan at Different Locations on the Field

Angle-resolved photoluminescence measurements at different locations on the sample are shown in figure A.5. The results show a good agreement with the simulated band structures and indicate that the resonance wavelength is location dependent as expected. The location dependence is due to the variation in the nano-ridge width across the field.

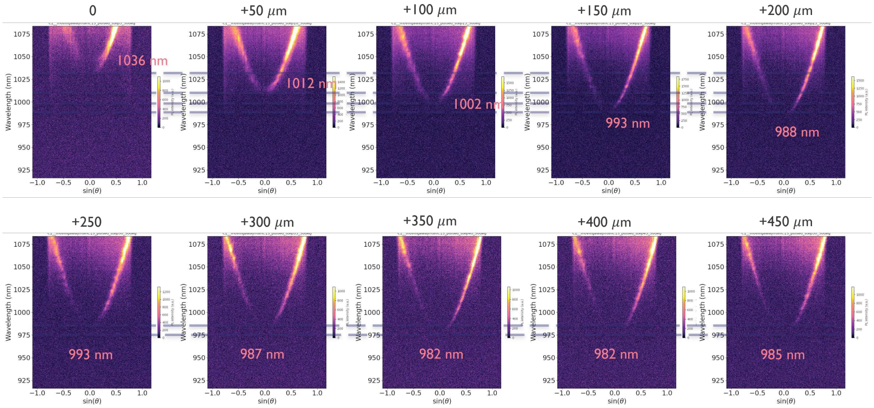

Figure A.5: Angle-resolved photoluminescence measurements at different locations on the sample.

A.5 Four-Wave Mixing

In our femtosecond pumping experiment, we observed new signals in addition to the primary pump and photo-resist peaks in three different NRSEL devices. Figures A.6, A.7, and A.8 show ARPL measurements where the FWM peaks are clearly visible. These peaks arise from nonlinear interactions within the nano-ridge structure, indicating strong third-order nonlinearity. The presence of these FWM signals suggests potential applications in wavelength conversion and all-optical signal processing using NRSELs. We are still not fully sure about the origin of these peaks and further investigation is needed to understand the underlying mechanisms.

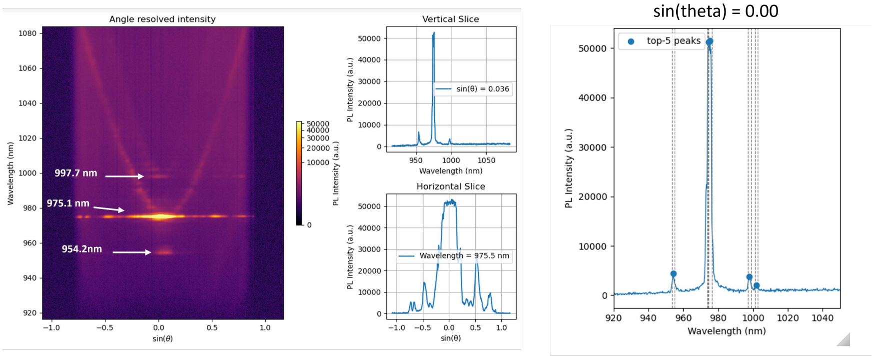

25 um cavity

Figure A.6: Angle-resolved photoluminescence measurement for a device of 25 um cavity, showing four wave mixing peaks.

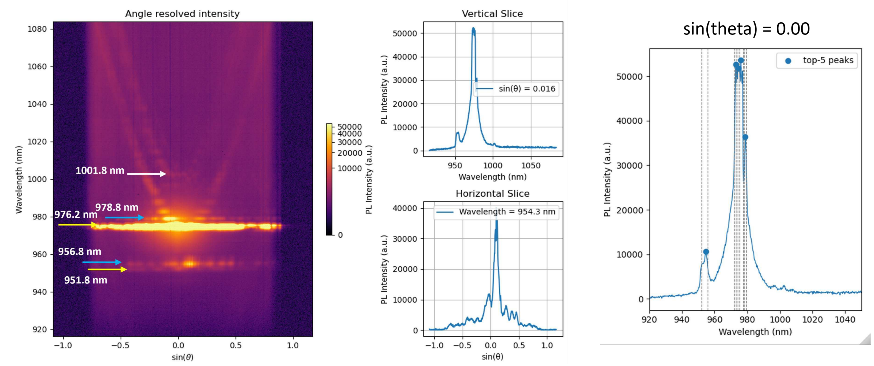

15 um cavity

Figure A.7: Angle-resolved photoluminescence measurement for a device of 15 um cavity, showing four wave mixing peaks.

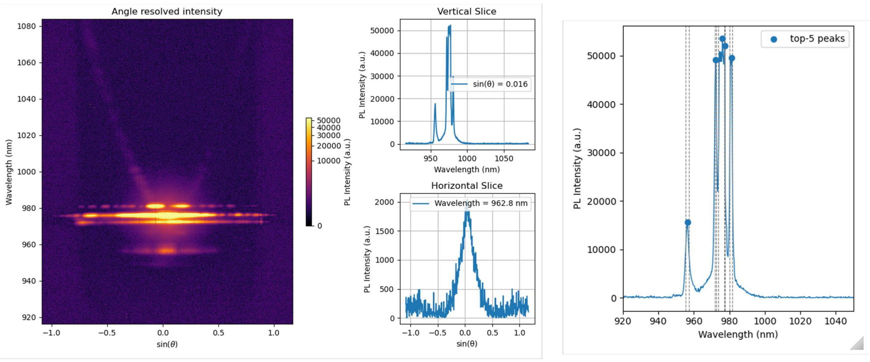

25 um cavity

Figure A.8: Angle-resolved photoluminescence measurement for a device of 25 um cavity, showing four wave mixing peaks.

The presence of a new peak at 954 nm is a signature of a third-order nonlinear interaction known as Four-Wave Mixing (FWM). Specifically, this is a degenerate FWM process where two photons from the intense pump (the fundamental band-edge lasing mode at 975 nm) interact with one photon from a secondary signal (associated with the photoresist band at 997.7 nm).

The physics follows the energy conservation law: $2\omega_{pump} = \omega_{signal} + \omega_{new}$, where the frequencies are related to the wavelengths by $\omega = c/\lambda$. By calculating the energy balance in terms of photon frequency (or ”inverse wavelength”), we find:

$$\frac{2}{975\text{ nm}} - \frac{1}{997.7\text{ nm}} \approx \frac{1}{953.3\text{ nm}}$$

This result closely matches the experimental observation of the generated peak at 954 nm.

A.6 Effect of Fabrication Variability on the Mode

To study the effect of fabrication variability on the cavity performance, we simulated the effect of the nano-ridge width variation on the Q factor and mode profile. The results are shown in figure A.9. Using random variations of the nano-ridge width with a standard deviation of 5 nm, we observed that the Q factor can vary significantly (decreases from 20000 to 9000 on average) and randomly, indicating that fabrication imperfections can have a substantial impact on cavity performance. The mode profile also showed distortions compared to the ideal case, which could affect lasing characteristics. This effect is known as anderson localization, where disorder in a periodic structure leads to the localization of light in parts of the cavity, as shown in figure A.9. This phenomenon can be detrimental to device performance, as it can increase losses and reduce the efficiency of light-matter interactions within the cavity. Therefore, controlling fabrication variability is crucial for optimizing NRSEL performance.

In our SEM measurements, we observed that the fabrication variability in our samples is around 10 nm on average for the period of interest $\Lambda = 380$ nm in wafer D03 (used in micro NRSELs fabrication). This suggests that the effects observed in the simulations are relevant to our experimental devices and highlights the importance of precise fabrication techniques to minimize variability and enhance device performance.

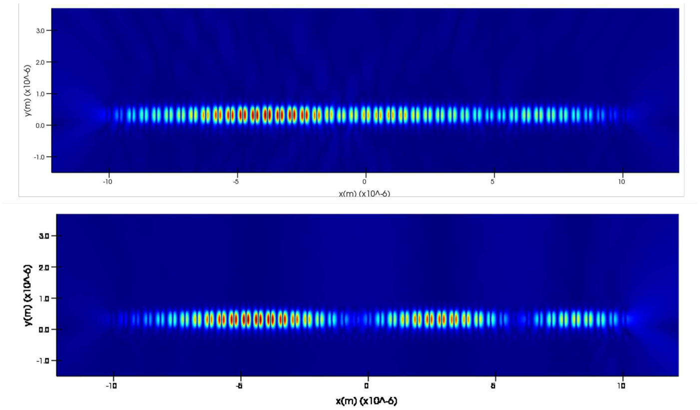

Figure A.9: FDTD simulation results showing the effect of fabrication variability on the cavity mode localization for two different random seeds.